

BULGARIAN CHEMICAL COMMUNICATIONS

2025 Volume 57 / Number 4

*Journal of the Chemical Institutes
of the Bulgarian Academy of Sciences
and of the Union of Chemists in Bulgaria*

Role of chemicals in dye-sensitized solar cells based on liquid-phase electrolyte for generation of electrical energy

A. Susawat¹, D. Meena¹, G. Meena¹, R.K. Meena¹, L. Baloat¹, Disha², A.S. Meena^{1*}

¹Department of Chemistry, University of Rajasthan, Jaipur, Rajasthan-302004, India

² Department of Applied Science and Humanities, BK Birla Institute of Engineering and Technology, Pilani, Rajasthan-333031, India

Received: May 03, 2024; Revised: September 11, 2025

The present study investigates the role of chemicals, such as methyl orange, in combination with fructose and sodium lauryl sulfate, in dye-sensitized solar cells (DSSCs) based on liquid-phase electrolyte for solar energy conversion. The liquid-phase electrolyte-based DSSC operates by converting solar energy into electrical energy through the formation of energy-rich intermediates that exhibit photogalvanic effect. The measured photovoltaic parameters of the cell include an open-circuit potential of 1090.0 mV and a short-circuit current of 670.0 μ A. The conversion efficiency and fill factor are calculated to be 4.68% and 0.2603, respectively. The storage capacity of the cell, evaluated in dark conditions, is determined to be 225.0 min. In addition, the influence of various parameters on the electrical output is examined, and the current-voltage (J-V) characteristics are analyzed. A possible mechanism for photocurrent generation in the electrolyte-based dye-sensitized solar cell is also proposed.

Keywords: photogalvanic effect, potential, current, conversion efficiency, storage capacity

INTRODUCTION

A large, affordable, and sustainable source of energy is essential for the progress of developing nations. Among the available non-conventional resources, solar energy represents the most abundant and freely accessible renewable option. The growing demand for renewable energy technologies has intensified the interest in liquid-phase electrolyte-based dye-sensitized solar cells (DSSCs) owing to their potential for efficient solar energy conversion and storage. These systems operate by converting solar energy into electrical energy through the formation of energy-rich intermediates that exhibit photogalvanic effect. This phenomenon was first identified by Rideal and Williams and was later systematically investigated by Rabinowitch [2, 3], followed by several other researchers. Over the years, extensive efforts have been devoted to improving the performance and efficiency of liquid-phase electrolyte-based dye-sensitized solar cells [4-8]. Research in this field has explored the use of various photosensitizers, mixed sensitizers with reductants, and electrolyte systems incorporating surfactants to enhance solar energy conversion and storage [9-15]. Recently, Meena and co-workers have developed liquid-phase electrolyte-based solar cells utilizing diverse photosensitizer-reductant combinations for electrical energy generation [16-18]. Building upon these advancements, the present

study focuses on investigating the role of chemical constituents in a liquid-phase electrolyte-based dye-sensitized solar cell employing chemicals such as methyl orange as photosensitive compound along with fructose as the reductant, and sodium lauryl sulfate as the surfactant.

Materials and methodology

Methyl orange (Merck), sodium lauryl sulfate (Loba Chemie), fructose (Merck), and NaOH (Merck) were employed in this study. All solutions were prepared using doubly distilled water. Stock solutions were obtained by direct weighing of the reagents and stored in light-protected containers.

The dye-sensitized solar cell (DSSC) based on a liquid-phase electrolyte was systematically assembled for photovoltaic studies [19-21]. The system consists of an electrochemically treated platinum foil as the working electrode and a saturated calomel electrode (SCE) as the reference electrode. The distance between illuminated and dark electrodes was maintained at 45 mm. Illumination was provided by a 200 W tungsten lamp, with a water filter used to eliminate infrared radiation. The photopotential was measured as the difference between the initial potential of the cell in the dark and the equilibrium potential attained under continuous illumination. Initially, the potential was recorded in the dark, and changes in potential upon illumination were monitored as a function of time. Prior to experimentation, the solutions were purged

* To whom all correspondence should be sent:
E-mail: anoopsingh10786@gmail.com

with purified nitrogen gas for approximately 20 min to remove dissolved oxygen.

The experimental solution, containing the dye, reductant, surfactant, and NaOH, was placed in an H-type glass cell. A platinum electrode ($1.0 \times 1.0 \text{ cm}^2$) was immersed in one arm of the H-tube, while the SCE was positioned in the other. The system was first stabilized in the dark, after which the platinum electrode arm was illuminated with the tungsten lamp, while the SCE arm was kept in the dark. The photochemical bleaching of methyl orange was monitored potentiometrically. A digital pH meter (Systronics Model-335) and a microammeter (Ruttonsha Simpson) were employed to measure the photopotential and photocurrent, respectively.

The current-voltage (J-V) characteristics of the solar cell were determined by applying an external load through a carbon potentiometer (log 470 K), connected in the circuit *via* a key to allow both open- and closed-circuit measurements. The overall experimental setup of the electrolyte-based dye-sensitized solar cell is shown in Figure 1. Furthermore, the influence of various parameters on the performance of the cell was systematically investigated [22-24]. The rate of potential decay after removal of illumination was determined to be 3.30 mV min^{-1} .

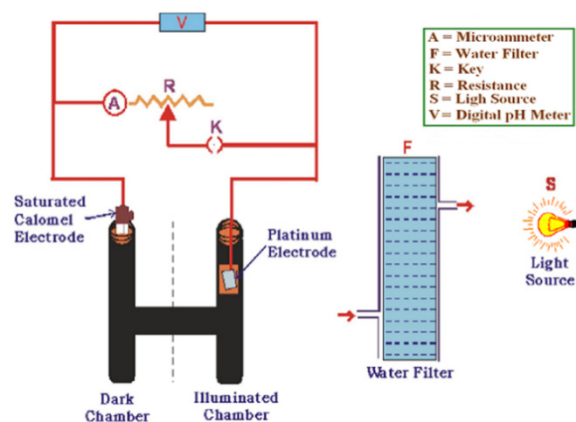


Figure 1. Experimental set-up of dye-sensitized solar cell (based on liquid phase electrolyte)

RESULTS AND DISCUSSION

Structure and absorption spectrum of the photosensitive compound (methyl orange)

Methyl orange (MO), chemically known as dimethylaminoazobenzene sulfonate, is a commonly

used anionic azo dye. It is a water-soluble compound primarily applied as a pH indicator. Due to its widespread use in the textile, paper, printing, and food industries, substantial quantities of methyl orange are released into industrial wastewater. Its distinct color variation with pH makes it particularly valuable in acid-base titrations. In acidic medium, methyl orange appears red, while in basic medium it exhibits a yellow coloration. This property makes it suitable for titrations involving moderately strong acids, as its transition occurs near the pK_a value. The molecular structure and UV-visible absorption spectrum of methyl orange ($\lambda_{\text{max}} = 464 \text{ nm}$) are presented in Figure 2.

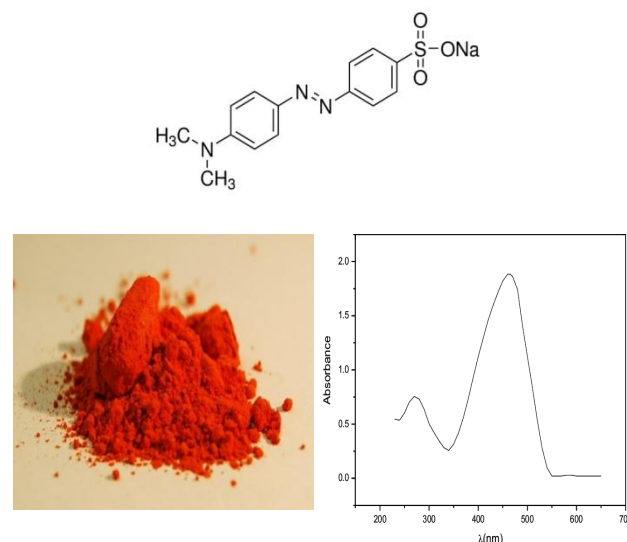


Figure 2. Structure and UV-vis spectrum of the photosensitive compound (methyl orange)

Variation of photovoltaic parameters with time

The photopotential of the dye-sensitized solar cell (DSSC) based on a liquid-phase electrolyte was measured at different pH values, with the maximum value observed at pH 12.70. Consequently, all subsequent experiments were carried out at this pH value. The variation of photopotential with time is shown in Figure 3(A). Upon illumination, the photopotential steadily increases and reaches 1090.0 mV within approximately 100.0 min, after which it remains constant despite continued illumination. When the light source is switched off, the system does not return to its initial potential, indicating incomplete reversibility.

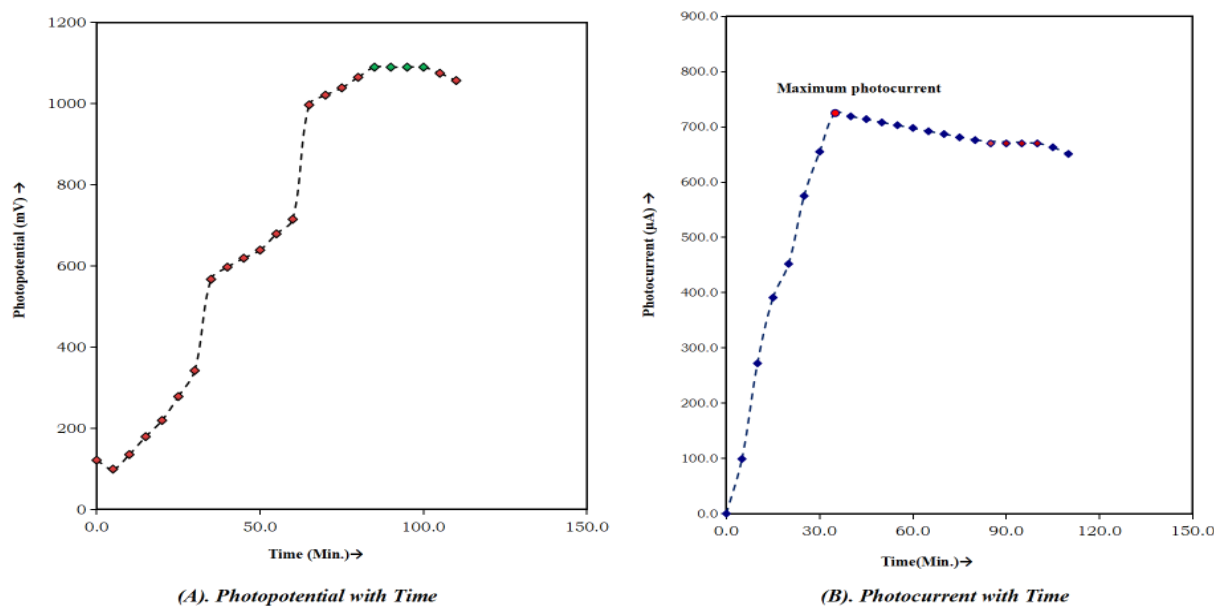


Figure 3. Variation of photovoltaic parameters with time

The photocurrent shows a rapid increase upon illumination and attains its maximum value, denoted as I_{\max} , within a few min. The short-circuit photocurrent of the DSSC containing the liquid electrolyte composed of methyl orange, fructose, and sodium lauryl sulfate is presented in Figure 3(B). Under illumination, the equilibrium photocurrent reaches 670.0 μA after 100.0 min for the cell containing the specific concentration ratio of the electrolyte components [23, 25].

Effect of electrolyte concentration on cell's photovoltaic parameters

The optimum cell performance is observed at a concentration of 2.28×10^{-5} M for the photosensitive compound, methyl orange (Figure 4A). At concentrations below this value, the electrical output decreases due to the limited number of photosensitive molecules available to absorb light and donate electrons to the platinum electrode. At concentrations above 2.28×10^{-5} M, excess photosensitive molecules prevent sufficient light from reaching the molecules near the electrode surface, resulting in a corresponding decrease in the cell's power output.

The optimum cell performance is observed at a concentration of 1.62×10^{-3} M for the reducing agent, fructose (Figure 4B). At lower concentrations, fewer fructose molecules are available to donate electrons to the photosensitive molecules, which reduces the electrical output. At higher concentrations, the increased presence of fructose promotes back electron transfer from the photosensitive molecules

to fructose and hinders the motion of photosensitive molecules toward the electrode, thereby causing a decline in cell power.

The role of micellar species is essential in enhancing the solubility of photosensitive molecules in dye-sensitized solar cells based on liquid-phase electrolytes. The photo-ejection of electrons from excited photosensitive molecules depends on the charge properties of surface-active agents such as sodium lauryl sulfate (SLS). These surfactant molecules facilitate the separation of photo-products through hydrophilic–hydrophobic interactions, thereby improving the conversion efficiency and storage capacity of the liquid-phase electrolyte in the dye-sensitized solar cell [26–28].

The optimum cell performance is observed at a concentration of 1.29×10^{-3} M for the surface-active compound, sodium lauryl sulfate (Figure 4C). The variation in electrical output arises because micelles solubilize photosensitive molecules to the greatest extent at or near their critical micelle concentration (CMC). Below this concentration, fewer photosensitive molecules dissolve in the electrolyte solution, leading to reduced electrical output. At concentrations above 1.29×10^{-3} M, excess surfactant prevents the proper dissolution of photosensitive molecules, as higher concentrations promote the formation of other aggregates such as lamellar structures and rod-like micelles in solution, as well as analogous bilayers and multilayers at interfaces, thereby causing a corresponding decrease in cell power [29–31].

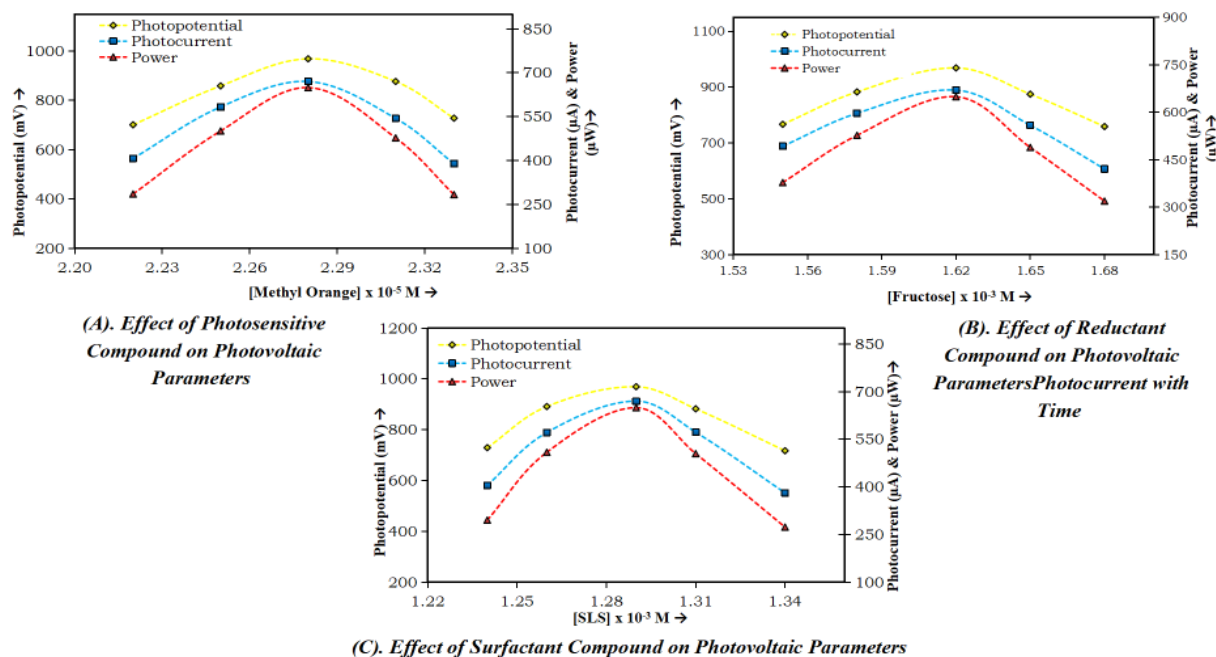


Figure 4. Effect of electrolyte concentration on cell's photovoltaic parameters

Table 1. Effect of pH of electrolyte solution on cell's photovoltaic parameters

[Methyl orange] = 2.28×10^{-5} M		Light intensity = 10.4 mW cm^{-2}			
[NaLS] = 1.29×10^{-3} M		Temperature = 303 K			
[Fructose] = 1.62×10^{-3} M					
pH					
Liquid phase electrolyte DSSCsI	12.62	12.66	12.70	12.74	12.78
Photopotential (mV)	727.0	873.0	969.0	859.0	709.0
Photocurrent (μA)	359.0	562.0	670.0	538.0	317.0
Power (μW)	260.99	490.63	649.23	462.14	224.75

Table 2. Effect of (A) Diffusion length and (B) Electrode area on cell's photovoltaic parameters

[Methyl orange] = 2.28×10^{-5} M		Light intensity = 10.4 mW cm^{-2}			
[NaLS] = 1.29×10^{-3} M		pH = 12.70			
[Fructose] = 1.62×10^{-3} M		Temperature = 303 K			
(A) Diffusion length (mm)					
Diffusion length (mm)	35.0	40.0	45.0	50.0	55.0
Maximum photocurrent I_{max} (μA)	707.0	716.0	725.0	733.0	741.0
Equilibrium photocurrent I_{eq} (μA)	688.0	679.0	670.0	661.0	652.0
Rate of photocurrent ($\mu\text{A min}^{-1}$)	20.20	20.46	20.71	20.94	21.17
(B) Electrode area (cm^2)					
Electrode area (cm^2)	0.70	0.85	1.00	1.15	1.30
Maximum photocurrent I_{max} (μA)	711.0	717.0	725.0	734.0	742.0
Equilibrium photocurrent I_{eq} (μA)	685.0	677.0	670.0	662.0	653.0

Effect of pH of electrolyte solution on cell's photovoltaic parameters

A liquid-phase electrolyte-based dye-sensitized solar cell (DSSC) exhibits pronounced sensitivity to the pH of the electrolyte solution. An increase in pH

within the alkaline range results in a corresponding enhancement of the photovoltaic parameters, namely potential and current, with maximum values recorded at pH 12.70. Beyond this point, further increases in pH cause a decline in electrical output.

The optimum pH condition was found to correlate with the pKa of the reductant, where the effective range occurred at $\text{pH} > \text{pKa}$. This behavior is attributed to the greater availability of the reductant molecules in their anionic form, which act as more efficient electron donors within the electrolyte solution. The corresponding results are summarized in Table 1.

Effect of diffusion length and area of electrode on cell's photovoltaic parameters

The influence of diffusion length, defined as the distance between the two electrodes, on the photoelectric parameters of the DSS cell, namely maximum photocurrent (I_{max}), equilibrium photocurrent (I_{eq}), and initial rate of photocurrent generation was investigated using a H-type cell based on liquid-phase electrolyte of varying dimensions. The effect of electrode area on these parameters was also examined. Results indicated that both I_{max} and initial rate of photocurrent generation ($\mu\text{A} \cdot \text{min}^{-1}$) increase with diffusion length, whereas I_{eq} shows a slight decrease. This variation in electrical output was attributed to the involvement of electroactive species, specifically the leuco or semi-leuco forms of the dye (photosensitizer) in the illuminated and dark chambers, respectively. The reductant molecules and their oxidation products serve exclusively as electron carriers within the electrolyte solution of the dye-sensitized solar cell. The dependence of the

photoelectric parameters on the diffusion length is summarized in Table 2A, while Table 2B presents the variation with electrode area. Furthermore, it is observed that I_{max} increases with electrode area, whereas I_{eq} correspondingly decreases.

$$\text{Fill Factor (FF)} = \frac{V_{pp} \times I_{pp}}{V_{oc} \times I_{sc}}$$

Current-voltage (J-V) characteristics of the dye-sensitized solar cell

The short-circuit current (I_{sc}) and open-circuit voltage (V_{oc}) of the cell were measured under closed- and open-circuit conditions using a digital pH meter and a multimeter, respectively [32-35]. Intermediate current and potential values between these two limits were obtained by applying an external load through a carbon potentiometer (log 470 K) connected to the multimeter circuit. The current-voltage (J-V) characteristics of the dye-sensitized solar cell are summarized in Table 3 and illustrated graphically in Figure 5.

Table 3. Current-voltage (J-V) characteristics of the DSS cell

Liquid phase electrolyte based DSS cell	V_{oc} (mV)	I_{sc} (μA)	V_{pp} (mV)	I_{pp} (μA)	FF
	1090.0	670.0	555.0	340.0	0.2584

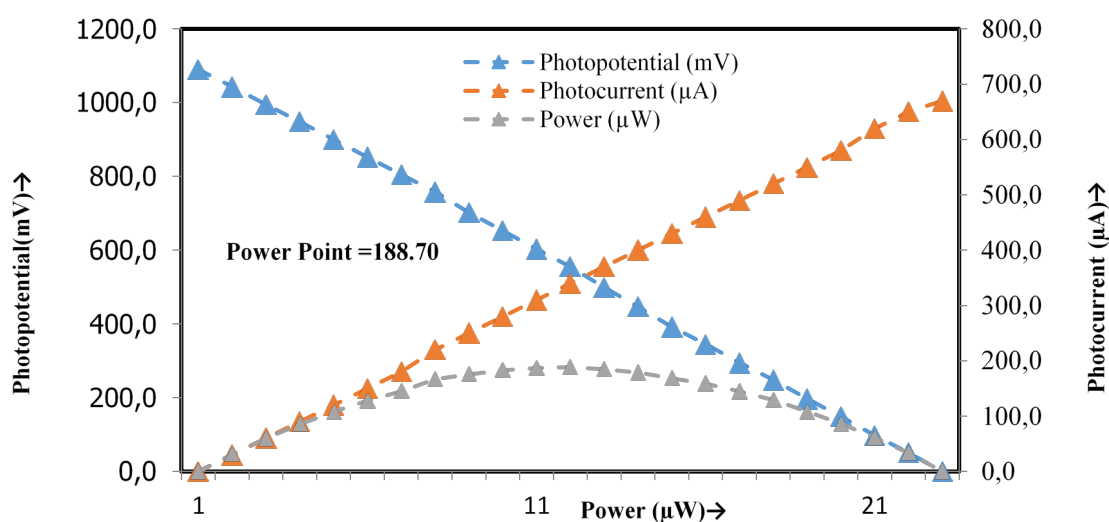


Figure 5. Current-voltage (J-V) characteristics of the cell.

Performance of the dye-sensitized solar cell

The performance of the dye-sensitized solar cell based on a liquid-phase electrolyte is evaluated by applying an external load after the light source is switched off, once the potential stabilizes (to achieve current at the power point, represented by red and green color symbols in Figure 5). The output power is assessed in terms of $t_{1/2}$, defined as the time required for the power to decay to 50% of its maximum value under dark conditions [36-38]. Experimental results demonstrate that the cell operates in complete darkness for up to 225 minutes. The corresponding data are summarized in Table 4 and are graphically presented in Figure 6.

Table 4. Performance of the dye-sensitized solar cell based on liquid phase electrolyte

Liquid phase electrolyte based DSS cell	Charging time (min)	Power (μ W)	Power at $t_{1/2}$ (μ W)	$t_{1/2}$ (min)
	100.0	188.70	95.01	225.0

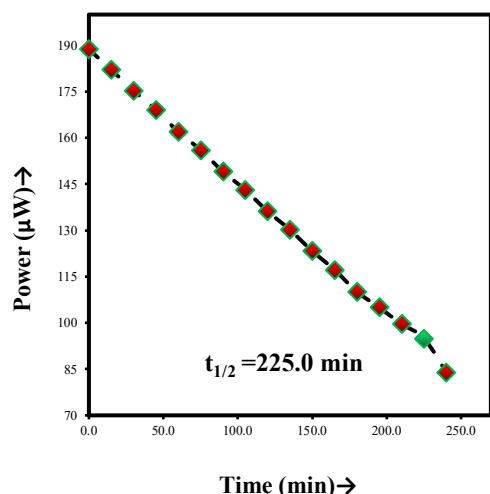


Figure 6. Performance of the dye-sensitized solar cell based on liquid phase electrolyte

Conversion efficiency of the cell [39-41]

The conversion efficiency of the cell was calculated from the photocurrent and photopotential values at the power point, together with the incident radiation power, and was found to be 4.68% (Table 5).

$$\text{Conversion efficiency (\%)} = \frac{V_{pp} \times i_{pp}}{10.4 \text{ mW cm}^{-2} \times \text{Electrode area (cm}^2\text{)}} \times 100$$

Table 5. Conversion efficiency of the dye-sensitized solar cell based on liquid phase electrolyte

Liquid phase electrolyte based DSS cell	FF	CE (%)	Storage capacity (%)
	0.2584	4.68	2.25 %

Mechanism

On the basis of these observations, the following mechanism is proposed for photocurrent generation in the liquid phase electrolyte-based dye-sensitized solar cell [42-44] (Fig. 7).

CONCLUSION

At present, the world is experiencing a severe energy crisis, and meeting the increasing energy demand remains a significant challenge for all nations. This situation necessitates the development of renewable energy devices capable of generating electrical energy for extended durations. In the present study, this issue is addressed through the utilization of a liquid-phase electrolyte containing suitable components in a dye-sensitized solar cell (DSSC), yielding promising results. The photovoltaic performance is investigated using an electrolyte composed of methyl orange as photosensitizer, fructose as reductant, and sodium lauryl sulfate as surfactant, with particular emphasis on the effects of pH, diffusion length, and electrode area. Based on the findings, it is concluded that an efficient liquid-phase electrolyte-based DSSC can be fabricated, exhibiting appreciable conversion efficiency and notable energy storage capacity [45-47].

Acknowledgement: The authors sincerely acknowledge the Head, Department of Chemistry, University of Rajasthan, Jaipur (Rajasthan-302004, India), for providing the necessary laboratory facilities to conduct this research. One of the authors (A.S. Meena) gratefully acknowledges the University Grants Commission (UGC), Government of India, New Delhi, for the financial assistance provided to this work.

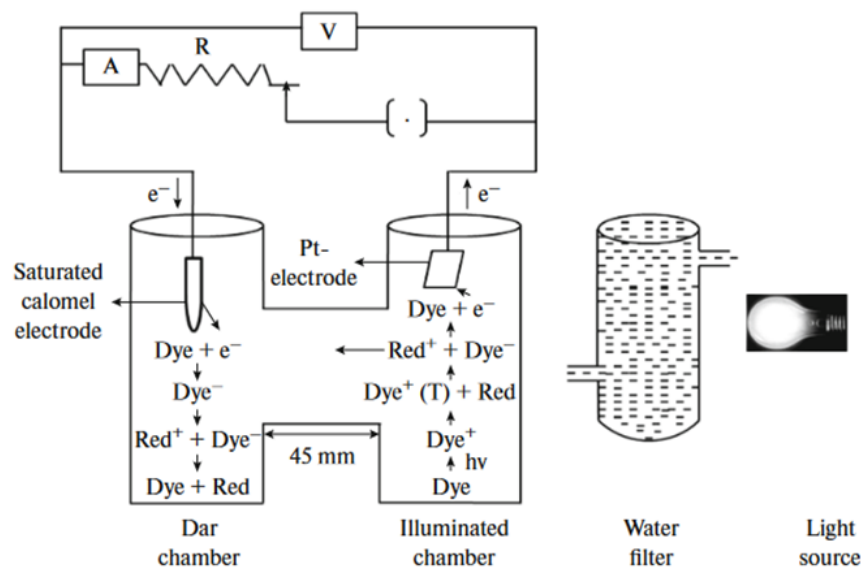


Figure 7. Mechanism of dye-sensitized solar cell based on liquid phase electrolyte

REFERENCES

1. E.K. Rideal, E.G. Williams, *Journal of the Chemical Society Transactions*, **127**, 258 (1925).
2. E. Rabinowitch, *The Journal of Chemical Physics*, **8**(7), 551 (1940).
3. E. Rabinowitch, *The Journal of Chemical Physics*, **8**(7), 560 (1940).
4. A.E. Potter Jr, L.H. Thaller, *Solar Energy*, **3**(4), 1 (1959).
5. K.M. Gangotri, C. Lal, *Proceedings of the Institution of Mechanical Engineers, Part A: Journal of Power and Energy*, **219**(5), 315 (2005).
6. S. Madhwani, J. Vardia, P.B. Punjabi, V.K. Sharma, *Proceedings of the Institution of Mechanical Engineers, Part A: Journal of Power and Energy*, **221**(1), 33 (2007).
7. S.C. Ameta, P.B. Punjabi, J. Vardia, S. Madhwani, S. Chaudhary, *Journal of Power Sources*, **159**(1), 747 (2006).
8. K.K. Rohatgi-Mukherjee, M. Bagchi, B.B. Bhowmik, *Electrochimica Acta*, **28**(3), 293 (1983).
9. C. Lal, *Journal of Power Sources*, **164**(2), 926(2007).
10. K.R. Genwa, M. Genwa, *Solar Energy Materials and Solar Cells*, **92**(5), 522 (2008).
11. K.R. Genwa, N.C. Khatri, *Energy & Fuels*, **23**(2), 1024 (2009).
12. P. Gangotri, P. Koli, *Sustainable Energy & Fuels*, **1**(4), 882 (2017).
13. S. Yadav, R.D. Yadav, G. Singh, *Int. J. Chem. Sci.*, **6**(4), 1960 (2008).
14. A. Malviya, P.P. Solanki, *Renewable and Sustainable Energy Reviews*, **59**, 662 (2016).
15. K.M. Gangotri, M.K. Bhimwal, *International Journal of Energy Research*, **35**(6), 545 (2011).
16. M. Chandra, R.C. Meena, *Research Journal of Chemical Sciences*, **1**, 1 (2011).
17. A.S. Meena, P.L. Meena, M. Chandra, R.C. Meena, *International Journal of Renewable Energy Research*, **3**(2), 276 (2013).
18. S.L. Meena, R.K. Bhupesh, L.C. Yadav, *Journal of Applied Science and Education (JASE)*, **3**(1), 1 (2023).
19. J. Rathore, A. Rakesh Kumar, P. Sharma, M. Lal, *Indian J. Sci. Technol.*, **15**(23), 1159 (2022).
20. Z. Li, S. Wang, J. Wu, W. Zhou, *Renewable and Sustainable Energy Reviews*, **156**, 111980 (2022).
21. S.R. Saini, S.L. Meena, R.C. Meena, *Advances in Chemical Engineering and Science*, **7**(2), 125 (2017).
22. W. Peng, M.Z. Shaik, C. Pascal, C. Raphael, R. Humphry-Baker, M. Gratzel, *J. Phys. Chem. B*, **107**, 14336 (2003).
23. M. Azzouzi, T. Kirchartz, J. Nelson, *Trends in Chemistry*, **1**(1), 49 (2019).
24. X. Liu, X. Du, J. Wang, C. Duan, X. Tang, T. Heumueller, G. Liu, Y. Li, Z. Wang, J. Wang, F. Liu, *Advanced Energy Materials*, **8**(26), 1801699 (2018).
25. S. Liu, J. Yuan, W. Deng, M. Luo, Y. Xie, Q. Liang, Y. Zou, Z. He, H. Wu, Y. Cao, *Nature Photonics*, **14**(5), 300 (2020).
26. H. Yao, Y. Cui, D. Qian, C.S. Ponseca Jr, A. Honarfar, Y. Xu, J. Xin, Z. Chen, L. Hong, B. Gao, R. Yu, *Journal of the American Chemical Society*, **141**(19), 7743 (2019).
27. F.D. Eisner, M. Azzouzi, Z. Fei, X. Hou, T.D. Anthopoulos, T.J.S. Dennis, M. Heeney, J. Nelson, *Journal of the American Chemical Society*, **141**(15), 6362 (2019).
28. E.T. Efaz, M.M. Rhaman, S. Al Imam, K.L. Bashar, F. Kabir, M.E. Mourtaza, S.N. Sakib, F.A. Mozahid, *Engineering Research Express*, **3**(3), 032001 (2021).
29. S.R. Fatemi Shariat Panahi, A. Abbasi, V. Ghods, M. Amirahmadi, *Journal of Materials Science: Materials in Electronics*, **31**(14), 11527 (2020).

30. A.S. Meena, L. Baloat, S.C. Meena, D. Meena, *Int. J. Creative Research Thoughts (IJCRT)*, **12**(8), 29 (2024).
31. A.S. Meena, Jayshree, L. Baloat, *Int. J. Creative Research Thoughts (IJCRT)*, **10**(7), 315 (2022).
32. A.M. Adeyinka, O.V. Mbelu, Y.B. Adediji, D.I. Yahya, *Int. J. Energy Power Eng.*, **17**(1), 1 (2023).
33. A.S. Meena, Sonika, *Int. J. Res. & Anal. Reviews (IJRAR)*, **9**(2), 454 (2022).
34. K. ElKhamisy, H. Abdelhamid, E.S.M. El-Rabaie, N. Abdel-Salam, *Plasmonics*, **19**(1), 1 (2024).
35. M.K. Bhimwal, K.M. Gangotri, A. Pareek, J. Kumar, *Int. J. Innovative Research in Technology*, **9**(3), 632 (2022).
36. M. Zghaibeh, P.C. Okonkwo, W. Emori, T. Ahmed, A.M.A. Mohamed, M. Aliyu, G.J. Ogunleye, *International Journal of Green Energy*, **20**(5), 555 (2023).
37. A.S. Meena, Jayshree, Sonika, D. Meena, *J. Emerging Tech.& Innovative Research (JETIR)*, **9**(6), 825 (2022).
38. S. Wijewardane, L.L. Kazmerski, *Solar Compass*, **7**, 100053 (2023).
39. A.S. Meena, *J. Modern Chemistry and Chemical Tech.*, **12**(1), 20 (2021).
40. G. Regmi, A. Ashok, P. Chawla, P. Semalti, S. Velumani, S.N. Sharma, H. Castaneda, *Journal of Materials Science: Materials in Electronics*, **31**(10), 7286 (2020).
41. A.S. Meena, Sonika, Jayshree, M. Akram, H. Posawl, M.L. Meena, J. Meena, *Asian J. Chemical & Envi. Res.*, **14**(1-4), 30 (2021).
42. S. Sivaraj, R. Rathanasamy, G.V. Kaliyannan, H. Panchal, A. Jawad Alrubaie, M. Musa Jaber, Z. Said, S. Memon, *Energies*, **15**(22), 8688 (2022).
43. M.G. Buonomenna, *Symmetry*, **15**(9), 1718 (2023).
44. N.S. Seroka, R. Taziwa, L. Khotseng, *Materials*, **15**(15), 5338 (2022).
45. R. Dallaev, T. Pisarenko, N. Papež, V. Holcman, *Materials*, **16**(17), 5839 (2023).
46. A. Maalouf, T. Okoroafor, Z. Jehl, V. Babu, S. Resalati, *Renewable and Sustainable Energy Reviews*, **186**, 113652 (2023).
47. S.M. Sivasankar, C.D.O. Amorim, A.F.D. Cunha, *Journal of Composites Science*, **9**(3), 143 (2025).

Unlocking the potential of computational fluid dynamics in Nigerian polymer research: current trends and future directions

T. Oyegoke*

*CAD Engineering of Processes & Reactive Interfaces Group, Department of Chemical Engineering,
Ahmadu Bello University, Zaria 234, Nigeria*

Received: June 19, 2024; Revised: July 18, 2025

Recent advancements in polymer research have focused on key challenges such as polymeric waste management, material degradation, property enhancement, and development of novel applications. Globally, researchers increasingly leverage both experimental and computational techniques to address these issues. However, in Nigeria, the application of computational methodologies—particularly Computational Fluid Dynamics (CFD)—remains significantly underutilized. This study underscores the transformative potential of CFD as a strategic tool for advancing polymer research in Nigeria. Through a comprehensive review of relevant literature, the current status of CFD adoption in polymer studies is examined, and prospective opportunities for its integration are identified. By articulating the benefits and implementation prospects of CFD within the Nigerian research context, this report aims to encourage its broader adoption, thereby fostering innovation, improving cost-efficiency, and driving the future direction of polymer science in the country.

Keywords: CFD, polymer; material design; modeling, computational approach, Nigeria.

INTRODUCTION

Secondary processing of polymers into functional products typically involves a melting phase facilitated through extrusion, injection molding, blow molding, transfer molding, and other techniques. In each of these processes, the polymer must be converted into a flowable state before being shaped into the desired article. Consequently, various process parameters—such as temperature, flow rate, and pressure—directly influence both the quality of the final product and the total processing time. For instance, in pelletization, the quality of polymer pellets is primarily governed by processing time, where shorter durations tend to stabilize product quality and boost production rate [1].

Importantly, the rheological and thermal behavior of polymers varies across different materials, necessitating precise and material-specific designs during extrusion and similar processes. The ability to predict and control polymer flow behavior is vital for ensuring seamless production and product consistency. In this context, Computational Fluid Dynamics (CFD) has emerged as an indispensable tool. CFD enables the mathematical modeling and numerical simulation of fluid flow phenomena, offering insights that aid in optimizing die design, reducing material waste, cutting down production time, and improving overall processing efficiency [1–3].

While CFD has become a well-established tool in polymer industries and academic research across

many developed countries, its integration into polymer research and industrial applications in developing nations—such as Nigeria—remains significantly underexplored and poorly documented. Existing literature and industry surveys [4–14] indicate a scarcity of empirical data and a lack of systematic reviews that assess adoption trends, practical applications, or policy support for CFD within Nigeria's polymer sector. Most existing studies primarily adopt experimental approaches, focusing on the synthesis of polymers or polymer-based materials from monomers or waste sources, as well as on performance evaluation and optimization. However, these studies often pay minimal attention to the potential applications of CFD, revealing a substantial gap in both knowledge and practice regarding its use in polymer science research in Nigeria. Addressing this gap is crucial, especially as Nigeria aspires to expand its local polymer production, improve material efficiency, and adopt modern processing technologies. The growing complexity of polymer processing in both academic and industrial contexts demands evidence-based decision-making, for which CFD can play a transformative role.

This paper, therefore, aims to critically assess the current trends, extent of adoption, and future prospects of CFD applications in Nigeria's polymer research landscape. It highlights the benefits of CFD integration, showcases successful case studies from advanced economies, and proposes strategic

* To whom all correspondence should be sent:
E-mail: OyegokeToyese@gmail.com

directions to foster greater adoption within Nigeria. By doing so, the paper underscores the urgent need to embrace computational modeling as a key enabler of innovation and competitiveness in the Nigerian polymer industry.

METHOD EMPLOYED IN THIS LITERATURE SURVEY

This study employed a two-pronged approach to assess the extent of Computational Fluid Dynamics (CFD) adoption in Nigerian polymer research. First, existing literature was reviewed to demonstrate the potentials of CFD and how it has been successfully utilized in global studies for product design, process optimization, and reduction of physical prototyping. These international reports provided the basis for highlighting the benefits CFD can offer in enhancing the quality and efficiency of polymer-related research and development.

The second aspect of the survey focused specifically on research carried out in Nigeria. A comprehensive review was conducted on selected Nigeria-based peer-reviewed journals that regularly publish studies in materials and polymer science. The journals examined include the Journal of the Nigerian Society of Physical Sciences (JNSPS), the Journal of the Chemical Society of Nigeria (JCSN), the Journal of the Nigerian Society of Chemical Engineers (JNSCHE), and the Nigerian Journal of Materials Science and Engineering (NJMSE). These journals were chosen due to their reputability and consistent publication of polymer-related research within the Nigerian academic context.

All articles published in these journals, from their maiden issues up to the year 2025, were manually reviewed volume-by-volume and issue-by-issue through their online databases. This manual screening process was carried out without the use of keywords to ensure a thorough identification of all relevant studies focused on polymers or polymer-based materials. Articles that involved polymer synthesis, property optimization, kinetic modeling, or polymer-related waste management were included. However, studies employing CFD outside the scope of polymer applications, such as those focused solely on fluid dynamics in unrelated fields, were excluded.

The survey methodology and scope are illustrated diagrammatically in Figure 1. Figure 1a presents a graphical overview of the research focus, specifically highlighting the core areas of polymer research explored in relation to CFD usage. Figure 1b outlines the schematic flow of the survey approach, indicating the journals analyzed, the screening procedure adopted, and the comparative

trend analysis carried out between conventional polymer research themes and the incorporation of CFD in those studies.

The purpose of this methodology was to provide a data-driven understanding of how CFD has been utilized—or overlooked—in Nigeria's polymer research landscape. It aims to quantify the level of attention given to computational modeling approaches in local publications and to identify potential gaps in adoption when compared with global trends. This forms the basis for highlighting the need for increased awareness and application of CFD in future Nigerian polymer science research.

CFD IN POLYMER RESEARCH: CURRENT PERSPECTIVES AND NIGERIAN CONTEXT

SimScale [15] described computational fluid dynamics (CFD) referring to a method of mathematically modeling a physical phenomenon that involves the flow of fluids inside a processing system unit and the solution of models that have been constructed numerically using computational tools. CFD is an approach to modeling a physical phenomenon. These computational tools have made the approach much easier with the advances reported in ICT and the introduction of different graphic user interfaces (GUI), making it more user-friendly to researchers. The significance of the CFD approach to a process scale-up cannot be overemphasized in terms of design, efficient management of mass, momentum, and energy transport involved in a production process [2, 3]. Technopedia [16] further indicated that the CFD approach goes a long way to give insight into patterns or forms of flow, which would be difficult, expensive, or impossible to study using traditional techniques.

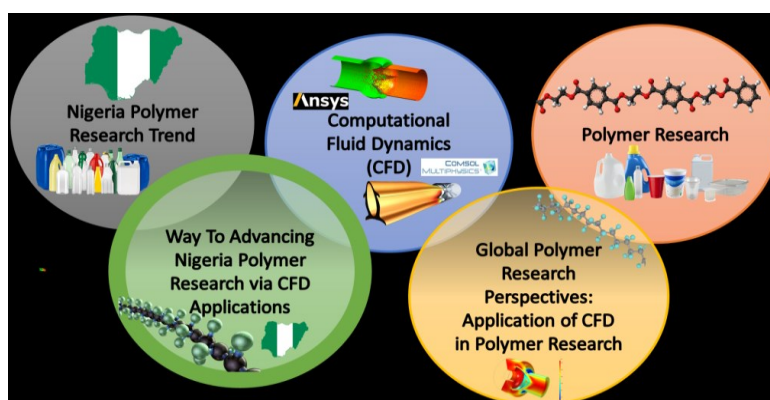
Applications of CFD in polymer design and analysis

The utilization of the computational fluid dynamic study approach in the design and analysis of high-performing new polymers has been demonstrated mainly in the literature, where it has been adopted in ascertaining the potential of a designed objective or goal [17]. A schematic block flow depicting the processes involved in the deployment of CFD is presented in Figure 2, as obtained from the literature [18].

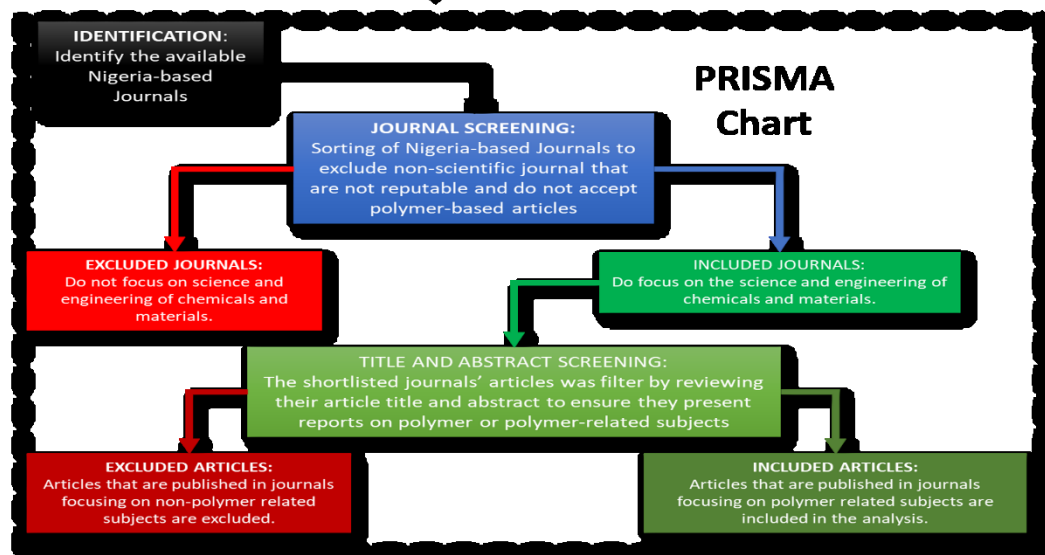
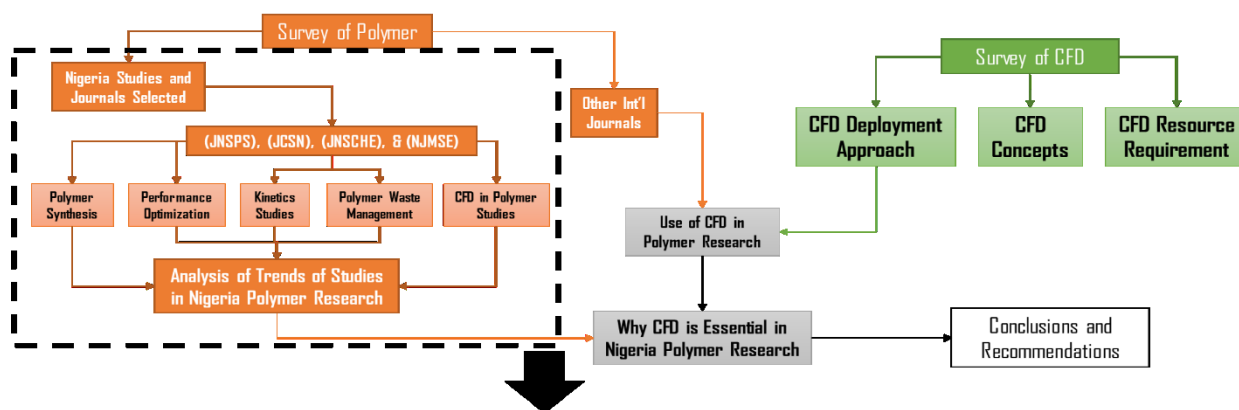
Many works have employed the computational fluid dynamic modeling approach in polymer processing studies. Some of the works investigated the behavior of materials in a reactor during the processing, including how some reactor operating parameters influenced the product's properties in terms of quality, conversion, and homogeneity.

Other studies employed the use of the approach to understanding the phenomena behind the experimental observations from a laboratory study, like understanding what promotes polymer adhesion

in a polymerizer, that is, polymerization reactor, which could be batch, CSTR, fluidized bed, and any other reactor model [18–20].



(a)



(b)

Figure 1. (a) Overview graphical illustration of the key components in the survey, and (b) Schematic approach deployed for the literature survey with the PRISMA chart for this report.

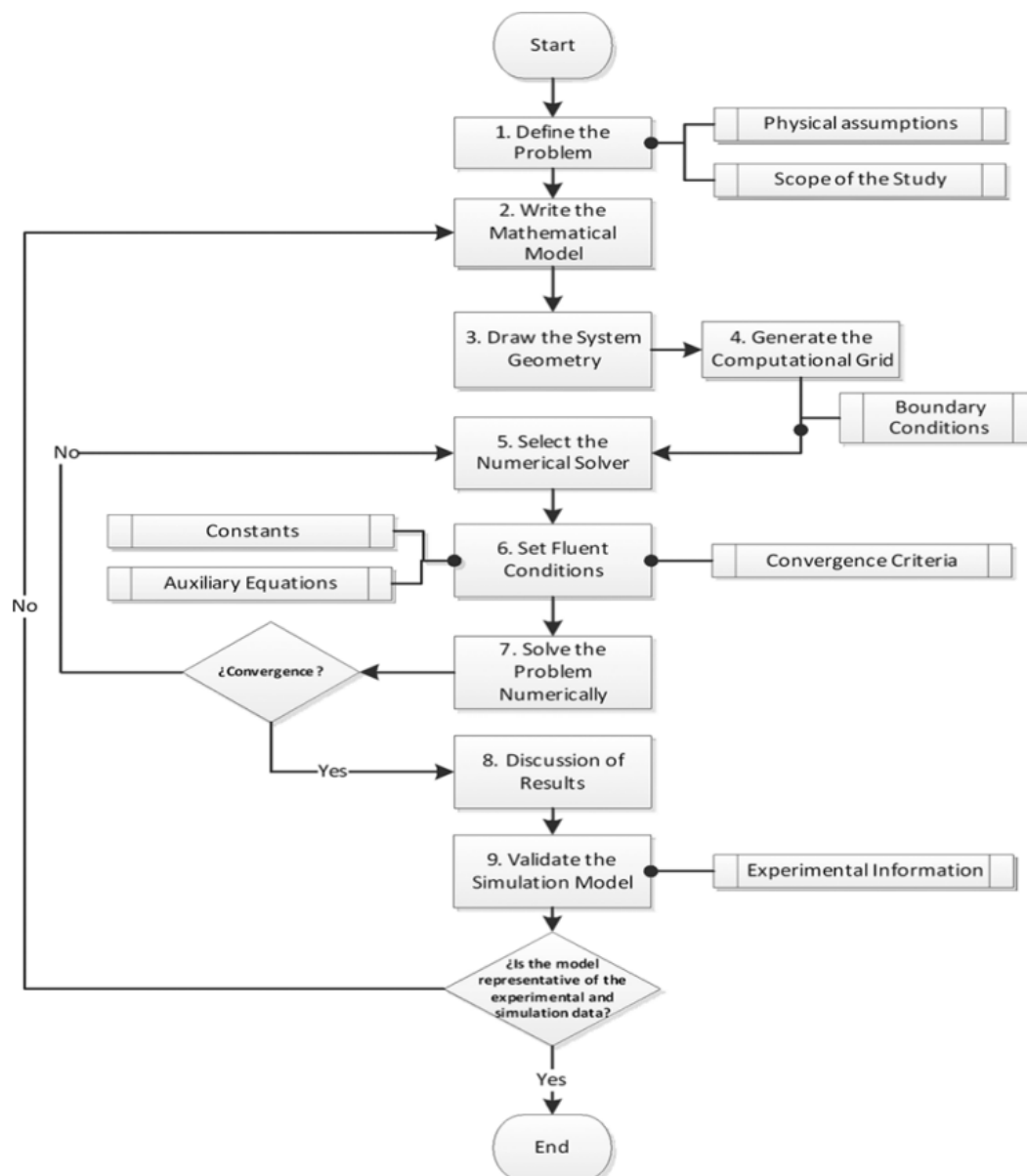


Figure 2. The block flow of serial steps involved in the deployment of CFD *via* the use of FLUENT simulation application package [18].

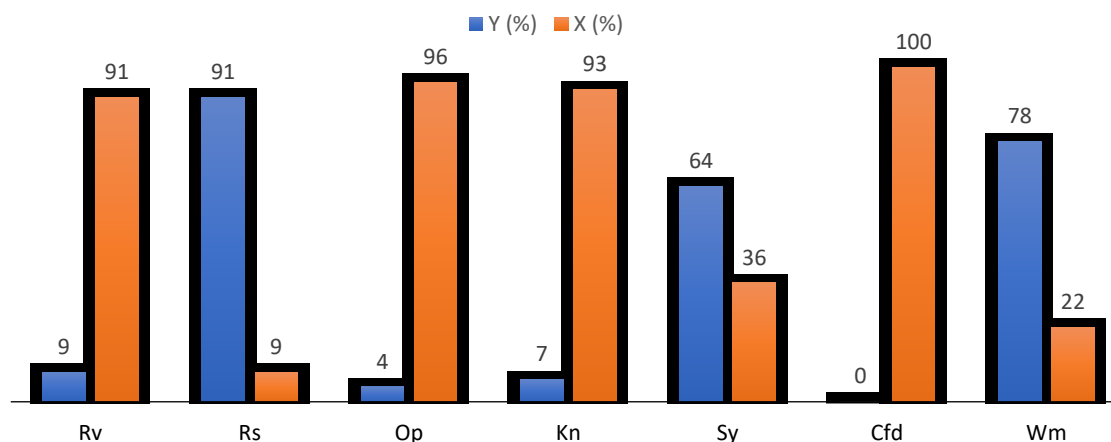


Figure 3. Distribution of research studies on polymer-based materials in Nigeria, obtained from the literature survey (Note: Rv = reviews, Rs = experimental research, Op = optimization, Kn = kinetic and thermodynamic studies, Sy = synthesis, CFD application, Wm = waste management and environments).

Some works deploy this approach to study the interaction of the polymer with selected materials of interest. Similar to studies that tend to investigate the interactions of selected polymers with oil droplets to see if the oil droplet deforms and how the elastic property of the polymer influences the deformation processes during the simulation of enhanced oil recovery (EOR) [21, 22]. The CFD approach is typically deployed in the independent study of each processing unit available singly in the processing of polymer's production networks, unlike those cases of the process modeling approach, which can evaluate the entire networks.

Current trends in polymer research in Nigeria

The extent of the application of CFD in polymer research by Nigerian experts, particularly in the design and analysis of secondary polymer processing technologies, is presented in Figure 3 and Table 1. Findings from the literature survey reveal that a significant portion of the reported research focuses on polymer synthesis, which accounts for approximately 64% of the total studies on Figure 3 identified across selected peer-reviewed Nigerian journals.

Other areas of research include kinetic modeling and optimization studies, which contribute 4% and 7% of the reported works, respectively. However, the application of CFD in polymer-based research remains strikingly absent. The data collected from the reviewed journals show that 0% of the studies utilized CFD, indicating a complete lack of attention to this valuable computational tool in the surveyed literature.

Table 1 summarizes the various works published in four reputable Nigeria-based journals: Journal of the Nigerian Society of Physical Sciences (JNSPS), Journal of the Chemical Society of Nigeria (JCSN), Nigerian Journal of Materials Science and Engineering (NJMSE), and Journal of the Nigerian Society of Chemical Engineers (JNSChE). Each entry details whether the study involved reviews (Rv), experimental research (Rs), optimization (Op), kinetic and thermodynamic studies (Kn), synthesis (Sy), CFD application, or waste management and environmental analysis (Wm).

A total of 78% (in Figure 3) of the analyzed studies addressed aspects of polymer waste management and environmental impact. These included investigations into polymer waste recycling [56], biodegradability of polymer [49, 52], synthesis of polymer composites using agro-wastes such as orange and plantain peels [54], sugarcane bagasse [52], palm kernel shell [50], banana stem [38], and other agro-wastes [39–41].

Despite this promising focus on sustainability (in Figure 3), the absence of CFD deployment across all reviewed studies is a significant gap. Notably, previous reviews have also failed to examine or highlight the potential or actual use of CFD in Nigerian polymer research. This lack of integration may be attributed to several factors, including limited research funding, shortage of expertise in CFD applications, and insufficient infrastructure or access to commercial CFD software and high-performance computing facilities.

In summary, while Nigerian polymer research demonstrates strength in synthesis and environmental sustainability, it falls short in adopting advanced computational tools like CFD as shown in Figure 3 and Table 1. Addressing this gap is critical for advancing process optimization, improving material properties, and reducing time and cost associated with experimental design. The promotion of CFD integration in polymer research would require deliberate investment in capacity building, infrastructure development, and academic-industry collaboration.

Trend of CFD deployment in polymer researches across the globe

A bibliometric analysis was conducted using the keywords “CFD” or “Computational Fluid Dynamics” and “polymer”, with the aid of Lens online platform (<https://www.lens.org/lens/search/scholar/analysis?q=CFD%20or%20Computational%20fluid%20dynamic%20AND%20polymer>). The global trend in CFD-related polymer research has shown continued growth, as evident in Figure 4a which illustrates annual publication counts.

Table 1. Works reported by Nigerian polymer experts (Note: Y=Yes, N=No, Mgt=Management)

Journal (References)	Reported study on the selected peer-reviewed material-based Journal (Available in the journal online database)	Review (Rv)	Research (Rs)	Optimization (Op)	Kinetics & Thermo (Kn)	Synthesis (Sy)	CFD	Waste Mgt & Environment (Wm)
JNSPS [6,14]	A review on Transforming plastic wastes into fuel	Y	N	N	N	N	N	Y
JNSPS [6,23]	Degradation of PET nanoplastic oligomers at the novel phl7 target:insights from molecular docking and machine learning	N	Y	Y	N	Y	N	N
JNSPS+ [6,24]	Enhancing cellulose fiber properties from chromolaena odorata and anana comosus through novel pulping chemical mixtures	N	Y	N	N	Y	N	N
JNSPS [6,25]	Polychlorinated biphenyls (PCBs) in sediments and fish from dredged tributaries and creeks of river Ethiope, South-South, Nigeria: sources, risk assessment and bioaccumulation	N	Y	N	N	N	N	Y
JNSPS [6,26]	Sustainable remediation of vancomycin polluted water using pyrolysis biochar of pressed oil palm fruit fibre	N	Y	N	N	Y	N	Y
JCSN [7,27]	Studies on the thermodynamic properties of natural rubber composites filled with clay and corn cob	N	Y	N	N	Y	N	Y
JCSN [7,28]	Development and evaluation of natural rubber membranes for sustained transdermal drug release applications	N	Y	N	N	Y	N	N
JCSN [7,29]	Isolation and characterization of cellulose from pentaclethra macrophylla benth pod biomass wastes for polymer reinforcement composite	N	Y	N	N	Y	N	Y
JCSN [7,30]	Study of using natural fillers on the biodegradation properties of virgin/waste low density polyethylene and virgin/waste high density polyethylene composites.	N	Y	N	N	Y	N	Y
JCSN [7,13]	Comparative study of the effect of poly(lactic- acid), starch, charcoal on physico-mechanical properties of virgin and waste low density polyethylene composites	N	Y	N	N	Y	N	Y
JCSN[7,31]	Spatial assessment and pollution analysis of packaged sachet water sold in selected local government areas of kano state, Nigeria	N	Y	N	N	N	N	Y
JCSN [7,12]	Polycyclic aromatic hydrocarbons (pahs) in the fruits of cucumis sativus from two markets within aba metropolis	N	Y	N	N	N	N	Y
JCSN [7,32]	Effect of dye sulphonation on the dyeing of nylon, 6, 6 with 1-hydroxy-2-phenylazo-6-[2-chloro-4-[phenylamino] triazin-6- ylamino] naphthalene- 3-sulphonic acid reactive dye	N	Y	N	N	N	N	Y
JCSN [7,33]	Development and evaluation of natural rubber membranes for sustained transdermal drug release applications	N	Y	N	N	Y	N	Y
J++CSN [7,31]	Spatial assessment and pollution analysis of packaged sachet water sold in selected local government areas of kano state, Nigeria	N	Y	N	N	N	N	Y
JCSN [7,12]	Polycyclic aromatic hydrocarbons (pahs) in the fruits of cucumis sativus from two markets within aba metropolis	N	Y	N	N	N	N	Y
JCSN [7,10]	Analysis of bottled drinking water sold in awka metropolis, anambra state, Nigeria	N	Y	N	N	N	N	Y
JCSN [7,11]	Molecular modeling analysis of per- and polyfluoroalkyl substances binding on human fertilization proteins - izumo1 and egg surface juno	N	Y	N	N	N	N	Y
JCSN [7,34]	Contamination of pet bottled carbonated soft drinks sold in nigeria after long storage due to antimony leaching: risk assessment	N	Y	N	N	N	N	Y
JCSN [7,35]	Isolation and characterization of cellulose from pentaclethra macrophylla benth pod biomass wastes for polymer reinforcement composite	N	Y	N	N	Y	N	Y
JCSN [6,36]	Use of natural cross linkers in molecularly imprinted polymer technology - past, present and future	Y	N	N	N	Y	N	N
JCSN [7,37]	Chitosan-starch polymeric blend hydrogels as scavengers of antibiotics from simulated effluent: sorbent characterization and sorption kinetic studies	N	Y	N	Y	Y	N	N

JCSN [7,38]	Properties of natural rubber compounded with modified banana pseudostem fibres and calcium carbonate	N	Y	N	N	Y	N	Y
JCSN [7,39]	Surface morphology characterization on green adhesive prepared using agricultural and plastic waste material as composites	N	Y	N	N	Y	N	Y
JCSN [7,40]	Graft copolymerization of dextrin onto concentrated natural rubber for the production of baby feeder teat.	N	Y	N	N	Y	N	N
JCSN [7,41]	Studies on the thermodynamic properties of natural rubber composites filled with clay and corn cob	N	Y	N	Y	Y	N	N
J+CSN [7,42]	Development and evaluation of natural rubber membranes for sustained transdermal drug release applications	N	Y	N	N	Y	N	N
JCSN [7,43]	Spatio-temporal occurrence, sources, and human health risk of 16-polycyclic aromatic hydrocarbons in anthropogenic vectored soils	N	Y	N	N	N	N	Y
+JCSN [7,44]	Proximate analysis and determination of polycyclic aromatic hydrocarbons in processed animal skin sold in major markets in south west nigeria	N	Y	N	N	N	N	Y
JCSN [7,45]	Study of using natural fillers on the biodegradation properties of virgin/waste low density polyethylene and virgin/waste high density polyethylene composites	N	Y	N	Y	Y	N	Y
JCSN [7,46]	Comparative study of the effect of poly(lactic- acid), starch, charcoal on physico-mechanical properties of virgin and waste low density polyethylene composites	N	Y	N	N	Y	N	Y
JCSN [7,47]	Polycyclic aromatic hydrocarbons (pahs) in the fruits of cucumis sativus from two markets within aba metropolis	N	Y	N	N	N	N	Y
JCSN [7,48]	Polycyclic aromatic hydrocarbon in sediment, ground and surface water resources in coastal areas of ondo state, nigeria	N	Y	N	N	N	N	Y
NJMSE [4,49]	Processing, degradation and applications of synthetic biodegradable polymers: a review	Y	N	N	N	Y	N	Y
NJMSE [4,50]	Fabrication of palm kernel shell epoxy composites and study of their mechanical properties	N	Y	N	N	Y	N	Y
NJMSE [5,51]	Production of uniformly disperse carbon nanotube/high density polyethylene nanocomposite using novel nanofeeder injection moulding machine	N	Y	N	N	Y	N	N
NJMSE [5,52]	Preparation and assessment of biodegradable polyurethane foams from sugar bagasse	N	Y	N	N	Y	N	Y
NJMSE [5,53]	Thermal and mechanical properties of high-density polyethylene (hdpe)/leather composite	N	Y	N	N	Y	N	N
NJMSE [5,51]	Properties of chemically modified baobab pod/sisal fiber reinforced low-density polyethylene hybrid composite	N	Y	N	N	Y	N	Y
JNSChE [4,54]	Optimization of microwave pretreatment conditions of orange and plantain peels for polygalacturonase production by aspergillus awamori cicc 2040	N	Y	Y	N	Y	N	Y
JNSChE [4,55]	Effect of temperature and catalyst modification on thermocatalytic degradation of low-density polyethylene	N	Y	N	N	Y	N	Y
JNSChE [4,56]	Recycling of rigid polyurethane waste –a cost reduction strategy in rigid polyurethane foam production	Y	N	N	N	Y	N	Y
JNSChE [4,9]	Air emissions from stepwise co-pyrolysis of plastic mixtures	N	Y	N	N	N	N	Y
JNSChE [4,8]	Flow and compaction properties of excipients developed from biopolymer waste snail shell and influencing factors	N	Y	N	N	Y	N	Y
JNSChE [4,57]	Air emissions from stepwise co-pyrolysis of plastic mixtures	N	Y	N	N	N	N	Y
Summary	Descriptions	Rv	Rs	Op	Kn	Sy	Cfd	Wm
	Frequency of works with Y	4	41	2	3	29	0	35
	Frequency of works with N	41	4	43	42	16	45	10

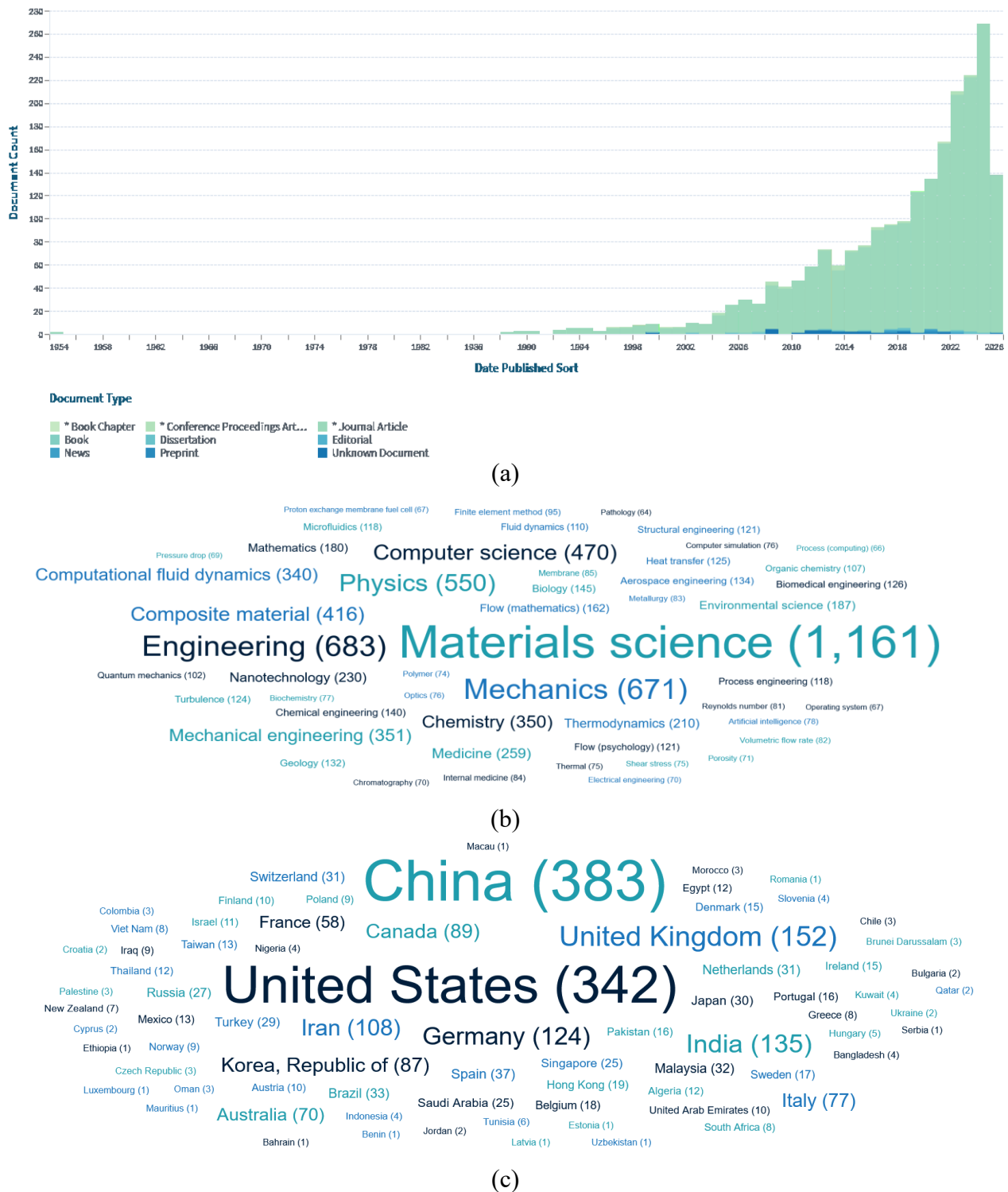


Figure 4. (a) Scholarly works over time, (b) Top fields of study in such research, and (c) Most active countries involved in the deployment of CFD in their polymer science research (Source: <https://www.lens.org/lens/search/scholar/analysis?q=CFD%20or%20Computational%20fluid%20dynamic%20AND%20polymer>)

Further insights from the analysis (see Figure 4b) show that fields such as materials science, engineering mechanics, and physics dominate the research in polymer science employing CFD. The analysis of active countries and regions (see Figure

4c) highlights China, the United States, the United Kingdom, India, Germany, and Iran as leading contributors. In contrast, Nigeria and other developing nations—including Benin, Bangladesh, Romania, and Kuwait—remain less active in CFD-

focused polymer research. This emphasizes the need for increased engagement and capacity development in these regions to leverage CFD's potential in advancing polymer science.

Potential impact of CFD on Nigeria's polymer research landscape.

Integrating CFD into polymer research offers significant advantages, particularly for Nigeria's scientific and industrial communities. CFD has the potential to reduce the cost and time associated with experimental trial-and-error by providing detailed insight into the impact of various constraints under controlled virtual environments. This makes it a powerful tool for enhancing process understanding, optimizing operating conditions, and facilitating efficient process scale-up in polymer production.

One major area where CFD adds value is in analyzing the effect of non-homogeneity and short-circuiting in polymerization reactors. For instance, Patel *et al.* [58] used CFD to study how impeller speed and residence time affect the flow pattern and conversion of styrene during polymerization. Their results showed how unreacted monomer distribution could be better managed to improve reactor performance. Similarly, Xie *et al.* [59] applied CFD to gain insights into anionic polymerization behavior in tubular reactors, further demonstrating its versatility.

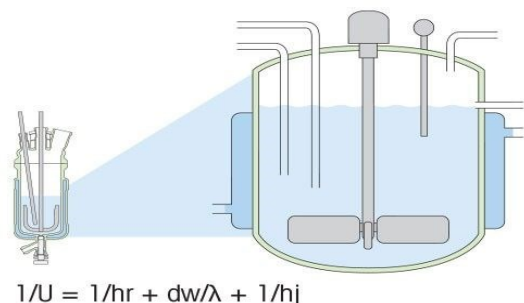


Figure 5. Process scale illustration for a chemical reactor [60].

CFD also plays a crucial role in process scale-up, offering the ability to simulate complex interactions of mass, heat, and momentum transfer that typically occur in large-scale reactors. By capturing these dynamics, researchers can translate laboratory findings presented in Figure 5 to industrial scales more reliably, ensuring better conversion efficiency and process performance.

Temperature distribution within reactors is another critical factor in polymer production. Jongpajit & Bumroongsri [61] utilized CFD to study the polymerization of propylene into polypropylene. Their work, shown in Figure 6, revealed that increasing monomer velocity led to a steadier

temperature distribution within the reactor bed, improving process stability and product consistency.

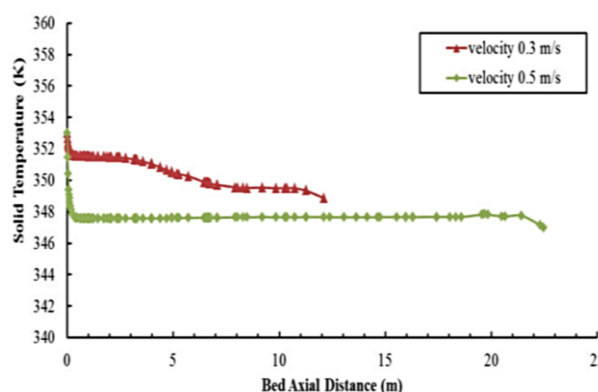


Figure 6. Effect of change in monomer velocity on polymerizer (reactor) temperature distribution in a propylene polymerization study performed with the use of CFD tool [61].

Furthermore, CFD can aid in the investigation of polymer rheology. Pineda-Torres *et al.* [18] modeled the influence of stirrer speed and time on the viscosity of a copolymer product. Their simulations provided a clearer understanding of how changes in operating parameters affect viscosity and other rheological properties. Figure 7 presents the block flow employed during the deployment of CFD in the polymer rheological studies.

Overall, deploying CFD tools in Nigeria's polymer research landscape can significantly enhance the quality and efficiency of research outcomes. By leveraging its capabilities, researchers can reduce dependence on costly experiments, improve process control, and contribute meaningfully to the country's technological advancement in polymer science.

Infrastructure and capacity needs for CFD implementation

The implementation of the CFD study approach in future polymer design research in Nigeria requires a range of essential resources to ensure effective and sustainable deployment. Chief among these is the access to high-performance computing (HPC) infrastructure, which may include institutional computing clusters, subscriptions to supercomputers, or cloud-based computing services (see Figure 8). These computational resources are critical for running the complex simulations involved in CFD studies.

In addition to hardware infrastructure, access to advanced software is vital. CFD simulation tools presented in Figure 9 like ANSYS Fluent, COMSOL Multiphysics, OpenFOAM, SimScale, SU2 Code, and Elmer are examples of platforms commonly used in computational modeling.

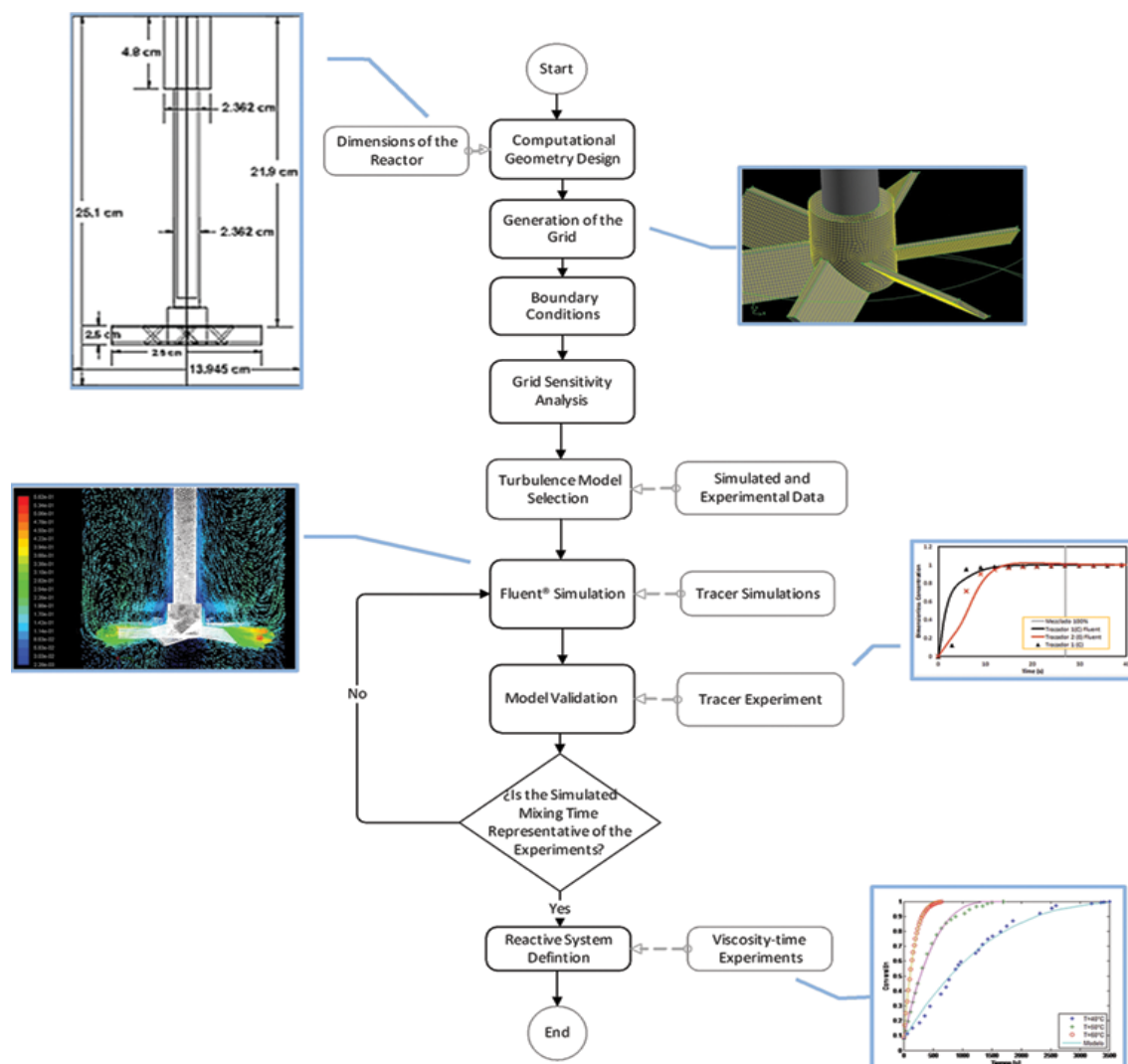


Figure 7. Method deployed by Pineda-Torres *et al.* [18] in their simulation in FLUENT.



Figure 8. Possible computing devices for the running of the simulation jobs.



Figure 9. Series of CFD software alternatives applicable for the modeling and simulation of the polymer science study.

Some of these tools require pre-processing and geometry development using computer-aided design (CAD) software such as AutoCAD. These software applications collectively form the digital ecosystem necessary for comprehensive CFD analysis, from geometry creation to meshing, simulation, and result interpretation [62–64].

Strategic directions and policy recommendations

To harness the full potential of CFD in Nigeria's polymer research and innovation landscape, deliberate policy actions and strategic investments are essential. First, universities and research institutions should integrate CFD modeling into polymer science and chemical engineering curricula

to build foundational expertise among emerging scientists and engineers. Complementing this, targeted training workshops and research internships especially through collaborations with international institutions experienced in CFD will accelerate local competence development.

Simultaneously, national and institutional research funding agencies should prioritize computational modeling within their grant portfolios. Providing access to licensed CFD software and high-performance computing (HPC) facilities will empower researchers to perform more accurate and efficient simulations. Interdisciplinary projects that combine CFD with experimental polymerization studies should also be encouraged, as such collaborations ensure result validation, strengthen theory–practice integration, and enhance real-world applicability.

Strategic partnerships among academia, industry, and government agencies must be fostered to promote knowledge transfer and facilitate the commercialization of CFD-optimized polymer processes. These alliances can unlock innovative solutions to local polymer design challenges, improve product performance, and reduce R&D costs. Policymakers and industry leaders must recognize CFD as a strategic enabler of research efficiency, innovation, and sustainable industrial development. Consequently, its integration into Nigeria's national science, technology, and innovation (STI) frameworks is imperative [65, 66].

To ensure tangible impact, policymakers—particularly those within the Federal Ministry of Science, Technology and Innovation, NITDA, and TETFund—should embed CFD initiatives into national STI strategies and funding instruments. A phased implementation strategy is recommended: in the short term, prioritize curriculum updates and pilot training programs; in the medium term, support software licensing, cloud-based HPC infrastructure, and interdisciplinary grants; and in the long term, drive industrial-scale applications and R&D commercialization. Periodic monitoring and evaluation should be institutionalized to track uptake, measure outcomes, and assess the return on investment (ROI) of CFD-integrated research efforts.

CONCLUSIONS AND OUTLOOK

This study has articulated the critical role that Computational Fluid Dynamics (CFD) can play in transforming polymer research in Nigeria. Drawing upon an extensive review of existing literature, the findings reveal a pronounced gap: polymer research within the country continues to rely heavily on

traditional laboratory experimentation, with limited adoption of CFD tools and techniques. This underutilization constrains the ability of researchers to explore complex fluid and thermodynamic behaviors inherent in polymer systems, thereby limiting innovation and efficiency.

In light of this, it is strongly recommended that future polymer research in Nigeria incorporates CFD methodologies as a complementary or alternative approach to experimental procedures. The integration of CFD offers several advantages: enhanced understanding of transport phenomena, predictive modeling of process parameters, reduction of experimental costs, and acceleration of polymer design and optimization processes.

To ensure successful implementation, research institutions should prioritize curriculum development, capacity building, and access to simulation software and high-performance computing resources. Moreover, strategic partnerships between academia, industry, and government will be essential to translate CFD insights into tangible product and process innovations. As Nigeria advances its national science and innovation agenda, embedding CFD within policy frameworks and funding mechanisms will be vital for sustaining long-term research excellence and industrial relevance in polymer science.

REFERENCES

1. N. Hagioka, H. Fukuoka, Y. Minegishi, K. Kodama, *IOP Conf. Ser. Mater. Sci. Eng.* **501**, 012061 (2019).
2. M. H. Zawawi, A. Saleha, A. Salwa, N. H. Hassan, N. M. Zahari, M. Z. Ramli, et al., *AIP Conf. Proc.*, **0202**, 52 (2018).
3. T. Oyegoke, Y. Adamu, E. C. Lawrence, A. N. Abiodun, *JESC*, **2**, 1 (2020).
4. Journal of Nig. Society of Chem. Engr. (JNSChE). <https://journal.nsche.org.ng/index.php/NSChE/abstract> (accessed 2025).
5. Nig. Journal of Mat. Sci. & Eng. (NJMSE). <https://njmse.msn.ng/> (accessed 2025).
6. Journal of Nig. Society of Phys. Sci. (JNSPS). <https://journal.nsps.org.ng/index.php/jnsps/about> (accessed 2025).
7. The Journal of Chem. Society of Nig. (JCSN). <http://journals.chemsociety.org.ng/index.php/jcsn/about> (accessed 2025).
8. A. Bkaefagomo, *JNSChE*, **38**, 32 (2023).
9. O. Aaojsja, *JNSChE*, **38**, 24 (2023).
10. G. C. Nwanisobi, C.I. Aghanwa, I. M. Odika, S. C. Muobike, I. L. Anarado, C. C. Chukwuebuka, et al., *JCSN*, **50**, 428 (2025).
11. M. A. Nnabuchi, C. E. Duru, G. I. Kalu, *Journal of Chemical Society of Nigeria*, **50**, 208 (2025).
12. O. U. Igwe, D. O. Agwu, Friday C, E. H. Oko, *JCSN*, **48**, 610 (2023).

13. I. A. Dina, C. E. Gimba, A. Hamza A, P. Ekwumengbo, *JCSN*, **48**, 585 (2023).
14. K. Manickavelan, S. Ahmed, K. Mithun, P. Sathish, R. Rajasekaran, N. Sellappan, *JNSPS*, **4**, 64 (2022).
15. SimScale. <https://www.simscale.com/docs/simwiki/cfd-computational-fluid-dynamics/what-is-cfd-computational-fluid-dynamics/> (accessed 2021).
16. Technopedia. <https://www.techopedia.com/definition/18247/computational-fluid-dynamics-cfd> (accessed 2021).
17. C. C. Chen, *CAST Comm.*, **1** (2002).
18. G. M. Pineda-Taorres, C. Durán-Valencia, F. Barragán-Aroche, S. López-Ramírez, *IntechOpen*, 2016.
19. Esmaeili H, Azizi S, Mojtaba Mousavi S, Hashemi SA. *Journal of Env. Treat. Techq.*, 272 (2020).
20. H. Patel, F. Ein-Mozaffari, R. Dhib, *Comput. Chem. Eng.*, **34**, 421 (2010).
21. A. Afsharpoor, M. T. Balhoff, Proceedings of SPE Annual Technical Conf. & Exhibtn., **1**, 527 (2013).
22. A. Afsharpoor, M. T. Balhoff, R. Bonnetcaze, C. J. Huh, *Pet Sci Eng.*, **94–95**, 79 (2012).
23. C. E. Duru, C. E. Enyoh, I. A. Duru, M. C. Enedoh, *JNSPS*, **5**, 1154 (2023).
24. O. O. Oluwasina, M. Z. Fahmi, O. O. Oluwasina, *JNSPS*, **6**, 2033 (2024).
25. O. B. Eyenubo, V. O. Peretomode, F. Egharevba, S. A. Osakwe, O. G. Avwioro, *JNSPS*, **6**, 1951 (2024).
26. A. O. Adeoye, R. O. Quadri, O. S. Lawal, *JNSPS*, **7**, 2558 (2025).
27. J. O. Arawande, G. O. Orodepo, W. B. Osungbemiro, *JCSN*, **47**, 50 (2022).
28. N. Y. Ilesanmi, A. K. Akinlabi, F. Y. Falope, A. M. Mosaku, A. A. Falomo, G. Oladipo, et al., *JCSN*, **47**, 334 (2022).
29. Itodo AU, Eneji IS, Weor TT. *JCSN*, **43**, 667 (2023).
30. I. A. Dina, C. E. Gimba, A. Hamza, P. Ekwumengbo, *JCSN*, **48**, 563 (2023).
31. S. E. Mohammed, N. I. Durumin-Iya, A. S. Abubakar, O. S. Ayanda, H. Badamasi, et al., *JCSN*, **48**, 785 (2023).
32. B. Ameh, K. A. Bello, I. Y. Chindo, A. I. Izang, *JCSN*, **49**, 586 (2024).
33. A. K. Akinlabi, S. B. Akinfenwa, T. D. Idowu, N. R. Laleye, F. Akinwunmi, A. M. Mosaku, et al., *JCSN*, **45**, 1048 (2020).
34. C. E. Umeocho, T. U. Onuegbu, E. N. Nwosu, R. O. Ohakwe, *JCSN*, **49**, 896 (2024).
35. O. P. Nsude, A Emmanuel A, E. C. Ezech, O. C. Ike, O. C. Omuluche, K. J. Orie, et al., *JCSN*, **47**, 334 (2022).
36. O. Ofoegbu, N. Umah, E. Akor, *JCSN*, **46**, 129 (2021).
37. A. U. Itodo, I. S. Eneji, T. T. Weor., *JCSN*, **43**, 667 (2018).
38. A. K. Akinlabi, T. O. Akinola, R. K. Quadri, O. S. Babajide, I. A. S. Bankole, *JCSN*, **41**, 36 (2016).
39. K. A. Baraya, D. E. A. Boryo, I. Y. Chindo, U. F. Hassan, *JCSN*, **46**, 718 (2021).
40. R. A. Maduagwu, E. T. Omotade, M. K. David, *JCSN*, **47**, 386 (2022).
41. J. O. Arawande, G. O. Orodepo, W. B. Osungbemiro, *JCSN*, **47**, 350 (2022).
42. N. Y. Ilesanmi, A. K. Akinlabi, F. Y. Falope, A. M. Mosaku, A. A. Falomo, G. Oladipo, et al., *JCSN*, **47**, 334 (2022).
43. O. O. Emoyan, E. Ohwo, E. E. Akporhonor, *JCSN*, **47**, 1059 (2022).
44. T. M. Osobamiro, O. T. Oluwole, S. O. Abdullah, *JCSN*, **48**, 501–13 (2023).
45. I. A. Dina, C. E. Gimba, A. Hamza, P. Ekwumengbo, *JCSN*, **48**, 563 (2023).
46. I. A. Dina, C. E. Gimba, A. Hamza, P. Ekwumengbo, *JCSN*, **48**, 585 (2023).
47. O. U. Igwe, D. O. Agwu, C. Friday, E. H. Oko, *JCSN*, **48**, 610 (2023).
48. T. A. Akinnifesi, F. B. Borokini, A. O. Adegun, E. Mafinuyomi, A. Olonisakin, N. B. Omodara, et al., *JCSN*, **49**, 261 (2024).
49. P. S. Ukanah, S. Gadimoh, S. U. Ameuru, *NJMSE*, **5**, 73 (2014).
50. E. O. Achukwu, A. M. Barnabas, A. Mamman, M. I. Uzochukwu, *NJMSE*, **6**, 32 (2015).
51. S. Gadimoh, H. D. Ibrahim, E. G. Kolawole, P. O. Nkeonye, A. Mustapha, *NJMSE*, **6**, 53 (2015).
52. L. Ekebafé, F. A. O. Akpa, D. A. Olugbemide, *NJMSE*, **10**, 109 (2020).
53. E. T. Musa, A. Hamza, A. S. Ahmed, U. S. Ishiuku, E. G. Kolawole, *NJMSE*, **7**, 35 (2016).
54. O. E. Adedeji, O. O. Ezekiel, *JNSChE*, **36**, 25 (2021).
55. A. A. Osigbesan, A. Y. Waziri, F. N. Dabai, O. Fasanya, A. Y. Atta, B. Y. Jibril, *JNSChE*, **34**, 28 (2019).
56. K. A. Akintayo, *JNSChE*, **33**, 19 (2018).
57. A. A. Oladunni, O. J. Odejobi, J.A. Sonibare, *JNSChE*, **38**, 24 (2023).
58. H. Patel, R. Dhib, F. Ein-Mozaffari, *Chem Eng Technol*, **33**, 258 (2010).
59. L. Xie, L. T. Zhu, Z. H. Luo, *Chem Eng Technol*, **39**, 857 (2016).
60. Mettler-Toledo. https://www.mt.com/sg/en/home/applications/L1_AutoChem_Applications/L2_ProcessDevelopment/wr_L3_appl_Scaleup.html (accessed 2021).
61. N. Jongpaajit, P. Bumroongsri, *Energy Procedia*, **138**, 901 (2017).
62. Ansys. <https://www.ansys.com/> (accessed 2021).
63. COMSOL Multiphysics. <https://www.comsol.fr/> (accessed 2021).
64. SimScale Report. <https://www.simscale.com/ppc-cloud-cfd-software/> (accessed 2021).
65. F. Oghomwen, K. Jiri, An Overview of Science, Technology and Innovation (STI) Policy. 33rd IBIMA Conference, Granada, Spain, 2019.
66. OSGF. NPSTIF - Sci. & Tech 2023. <https://www.osgf.gov.ng/resources/policies/science-and-technology/> (accessed 2025).

Purification and characterization of lipoxygenase enzyme from Iraqi patients with type 2 diabetes mellitus

M. T. Lateef^{1*}, H. Abd Alhassan Mahmood¹, Yu. S. Abdulsahib²

¹ Department of Applied Chemistry, College of Applied Sciences, University of Fallujah, Iraq

² Department of Clinical Pharmacy, College of Pharmacy, University of Misan, Iraq

Received: May 25, 2025; Revised: August 28, 2025

Lipoxygenase (LOX) enzyme was partially purified from the sera of type 2 diabetic mellitus patients (T2DM) in the current study. The results indicated that three peaks from ion exchange chromatography and one peak from gel filtration chromatography had high activity for the patients. The solution was obtained by ammonium sulfate precipitation (30–50%) following a dialysis process, and the sample was purified by gel filtration using Sephadex G-100 column with purification folds up to (2.65) (10.65), respectively. The optimum temperature for the LOX enzyme was 40°C, and its pH was 8.0. According to SDS-PAGE electrophoresis, the enzyme's approximate molecular weight was 70 kD.

Key words: Diabetes mellitus, lipoxygenase ([LOX), oxidative stress, purification of enzyme.

INTRODUCTION

Diabetes mellitus (DM) and its consequences are the most important diseases that affect human health and pose a serious threat to worldwide public health [1]. DM is a multifaceted metabolic disorder that is categorized through chronic hyperglycemia occasioning from insulin product deficiencies, action of insulin, or both. The many complications caused by this disorder severely impact the body's organs and total systems [2]. Oxidative stress particularly mediated by free radicals including ROS and RNS is the foremost source of DM complaints. There is a relationship between hyperglycemia and oxidative stress in the development of diabetic complications, for instance: nephropathy neuropathy, retinopathy, besides cardiovascular diseases [3]. Hyperglycemia-induced oxidative stress begins with the excessive production of ROS due to elevated glucose levels [4].

Moreover, high levels of glucose (hyperglycemia) rise the generation of advanced glycation end products (AGEs) from a non-enzymatic reaction of the reducing sugars with cellular components as proteins, lipids or nucleic acids. In the meantime, AGEs are responsible for ROS creation by different pathways, as well as for metal-catalyzed oxidations. This series of oxidative stress might result in cellular dysfunction, injury and significantly affect various tissues and organs [5, 6]. Unlike healthy people, people with DM2 who are not on any medication, are inevitably at risk of developing peripheral vascular disease, stroke, and cardiovascular disease [7].

Lipoxygenases (EC 1.13.11.12) (LOXs) are a group of dioxygenases that contain non-heme iron and catalyze the bi-oxidation of polyunsaturated fatty acids (PUFAS) containing 1-cis-4-cis-pentadiene to convert them into fatty acid hydroperoxides [8]. Lipoxygenases come in three different isoforms: 5-, 12-, and 15-lipoxygenase. The 5-lipoxygenase isoform contributes leukotrienes which are potent inflammatory mediators implicated in a number of chronic inflammatory illnesses, such as asthma and allergic reactions. 12-Hydroxyeicosatetraenoic acid is synthesized by the 12-lipoxygenase isoform. The 15-lipoxygenase isoform contributes to the synthesis of lipoxins which have anti-inflammatory properties and help regulate the resolution of inflammation [9]. In addition to their role in inflammation, lipoxygenase isoforms have been linked to a number of physiological functions. Adipogenesis and development of adipose tissue have been associated with particular lipoxygenase variations, suggesting a potential role in controlling body weight and metabolism [10].

The diabetes disorder is linked with chronic inflammation [11]. Lipoxygenase, a rate-limiting enzyme that facilitates the process of arachidonic acid metabolism into leukotriene (LT), promotes inflammation by activating the production of inflammatory cells (neutrophils) and cytokines. A significant way to preventing inflammation is by reducing the production of LT through inhibition of the LOX enzyme in the body [12].

* To whom all correspondence should be sent:
E-mail: mohammedtalib@uofallujah.edu.iq

MATERIALS AND METHODS

The blood samples were collected in the period from January 1st, 2022 until the end of September, 2023 from Falluja Hospital. The study included 50 T2DM patients from both sexes, ages ranged between 35-65 years. Venous blood samples of 5 mL were obtained from each patient in a plain laboratory and the following laboratory experiments were performed.

Precipitation by concentrated ammonium sulfate (30%-55%) with dialysis

Solid ammonium sulfate was progressively added to the serum (5 mL) in order to precipitate the enzyme while constantly stirring at 5°C approximately till the solution became turbid. Then the mixture was centrifuged for 20 min at 4000 rpm to separate the precipitate from the supernatant. The precipitate was dissolved in Tris-HCl buffer (10 mM, pH 7.4) [13]. To perform dialysis, the protein solution made in the previous stage was put on the bottom of a tightly sealed cellophane bag into a Tris-HCl [10 mM, pH 7.4] buffer solution at 4°C while being continuously stirred. After the process of dialysis was completed, enzyme activity and protein concentration were determined and the final volume of the solution was calculated.

Ion exchange chromatography

Following column balancing and Tris-HCl (10 mM, pH 7.4) washing, the samples from the aforementioned procedures were run through a 15 cm DEAE-Sepharose anion column. In each pipeline, a 3 mL fraction aliquot was collected at a flow rate of 0.5 mL/min. An UV-VIS spectrophotometer was used to measure the absorbance at 280 nm. The fractions that provided the highest absorption were collected. Following measurements of the protein volume and enzyme activity, bound proteins were eluted using 100 mL of Tris-HCl (10 mM, pH 7.4) which included a linear gradient of NaCl (0.1–1M). A 3 mL fraction was collected at a flow rate of 0.5 mL/min in all pipelines. For all fractions, the amount of protein and enzyme activity was determined.

Gel filtration chromatography

After equilibrating and eluting with Tris-HCl buffer (10 mM, pH 7.4), the sample was loaded to a Sephadex G-200 column (20 × 1.5 cm). In each pipeline, an aliquot of 3 mL fraction was collected at a flow rate of 1 mL/min. Each fraction's absorbance was measured at 280 nm using a UV-VIS spectrophotometer, and the fractions with the highest

absorption were used to gauge the activity of proteins and enzymes.

Lipoxygenase (LOX) activity assay

The activity of lipoxygenase to convert linoleate to its hydroperoxide was assayed by the Holman method using the LOX activity assay kit of Abcam company (China) [14].

Estimation of protein concentration [15, 16].

The total concentration of proteins in the serum was estimated using the kit biuret method of SPINREACT Company (Spain).

Estimation of molecular weight by electrophoresis using SDS – PAGE [17, 18].

Enzymes from diabetic patients were purified by SDS-PAGE gel electrophoresis at the University of Baghdad, Ibn Al-Haitham College of Education for Pure Science.

Kinetics properties

- Effect of pH on enzyme activity: The activity was determined using the eluted fractions from the Sephadex G- 100 column at optimum reaction conditions with several buffers in the pH range from 3 to 9 (glycine, Na-acetate and Tris-HCl). The rate of reaction was plotted *versus* pH to determine the optimum pH for LOX reaction.
- Effect of temperature: The activity of LOX was determined at temperatures of 25, 30, 35, 40, 45, 50, and 55°C in 10 mM Tris-HCl buffer of pH 8.

RESULTS AND DISCUSSION

Ion exchange chromatography

Patients with type 2 diabetes mellitus were used as a source of lipoxygenase which was isolated from their serum. (NH₄)₂ SO₄ and dialysis process were used to precipitate 5 ml of serum for each patient. Proteins are usually concentrated in the first steps of enzyme removal by using a suitable amount of salt and water in order to reach a high level of purity. Ammonium sulfate is commonly used to concentrate proteins which dissolve easily in water, where salts are produced as a result of neutralizing the charge of protein in order to make salt. This decreases protein solubility and sedimentation, known as salting out effect [19]. Owing to its high efficiency, fast production and ability to separate bioactive compounds using simple reactions, it has a wide range of uses [20]. After the dialysis process, the samples were eluted using 50 mM Tris-HCl buffer with graded NaCl concentration at a pH of 7.0 using a DEAE-Sepharose column.

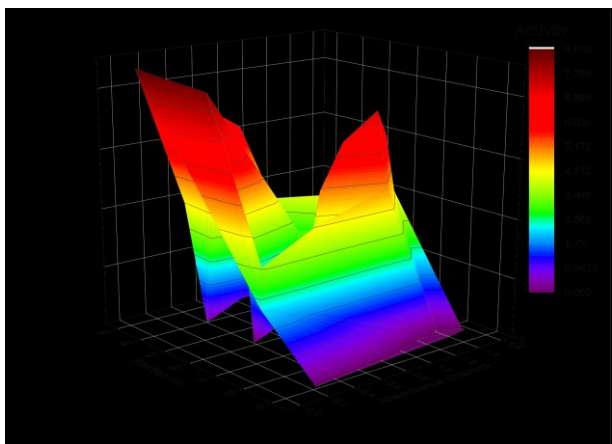


Fig. 1. Purification of LOX from sera of T2DM patients by ion exchange chromatography.

Three protein peaks (protein concentration and LOX activity) were identified, LOX data found in the beginning, wash fractions falling within 7–15 fractions. Three protein peaks are shown in Fig. 1, one in fractional washings, and two in rinsing fractions.

Gel filtration chromatography

Size-exclusive chromatography, which relies on the size of the particles separated, was employed as a crucial purification step. The concentrated active portion from the earlier stage made it through. After being cleaned and eluted with washing buffer, a 1.5×20 cm Sepharose 6B column was employed in this phase. The one active protein peak, shown by the fraction number [4-9] in Fig. 2, shows the lipoxygenase activity. Fig. 2 also shows the LOX activity in the fraction number [3-13] which indicates a single peak of protein.

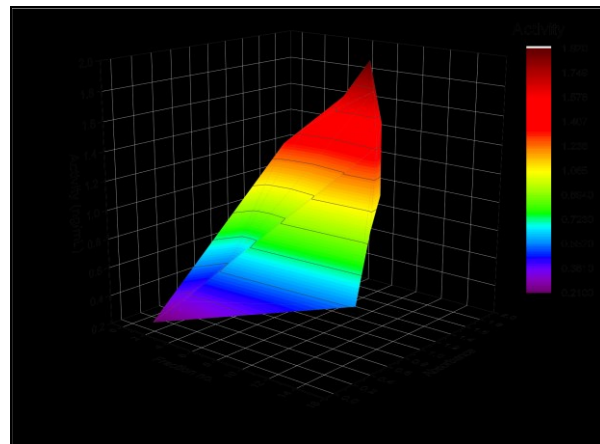


Fig. 2. Purification of LOX from sera of T2DM by gel filtration chromatography.

Ion exchange produced three isomers, the specific activity of which was 8.92 mg.ng^{-1} for the first, 11.14 mg.ng^{-1} for the second, and 13.32 mg.ng^{-1} for the third isomer. The purification folds were 1.2, 1.77, 2.22, 2.65, 10.65 and the yield percentages were 93.2, 77.12, 52.41, 32.41, 32.94, 27.48, respectively. The final step was gel filtration, which gave 53.4 mg.ng^{-1} specific activity (see Table 1).

SDS-PAGE electrophoresis

SDS-PAGE electrophoresis was used to determine the approximate molecular weight of LOX. The first two peaks in the ion exchange chromatography patterns represented LOX activity whereas a sharp peak was obtained in gel filtration chromatography. The sample insert in SDS-PAGE electrophoresis (Fig. 3) shows an approximate molecular weight of LOX of $\sim 70\,000$.

Table 1. Purification steps of LOX enzyme

	Volume, mL	Protein conc., mg/mL	Activity of LOX, ng/mL	Specific activity, mg/ng	Purification fold	Yield %
Crude	5	3.14	15.74	5.012	1	100
Participation $(\text{NH}_4)_2\text{SO}_4$	5	2.34	14.67	6.037	1.2	93.2
Ion exchange isoenzyme I	5	1.36	12.14	8.92	1.77	77.12
Ion exchange isoenzyme II	5	0.74	8.25	11.14	2.22	52.41
Ion exchange isoenzyme III	5	0.46	6.13	13.32	2.65	32.94
Gel filtration Sephadex G- 100	3	0.135	7.21	53.4	10.65	27.48

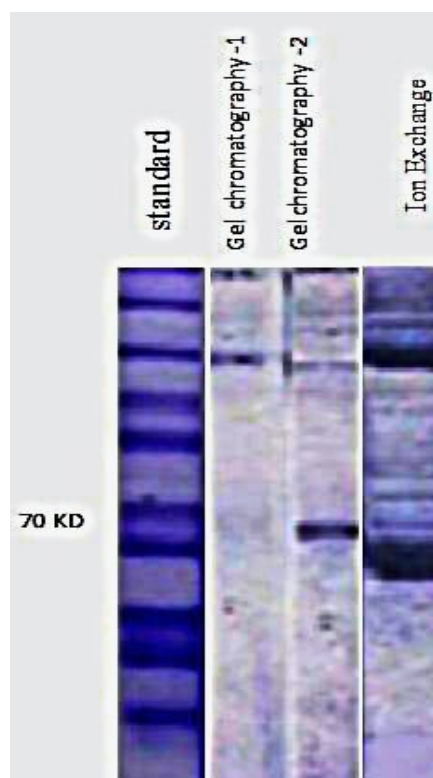


Fig. 3. Polyacrylamide gel electrophoresis of partially purified LOX enzyme from sera of T2DM patients.

Optimum temperature

The optimum temperature for enzyme activity was established, and the LOX assay was performed at 25–55 °C in 50 mM Tris-HCl buffer of pH 7.4, at 5-min intervals. The enzyme solution was placed in a water bath for 30 min and then allowed to stay at room temperature for 10 min in order to access thermal stability. Fig. 4 shows the measurement of LOX activity. Three repetitions of the experiments were made. The optimum temperature was 40°C.

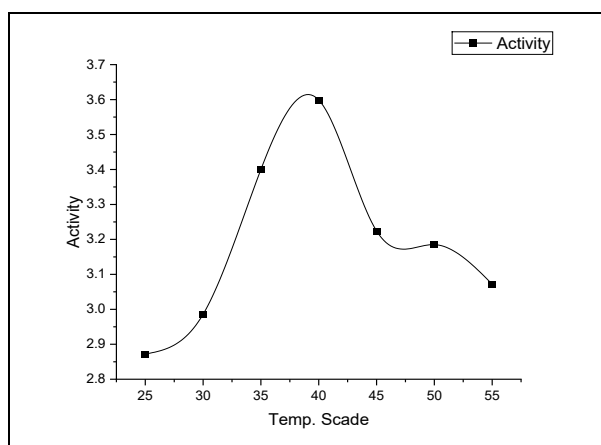


Fig. 4. Effect of temperature on the velocity of the LOX enzyme purified from the serum of T2DM patients.

The current study's findings indicated that the crude patients' specific activity was 5.012 mg.ng⁻¹, followed by 6.037 mg.ng⁻¹ in the precipitation step with ammonium sulfate.

Optimum pH

Citrate-phosphate buffer (50 mM, pH 3-5), sodium phosphate buffer (50 mM, pH 6-8), and Tris-HCl (50 mM, pH 8-10) were the buffer systems used. The optimum pH for enzyme activity was found to be between 3 and 10. After 30 min at 40°C with the enzyme solution in each buffer (at the optimum pH 8), LOX activity was measured with linoleic acid present. The plot of LOX activity vs pH is shown in Fig. 5.

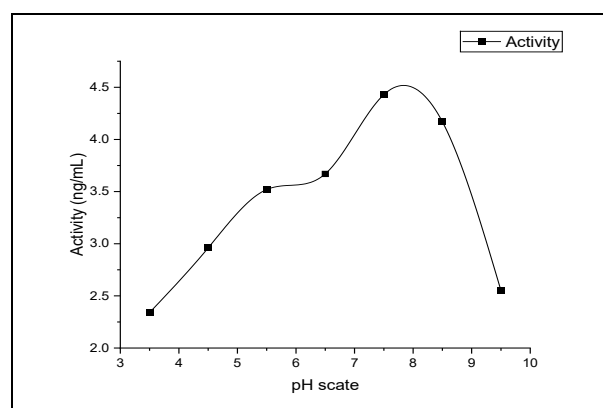


Fig. 5. Effect of pH on LOX activity.

CONCLUSION

The present study aimed to utilize sera of type 2 diabetic patients to purify lipoxygenase enzyme (LOX) by using protocol purification methods. The approximate molecular weight of LOX was estimated to be 70000 Dalton by using SDS-PAGE electrophoresis. The optimum pH was 8.0 and the optimum temperature - 40°C.

REFERENCES

1. P. Liu, Z. Zhang, Y. Cai, Z. Li, Q. Zhou, Q. Chen, *Ageing Research Reviews*, **94**, 102 (2024). Doi: 10.1016/J.Arr.2024.102201
2. N. Chandimali, S. Gyeong Bak, E. Hyun Park, H.-Jin Lim, Y.-Seon Won, E.-Kyung Kim, S.-Ik Park S. Jae Lee, *Cell Death Discovery*, **19**, 11 (2025), Doi: 10.1038/S41420-024-02278-8
3. A. Caturano, M. D'angelo, A. Mormone, V. Russo, M.P. Mollica, T. Salvatore, et al., *Curr Issues Mol Biol.*, **45**, 51 (2023), Doi: 10.3390/Cimb45080420
4. P. González, P. Lozano, G. Ros, F. Solano, *Int. J. Mol. Sci.*, **52**, 24 (2023). Doi: 10.3390/Ijms24119352
5. M. Khalid, G. Petroianu, A. Adem, *Biomolecules*, **5**, 12 (2022). Doi: 10.3390/Biom12040542
6. A.B. Uceda, L. Mariño, R. Casasnovas, M. Adrover, *Biophys. Rev.*, **16**, 189 (2024). Doi: Org/10.1007/S12551-024-01188-4

7. R.L. Morley, A. Sharma, A.D. Horsch R.J. Hinchliffe, *BMJ*, **360** (2018), Doi: 10.1136/Bmj.J5842
8. H. Kuhn, S. Banthiya K. Van, *Biochim. Biophys. Acta*, **1851**(4), 308 (2015). Doi: 10.1016/J.Bbalip.2014.10.002
9. Y. Imai, A. D. Dobrian, M. A. Morris, D. A. Taylor-Fishwick J. L. Nadler, *Diabetologia*, **59**(4), 673 (2016), Doi: 10.1007/S00125-016-3890-Y
10. B. B. A. Castro, O. Foresto-Neto, N. O. Saraiva-Camara, H. Sanders-Pinheiro, *Clin. Exp. Pharmacol. Physiol*, **48**(12), 1579 (2021). Doi: 10.1111/1440-1681.13556
11. D. Pedicino, G. Liuzzo, F. Trotta, A.F. Giglio, S. Giubilato, F. Martini, F. Zaccardi, G. Scavone, M. Previtero, G. Massaro, P. Cialdella, M.T. Cardillo, D. Pitocco, G. Ghirlanda, F. Crea, *J. Diabetes Res.*, **1**, 11 (2013). Doi: 10.1155/2013/184258
12. E.N. Agboa, R.S. Segodia, N.J. Gumede, K.W. Poopedic, T.C. Lebohoa, R.M. Mampaa, W. Nxumalo, *Results in Chemistry*, **14**, 102 (2025). Doi:10.1016/J.Rechem.2025.102102
13. P. T. Wingfield, *Curr. Protoc. Protein Sci.*, **3**, 5 (2001) Doi:10.1002/0471140864.Psa03fs13
14. S. M. Rappoport, T. Schewe, R. Wiesner, *Eur. J. Biochem.*, **96**, 545 (1979).
15. R. J. Henry, C. Sobel, S. Berkman, *Anal. Chem.*, **29**, 1491 (1957).
16. T. Peters Jr, *Clin. Chem.*, **14**, 1147 (1968). Doi:Org/10.1093/Clinchem/14.12.1147
17. B. D. Hames, *Gel Electrophor. Proteins*, **5**, 41 (1981).
18. C. Ch. Gu, J. K.Wang, T. M. Huang, H.J. Lee, W.Y. Chou, C. L. Meng, *Eur. J. Biochem.*, **202**, 681 (1991). Doi: Org/10.1111/J.1432-1033.1991.Tb16423.X
19. E. Karlsson, L. Ryden, J. Brewer, *Protein Purification, High Resolution Methods and Applications*, **59**, 145 (1998).
20. M. T. Lateef, N. A. Naji, N. K. Shafeeq, *Biochem. Cell. Arch.*, **20** (2020).

Eco-engineered ZnO nanoparticles via *Convolvulus prostratus* with Al- and Zr-doping: structural, mechanical, and antifungal enhancement for sustainable construction applications

N. J. Sai Varun¹, N. Sai Aishwarya Reddy¹, S. Pradeepa¹, H. S. Lalithamba², Srilatha Rao³,
G. K. Prashanth^{4,5*}

¹ Department of Civil Engineering, Sir M. Visvesvaraya Institute of Technology, Bengaluru-562 157, India

² Department of Chemistry, Siddaganga Institute of Technology, Tumkur-572 103, India

³ Department of Chemistry, Nitte Meenaskhi Institute of Technology, (Deemed to be University), Bengaluru-560 064, India

⁴ Research and Development Centre, Department of Chemistry, Sir M. Visvesvaraya Institute of Technology, Bengaluru-562 157, India

⁵ Visvesvaraya Technological University, Belagavi-590 018, India

Received: June 07, 2025; Revised: July 05, 2025

This study presents the green synthesis of undoped and doped zinc oxide (ZnO) nanoparticles (NPs) using *Convolvulus prostratus* (*C. prostratus*) flower extract via the solution combustion synthesis (SCS) method. The plant extract, rich in phytochemicals, acts as a bio-reductant and combustion fuel, enabling eco-friendly nanoparticle fabrication. Aluminum (Al³⁺) and zirconium (Zr⁴⁺) ions were introduced as dopants at 3%, 5%, and 7% by co-dissolving their respective nitrates with zinc nitrate. Post-synthesis calcination at 600°C enhanced the crystallinity and phase purity of the resulting ZnO NPs. Structural characterization using powder X-ray diffraction (PXRD) confirmed a hexagonal wurtzite crystal structure with crystallite sizes ranging from 8.8 to 16.1 nm. Fourier transform infrared spectroscopy (FTIR), scanning electron microscopy with energy-dispersive X-ray spectroscopy (SEM-EDX), transmission electron microscopy (TEM), and ultraviolet-visible (UV-Vis) spectroscopy analyses revealed dopant-induced lattice distortion, morphological refinement, and tunable optical properties (band gap up to 3.77 eV). Mechanical testing of concrete blocks with the embedded ZnO NPs revealed that 7 mol% of Zr-doped ZnO imparted the highest compressive strength (49.96 MPa). Moreover, antifungal inspection demonstrated strong resistance against fungal colonization in doped samples. These results demonstrate the multifunctional potential of green-synthesized doped ZnO NPs in sustainable construction and antimicrobial material development.

Keywords: Green synthesis; zinc oxide NPs; *Convolvulus prostratus*; doping; aluminum; zirconium; PXRD; FTIR; SEM; sustainable concrete; antimicrobial activity; eco-friendly nanomaterials

INTRODUCTION

Nanotechnology has emerged as one of the most promising and transformative frontiers in material science, offering a vast spectrum of applications across disciplines such as medicine, catalysis, electronics, energy, and environmental protection [1-3]. Among various nanomaterials, zinc oxide NPs (ZnO NPs) have attracted significant attention due to their distinctive properties, including a wide band gap of 3.37 eV, high exciton binding energy (~60 meV), excellent chemical stability, biocompatibility, and multifunctional characteristics. These attributes render ZnO NPs suitable for diverse applications, ranging from ultraviolet (UV) shielding and gas sensing to photocatalysis, antimicrobial treatment, and optoelectronic device fabrication [4, 5].

Conventional synthesis techniques for ZnO NPs—such as sol-gel, hydrothermal, and chemical vapor deposition—are well-established but typically involve high energy consumption, toxic chemicals, and costly instrumentation. These drawbacks raise concerns about their long-term environmental sustainability and practical scalability [6–10]. In light of these limitations, green synthesis methodologies have gained considerable momentum as they align with the principles of green chemistry—minimizing hazardous by-products, reducing energy demands, and utilizing renewable natural sources.

Among green synthesis strategies, plant-mediated synthesis has emerged as a particularly eco-friendly and cost-effective approach. Plants are inherently rich in phytochemicals such as flavonoids, alkaloids, terpenoids, phenolics,

* To whom all correspondence should be sent:

E-mail: prashanth_chem@sirmvit.edu
prashaanthgk@gmail.com

glycosides, and proteins, which serve as natural reducing and stabilizing agents during nanoparticle formation. These bioactive compounds facilitate metal ion reduction and particle stabilization under mild, ambient conditions, enabling sustainable and large-scale nanoparticle synthesis without compromising efficiency or performance [11–16].

In our previous research, we have successfully synthesized ZnO NPs using a variety of plant-based materials, such as *Abutilon indicum*, *Melia azedarach*, *Indigofera tinctoria* [17], *Tamarindus indica*, *Punica granatum* [18], *Piper betle* [19], *Citrus limon* [20, 21], *Caesalpinia sappan* [22], *Mirabilis jalapa* [23], *Mimosa pudica* [24], *Simarouba glauca* [25] and explored their potential biological applications. In the present study, *Convolvulus prostratus*—commonly known as Shankpushpi—was employed as a green precursor for the biosynthesis of ZnO NPs. A perennial herb from the *Convolvulaceae* family, *C. prostratus* is extensively distributed across India and has long-standing medicinal significance in Ayurvedic practices, where it is reputed for its neuroprotective, memory-enhancing, and cognitive-boosting properties. The flower extract of this plant is particularly rich in bioactive secondary metabolites such as flavonoids, phenolic acids, alkaloids, and coumarins, which are ideally suited for nanoparticle synthesis due to their reducing, chelating, and stabilizing capabilities [26–30].

Utilizing *C. prostratus* flower extract in nanoparticle synthesis presents dual benefits: (i) it leverages a renewable, non-toxic botanical source abundant in natural phytochemicals, and (ii) it enables the production of biocompatible, functionally enhanced ZnO NPs. To further modulate the physicochemical and functional properties of ZnO, doping with metal ions such as aluminum (Al^{3+}) and zirconium (Zr^{4+}) has been employed. Metal ion doping introduces structural and electronic modifications that can result in enhanced photoluminescence, modified band gap energy, and improved catalytic or antimicrobial performance, broadening the application potential of the resulting nanomaterials.

Concrete, one of the most widely used construction materials globally, is renowned for its mechanical strength, durability, and cost-effectiveness. However, modern sustainability challenges have necessitated innovation in concrete technology to develop more environmentally responsible and functionally superior materials. The integration of nanotechnology, particularly ZnO NPs—both undoped and doped—into concrete composites has shown promising results in this

regard. ZnO NPs possess excellent photocatalytic, antimicrobial, and antifungal properties, which can significantly enhance the lifespan and hygienic quality of concrete structures [31–34]. Moreover, doping ZnO with Al and Zr further improves its surface reactivity and structural stability, optimizing its performance under real-world conditions.

From an ecological standpoint, the incorporation of ZnO NPs into concrete formulations can potentially reduce the overall carbon footprint by minimizing the dependence on traditional cement, a major contributor to CO_2 emissions. These nanomaterials also contribute to improved compressive strength, chemical resistance, and durability of concrete, while supporting circular construction practices through the efficient use of recycled aggregates and water. Additionally, the inherent antimicrobial and antifungal properties of doped ZnO help in mitigating microbial growth in moist environments, thereby preventing surface degradation and associated health hazards. The photocatalytic attributes further impart self-cleaning functionalities, making such materials especially suitable for use in public infrastructure and high-humidity settings [31–34]. Hence, the core objective of this research is to develop a green, simple, and sustainable route for synthesizing undoped and Al/Zr-doped ZnO NPs using *C. prostratus* flower extract through a solution combustion method. The synthesized nanomaterials were thoroughly characterized using modern analytical techniques such as X-ray diffraction (XRD), Fourier transform infrared spectroscopy (FTIR), scanning electron microscopy (SEM), and UV-Vis spectroscopy to understand their structural, morphological, and optical features. Furthermore, the synthesized NPs were embedded into concrete block formulations to evaluate their mechanical performance and antifungal activity. This work aims to contribute to the development of multifunctional, sustainable construction materials that combine environmental responsibility with superior structural and hygienic performance.

MATERIALS AND METHODS

Chemicals and reagents

Zinc nitrate hexahydrate [$\text{Zn}(\text{NO}_3)_2 \cdot 6\text{H}_2\text{O}$, AR, $[\text{ZrO}(\text{NO}_3)_2 \cdot 4\text{H}_2\text{O}$, AR, 99% SD fine], aluminum nitrate nonahydrate [$\text{Al}(\text{NO}_3)_3 \cdot 9\text{H}_2\text{O}$, Fisher, AR, 99 %].

Flower collection

Fresh *C. prostratus* flowers (Figure 1) were collected from the vicinity of Malleswaram, Bengaluru, Karnataka, India. The collected flowers

were thoroughly cleaned with tap water to remove any adhering dust or soil, followed by rinsing with distilled water to eliminate residual impurities. The clean flowers were then shade-dried for 15 days to preserve the active phyto-constituents. After drying, the flowers were cut into small pieces and finely powdered using a mechanical grinder. The resulting powder was stored in an airtight container for further use in the green synthesis of NPs.



Figure 1. Flowers of *Convolvulus prostratus*

Preparation of flower extract

The aqueous extract of *C. prostratus* flowers was prepared using the Soxhlet extraction method. For this, 20.0 g of finely powdered, shade-dried *C. prostratus* flowers were loaded into the Soxhlet apparatus and extracted using 150 mL of double-distilled water as the solvent. The extraction process was carried out for several hours until the solvent in the siphon tube appeared clear, indicating complete extraction of water-soluble phytochemicals.

After completion of the extraction cycle, the resulting extract was allowed to cool to room temperature and then filtered using Whatman No. 1 filter paper to remove any residual plant debris. The clear aqueous filtrate was collected and stored in a clean, airtight container under refrigerated conditions for further use in the green synthesis of undoped and doped zinc oxide NPs.

Phytochemical analysis of C. prostratus flowers

To evaluate the presence of bioactive constituents responsible for the green synthesis of metal oxide NPs, a preliminary phytochemical screening of the aqueous extract of *C. prostratus* flowers was conducted using standard qualitative methods. The extract was tested for major phytochemical groups known to contribute to metal ion reduction, capping, and stabilization during nanoparticle formation.

The analysis confirmed the presence of various phytochemicals such as flavonoids, phenolic compounds, alkaloids, tannins, saponins, and glycosides, which are well known for their electron-donating ability and capability to form complexes with metal ions (Table 1). These compounds play a crucial role in converting metal precursors into stable NPs under ambient or combustion conditions.

The abundance of polyphenolic and flavonoid content in *C. prostratus* extract is particularly significant, as these compounds not only facilitate the reduction of metal ions (Zn^{2+} , Al^{3+} , Zr^{4+}) but also contribute to the stabilization of the resulting ZnO NPs by capping their surface, thereby preventing agglomeration.

Table 1. Phytochemical constituents present in *C. prostratus* flower extract

S. No.	Phytochemical group	Observation	Results (+/-)
1	Alkaloids	White precipitate (Wagner's test)	+
2	Flavonoids	Yellow coloration (Alkaline reagent test)	+
3	Phenolic compounds	Blue-black color (Ferric chloride test)	+
4	Tannins	Greenish-black color (Lead acetate test)	+
5	Saponins	Stable froth formation (Foam test)	+
6	Glycosides	Brick-red precipitate (Keller–Killiani test)	+
7	Terpenoids	Reddish-brown interface (Salkowski's test)	+/-
8	Proteins	Violet color (Biuret test)	–

Note: (+) Present; (–) Absent; (+/-) Trace or weak presence

Synthesis of undoped, Al- and Zr-doped ZnO NPs by solution combustion method

The solution combustion synthesis (SCS) method was employed for the green synthesis of undoped and doped zinc oxide NPs using *C. prostratus* flower extract as a natural bio-reductant and fuel. The procedure followed a modified version of the methodology reported in our previous publication.

For the synthesis of undoped ZnO NPs, 2.0 g of zinc nitrate hexahydrate was dissolved in 20 mL of double-distilled water under constant magnetic stirring until a clear solution was obtained. To this solution, 5.0 mL of the prepared plant extract was added and thoroughly mixed. The homogeneous mixture was then transferred into a ceramic crystallizing dish and introduced into a preheated muffle furnace set at $400 \pm 15^\circ\text{C}$. Within a few minutes, the solution formed a transparent gel which subsequently underwent spontaneous combustion due to the presence of the bio-fuel, resulting in a voluminous, fluffy powder of ZnO NPs.

For the synthesis of doped ZnO NPs, the same procedure was followed with the addition of dopant precursors—aluminum nitrate nonahydrate or zirconyl nitrate tetrahydrate (at specific molar

substitution levels of $x = 0.03, 0.05, \text{ and } 0.07$), following the general formula $\text{Zn}_{1-x}\text{M}_x\text{O}$, where $\text{M} = \text{Al}$ or Zr . The calculated amount of dopant salt was co-dissolved with zinc nitrate in the aqueous medium before the addition of the plant extract, ensuring uniform distribution of dopant ions within the precursor solution.

Physico-chemical characterization of NPs

Various analytical methods were employed to characterize the synthesized NPs, including PXRD, FTIR spectroscopy, SEM with EDAX, TEM, and UV-Vis spectroscopy. XRD patterns were recorded using a Shimadzu PXRD 7000 diffractometer with $\text{Cu K}\alpha$ radiation ($\lambda = 1.5406 \text{ \AA}$) over a 2θ range of $30^\circ\text{--}75^\circ$. The surface morphology was analyzed with a JEOL JSM 6390 scanning electron microscope. UV-Vis absorption spectra were obtained using a Perkin Elmer Lambda 35 spectrophotometer in diffuse reflectance mode, covering wavelengths between 200 and 800 nm. FTIR spectroscopy was used to study chemical bonding in the ZnO NPs, employing a Bruker Alpha-1 spectrometer with KBr windows and a resolution of 2 cm^{-1} over the range of $400\text{--}4000 \text{ cm}^{-1}$. TEM measurement was carried out on a Philips 200 instrument.

- *Concrete block preparation and mechanical testing conditions.* Concrete blocks were prepared with a cement: sand: aggregate mix ratio of 1:2:4, using a water-to-cement ratio of 0.5. The blocks were cured for 28 days in water at $27 \pm 2^\circ\text{C}$ before testing. All compressive strength measurements were carried out following IS 516–1959 in triplicate, and the average values are reported.

- *Mechanical strength testing.* After curing, compressive strength tests were carried out according to IS 516–1959 using a compression testing machine. Each value reported is an average of three replicate measurements.

- *Antifungal activity testing.* The antifungal testing involved block exposure to fungal cultures with observations made after 72 h. Although inhibition zones were noted visually, no numerical data such as inhibition diameters or CFU counts were recorded in this study. This is now acknowledged as a limitation, and future work will incorporate quantitative microbiological analysis. The antifungal activity was tested in triplicate to ensure reproducibility.

RESULTS AND DISCUSSION

Formation mechanism of undoped and doped ZnO NPs

The green synthesis of undoped and doped ZnO NPs using *C. prostratus* flower extract operates through a phytochemical-mediated solution

combustion mechanism. The extract, rich in bioactive compounds such as flavonoids, phenolics, alkaloids, tannins, and saponins, plays a critical role in the reduction of metal precursors, stabilization of nanoparticle surfaces, and control over particle growth and morphology. These naturally occurring phytochemicals not only serve as eco-friendly reducing and stabilizing agents but also act as combustion fuels during synthesis. In the initial stage, $\text{Zn}(\text{NO}_3)_2 \cdot 6\text{H}_2\text{O}$ and the plant extract are mixed in aqueous medium, where phytochemicals chelate with Zn^{2+} ions through functional groups such as hydroxyl, carbonyl, or amine. This interaction results in the formation of a Zn^{2+} –phytocomplex, which is further transformed into a gel-like precursor under heating. The addition of dopant salts such as aluminum nitrate or zirconyl nitrate enables the co-complexation of Al^{3+} or Zr^{4+} ions into the gel matrix, forming $\text{Zn}_{1-x}\text{M}_x\text{O}$ ($\text{M} = \text{Al}$ or Zr ; $x = 0.03, 0.05, 0.07$) compositions. Upon heating the precursor gel in a preheated muffle furnace at around $400 \pm 15^\circ\text{C}$, spontaneous combustion takes place due to the redox reaction between the oxidizing metal nitrates and the reducing organic compounds in the extract. This exothermic reaction results in the rapid evolution of gases such as CO_2 , NO_x , and H_2O vapor, which causes the gel to swell and combust, yielding voluminous, porous, and fine ZnO NPs. The presence of phytochemicals ensures uniform combustion and prevents the agglomeration of NPs by acting as surface capping agents. In the case of doped ZnO, the Al^{3+} or Zr^{4+} ions substitute Zn^{2+} ions within the crystal lattice of ZnO during the combustion process. These dopant ions cause local distortions in the crystal lattice, affect the crystallite size, and modify the electronic structure, resulting in enhanced optical and structural properties of the final NPs. The uniform distribution of dopants is facilitated by the homogenous mixing in the aqueous phase prior to combustion. To improve crystallinity and remove residual organic content, all synthesized nanoparticle samples are further subjected to calcination at 600°C for 1 h. This step also promotes better dopant incorporation into the ZnO matrix and ensures the development of a pure wurtzite crystalline structure.

The green solution combustion synthesis using *C. prostratus* flower extract provides a simple, efficient, and eco-friendly route to fabricate undoped and Al/Zr-doped ZnO NPs. The mechanism involves complexation, gel formation, combustion-driven nanoparticle generation, and thermal treatment—all aided by the multifunctional properties of the phytochemicals present in the flower extract. A

proposed mechanism for the formation of ZnO NPs is illustrated in Figure 2.

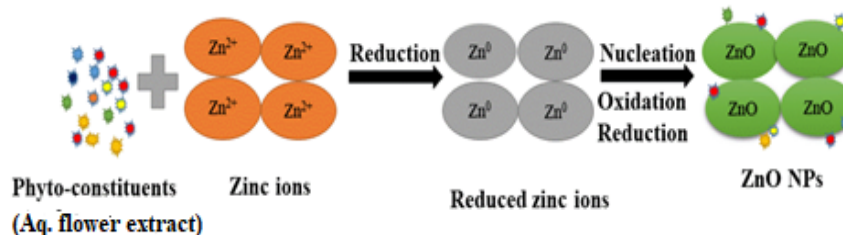


Figure 2. Plausible mechanism of formation of ZnO-NPs

Powder X-ray diffraction (PXRD) analysis

The crystalline nature and phase purity of the synthesized undoped and doped ZnO NPs were confirmed through X-ray diffraction (XRD) analysis. The diffraction patterns of all samples, as shown in Figure 3, exhibit sharp and intense peaks, indicating high crystallinity. The observed diffraction peaks at 2θ values of approximately 31.8° (100), 34.4° (002), 36.2° (101), 47.5° (102), 56.6° (110), 62.9° (103), and 68.0° (112) correspond to the hexagonal wurtzite structure of ZnO with the space group $P6_3mc$. These peak positions are in good agreement with the standard JCPDS card no. 36-1451, confirming the successful formation of ZnO NPs.

Importantly, no additional peaks corresponding to impurity phases such as Al_2O_3 or ZrO_2 were detected in the doped samples, indicating the successful substitution of Al^{3+} and Zr^{4+} into the Zn^{2+} lattice without altering the host ZnO phase. This implies that doping did not disturb the hexagonal crystal structure and that the synthesized NPs maintained high phase purity. The consistency in peak positions across all samples further supports this conclusion.

The average crystallite size (D) of the NPs was estimated using the Debye–Scherrer equation, $D = (k\lambda)/(\beta\cos\theta)$, where $k=0.9$, $\lambda=0.15406$ nm (Cu $K\alpha$ radiation), β is the full width at half maximum (FWHM) of the most intense peak (101 plane), and θ is the corresponding Bragg angle. Crystallite sizes ranged from 8.8 nm to 16.1 nm, depending on the dopant type and concentration. The largest crystallite size (16.1 nm) was observed for $Zn_{0.93}Zr_{0.07}O$, while the smallest size (8.8 nm) was found in $Zn_{0.93}Al_{0.07}O$, indicating that Al doping at higher concentration inhibited crystal growth more significantly than Zr doping.

Additionally, the micro-strain (ϵ) in the samples was calculated using the relation $\epsilon = (\beta\cos\theta)/4$. The strain values varied from 0.136 ($Zn_{0.93}Zr_{0.07}O$) to 0.222 ($Zn_{0.95}Zr_{0.05}O$), showing that doping induces lattice distortion, which is slightly more pronounced in Zr-doped samples due to the larger ionic radius of Zr^{4+} compared to Zn^{2+} .

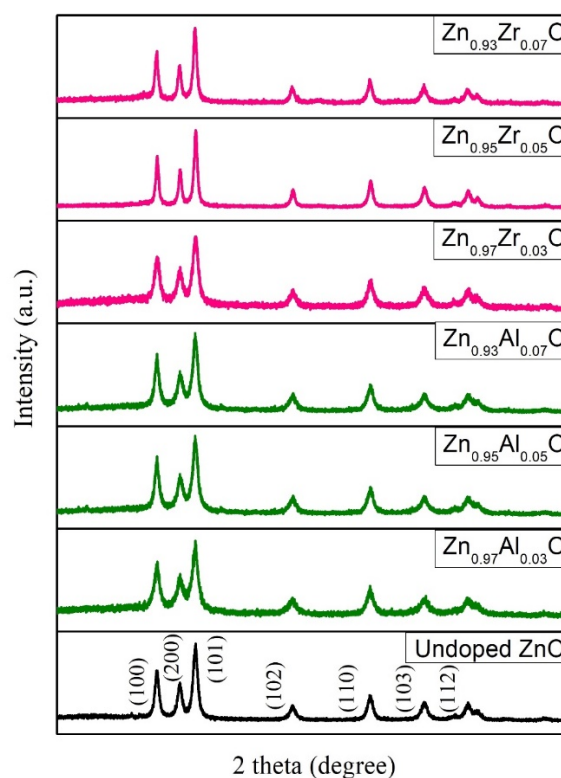


Figure 3. PXRD patterns of undoped and doped ZnO NPs

The detailed XRD parameters, including peak position (2θ), FWHM, intensity, crystallite size (D), and micro-strain (ϵ) for all samples, are summarized in Table 2.

Table 2. 2 θ , FWHM, intensity (101) plane, D, and micro-strain (ϵ) of NPs

Sample	Peak position (2 θ)	FWHM (2 θ)	Intensity (cps)	D (nm) crystallite size	ϵ
Undoped ZnO	36.15	0.67	762.3	12.5	0.1763
Zn _{0.97} Al _{0.03} O	36.16	0.81	416.47	10.3	0.213
Zn _{0.95} Al _{0.05} O	36.11	0.69	572	12.1	0.1815
Zn _{0.93} Al _{0.07} O	36.11	0.74	570	8.8	0.194
Zn _{0.97} Zr _{0.03} O	36.11	0.72	572.5	11.6	0.189
Zn _{0.95} Zr _{0.05} O	36.15	0.86	372	9.7	0.222
Zn _{0.93} Zr _{0.07} O	36.11	0.52	585.2	16.1	0.136

Table 3. FTIR spectral band assignments of pure and doped ZnO NPs

Observed wavenumber (cm ⁻¹)	Assignment	Sample(s)	Reference
443.92	Zn–O stretching vibration (wurtzite phase)	ZnO	[35, 36]
439.7–448.71	Shifted Zn–O stretching due to Al ³⁺ doping	Zn _{0.97} Al _{0.03} O to Zn _{0.93} Al _{0.07} O	[37, 38]
445.61–479.90	Shifted Zn–O stretching due to Zr ⁴⁺ doping	Zn _{0.97} Zr _{0.03} O to Zn _{0.93} Zr _{0.07} O	[39, 40]
3424.79–3442.51	O–H stretching of surface hydroxyl or adsorbed water	All samples	[37, 38]
1384.27–1403.34	Symmetric stretching of CO ₃ ²⁻ or C=O group (adsorbed CO ₂)	Al- and Zr-doped ZnO	[39, 41]
1116.33–1117.68	C–O stretching (possibly from residual organic precursors)	Al- and Zr-doped ZnO	[39, 41]

FTIR analysis

The Fourier transform infrared (FTIR) spectra of pure and doped ZnO NPs synthesized by the solution combustion method are presented in Figure 4 and Table 3. The FTIR data provide crucial insights into the bonding environment, functional groups, and lattice distortions arising from Al³⁺ and Zr⁴⁺ doping.

In the undoped ZnO sample, a prominent absorption band appears at 443.92 cm⁻¹, corresponding to the Zn–O stretching vibration, confirming the formation of the wurtzite phase of ZnO [35, 36]. A broad band around 3424.79 cm⁻¹ is assigned to the O–H stretching vibration arising from surface-adsorbed moisture or hydroxyl groups [37].

Doping with Al³⁺ leads to noticeable shifts in the Zn–O vibration bands to 439.76 cm⁻¹ (Zn_{0.97}Al_{0.03}O), 448.71 cm⁻¹ (Zn_{0.95}Al_{0.05}O), and 443.65 cm⁻¹ (Zn_{0.93}Al_{0.07}O). These variations reflect substitutional incorporation of Al³⁺ into the ZnO lattice, resulting in minor distortions due to the smaller ionic radius of Al³⁺ (0.53 Å) compared to Zn²⁺ (0.74 Å) [38]. Additionally, distinct bands at

~ 1116–1117 cm⁻¹ and ~ 1384–1403 cm⁻¹ are observed in the doped samples, which are attributed to C–O stretching vibrations and symmetric stretching of carbonate groups, respectively. These likely originate from residual organic precursors or atmospheric CO₂ adsorption during synthesis and handling [39].

Similarly, Zr-doped ZnO samples show Zn–O stretching peaks at 445.61 cm⁻¹ (Zn_{0.97}Zr_{0.03}O), and further shifting to higher wavenumbers in Zn_{0.95}Zr_{0.05}O (479.90 cm⁻¹) and Zn_{0.93}Zr_{0.07}O (479.29 cm⁻¹), indicating substantial lattice distortion due to the substitution of larger Zr⁴⁺ ions (0.72 Å) [40]. Broad absorption in the region of 3418–3442 cm⁻¹ in these samples confirms the presence of surface hydroxyl groups. The presence of bands around 1116 cm⁻¹ and 1403 cm⁻¹ in Zr-doped samples is consistent with the features seen in Al-doped ZnO. These spectral shifts and the appearance of new bands suggest successful incorporation of dopant ions into the ZnO matrix and modification of surface chemistry, which are expected to impact the material's physicochemical and optical properties.

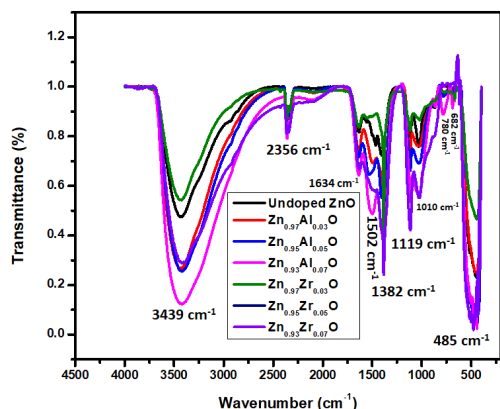


Figure 4. FTIR spectra of (black) undoped ZnO, (red) 3 mol % Al-doped ZnO, (blue) 5 mol % Al-doped ZnO, (pink) 7 mol % Al-doped ZnO, (green) 3 mol % Zr-doped ZnO, (navy blue) 5 mol % Zr-doped ZnO, and (purple) 7 mol % Zr-doped ZnO.

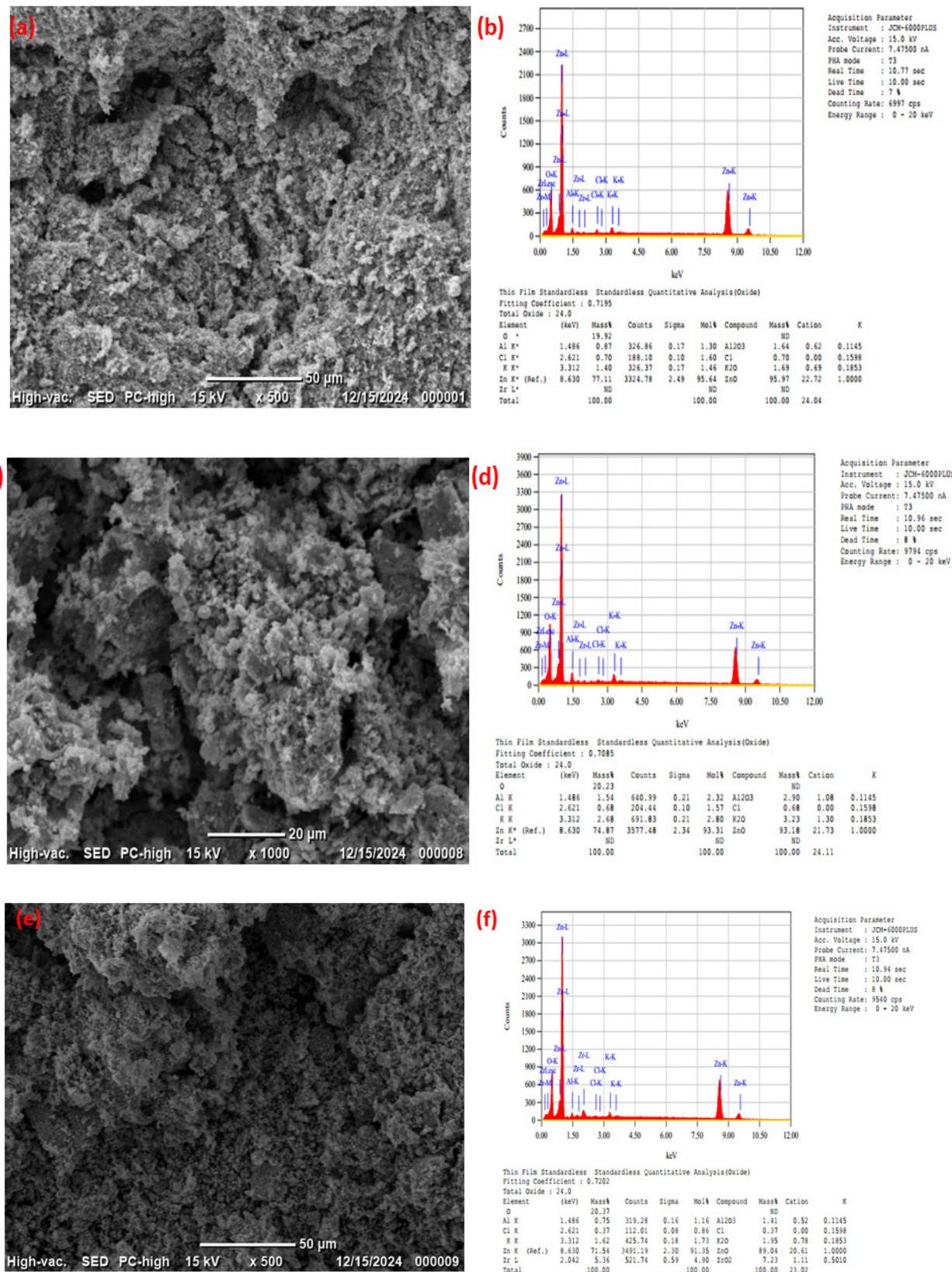
SEM and EDX analysis of NPs

- **Undoped ZnO NPs.** The SEM image of undoped ZnO NPs (Figure 5a) shows highly agglomerated structures with irregular morphology. The particles appear to be interconnected, forming porous clusters that are likely a result of rapid combustion reactions during synthesis, which release large volumes of gases (CO_2 , H_2O) that create voids in the matrix. This sponge-like morphology is typical of combustion-synthesized ZnO nanostructures [42]. The corresponding EDX spectrum (Figure 5b) confirms the presence of elemental Zn and O, with no detectable impurities, validating the purity of the synthesized ZnO. The atomic percentages of Zn and O are 73.95% and 26.05%, respectively, consistent with stoichiometric ZnO.

- **7 mol% Al-doped ZnO NPs.** Upon doping with 7 mol% aluminum, the SEM micrograph (Figure 5c) shows a noticeable morphological transformation. The particles become finer and

exhibit a more uniform distribution compared to undoped ZnO, suggesting that Al^{3+} ions help regulate the nucleation and growth processes during synthesis. The decrease in agglomeration and increased surface roughness can enhance the surface area and catalytic properties of the material [43]. EDX analysis (Figure 5d) confirms the successful incorporation of aluminum, with elemental signals for Zn, O, and Al clearly observed. The calculated Al content aligns well with the intended doping level, with a measured atomic percentage of 2.91%.

- **7 mol% Zr-doped ZnO NPs.** The SEM image of Zr-doped ZnO (Figure 5e) reveals a denser, more compact morphology with larger clusters than both undoped and Al-doped samples. The Zr doping appears to promote grain growth and aggregation due to the ionic size mismatch between Zr^{4+} and Zn^{2+} , which induces lattice strain and modifies crystallization behavior [44]. This results in a tightly packed structure with reduced porosity. The EDX spectrum (Figure 5f) confirms the presence of Zr along with Zn and O, validating successful doping. The atomic percentage of Zr is 3.11%, closely matching the theoretical 7 mol% substitution. The TEM image of undoped ZnO NPs (Figure 5g) reveals quasi-spherical particles with a moderate degree of agglomeration, consistent with observations from SEM analysis. Individual particles are generally in the nanoscale range, with estimated sizes between 20–40 nm, and appear to be embedded within loosely packed clusters. The relatively uniform contrast across the particles suggests good crystallinity, while the slight aggregation may stem from van der Waals interactions and the absence of surface stabilizers. The particle boundaries are discernible, indicating a distinct nanocrystalline nature. These features further confirm that the combustion synthesis route effectively yields nanosized ZnO with fine morphological control.



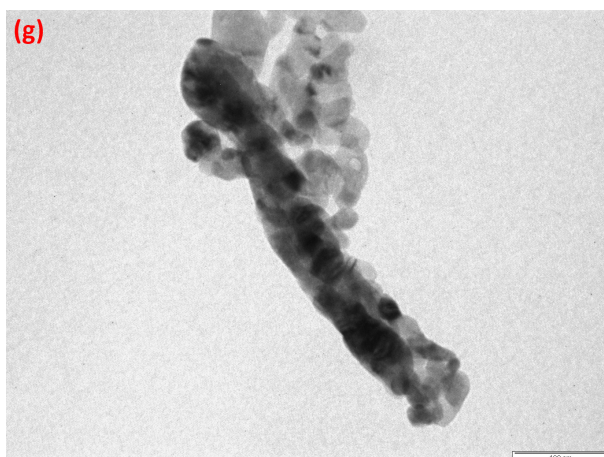


Figure 5 (a) SEM and (b) EDX of undoped ZnO NPs; (c) SEM and (d) EDX of 7 mol % Al-doped ZnO NPs; (e) SEM and (f) EDX of 7 mol % Zr-doped ZnO NPs (g) TEM image of undoped ZnO NPs

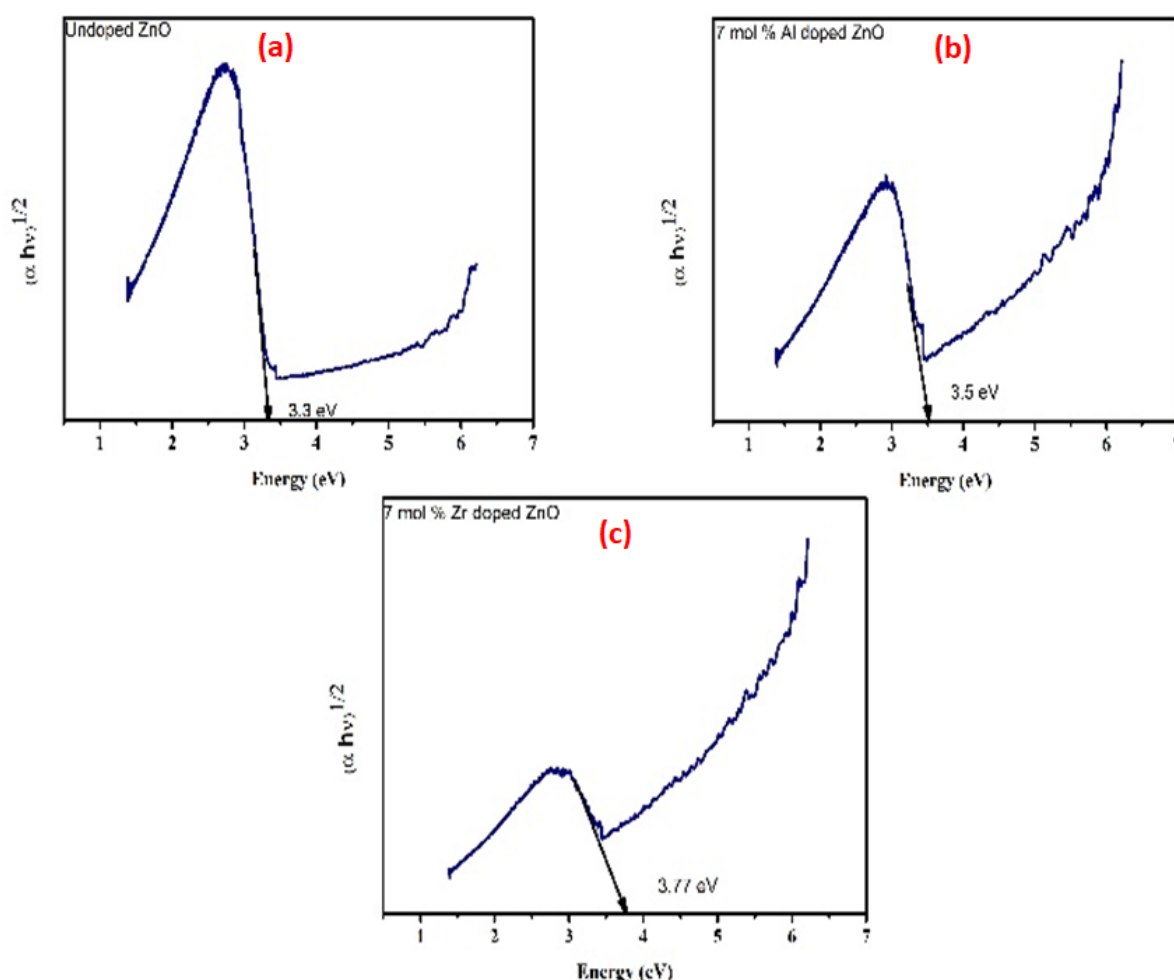


Figure 6. Band gap calculation of (a) undoped ZnO NPs, (b) 7 mol % Al-doped ZnO NPs, and (c) 7 mol % Zr-doped ZnO NPs

Mechanical properties of concrete blocks

The results of the experimental study are visually represented in the comparative bar graph, highlighting both the cubic weight (kg) and compressive strength (MPa) of four different types of concrete blocks—Plain concrete block, ZnO

mixed block, Al + ZnO mixed block, and Zr + ZnO mixed block (Table 4 and Figure 7). The evaluation of these samples allows for an understanding of how nanomaterial admixtures, particularly doped ZnO variants, affect the physical and mechanical properties of concrete.

In terms of cubic weight, all concrete blocks show very close values, ranging from 8.25 kg to 8.32 kg. The plain concrete block recorded a weight of 8.25 kg, while the ZnO, Al + ZnO, and Zr + ZnO mixed blocks had weights of 8.3 kg, 8.32 kg, and 8.31 kg, respectively. These marginal differences indicate that the incorporation of ZnO and its doped variants in small percentages (0.5%–1%) does not significantly influence the overall density of the concrete. This consistency confirms that mix proportions and compaction practices were uniformly maintained across all samples, allowing a fair comparison of their mechanical performance.

When examining compressive strength, distinct variations become evident. The plain concrete block achieved a compressive strength of 35 MPa, serving as the baseline for performance comparison. Interestingly, the inclusion of undoped ZnO led to a reduction in strength to 32 MPa, suggesting that ZnO alone may slightly disrupt the internal bonding or hydration processes. A further drop was observed with Al + ZnO mixed blocks, which registered a compressive strength of 30.5 MPa. This could be attributed to agglomeration of NPs or interference with cement hydration at higher dosages, highlighting the importance of optimizing the amount and dispersion of such additives.

In contrast, the Zr + ZnO mixed block demonstrated superior performance, achieving a compressive strength of 37.5 MPa, the highest among all tested samples. This suggests that Zr doping significantly enhances the pozzolanic or micro-filling effects of ZnO NPs, potentially improving the microstructure of the cement matrix and resulting in higher load-bearing capacity. The effectiveness of Zr as a dopant may stem from its ability to promote better hydration reactions or denser matrix formation compared to Al.

The results clearly indicate that while nano-admixtures can modify concrete properties, their effectiveness strongly depends on the type and concentration of the dopant. Zr-doped ZnO, in particular, stands out as a promising additive for enhancing compressive strength without compromising the workability or mass of the concrete. However, the decrease in strength observed with ZnO and Al-doped mixes also underscores the need for further microstructural studies to understand their dispersion behavior and interaction with the cement matrix.

Table 4. Compressive strength test values

S. No	DOC	Cubic weight (Kg)	Load (KN)	Strength (M Pa)	Admixture
1	25/11	8.520	744.1	33.07	-
2	25/11	8.010	908.7	40.39	-
3	25/11	8.370	705.4	31.35	ZnO (0.5%)
4	25/11	8.270	754.6	33.35	ZnO (1%)
5	25/11	8.300	695.9	30.92	Al-doped ZnO – 3 mol % (0.5%)
6	25/11	8.720	466.1	20.71	Al-doped ZnO – 3 mol % (1%)
7	25/11	8.850	1124.1	49.96	Al-doped ZnO – 5 mol % (0.5%)
8	25/11	8.190	534.4	23.75	Al-doped ZnO – 5 mol % (1%)
9	25/11	8.130	552.6	24.56	Al-doped ZnO – 7 mol % (0.5%)
10	25/11	8.290	703.7	31.27	Al-doped ZnO – 7 mol % (1%)
11	25/11	8.300	983.8	43.72	Zr-doped ZnO – 3 mol % (0.5%)
12	25/11	8.320	753.8	33.50	Zr-doped ZnO – 3 mol % (1%)
13	25/11	8.380	869.8	38.65	Zr-doped ZnO – 5 mol % (0.5%)
14	25/11	8,290	799.9	35.55	Zr-doped ZnO – 5 mol % (1%)
15	25/11	8.530	680.9	30.26	Zr-doped ZnO – 7 mol % (0.5%)
16	25/11	8.110	825.9	36.79	Zr-doped ZnO – 7 mol % (1%)

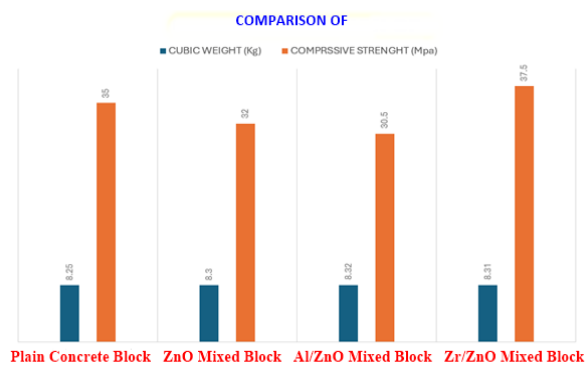


Figure 7. Compressive strength

- *Antifungal activity evaluation through visual inspection.* The antifungal efficacy of the developed concrete blocks was assessed through a simple yet effective visual inspection method. As depicted in the image, two types of concrete blocks were compared: an antifungal block embedded with ZnO NPs (doped and/or undoped) and a plain concrete block without any nanoparticle incorporation. After exposure to conditions favorable for microbial growth, particularly high humidity, the blocks were examined for signs of fungal colonization on their surfaces. The results are presented in Figure 8.

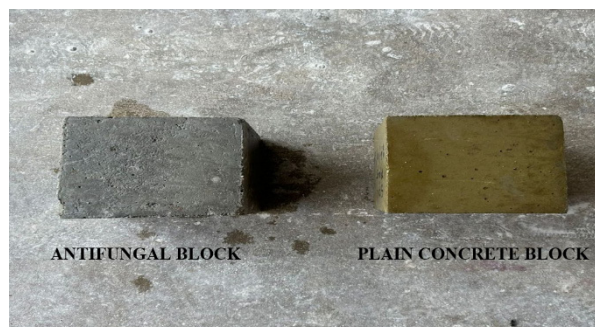


Figure 8. Comparison of antifungal block and plain concrete block

The plain concrete block displayed a visibly discolored surface with potential spots that are typically associated with initial stages of fungal growth. In contrast, the antifungal block exhibited a cleaner, uniformly gray surface, with no visible signs of fungal growth, indicating its superior resistance to microbial contamination. This clear visual distinction confirms the antifungal activity of the ZnO nanoparticle-enhanced concrete. The NPs likely disrupt fungal cell membranes through the generation of reactive oxygen species (ROS), a mechanism further enhanced by doping with Al and Zr, which increases surface reactivity. Such

antifungal performance not only prolongs the lifespan of the concrete but also ensures improved sanitation, particularly in moisture-prone environments such as bathrooms, basements, public facilities, and humid climates.

The antifungal efficacy of ZnO NPs incorporated in concrete might largely be attributable to their surface exposure, facilitating direct interaction with fungal cells. ZnO is recognized for producing reactive oxygen species (ROS) that compromise fungal cell membranes [45]. The antifungal action is thought to be surface-mediated, resulting from NPs included inside the concrete rather than applied as a coating, and is derived from those at the exposed concrete interface [46]. This indicates that fungal proliferation is predominantly suppressed at the block surface where the ZnO NPs are available. The statement means that the presence of ZnO NPs effectively inhibits fungal growth, particularly at the surface where the NPs are located. This localized effect suggests that the ZnO NPs are interacting with and suppressing fungal proliferation directly at the site of their application [47]. This study did not implement a distinct surface coating approach; the NPs were uniformly integrated during the concrete mixing process.

The antifungal activity of ZnO NPs embedded in concrete is likely due to their surface-exposed presence, enabling direct interaction with fungal cells. Since the NPs were uniformly dispersed during concrete mixing and not applied as a surface coating, the inhibition is primarily surface-mediated, resulting from exposed NPs at the block surface.

A schematic diagram (Figure 9) illustrates the proposed cellular-level antifungal mechanisms by which ZnO NPs may inhibit fungal growth. These mechanisms include: (A) generation of ROS inducing lipid peroxidation, (B) disruption of fungal membranes, (C) pore formation, (D) leakage of intracellular content, (E) metal ion release, (F) DNA intercalation and fragmentation, (G) gene expression alterations, (H) amplified oxidative stress, (I) mitochondrial cytochrome C release triggering apoptosis, (J) ribosomal disassembly, and (K) inhibition of biofilm formation *via* binding to extracellular polymeric substances (EPS).

Although these mechanisms have been widely reported for nanoparticle–fungus systems, further research is required to confirm and visualize such effects specifically within concrete matrices.

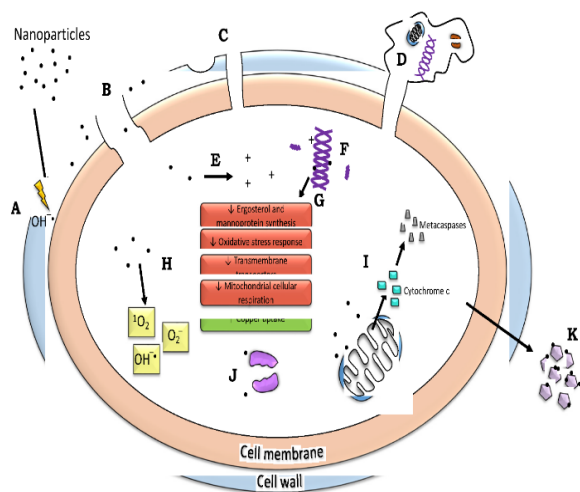


Figure 9. The cellular-level antifungal mechanisms of NPs involve multiple pathways: (A) induction of ROS that trigger lipid peroxidation; (B) interaction with and disruption of the fungal cell wall and membrane through adsorption and embedment; (C) formation of pits and pores; (D) leakage of intracellular contents including DNA and organelles; (E) release of metal ions; (F) intercalation with DNA leading to its condensation and fragmentation; (G) alterations in gene expression; (H) enhanced ROS production; (I) mitochondrial release of cytochrome C into the cytoplasm, which elevates metacaspase activity and initiates apoptotic pathways; (J) disassembly of ribosomes; and (K) binding to extracellular polymeric substances (EPS), thereby inhibiting biofilm development [47].

CONCLUSION

The green synthesis of undoped and Al/Zr-doped ZnO NPs using *C. prostratus* flower extract via solution combustion synthesis offers a sustainable and efficient method for producing nanomaterials with tailored properties. The incorporation of Al³⁺ and Zr⁴⁺ ions into the ZnO lattice was successfully achieved without compromising the wurtzite crystal structure, as confirmed by PXRD and FTIR analyses. TEM, SEM-EDX characterizations revealed morphological changes and uniform dopant distribution, while UV-Vis spectroscopy indicated tunable band gap energies, with Zr-doped ZnO exhibiting the highest band gap of 3.77 eV. The crystallite sizes ranged from 8.8 nm (for 7 mol% Al-doped ZnO) to 16.1 nm (for 7 mol% Zr-doped ZnO). The application of these NPs in concrete blocks demonstrated that 7 mol% Zr-doped ZnO significantly enhances compressive strength to 49.96 MPa and provides antifungal properties, surpassing the performance of undoped and Al-doped counterparts. These findings underscore the potential of Zr-doped ZnO NPs as multifunctional additives in construction materials, offering both mechanical reinforcement and antimicrobial

protection. Future research should focus on optimizing dopant concentrations and exploring the long-term durability and environmental impact of such nanocomposite materials in real-world applications.

Limitations and future plans

The current work gives us useful information about how to make Al- and Zr-doped ZnO nanoparticles in concrete and how well they can accomplish more than one thing. However, there are still certain limitations. There was no quantitative evaluation of antifungal action, including measuring inhibition zones and counting CFUs. This should be done in future work. Also, even though the antifungal action seemed to be surface-mediated, no surface coating was used, and the distribution of nanoparticles in the concrete matrix was not clearly defined. Future research will look at how to use surface-functionalized coatings, how long antifungal action lasts when exposed to the environment, and how to get the most nanoparticles into construction materials that can be scaled up.

Declarations:

Funding: Nil;

Conflict of interest: None;

Ethical approval: Not applicable.

REFERENCES

1. M.A. Beach, Nayanathara, U., Gao, Y., Zhang, C., Xiong, Y., Wang, Y. Such, G.K., *Chemical Reviews*, **124**(9), 5505 (2024).
2. A.N. Al-Thani, Jan, A.G., Abbas, M., Geetha, M. Sadasivuni, K.K. *Life Sciences*, 22899 (2024).
3. T. Yu, Chen, H., Hu, T., Feng, J., Xing, W., Tang, L. Tang, W., *Applied Catalysis B: Environmental*, **342**, 123401 (2024).
4. S. Kumar, Mirzaei, A., Kumar, A., Lee, M.H., Ghahremani, Z., Kim, T.U., Kim, J.Y., Kwoka, M., Kumar, M., Kim, S.S. Kim, H.W., *Coordination Chemistry Reviews*, **503**, 215657 (2024).
5. B. Rezaei, Yari, P., Sanders, S.M., Wang, H., Chugh, V.K., Liang, S., Mostufa, S., Xu, K., Wang, J.P., Gómez-Pastora, J. Wu, K., *Small*, **20**(5), 2304848 (2024).
6. M.Y. Al-darwesh, Ibrahim, S.S. Mohammed, M.A., *Results in Chemistry*, **7**, 101368 (2024).
7. J. Du, Arwa, A.H., Cao, Y., Yao, H., Sun, Y., Garaleh, M., Massoud, E.E.S., Ali, E., Assilzadeh, H. Escorcia-Gutierrez, J., *Environmental Research*, **258**, 119204 (2024).
8. S. Goswami, Bishnoi, A., Tank, D., Patel, P., Chahar, M., Khaturia, S., Modi, N., Khalid, M., Alam, M.W., Yadav, V.K. Alreshidi, M.A., *Inorganica Chimica Acta*, 122350 (2024).
9. G. Umadevi, K.G. Krishna, *Sensors and Actuators A: Physical*, **374**, 115479 (2024).

10. B. Ranjithkumar, D. Sudha, E.R. Kumar, S.S. Alharthi, *Ceramics International*, **50**(16), 27679 (2024).
11. B. Mahant, Patel, D., Kushwaha, O.S. Kumar, R., *Energy & Fuels*, **37**(24), 19621 (2023).
12. M. Vaseem, Umar, A. Hahn, Y.B., *Metal Oxide Nanostructures and Their Applications*, **5**(1), 10 (2010).
13. M. Abdi-Khanghah, Adelizadeh, M., Naserzadeh, Z. Barati, H. *Journal of Natural Gas Science and Engineering*, **54**, 120 (2018).
14. H. Jan, Shah, M., Andleeb, A., Faisal, S., Khattak, A., Rizwan, M., Drouet, S., Hano, C. Abbasi, B.H., *Oxidative Medicine and Cellular Longevity*, **2021**(1), p.4786227 (2021).
15. M. Ehsan, Waheed, A., Ullah, A., Kazmi, A., Ali, A., Raja, N.I., Mashwani, Z.U.R., Sultana, T., Mustafa, N., Ikram, M. Li, H., *BioMed Research International*, **2022**(1), 215183 (2022).
16. M. Alhujaily, Albukhaty, S., Yusuf, M., Mohammed, M.K., Sulaiman, G.M., Al-Karagoly, H., Alyamani, A.A., Albaqami, J. AlMalki, F.A. *Bioengineering*, **9**(10), 541 (2022).
17. G.K. Prashanth, Prashanth, P.A., Nagabhushana, B.M., Ananda, S., Krishnaiah, G.M., Nagendra, H.G., Sathyananda, H.M., Rajendra Singh, C., Yogisha, S., Anand, S. Tejabhiram, Y., *Artificial Cells, Nanomedicine, and Biotechnology*, **46**(5), 968 (2018).
18. G.K. Prashanth, Prashanth, P.A., Bora, U., Gadewar, M., Nagabhushana, B.M., Ananda, S., Krishnaiah, G.M. Sathyananda, H.M. *Karbala International Journal of Modern Science*, **1**(2), 67 (2015).
19. S. Nagarajaiah, Nanda, N., Manjappa, P., Nagabhushana, B.M., Gadewar, M., Rao, S. Krishna, P.G., *Applied Physics A*, **129**(6), 461 (2023).
20. P.G. Krishna, Ananthaswamy, P.P., Trivedi, P., Chaturvedi, V., Mutta, N.B., Sannaiah, A., Erra, A. Yadavalli, T., *Materials Science and Engineering: C*, **75**, 1026 (2017).
21. G. K, Prashanth, Prashanth P. A, Meghana Ramani, Ananda S, Nagabhushana B. M, Krishnaiah G. M, Nagendra H. G, Sathyananda H. M, Mutthuraju M, Rajendra Singh C. *BioNanoScience*, **e9** (4), 799 (2019).
22. Siddekha, Aisha, Lalithamba HS, and Prashanth GK. *Materials Research Innovations*, **29** (4), 215 (2025).
23. G.K. Prashanth, M. Gadewar, S. Rao, H.S. Lalithamba, S.H. Prashant, M. Mahadevaswamy, N.P. Bhagya, B.M. Nagabhushana, in: *Advanced Materials in Engineering Applications*, CRC Press, 2024, p. 329.
24. G.K. Prashanth, S. Rao, M. Gadewar, H.S. Lalithamba, M.M. Swamy, A.S. Sowmyashree, *Journal of Physics: Conference Series*, **2748** (1), 012001, IOP Publishing, April, 2024.
25. G.K. Prashanth, A.S. Giresha, H.S. Lalithamba, M. Aman, S. Rao, K.N. Ravindra, M. Gadewar, N.P. Bhagya, M.M. Swamy, V. Chaturvedi, *Inorganic Chemistry Communications*, **171**, 113592 (2025).
26. V.U. Nallal, Prabha, K., Muthupandi, S. Razia, M., *Materials Today: Proceedings*, **49**, 2632 (2022).
27. N.T.T. Nguyen, Nguyen, L.M., Nguyen, T.T.T., Nguyen, D.T.C. Tran, T.V., *Environmental Chemistry Letters*, **20**(4), 2531 (2022).
28. S. Ahmed, Chaudhry, S.A. Ikram, S., *Journal of Photochemistry and Photobiology B: Biology*, **166**, 272 (2017).
29. V. Mohammadzadeh, Barani, M., Amiri, M.S., Yazdi, M.E.T., Hassanisaadi, M., Rahdar, A. Varma, R.S., *Sustainable Chemistry and Pharmacy*, **25**, 100606 (2022).
30. A. Balkrishna, Thakur, P. Varshney, A., *Frontiers in Pharmacology*, **11**, 171 (2020).
31. E. Ghafari, Ghahari, S.A., Feng, Y., Severgnini, F. Lu, N., *Composites Part B: Engineering*, **105**, 160 (2016).
32. F.E.Z.M. Mostafa, Smarzewski, P., El Hafez, G.M.A., Farghali, A.A., Morsi, W.M., Faried, A.S. Tawfik, T.A., *Materials*, **16**(21), 6909 (2023).
33. B.O. Bica, J.V.S. de Melo, *Construction and Building Materials*, **252**, 119120 (2020).
34. M. Kumar, M. Bansal, R. Garg, *Materials Today: Proceedings*, **43**, 892 (2021).
35. M.G. Faraj, Ibrahim, K. Salhin, A., *Materials in Semiconductor Processing*, **15**(2), 206 (2012).
36. R.B.M. Cross, De Souza, M.M. Narayanan, E.S., *Nanotechnology*, **16**(10), 2188 (2005).
37. S.H. Moon, Choi, J.H., Chae, K.W., Kim, J.S. Cheon, C.I., *Ceramics International*, **39**(3), 2431 (2013).
38. S. Baruah, Dutta, J., *Science and Technology of Advanced Materials*, **10**(1), 013001 (2009).
39. X. Yang, Takeichi, N., Shida, K., Tanaka, H., Kuriyama, N. Sakai, T., *Journal of Alloys and Compounds*, **509**(4), 1211 (2011).
40. M. Golmohammadi, Towfighi, J., Hosseinpour, M. Ahmadi, S.J., *The Journal of Supercritical Fluids*, **107**, 699 (2016).
41. H. Ueda, Tanaka, Y., Wakabayashi, Y. Kimura, T., *Physica B: Condensed Matter*, **536**, 118 (2018).
42. X. Zha, Yang, C., Huang, X., Ding, J. Ding, Z., *Environmental Pollutants and Bioavailability*, **36**(1), 2376827 (2024).
43. S. Özkar, *Applied Surface Science*, **256** (5), 1272 (2009).
44. I. Khan, Khan, S., Nongjai, R., Ahmed, H. Khan, W., *Optical Materials*, **35**(6), 1189 (2013).
45. K. A. Nxumalo, J. O. Adeyemi, T. B. Leta, T. M. Pfukwa, S. N. Okafor, O. A. Fawole, *Scientific Reports* **14**(1), 18071 (2024).
46. S. Bhattacharyya, Sh. Akhtar, A. Chaudhuri, Sh. Mahanty, P. Chaudhuri, M. Sudarshan, *Case Studies in Construction Materials*, **17**, e01258 (2022).
47. Y. N. Slavin, H. Bach, *Nanomaterials*, **12** (24), 4470 (2022), <https://doi.org/10.3390/nano12244470>.

Efficiency of algae-assisted photo-bioelectrochemical system in anaerobic wastewater treatment

A. T. Angelov*, S. G. Bratkova, K. T. Nikolova, S. K. Plochev, P. G. Genova, R. V. Ivanov, P. G. Velichkova

Department of Engineering Geocology, University of Mining and Geology "St. Ivan Rilski", Sofia 1700, Bulgaria

Received: June 05, 2025; Revised: September 14, 2025

Bioelectrochemical systems offer various potential applications for environmental protection. The present study examines the performance of a photo-bioelectrochemical system (PBES) consisting of a microbial fuel cell (MFC) and a column photobioreactor with a mixed culture of microalgae. The generation of significant amounts of oxygen in the medium by the algae during photosynthesis is a key factor in their usage in the cathodic zone of bioelectrochemical systems. In the anodic area of a microbial fuel cell, two waste organic substrates (ethanol stillage and vinasse) used as electron donors for the microbial sulfate reduction process were compared. At different operating modes, there were determined and analyzed the main electrochemical parameters of a PBES - open circuit voltage (436 – 510 mV), maximum power (8.0 – 14.5 W/m²), current density (34.8- 64.1 mA/m²), internal resistance, coulombic efficiency, etc.

Keywords: Bioelectrochemical systems, Coulombic efficiency, microalgae, microbial fuel cells, oxygen generation, microbial sulfate reduction.

INTRODUCTION

The current economic situation and the required sustainable development in terms of the environment create an urgent need to develop energy-efficient and eco-friendly technologies for the treatment of wastewater fluids [1]. Innovative technologies in the field of bioelectrochemical systems (BES), such as microbial fuel cells (MFCs) and MFCs with microalgae (mMFC) cultivated in photobioreactors (PBR), create the opportunity of electricity generation, CO₂ removal from gas mixtures and wastewater treatment [2].

MFCs can successfully be applied to remove both organic and inorganic pollutants from wastewaters [3]. The main process is the oxidation of an organic electron donor, and the removed electrons are transferred to an insoluble anode of the BES, instead of the corresponding natural acceptors (oxygen, sulfates, ferric ions, nitrates, etc.) [4]. The typical MFC consists of anode and cathode chambers separated by an ion exchange membrane. BES such as MFCs can also be used for microalgae cultivation and bioelectricity production, offering advantages over conventional microalgae cultivation systems.

Microalgae microbial fuel cells are a type of

MFCs with microalgae as a biocatalyst. The photobioreactor can function as part of the cathode zone of the mMFC for the cultivation of microalgae [5]. Oxygen generation in the cathode zone is achieved by a connected PBR or by cultivating microalgae directly in the cathode zone [6]. Photobioreactors are closed systems (isolated from the environment) for cultivating microalgae in transparent containers with different shapes and sizes. These systems have a number of advantages, such as low contamination levels, high productivity, easy control of temperature and pressure, good light illumination, small water losses [7]. The most commonly used types of PBRs are tubular (cylindrical), column type with aeration, flat, combinations of several types, etc.

Combined BES with microalgae in the cathode zone and anaerobic processes (biomethanization, microbial sulfate reduction, denitrification, etc.) in the anode zone are the preferred option because the cultivation of microalgae in the cathode zone (mMFCs) increases the oxygen content as a result of photosynthesis, which increases the electricity production. In addition, the process reduces the amount of CO₂ [8].

* To whom all correspondence should be sent:

E-mail: tonyagev@mgu.bg

Recent studies have shown that various types of wastewater can be used as an organic substrate in the anode zone, which increases the efficiency of the system [9]. Typical examples of such waste organic substrates are ethanol stillage and vinasse. The ethanol stillage is a liquid waste from the distillation of ethanol from alcoholic fermentation of raw materials containing starch (corn, wheat, barley, etc.). The vinasse is derived mainly from the fermentation and distillation of molasses, most often in the production of ethanol from sugar cane or sugar beet. Organic wastewaters from beer production, such as ethanol stillage and vinasse, are substrates that are successfully utilized in the anaerobic biomethanization process. They are characterized by high acidity (pH: 3.5-4), high organic content (COD: 50 - 150 g/l), and often contain large amounts of nitrogen compounds and sulfates [10].

It is important to pay attention to the high concentration of sulfates in these waste effluents. High sulfate concentrations can affect further water treatment. During anaerobic digestion, sulfates are converted to more toxic sulfides (e.g. hydrogen sulfide). In general, inhibition of the biomethanization process by sulfides does not occur when the COD/SO₄ ratio in the wastewater is greater than 10 g/g. Inhibition of anaerobic digestion is strong when the COD/SO₄ ratio is less than 0.5 g/g. Thus, vinasse and ethanol stillage can form wastewaters that are difficult to treat, not only due to their characteristics, but also due to their significant volume [11].

Sulfate removal in nature is achieved through the process of microbial sulfate reduction (MSR). This process is widely used in bioelectrochemical systems such as MFCs [12]. In heterotrophic MSR, the process takes place in the anode zone of the MFC, and it is known that in this case there is no necessity of additional mediators, since the hydrogen sulfide plays the role of such, and the generation of electricity in the system occurs during the oxidation of part of the produced hydrogen sulfide on the surface of the anode [13, 14]. An important effect of the process is the reduction of sulfates to biogenic H₂S, which is a mediator in the electron transfer, being oxidized in the anode chamber on the anode surface to elemental sulfur (S⁰) and its other forms [12]. Unlike classical MFCs, where during the oxidation of an organic electron donor, the electrons taken away are transferred to the insoluble anode, in this case, a significant part of the electrons from the organic substrate go to the reduction of sulfates. Sulfate-reducing bacteria (SRB) and electrogenic microorganisms often use the same electron donors, such as lactate, acetate or propionate. In the anode

chamber of the MFC, SRB can reduce sulfate to sulfide using these donors, which can reduce their availability to electrogenic bacteria and thus limit electricity production. Furthermore, in terms of electron transfer mechanisms, SRB can participate in direct or indirect extracellular electron transfer (EET) to the anode. These mechanisms include direct contact, use of conductive nanowires, or redox mediators [12].

The main objective of this study is to analyze the performance of a newly designed photo-bioelectrochemical system combining a photobioreactor and an MFC. Another important task is to determine the efficiency of mMFCs with vinasse and ethanol stillage as electron donors for the MSR process in the anode zone of the fuel cell, and utilizing them, removing the sulfates and producing energy.

MATERIALS AND METHODS

Substrates, inoculum and enrichment of microbial communities

For the microbial sulfate reduction process in the anode zone of mMFC were used two types of wastewater - vinasse (from wine brandy production) and ethanol stillage (from a plant for ethanol production from hydrolyzed wheat using a sulfuric acid solution). The wastewaters used in this study are characterized in Table 1.

Table 1. Basic characteristics of the wastewater

Parameter	Vinasse	Ethanol stillage
pH	3.41	3.52
TKN (Total Kjeldahl nitrogen), mg/l	159.3	103.7
COD, gO ₂ /l	53.6	79.2
Dry matter, %	3.11	3.31
SO ₄ ²⁻ , g/l	0.969	1.165

Before usage for the MSR process in the anode zone of mMFC, the vinasse and ethanol stillage were diluted with distilled water in a ratio of 1:1, the pH was adjusted to 7.5 using 4N NaOH solution and anhydrous NaSO₄ was added until the sulfate concentration reached 3.2 g/l. During the experiments, the solutions with organic substrates were stored at 4 °C in a refrigerator.

A mixed culture of microalgae of *Scenedesmus* sp. and *Chlorella* sp., isolated from natural water sources, was used in the cathode zone of the mMFC, which were cultivated on a modified nutrient medium BG11, with a chemical composition specified in a previous study [15]. The amount of microalgae inoculum was approximately 10% of the working volume of the photobioreactor and the

cathode zone of the MFC. The cultivation of microalgae was done at room temperature in the range of 22 - 25 °C.

For the process of heterotrophic microbial sulfate reduction, a microbial consortium isolated from natural habitats and immobilized on natural zeolite - clinoptilolite was used.

The pretreatment and characterization of the natural zeolite used have been presented in a previous study [13]. The composition of the microbial consortium of sulfate-reducing bacteria and metabolically related groups of microorganisms has been presented in a previous study [14].

Laboratory set up description

A new design of a combined photo-bioelectrochemical system was used for the experiments, including a microbial fuel cell (MFC) and a column-type photobioreactor integrated into the cathode zone (Figs. 1 and 2).

The base of the bioelectrochemical system is 3D printed from PETG (glycol-modified polyethylene terephthalate) filament, containing the anode (with a volume of 0.1 dm³) and cathode zones (with a volume of 1 dm³).

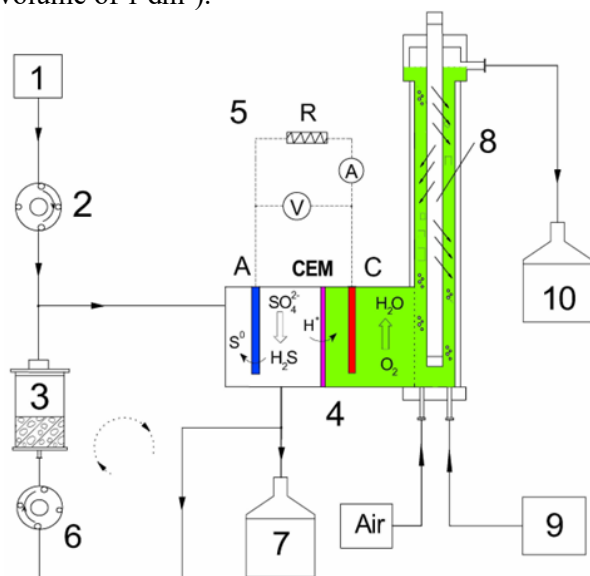


Figure 1. Experimental setup. 1 - organic substrate input, 2 - dosing peristaltic pump, 3 - sulfidogenic bioreactor, 4 - mMFC, 5 - load circuit between anode and cathode, 6 - recirculation pump, 7 - output solution after MSR, 8 - photobioreactor, 9 - nutrient medium for microalgae, 10 - output solution from PBR.

For the cathode and anode, two identical graphite plates with dimensions 100x100x6 mm were used. For the separator in mMFC, a cation exchange membrane type CMI-7000 with dimensions 100x100 mm was used. The column-type photobioreactor (made of plexiglass) is connected to the cathode zone of the MFC, together forming a

working volume of 3.5 dm³. In the central part of the photobioreactor a tubular LED light source (8) is placed with a power of 16 W and a wavelength in the range of 400÷700 nm, which provides a light flux with an intensity in the range of - 3600 - 4500 Lx, in mode - 12 h light to 12 h dark.

The oxygenic photosynthesis zone in the combined photobioreactor with the cathode zone of the mMFC (3) is supplied with air at a flow rate of 1.5 dm³/60 s, without additional CO₂ (Fig. 1).

For the cultivation of SRB in the anode zone of mMFC, a sulfidogenic bioreactor with immobilized biomass was used (position 3 in Fig. 1), in which approximately half the volume of 0.7 dm³ was filled with 0.3 kg of modified zeolite.

The described mMFC design consists of two zones - an anaerobic anode zone, where the electroactive biofilm of SRB extracts electrons from waste organic substrates, reduces sulfates to H₂S, which in turn is oxidized on the anode to S⁰ and an aerobic cathode zone, where the oxygen produced during the light phase of photosynthesis is the final electron acceptor and reacts with the released protons passed through the CEM, resulting in water (Fig.1).



Figure 2. The mMFC and the laboratory setup.

Operations of laboratory installation

Maintaining constant high values of the cathode potential is directly dependent on the amount of oxygen produced in the catholyte by the oxygenic microalgae [16]. For this purpose, in advance, in a periodic cultivation mode, the stages of microalgae growth, the change in cathodic and anodic potentials (relative to a comparative calomel electrode) and the oxygen concentration in the catholyte were determined. Regarding the anode zone of the mMFC, where the MSR process is implemented, in previous studies [17], optimal contact times in the range of 14 to 34 h have been determined for the two types of wastewater used. The continuous supply of the anode zone with waste organic substrate (vinasse and/or ethanol stillage) was realized by peristaltic pump 2 (Fig. 1), with a flow rate of 300 dm³/24 h, in a working volume of 400 dm³ (100 dm³ - volume of the anode zone in the mMFC and 300 dm³ - volume of the liquid phase in the sulfidogenic bioreactor), achieving a contact time of 30 h. During the experiments, the anolyte was continuously recirculated between the volume of the sulfidogenic bioreactor and the anode zone of the mMFC, by peristaltic pump 6 (Fig. 1).

Analytical methods

At various points in the laboratory installation is provided the possibility of sampling and continuous (online) measurement of dissolved oxygen, pH, voltage, electrical conductivity, temperature and light illumination, using Vernier^R BTA sensors and visualization and recording of data *via* the interface LabQuest^R.

Chemical oxygen demand (COD) was measured with Merck instruments reagents according to APHA [18]. pH and ORP were measured with pH/ORP/EC-Meter "Elmetron CRC-461". The sulfate concentration was determined using a spectrophotometric method at λ - 420 nm, using a BaCl₂ reagent. The concentration of hydrogen sulfide in the liquid phase was measured using Nanocolor test 1-88/05.09 at λ = 620 nm.

A light microscope (Boeco^R, BM-800) was used to observe the microalgae and their growth phases; the optical density of the cell suspension was determined during the cultivation of the microalgae at a wavelength of 650 nm and a red filter.

Electrochemical analysis

The electrical parameters of mMFC were measured with a digital multimeter Mastech MS8229, and a precision potentiometer with a range of values from 10 Ω to 11 k Ω was used for the load resistance. In this range of external resistance variation, the polarization characteristics and power

curves were also measured. A fixed external load resistance value of 100 Ω was used during the experiments, which was optimal in the mMFC power curves shown below.

The power density (P), relative to the geometric anode surface area, was calculated using the equation $P=U^2/(R_T.A)$, where A(m²) is the anode surface area, RT (Ω) is the external load resistance, and U (V) is the mMFC voltage.

To measure the cyclic VA-characteristics of mMFC, a potentiometer Squidstat Plus, with a calomel reference electrode, was used at a scan rate of 1 mV/s, in the range from 750 mV to -750 mV, and the data were visualized and recorded in real time on a computer.

The value of the coulombic efficiency (CE) was determined by the value of COD in the anolyte as the difference between the values without external resistance (R_T) and with resistance. In this way, a distinction can be made as to what part of the organic substances in microbial sulfate reduction are oxidized biologically and what part electrochemically to produce electricity.

For the calculation of CE was used:

$$CE = \frac{M.I.t}{F.b.V_{an}.\Delta COD} \times 100\% \quad (1)$$

where: M= 32 - molar mass of O₂, t(s) - time, I - average current value during the experiment (A), F (Faraday constant) = 96845 C/mol, b = 4 - number of electrons required for oxidation of 1 mol O₂, Δ COD - difference between the initial and final COD values (gO₂/l), V_{an} - volume of the anode chamber (l).

RESULTS AND DISCUSSION

Influence on the cathodic and anodic potential of mMFC in batch mode

Initially, to determine the optimal values of the cathode potential of the mMFC, the microalgae were cultivated in batch mode for 22 days, during which the anode and cathode potentials, as well as the dissolved oxygen and optical density in the catholyte, were measured. In the same time, in the anode zone, an MSR process was started, with ethanol stillage as electron donor. Figure 3 shows the change in the values of the cathodic and anodic potential, the oxygen concentration, and the dynamics of the optical density of the catholyte. The results show that the highest values of the cathodic potential are obtained at the end of the exponential phase (between 10 and 15 days), which is consistent with the results of a previous study [15]. It was found that after 5 days, the anodic potential stabilized in the

range of 215 - 226 mV. These potential values and oxygen concentrations were measured during the light phase of photosynthesis.

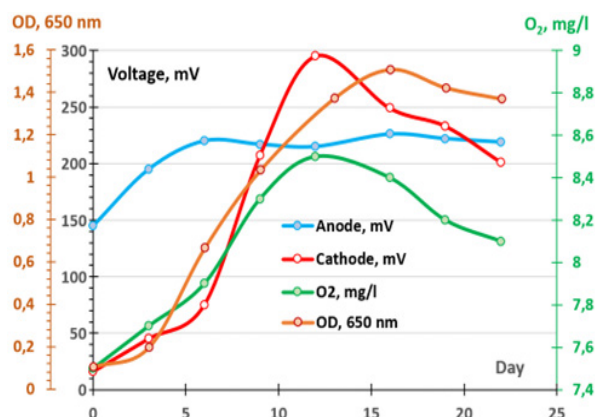


Figure 3. Dynamics of anodic potential, cathodic potential, dissolved oxygen and optical density (OD).

Based on these results, the PBR (resp. the cathode zone of the mMFC) was fed daily with fresh nutrient medium (modified BG11) with a flow rate of 350 dm³/24h, achieving a contact time of 10 days (Fig. 1), which in this case was considered optimal with respect to the cathode potential of the mMFC.

Research on the influence of the electron donor on the electrochemical characteristics of the mMFC

To study the influence of ethanol stillage and vinasse (electron donors in the anode zone of mMFC) on the efficiency of the mMFC, polarization curves and power curves were plotted for both substrates (Fig. 4). These curves were measured during the light phase of photosynthesis, in continuous operation mode, in both anode and cathode zones. From the data above, it is evident that the maximum power density for ethanol stillage is 14.5 W/m², and for vinasse it is 8.0 W/m². The current density values are respectively 64.1 mA/m² (ethanol stillage) and 34.8 mA/m² (vinasse).

These values were obtained at a fixed external load resistance of 100 Ω (for the ethanol stillage) and 200 Ω (for the vinasse), which shows that the corresponding internal resistances of the mMFC are close to these values. A more accurate analysis of the internal resistance (R_{int}) was made based on the cyclic voltammetry characteristic presented in Fig. 5. Accordingly, for two linear sections of these characteristics, it was found that the internal resistance of the ethanol stillage is 83.3 Ω , and that of the vinasse is 125 Ω . The lower internal resistance of the ethanol stillage variant compared to the vinasse is probably due to the significant difference in their electrical conductivities (Table 2), both in the initial substrate and in the anolyte with and without load. When analyzing the cyclic voltammetry

characteristics, additional data were obtained for the two studied variants. Accordingly, the slope of the cyclic voltammetry characteristic curve for the ethanol stillage is greater than that for the vinasse, and significant differences in their areas are also noticeable (Fig. 5).

Determining the coulombic efficiency (CE) in a microbial fuel cell with an MSR process in the anode zone is an interesting problem. CE in a microbial fuel cell is calculated as the ratio between the actual electrical charge produced and the theoretical electrical charge that could be obtained from the complete oxidation of the supplied electron donor. Measurements of the COD change with and without mMFC load resistance were made to separate what part of the electron donor is spent on the MSR process and what part on electrogenesis, and are presented in Tables 2 and 3.

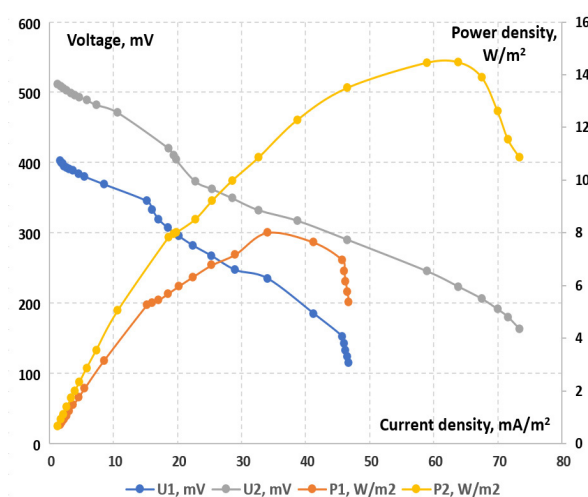


Figure 4. Polarization curves and power curves of mMFC with different electron donors in the anode zone. U1, P1- voltage and power density in ethanol stillage, U2, P2- voltage and power density in vinasse.

Table 2. Values of the main technological parameters in the anolyte, with and without mMFC load.

Parameter	SO ₄ , mg/l	EC, mS/cm	COD, gO ₂ /l	H ₂ S, mg/l	OCV, mV
Ethanol stillage					
Input	3234	15.12	39.6	-	-
Output $R_T = \infty$	260	19.87	29.6	141	512
Output $R_T = 100 \Omega$	484	16.55	23.3	35	436
Vinasse					
Input	3320	13.08	28.6	-	-
Output $R_T = \infty$	1095	18.34	24.2	118	350
Output $R_T = 100 \Omega$	1358	15.21	21.5	94	310

The results in Table 3 show that the rate of microbial sulfate reduction in the ethanol stillage is 99.1 mg/l.h (without load) and 91.7 mg/l.h (with load), while in the vinasse it is 74.2 mg/l.h (without load) and 65.4 mg/l.h (with load). Accordingly, the degree of sulfate removal is 91.9% (ethanol stillage) and 67.02% (vinasse).

A relationship is observed between OCV (open circuit voltage) and the concentration of H_2S in the anolyte, their values being higher in the stillage than in the vinasse.

The increase of the sulfates in the anolyte with the application of external load resistance (Table 2) is probably due to the stimulation of oxidation processes in the anode zone during the oxidation of H_2S . A particular interest from the obtained results is what part of the electron donor (ethanol stillage and vinasse) was oxidized as a result of microbial sulfate reduction (MSR), and what part is for electrogenesis when applying an electrical load (R_T), between the anode and the cathode of the microbial fuel cell (mMFC). The results (Table 3) show that the sulfates and the anode are in constant competition as electron acceptors for both studied substrates, and the sulfates are the preferred electron acceptor.

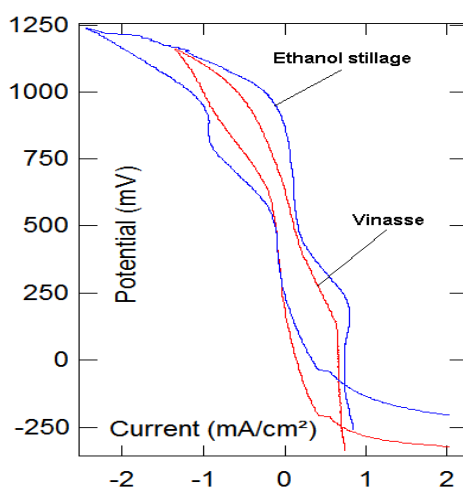


Figure 5. Cyclic voltammetry characteristics in mMFC with Ethanol stillage and Vinasse.

Fig. 6 shows the amount of substrate utilized, estimated by COD, for the MSR process (1), for

electrogenesis (2) and that part of COD (3) that remains unused in these processes.

The ethanol stillage, compared to the vinasse, shows better results in terms of microbial sulfate reduction rate, COD and sulfate removal rate and lower internal resistance in the anode zone of mMFC. Regarding the obtained calculated values of the coulombic efficiency, similar values are found for ethanol stillage (17.1%) and vinasse (14.8%). These values for the coulombic efficiency are comparable to those obtained by Akgul *et al.* [19].

For both substrates studied, a higher relative participation in the MSR process was observed compared to electrogenesis – with the ethanol stillage (25.5% vs. 15.15%), and with the vinasse (15.38% vs. 9.45%). This indicates that sulfate-reducing microorganisms are metabolically more active in the anodic zone and largely compete with electrogenic bacteria for available electrons. The better digestibility of organic substances when used for ethanol stillage compared to vinasse indicates the better bioavailability and biodegradability of organic compounds in the ethanol stillage.

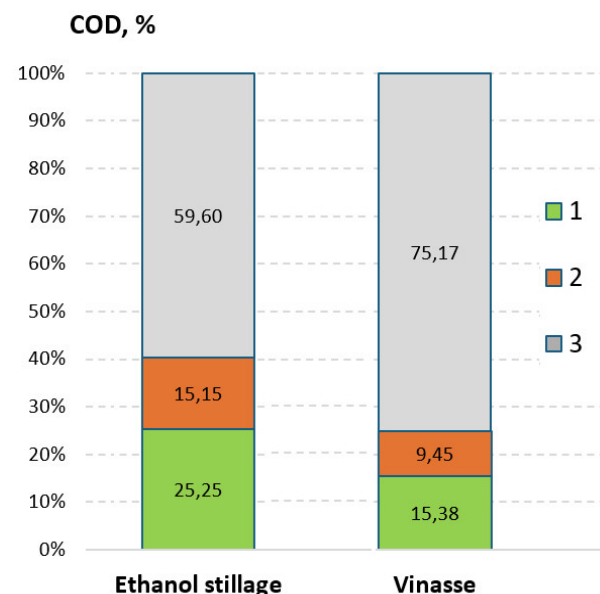


Figure 6. Comparison between the rates of COD absorption in the MSR process in the anode zone, with and without external load. 1 - only for the MSR process ($R_T=\infty$), 2 - only for electrogenesis ($R_T=100 \Omega$), 3 - residual part of COD.

Table 3. SO_4 and COD removal in the anolyte and coulombic efficiency (CE) values in mMFC.

Anolyte	SO_4 -reduction rate, SO_4 , mg/l. h	SO_4 -removal, %	COD-total removal, %	COD (without R_T), %	COD ($R_T=100 \Omega$), %	CE, %
Ethanol stillage	99.1*-91.7**	91.9*- 85.0**	41.2	25.3	15.9	17.1
Vinasse	74.2*- 65.4**	67.0*- 59.1**	24.8	15.4	9.4	14.8

*- with open circuit, ** - with external load ($R_T=100 \Omega$)

CONCLUSIONS

A combined bioelectrochemical system of a photobioreactor and MFC was studied. The efficiency of the combined mMFC depends on both the cathodic and anodic potentials, which are influenced by various medium factors, and on the type of electron donor for the MSR process in the anode zone. The competition between microbial sulfate reduction (MSR) and electrogenesis in the anode chamber of the mMFC, especially with respect to the distribution of electron donors between these two processes, is decisive for the operating efficiency of the studied photo-bioelectrochemical system.

Acknowledgement: This research was supported by the Bulgarian National Science Fund, Grant № KP-06-H67/3, 2022.

REFERENCES

1. B. S. Dhanya, A. Mishra, A. K. Chandel, M. L. Verma, *Sci. Total Environ.*, **723**, 138109 (2020), <https://doi.org/10.1016/j.scitotenv.2020.138109>
2. A. Khandelwal & Lens, *Environ. Technol.*, **45** (21), 4181 (2023), doi:10.1080/09593330 P. N. L..2023.2243544.
3. S. Venkata Mohan, G. Velvizhi, K. Vamshi Krishna, M. Lenin Babu, *Bioresour. Technol.*, **165**, 355 (2014), doi:10.1016/j.biortech.2014.03.048
4. R. Kumar, L. Singh, Z. A. Wahid, *Microb. Cell Fact.*, **135** (2015). doi:10.1007/978-81-322-2598-0_9
5. S. Luo, Z.-W. Wang, Z. He, *Energy*, **124**, 227 (2017), ISSN 0360-5442, <https://doi.org/10.1016/j.energy.2017.02.039>
6. C. Nagendranatha Reddy, H. T. H. Nguyen, M. T. Noori, B. Min, *Bioresour. Technol.*, **292**, 122010 (2019). ISSN 0960-8524, <https://doi.org/10.1016/j.biortech.2019.122010>
7. R. N. Singh, S. Sharma, *Renew. Sustain. Energy Rev.*, **16**(4), 2347 (2012), <https://doi.org/10.1016/j.rser.2012.01.026>.
8. P. J. Sarma, B. Malakar, K. Mohanty, *Biomass Convers. Biorefin.*, **14**, 16973, (2023), <https://doi.org/10.1007/s13399-023-03848-z>
9. Z. Ullah, Z. Sheikh, W. Q. Zaman, M. Zeeshan, W. Miran, J. Li, M. A. N. Khan, S. Saleem, S. Shabbir, *J. Water Process Eng.*, **56**, 104358 (2023).
10. W. Mikucka, M. Zielińska, *Appl. Biochem. Biotechnol.*, **192**, 770, (2020) doi:10.1007/s12010-020-03343-5
11. Y. Yuan, H. Cheng, F. Chen, Y. Zhang, X. Xu, C. Huang, C. Chen, W. Liu, C. Ding, Z. Li, T. Chen, A. Wang, *Environ. Int.*, **136**, 105503, (2020). ISSN 0160-4120, <https://doi.org/10.1016/j.envint.2020.105503>
12. I. C. B. Rodrigues, V. A. Leão, *Environ. Sci. Pollut. Res.*, **27**, 36075 (2020). <https://doi.org/10.1007/s11356-020-09728-7>
13. A. Angelov, S. Bratkova, A. Loukanov, *Energy Convers. Manag.*, **67**, 283 (2013), doi: 10.1016/j.enconman.2012.11.024
14. S. Bratkova, Z. Alexieva, A. Angelov, K. Nikolova, P. Genova, R. Ivanov, M. Gerginova, N. Peneva, V. Beschkov, *Int. J. Environ. Sci. Technol.*, **16**, 6145, (2019), <https://doi.org/10.1007/s13762-019-02223-8>
15. A. T. Angelov, S. G. Bratkova, R. V. Ivanov, P. G. Velichkova, *Bulg. Chem. Commun.*, **55**(1), 53 (2023).
16. A. Khandelwal, M. Chhabra, P. N. L. Lens, *Front. Plant Sci.*, **14**, 1081108 (2023), doi: 10.3389/fpls.2023.1081108
17. P. Velichkova, S. Bratkova, A. Angelov, K. Nikolova, P. Genova, R. Ivanov, *J. Ecol. Nat. Resour.*, (JENR), ISSN: 2578-4994, DOI: 10.23880/jenr-16000410 (2025).
18. APHA, AWWA and WPCF, Washington, DC (1992).
19. V. Akgul, K. Cirik, A. Duyar, S. Basak, D. Akman, *Global NEST J.*, **21**(3), (2019) <https://doi.org/10.30955/gnj.002926>

One-step chemical modification of pine cones for the removal of methyl orange from aqueous media

S. M. Al-Mahmoud*

Department of Chemistry, College of Education for Women, Tikrit University, Tikrit, 34001, Iraq

Received: August 04, 2025; Revised: September 21, 2025

Water pollution is a significant and serious problem because it poses an enormous threat to the environment. Agricultural materials may emerge as an elegant solution to overcome this problem. In this study, a carbonaceous adsorbent from Aleppo pine cones was prepared by chemical modification using a simple chemical treatment with sulfuric acid. The adsorption process is extremely influenced by the operating conditions. The optimal elimination of methyl orange was achieved at a concentration of 50 mg/L, an adsorbent dosage of 0.12 g, an adsorption time of 50 min, and a temperature of 25 °C. The spontaneous exothermic behavior of the removal system was proved by the negative values of ΔG and ΔH , respectively. The kinetic representation by employing a pseudo-second order equation demonstrates consistency of the adsorption data with the supreme correlation coefficient close to unity. The isotherm investigation reveals that the Langmuir equation is most applicable to presenting the removal experimental data. These results emphasize that modified Aleppo pine cone powder can act as an interesting adsorbent for eliminating methyl orange from untreated contaminated water.

Keywords: Chemical treatment, Water pollution, Methyl orange, Aleppo pine cones.

INTRODUCTION

Water treatment results in significant financial losses because it requires an effective method to eliminate the contaminated materials that pose a critical intimidation to the environment and living things. With the fast growth in the industry fields to meet human needs, the amount of industrial hazardous waste is also growing, and dyes can represent one of the main pollutants that contaminate water bodies [1]. Dyes are chemical compounds that play a major role in the textile industry. They can pose a manifested threat to the water circumference if subtracted without any handling [2]. Therefore, an efficient removal of dyes is highly important.

New policies concerning the environment have obliged factories to utilize methods that can minimize the size of waste that they deposit into the environment [3]. The strategy taken to reduce water contamination is to remove the contaminated materials from the water. Various sophisticated wastewater remediation techniques have been applied to the elimination of pollutants, including photo catalysis [4], coagulation [5], electro Fenton [6], electrochemical filtration [7], and adsorption [8]. Adsorption is considered an efficient, simple and easy-to-control technique to treat emerging water contaminants, and it plays a substantial role in environmental redemption [9]. Adsorption is often

used for reducing contamination by adding adsorbent materials to the contaminated medium.

Agricultural materials are considered a viable alternative adsorbent in the adsorption technology being environmentally friendly, available, and of low economic cost [10]. Their unique chemical composition contains various compounds, including cellulose, hemicellulose and lignin. These compounds can adsorb a variety of contaminated species and can greatly improve the removal of aquatic pollutants [11]. Aleppo pine is a natural tree widely propagated in the Mediterranean countries due to its unique properties, such as adaptability and rapid and abundant production [12]. Enormous quantities of remains (needles, cones, branches and bark) will be generated as a result of logging the trees. These low-value wastes need sustainable processing in order to mutate into more valuable substances [13].

Although agricultural materials as adsorbents can give a passable ability in removing pollutants, their use is still lower than that of porous carbon material [14]. This may be a substantial limitation for their employment in water treatment [15]. The necessity to reduce the amount of contaminated materials led to the search for ways to improve the adsorption process. Chemical treatment of agricultural materials [16-19] is one way that is used in

* To whom all correspondence should be sent:
E-mail: s_almahmoud@tu.edu.iq

adsorption technology that improves the adsorbent surface by using a proper activation agent. Sulfuric acid (H₂SO₄) is an excellent oxidizing agent that is used continually for the production of carbonaceous materials with a rich oxygen content of the surface active groups such as carboxylic and hydroxylic groups [17].

The purpose of this research is to prepare a carbonaceous adsorbent from Aleppo pine cones using a simple chemical treatment method and to examine the influence of chemically modified Aleppo pine cone powder on the elimination of methyl orange dye from untreated contaminated water.

EXPERIMENTAL

Chemicals

The chemicals in this study were utilized as obtained without any additional purification. Methyl orange (MO) of analytical grade was acquired from Fluka. Its chemical formula is C₁₄H₁₄N₃NaO₃S, M. Wt. 327.33 g/mol, and it absorbs at λ_{max} of 464 nm [20]. Sulfuric acid was supplied by Sigma Aldrich.

Preparation of the adsorbent

The Aleppo pine cones were collected from Duhok, Iraq. They were cut into little pieces, rinsed thoroughly with distilled water (DW) so as to remove any dust or impurities, and dried using a drying oven (LabTech, Korea) at 100 °C for 6 h. The dried material was grinded using an electric food grinder, and then sieved by a molecular sieve to gain Aleppo pine cone powder with small particles not more than 150 μm .

The modification of Aleppo pine cones by sulfuric acid was carried out at room temperature for 24 h. Firstly, 20 g of the Aleppo pine cone powder was put in a beaker. 50 ml of concentrated H₂SO₄ was added to the powder and mixed mechanically for 1 h. The blend was then left at 25 °C for 24 h, and the resulting black product was filtered and thoroughly rinsed with DW. The obtained black solid was then dried for 4 h at 100 °C. The chemically modified Aleppo pine cone powder was labelled as CAPC, and was characterized using Fourier transform infrared spectrometry on a Shimadzu, Japan instrument, and field emission scanning electron microscopy (Mira 3, TESCAN microscope).

Adsorption experiments

A batch method was utilized in this investigation to examine the adsorption properties of CAPC toward methyl orange. The adsorption experiment setup was performed using 25 mL of the desired methyl orange solution. Various parameters were

investigated using one-variable approach on a time procedure to define the optimal removal conditions. The variables included: amount of carbonaceous Aleppo pine cones (0.02, 0.04, 0.06, 0.08, 0.1, 0.12, 0.15, and 0.2 g), concentration of methyl orange (25, 50, 75, 100, 125, and 150 mg/L), temperature of the adsorption system (298, 308, 318, 328 K), and uptake time (10, 20, 30, 40, 50, 60, 80, and 100 min.). The solutions (suspensions) were agitated continuously in a heated shaking bath (GFL, Germany) and then separated at a speed of 3000 rpm in a centrifuge 8-tubes (Gallenkamp, England) to gain a clear supernatant. The concentration of methyl orange residual was estimated by ultraviolet-visible spectroscopy (UV-1800, Shimadzu) at 464 nm. The value of methyl orange adsorbance onto CAPC was estimated from the concentration variance.

The adsorption capacity at equilibrium (q_e) was recorded from equation (1), and the removal efficiency (% R) was determined from equation (2).

$$q_e = \frac{(C_0 - C_e)V}{m} \quad (1)$$

$$\% R = \frac{(C_0 - C_e)}{C_0} \times 100 \quad (2)$$

where C_0 and C_e represent the starting and equilibrium MO concentration in mg/L, V symbolizes the volume of MO solution in L, and m refers to the CAPC amount in g.

The thermodynamic parameters for the MO dye adsorption onto the CAPC surface were estimated from equations (3) and (4):

$$\Delta G^\circ = -RT \ln K \quad (3)$$

$$\ln K = \frac{\Delta S}{R} - \frac{\Delta H}{RT} \quad (4)$$

where K is the equilibrium constant, T is the absolute temperature (K), and R is the gas constant (8.314 J K⁻¹ mol⁻¹).

In addition, four equations were applied in the kinetic investigation: pseudo-first order (equation 5), pseudo-second order (equation 6), intra-particle diffusion (equation 7), and Elovich model (equation 8).

$$\ln(q_e - q_t) = \ln q_e - k_1 t \quad (5)$$

$$\frac{t}{q_t} = \left(\frac{1}{k_2 q_e^2} \right) + \left(\frac{1}{q_e} \right) t \quad (6)$$

$$q_t = k_{int} t^{1/2} + C \quad (7)$$

$$q_t = \left(\frac{1}{\beta} \right) \ln \alpha \beta + \left(\frac{1}{\beta} \right) \ln t \quad (8)$$

where q_e is the adsorption capacity at equilibrium, q_t is the adsorption capacity at time t , k_1 and k_2 are the PFO and PSO rate constants,

respectively, k_{int} is the IPD constant, and α and β are the EV constants.

Finally, the isotherm analysis was performed by applying the Langmuir and the Freundlich models, whose linearized forms are displayed in equations (9) and (10), respectively.

$$\frac{1}{q_e} = \frac{1}{q_m K_L C_e} + \frac{1}{q_m} \quad (9)$$

$$\ln q_e = \ln K_F + \frac{1}{n} \ln C_e \quad (10)$$

where q_m represents the ultimate adsorption capacity, K_L denotes the Langmuir constant, and K_F and n symbolize the Freundlich constants.

RESULTS AND DISCUSSION

CAPC characterization

It was established that the existence of amine, hydroxyl, and carbonyl groups on the surface of the adsorbent materials can ameliorate the adsorption process [21-23]. The functional groups on the surface of carbonaceous Aleppo pine cone powder (CAPC) were detected using FT-IR spectrophotometry. The FT-IR spectra of CAPC are presented in Figure 1. Various bands between 461 – 781 cm^{-1} were recorded that were related to wagging vibration of C–H in aromatic compounds [24]. The peak at 1045 cm^{-1} may be attributed to the C–N stretching in amines [25]. The broad band at 1165 cm^{-1} can be assigned to C–C and C–O stretching vibrations in esters, alcohols, or phenols [26]. The prominent peak at 1626 cm^{-1} can be attributed to the C=C stretching of the aromatic ring [1]. The notable band at 1707 cm^{-1} represents the carbonyl group, which emphasizes the existence of aldehydes and carboxylic acids [9]. The wide band at 3416 cm^{-1} can be referred to the N–H vibration in amines [24]. The sharp band at 3616 cm^{-1} can be referred to the hydroxyl groups in alcohols and phenols [21].

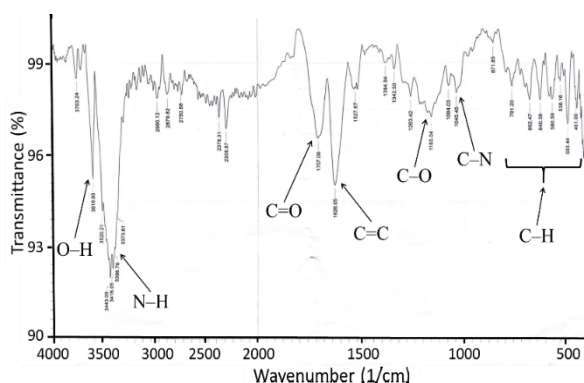


Fig. 1. FT-IR spectra of the CAPC surface.

The morphological analysis of CAPC was documented using a FESEM microscope. Figure 2 demonstrates the FESEM micrograph of the CAPC surface. A uniform surface containing adequate grooves can be observed, which can facilitate the transport of MO dye molecules within the CAPC particles and thus increase the removal process.

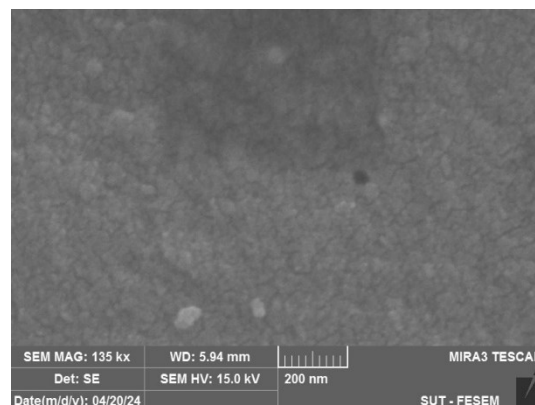


Fig. 2. FESEM image of the CAPC surface.

Adsorption study

One of the main variables that influences the removal of MO dye on the CAPC surface is the adsorbent amount. It was studied using various CAPC doses (between 0.02 – 0.2 g), 50 mg/L initial MO concentration, 50 min uptake time, at 25 °C. As seen in Figure 3, changing the adsorbent dose will affect the removal efficiency. A minimum removal efficacy of 32% was observed at a low adsorbent dosage, and the removal efficacy increases with the rise in the amount of adsorbent to accomplish its ultimate removal percentage of 94% using 0.12 g of CAPC. The reason for this increase is that at a fixed concentration of MO, increasing the CAPC dosage leads to a prominent increase in the free effective sites eligible for adsorption, which thus increases the removal efficacy. An additional increase in the adsorbent amount would show no significant improvement, which means that the uptake process attains its equilibrium state.

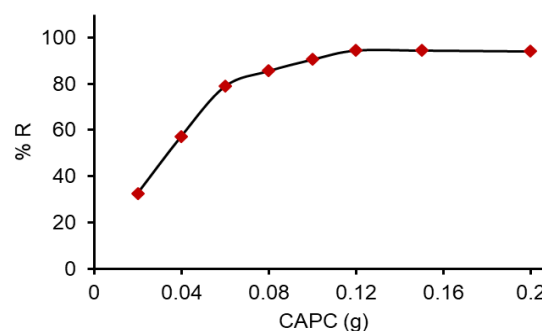


Fig. 3. Influence of the CAPC dosage on the elimination of MO dye.

The effectiveness of the experiment time on the uptake of MO dye on the CAPC surface was investigated with different adsorption times between 10 - 100 min, and 50 mg/L initial MO concentration, 0.12 g of CAPC mass, at 25 °C. Figure 4 shows a good uptake level at the beginning of the adsorption, that can be associated with the affinity between MO molecules and CAPC particles. Also, the removal efficiency increases as the contact time increases to accomplish its ultimate value of 94% at a time of 50 min, which can be considered as the removal equilibrium time. This is attributed to the fact that increasing the uptake time will give adequate time for MO molecules to be adsorbed on the available CAPC adsorption sites, which leads to the removal enhancement.

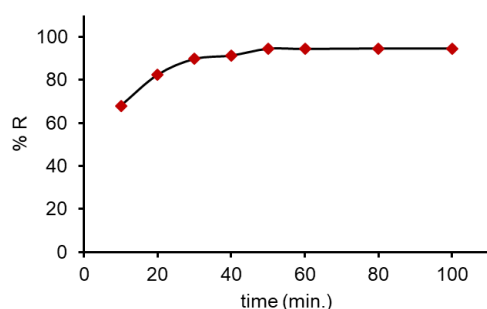


Fig. 4. Influence of time on the elimination of MO dye on the CAPC surface.

The impact of the starting MO dye concentration is presented in Figure 5. It was tested using varied initial MO concentrations (between 25 – 150 mg/L), 0.12 g CAPC doses, 50 min uptake time, at 25 °C. Figure 5 shows a decrease in the removal efficacy as the starting concentration of MO dye increases, which is referred to the presence of vacant efficient removal sites on the CAPC particle that are required to accommodate the molecules of MO dye. Increasing the initial MO dye concentration will provide more dye molecules that require more vacant sites, which reduces the removal efficiency.

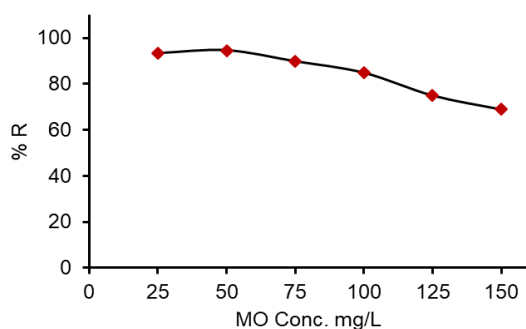


Fig. 5. Influence of the initial MO dye concentration on the elimination process.

The impact of the temperature on the uptake of MO dye onto the CAPC surface was also investigated at different temperatures (298, 308, 318, 328 K), 50 mg/L initial MO concentration, 0.12 g CAPC doses, and 50 min uptake time. Figure 6 displays a gradual decrease in the removal level with rising temperature. Increasing the temperature may provide more energy for MO molecules to be able to flee from the CAPC surface and return to the bulk solution, which will reduce the removal efficiency.

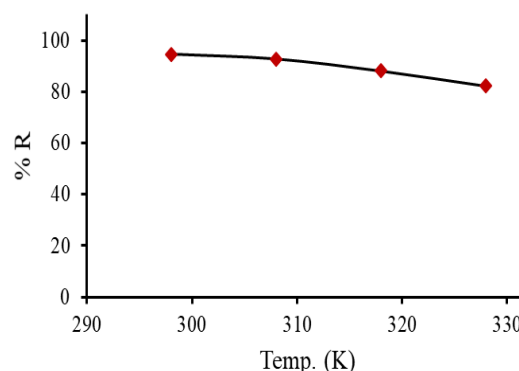


Fig. 6. Influence of the temperature on the elimination of MO dye on the CAPC surface.

Thermodynamic study

The thermodynamic assessment was carried out by analyzing the experimental data recorded from the temperature effect to calculate the essential thermodynamic parameters. These parameters are the Gibbs free energy change (ΔG) that can be estimated using equation (3), the entropy change (ΔS) and the enthalpy change (ΔH) that can be evaluated from the intercept and slope of the straight line obtained from the Van't Hoff plot as shown in Figure 6. The results obtained are presented in Table 1.

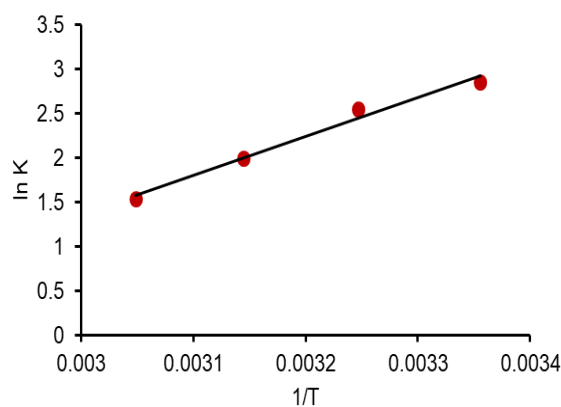


Fig. 7. Van't Hoff plot for the removal of MO dye on the CAPC surface.

Table 1. Thermodynamic parameters of MO dye removal on the CAPC surface at diverse temperatures

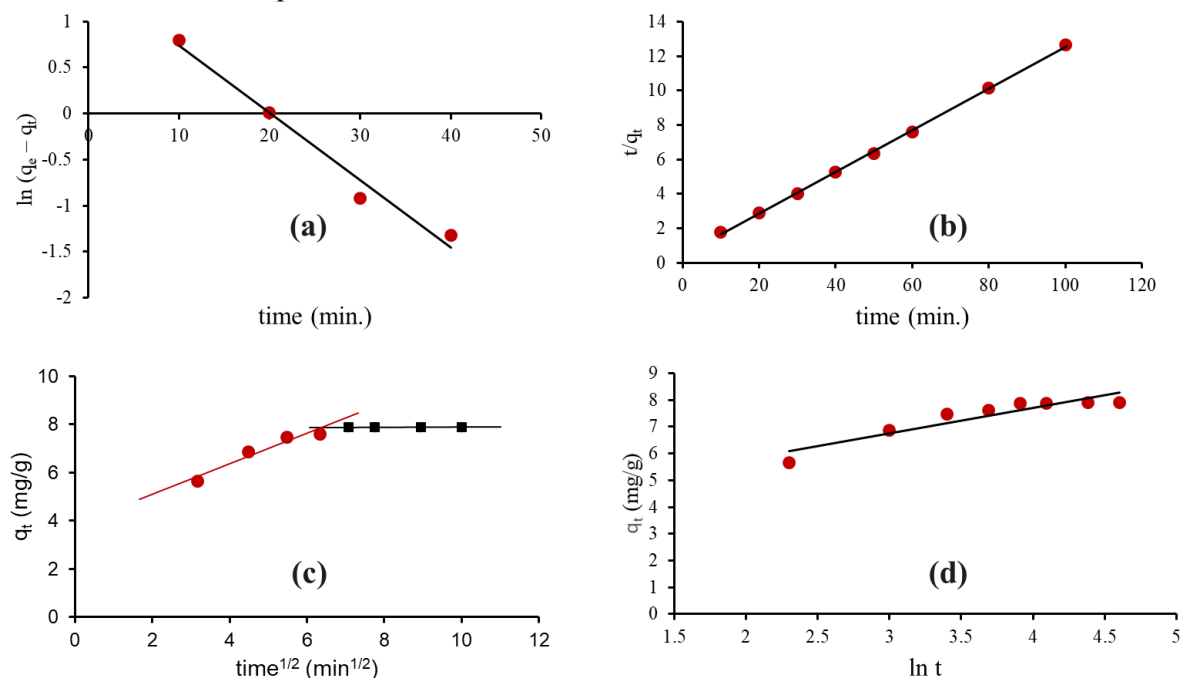
T (K)	ΔG° (kJ/mol)	ΔH (kJ/mol)	ΔS (J/mol K)	R^2
298	-7.076	-3.654	-98.34	0.98
308	-6.514			
318	-5.282			
328	-4.186			

The negative value of ΔS clearly signifies a drop in the randomness that was fulfilled as a result of the linkage between the MO molecules and the CAPC particles. Also, the negative value of ΔH signifies that the behavior of the elimination system is exothermic. In addition, the spontaneous behavior

of the removal process was evidenced by the negative value of ΔG , and raising the temperature will decrease the spontaneity of the MO molecules' elimination onto the CAPC surface.

Kinetic study

The kinetic study was performed by applying the linearized form of four kinetic equations to the data obtained from the contact time experiment: the pseudo-first order (PFO), the pseudo-second order (PSO), the intra-particle diffusion (IPD), and the Elovich model (EV), whose equations are given in equations (5) – (8), and their plots are displayed in Figure 8. The kinetic outcomes are recorded in Table 2.

**Fig. 8.** Kinetic models (a) PFO, (b) PSO, (c) IPD, and (d) Elovich plots for the removal of MO dye on the CAPC surface.**Table 2.** Kinetic parameters of MO dye removal on the CAPC surface

q_e exp.	Pseudo-first order			Pseudo-second order			Intra-particle diffusion			Elovich			
	k_1	q_e cal.	R^2	k_2	q_e cal.	R^2	k_{int}	q_e cal.	R^2	α	β	q_e cal.	R^2
7.88	0.16	4.33	0.97	0.03	8.24	0.99	0.63	8.73	0.93	61.36	1.11	7.48	0.85

Table 3. Isotherm parameters of MO dye removal on the CAPC surface

Langmuir model			Freundlich model		
k_L	q_m	R^2	K_F	n	R^2
0.14	21.32	0.93	0.05	0.45	0.87

The PSO kinetic equation displays a more compatible fit of the adsorption experimental data compared to the other models. The PSO model gives the greatest correlation coefficient (R^2) of 0.99 and the closest calculated removal capacity (q_e cal.) of 8.24 mg. g⁻¹. This confirms that the removal of MO molecules onto the CAPC surface obeys the kinetics of the PSO equation, and the removal process might be controlled by chemical adsorption. In addition, one of the interesting results is found when applying the IPD equation. Three steps were suggested to elucidate the adsorption system according to this model. Firstly, the boundary layer of the adsorbent outer surface experiences mass transfer and secondly, intra-particle diffusion across the interior adsorbent structure. The adsorption then takes place at the final step. Figure 8 (c) displays a nonlinear intra-particle diffusion plot over the entire time period, which denotes that more than one step is involved in the removal system. The vanishing of the first step in the IPD plot signifies that the outer adsorbent transfer is extremely fast, which can refer to the significant affinity between the MO molecules and the CAPC particles, as mentioned before, which leads to the intra-particle diffusion starting quickly.

Isotherm study

The isotherm analysis was conducted by employing two isotherm equations to the experimental data collected from the impact of initial MO concentration. The Langmuir and the Freundlich isotherms, whose mathematical expressions are used in this investigation, are shown in equations (9) and (10), respectively. The resulting parameters of these isotherms are recorded in Table 3.

From the results in Table 3 it is obvious that the Langmuir model is more proper than the Freundlich model for modeling the removal process. With the highest correlation coefficient of approximately 0.93, the Langmuir isotherm describes the monolayer formation of MO dye coverage on the homogeneous CAPC surface.

CONCLUSIONS

The present investigation examines the removal of methyl orange dye using chemically modified Aleppo pine cones. The removal behavior was illustrated with the alteration in the process-affected factors. The adsorption study reveals that the optimum operating variables were found to be 0.12 g of the modified biosorbent CAPC, 50 min contact time to attain equilibrium, adsorption temperature of 25 °C, and 50 mg/L of starting MO concentration. The thermodynamic assessment reveals that the

removal system is exothermic and spontaneous. The kinetic study demonstrates that the best fit of the adsorption data was achieved by applying the pseudo-second order equation. The isotherm study validates that the Langmuir model is more acceptable to depict the uptake system. This investigation provides premeditation into the use of modified agricultural material in the removal process and offers direction for further exploration of new biosorbents to modulate the uptake level of pollutants from water.

Acknowledgement: *The Author thanks the Department of Chemistry, College of Education for Women, Tikrit University, Ministry of Higher Education and Scientific Research, Iraq, for supporting this research.*

REFERENCES

1. O. S. Ali, D. E. AL-Mammar, *Iraqi J. Sci.*, **65**, 1824 (2024).
2. N. Samghouli, L. Rghioui, S. Sebbahi, A. El Hajji, L. Guennoun, R. Khaoulaf, M. S. Idrissi, S. El Hajjaji, *Bulg. Chem. Commun.*, **57**, 85 (2025).
3. S. Karishma, V. C. Deivayanai, P. Thamarai, A. Saravanan, P. R. Yaashikaa, *Sustain. Chem. Environ.*, **7**, 100143 (2024).
4. K. Tohdee, S. Mukjinda, S. Semmad, A. Jotisankasa, P. Praserttham, B. Jongsomjit, *J. Taiwan Inst. Chem. Eng.*, **142**, 104670 (2023).
5. B. Narindri Rara Winayu, C. C. Chou, H. Chu, *J. Taiwan Inst. Chem. Eng.*, **139**, 104529 (2022).
6. A. Hadadi, A. Imessaoudene, J. C. Bollinger, A. Bouzaza, A. Amrane, H. Tahraoui, L. Mouni, *J. Environ. Manage.*, **331**, 117286 (2023).
7. Z. Cao, Q. Li, P. Yan, X. Jing, J. Zhang, *J. Taiwan Inst. Chem. Eng.*, **161**, 105537 (2024).
8. K. Qi, M. Chen, R. Dai, Q. Li, M. Lai, Z. Wang, *Water (Switzerland)*, **12**, 1 (2020).
9. S. M. Al-Mahmoud, *Egypt. J. Chem.*, **63**, 2947 (2020).
10. S. T. Nipa, N. R. Shefa, S. Parvin, M. A. Khatun, M. J. Alam, S. Chowdhury, M. A. R. Khan, S. M. A. Z. Shawon, B. K. Biswas, M. W. Rahman, *Results Eng.*, **17**, 100857 (2023).
11. A. Bhatnagar, M. Sillanpää, A. Witek-Krowiak, *Chem. Eng. J.*, **270**, 244 (2015).
12. Y. Zhou, J. Lu, Y. Zhou, Y. Liu, *Environ. Pollut.*, **252**, 352 (2019).
13. A. N. Olaimat, A. M. Ababneh, M. Al-Holy, A. Al-Nabulsi, A. A. Qatatsheh, Z. W. Jaradat, B. A. Albiss, T. Osaili, R. A. Holley, *Food Control*, **164**, 110587 (2024).
14. M. Chebbi, S. Ounoki, L. Youcef, A. Amrane, *J. Ind. Eng. Chem.*, **126**, 327 (2023).
15. V. C. G. Dos Santos, J. V. T. M. De Souza, C. R. T. Tarley, J. Caetano, D. C. Dragunski, *Water. Air. Soil Pollut.*, **216**, 351 (2011).

16. D. Schwantes, A. C. Gonçalves, G. F. Coelho, M. A. Campagnolo, D. C. Dragunski, C. R. T. Tarley, A. J. Miola, E. A. V. Leismann, *J. Chem.*, **2016**, 1 (2016).
17. M. Bhaumik, H. J. Choi, M. P. Seopela, R. I. McCrindle, A. Maity, *Ind. Eng. Chem. Res.*, **53**, 1214 (2014).
18. A. H. Jawad, R. A. Rashid, M. A. M. Ishak, K. Ismail, *J. Taibah Univ. Sci.*, **12**, 809 (2018).
19. A. H. Jawad, A. S. Abdulhameed, M. S. Mastuli, *J. Taibah Univ. Sci.*, **14**, 305 (2020).
20. I. A. W. Khalaf, S. M. Al-Mahmoud, *Macromol. Symp.*, **414**, 2400223 (2025).
21. S. Rattanapan, J. Srikram, P. Kongsune, *Energy Procedia*, **138**, 949 (2017).
22. M. J. Ahmed, M. A. Islam, M. Asif, B. H. Hameed, *Bioresour. Technol.*, **243**, 778 (2017).
23. A. H. Jawad, Y. S. Ngoh, K. A. Radzun, *J. Taibah Univ. Sci.*, **12**, 371 (2018).
24. K. Mabalane, N. D. Shooto, P. M. Thabede, *Case Stud. Chem. Environ. Eng.*, **10**, 100782 (2024).
25. M. Choudhary, R. Kumar, S. Neogi, *J. Hazard. Mater.*, **392**, 122441 (2020).
26. A. A. Alsarayreh, S. A. Ibrahim, S. J. Alhamd, T. A. Ibrahim, M. N. Abbas, *Karbala Int. J. Mod. Sci.*, **10**, 511 (2024).
27. Y. Raji, A. Nadi, I. Mechnou, M. Saadouni, O. Cherkaoui, S. Zyade, *Diam. Relat. Mater.*, **135**, 109834 (2023).

Computational study of propane dehydrogenation into propylene over chromium oxide *via* a combined use of central composite design & microkinetic simulation

T. Oyegoke*

CEPRIs – CAD Engineering of Processes & Reactive Interfaces Group, Chemical Engineering Department, Ahmadu Bello University, Zaria 234, Nigeria

Received: November 3, 2024, Revised: September 13, 2025

The global demand for propylene continues to increase due to its extensive application in the production of petrochemicals. While fluid catalytic cracking (FCC) remains a major source of propylene, the growing need for targeted production has directed attention to on-purpose processes such as propane dehydrogenation (PDH). However, PDH performance is often hindered by low propylene yields, especially when chromium oxide is used as the catalyst. In this study, microkinetic modeling was integrated with central composite design (CCD) to evaluate the influence of flow rate, pressure, catalyst porosity, and temperature on the kinetics of propane dehydrogenation over chromium oxide. Rate-control analysis was further employed to identify the kinetically relevant steps governing the overall reaction rate. The results demonstrate that increases in flow rate (-5.69%), pressure (-9.28%), and porosity (-62.40%) reduce the reaction rate, whereas temperature (+22.63%) elevation enhances it, confirming the endothermic nature of the reaction. Among all variables, catalyst porosity exhibited the highest influence (-62.40%) on the reaction rate, while flow rate had the least (+5.69%). Rate-control analysis revealed that the first hydrogen abstraction step is the rate-determining transition state ($X_{TRC,TS} = -4$), and adsorbed propane is the rate-controlling intermediate ($X_{TRC,IS} = +4$). These findings suggest that improving catalyst porosity and introducing suitable promoters could lower the energy barrier of the rate-limiting step or destabilize the intermediate, thus enhancing the overall reaction rate beyond what is attainable through thermodynamic optimization alone.

Keywords: Dehydrogenation, Olefins, Paraffins, Microkinetics, Density Functional Theory, Modeling.

INTRODUCTION

Dehydrogenation is a crucial value-adding process that converts paraffins into olefins, which are key building blocks for the chemical industries due to their high reactivity [1]. Propylene, in particular, is one of the most valuable olefins, serving as an essential feedstock for the production of a wide range of petrochemical products, including polypropylene, isopropanol, propylene oxide, acrylonitrile, and many other useful materials [2, 3].

Traditionally, steam cracking and fluid catalytic cracking (FCC) processes [4–6] have been the primary sources through which the bulk of the propylene consumed in the industries was produced. However, only a small fraction of the global propylene supply currently comes from the on-purpose method, otherwise known as propane dehydrogenation [7, 8]. Recent development, particularly the decline or drop in the price of shale gas, have renewed the interest in the propane dehydrogenation technologies. This shift is further supported by the rising post-pandemic demand for propylene in the petrochemical sector. As a result, there is a growing need to enhance propylene yield

and selectivity in the dehydrogenation propane into propylene, which is often hindered by challenges such as low conversion rates and poor selectivity of conventional catalysts like platinum (Pt) and chromium oxide used in the conversion processes [7].

Several studies [4, 8–32] have explored various strategies to overcome these limitations. For example, Rimax *et al.* [33] improved the stability and selectivity of platinum-based catalysts for propylene production by alloying Pt with germanium (Ge). In another study, Yang *et al.* [34] demonstrated that incorporating magnesium oxide into a gallium-based catalyst supported on ZSM-5 increased propylene selectivity to 90.80%. A review of the literature indicates that most studies have focused on metallic catalysts [30, 35–38] — particularly platinum — for propane dehydrogenation. In contrast, metal oxides such as chromium oxide have received relatively less attention in computational investigations. Among the few existing studies, Kim *et al.* [39] reported that enhancing the lattice oxygen content of chromium oxide (CrO) catalysts significantly improved their

* To whom all correspondence should be sent:
E-mail: OyegokeToyese@gmail.com

catalytic performance in the propane dehydrogenation process.

These findings of Kim *et al.* aligned with the previous computational studies [15, 26] on propane dehydrogenation on CrO surface, which showed that the chromium (Cr) sites on the CrO catalysts are highly reactive and more abundant on the catalyst surface than the oxygen (O) sites. The Cr-sites dominance may hinder propylene desorption, potentially resulting in deep dehydrogenation and possible cracking of propylene to produce undesired products like ethylene, methane, and other lighter hydrocarbons due to the domination of the Cr-site, according to the established literature [25].

To support fuO methods, this work addresses the challenge of low yields commonly reported for chromium oxide (CrO) catalysts [7], as well as the limited number of computational studies focused on this material. A combined approach involving microkinetic modeling and central composite design (CCD) was employed to examine the effects of flow rate, pressure, porosity, and temperature on the kinetics of propane dehydrogenation over chromium oxide. Unlike the traditional one-factor-at-a-time (OFAT) method, CCD enables effective quantification of the individual and interactive contributions of these parameters to the rate of propane conversion to propylene in the presence of the catalyst. Additionally, rate-control analysis was performed to evaluate the influence of individual reaction steps on the overall reaction kinetics. The investigation employed density functional theory (DFT) energies previously computed for the propane dehydrogenation process over chromium oxide in earlier work [26], where the underlying reaction mechanism was elucidated (as shown in Figure 1) for the conversion of propane to propylene on the catalyst surface. The findings identify key reaction steps—particularly those highlighted by the rate-control analysis—that can be further explored to improve catalyst performance during the design and synthesis of next-generation chromium-based catalysts.

COMPUTATIONAL METHOD

Kinetic modeling & simulation of propane dehydrogenation

The kinetics of propane dehydrogenation to propylene over chromium oxide was modeled using a microkinetic simulation approach, supported by

relevant computational tools. This study aimed to identify the key parameters governing the reaction rate. A schematic overview of the simulation approach is presented in Figure 2. The details of the density functional theory (DFT) calculations used to obtain the energy profiles for the elementary steps have been reported in our previous work [26].

Elementary adsorption, desorption, and surface reaction rate

The elementary reaction rates for the various steps in the propane dehydrogenation mechanism—from initiation to termination—were incorporated into the reaction network. However, less stable intermediate states involved in certain steps were excluded from the modeling. The elementary reaction rates used in the simulation are summarized in Table 1.

The rate constants were calculated using the mathematical model presented in Equation (1):

$$k_i = P_{corr} * (k_B * T/h) * \exp(-G^\# / RT) \quad (1)$$

where R_{fi} or R_{bi} is the reaction rate, P is the pressure, X is the surface site concentration (i.e., normalized form), k is the rate constant, P_{corr} is the correction term expressed in the model presented in Equation (2):

$$P_{corr} = P_0^{-N_{ns}} * X_0^{1-N_s} \quad (2)$$

$G^\#$ is the reaction activation energy computed using the expression presented in Equation (3):

$$G^\# = G_{TS} - G_R \quad (3)$$

P_0 is the standard pressure, T is the reaction temperature, X_0 is the standard surface concentration obtained from the literature reports [40–42], R is the gas constant, k_B is the Boltzmann constant, h is the Planck constant, N_s is the surface species stoichiometric coefficient, N_{ns} is the non-surface species stoichiometric coefficient, X is the empty surface site concentration, and X_i is the species (i) surface site concentration.

Surface reaction activity models

Here, the surface reaction activities displaying the evolution, transformation, and disappearance of surface species during propane dehydrogenation into propylene over a chromium oxide catalyst were expressed in the following equations [43].

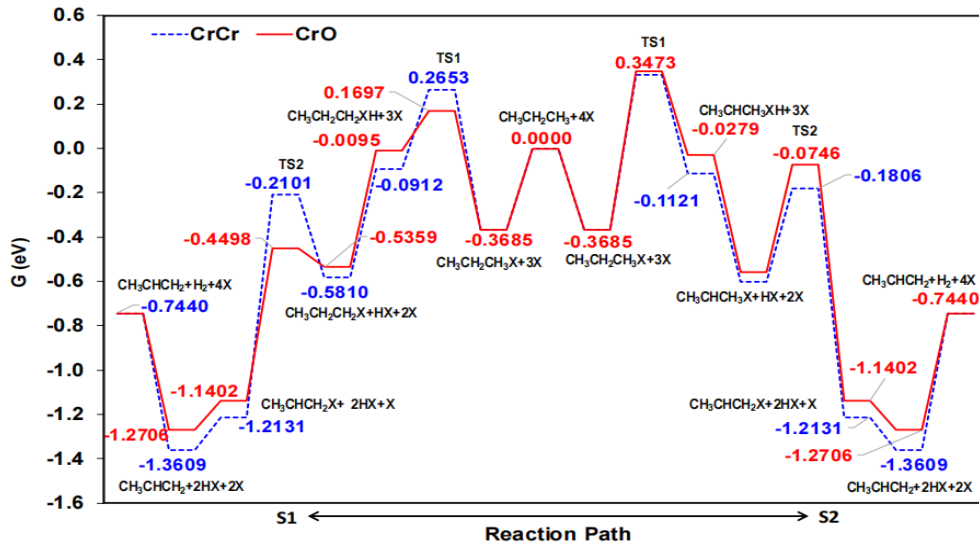


Figure 1. Propane dehydrogenation reaction mechanism across Cr-Cr and Cr-O pair sites with the energy profile using the reaction schemes 1 (LHS) and 2 (RHS) (all in eV), where LHS is the left-hand side, RHS is the right-hand side [26].

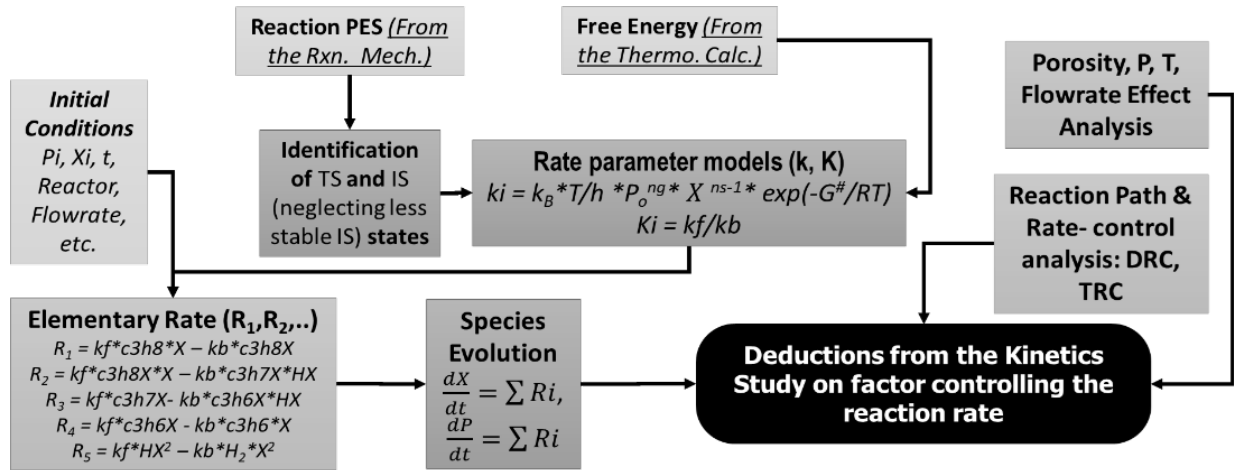


Figure 2. Flow chart showing the approach employed in the kinetics simulation

Table 1. List of elementary steps, including the rate expression for the backward & forward.

Elementary step	Forward reaction rate	Backward reaction rate
Propane adsorption	$R_{f1} = k_{f1} * P_{C3H8} * X$	$R_{b1} = k_{b1} * X_{C3H8}$
First hydrogen abstraction	$R_{f2} = k_{f2} * X_{C3H8} * X$	$R_{b2} = k_{b2} * X_{C3H7} * X_H$
Second hydrogen abstraction	$R_{f3} = k_{f3} * X_{C3H7} * X$	$R_{b3} = k_{b3} * X_{C3H6} * X_H$
Propylene adsorption	$R_{f4} = k_{f4} * X_{C3H6}$	$R_{b4} = k_{b4} * P_{C3H6} * X$
Hydrogen adsorption	$R_{f5} = k_{f5} * X_H^2$	$R_{b5} = k_{b5} * P_{H2} * X^2$

The expression for the evolution, transformation and disappearance of the adsorbed propane is presented in Equation (4):

$$\frac{dS_{C3H8}}{dt} = \frac{1}{X_{t=0}} \frac{dX_{C3H8}}{dt} = \frac{1}{X_{t=0}} \sum R_i \quad (4)$$

The expression for the propyl evolution, transformation, and disappearance in the reaction network is presented in Equation (5):

$$\frac{dS_{C3H7}}{dt} = \frac{1}{X_{t=0}} \sum R_i \quad (5)$$

The expression for the evolution, transformation and disappearance of propylene in the reaction network is presented in Equation (6):

$$\frac{dS_{C_3H_6}}{dt} = \frac{1}{X_{t=0}} \frac{dX_{C_3H_6}}{dt} = \sum R_i \quad (6)$$

The expression for the evolution, transformation and disappearance of hydrogen in the reaction network is presented in Equation (7):

$$\frac{dS_{H_2}}{dt} = \frac{1}{X_{t=0}} \sum R_i \quad (3)$$

where $X_{t=0}$ is the initial surface concentration at time $t=0$, S_{H_2} is the normalized surface concentration expressed as a function of $\frac{X_{C_3H_8}}{X_{t=0}}$ and $\sum R_i$ is the overall reaction rate for the concerned species.

Reactor models

A choice of continuous stirred-tank reactor model (CSTR) [44, 45] was made for the microkinetic simulation in this study. A set of ordinary differential equations (ODEs) are used in modeling the rate of propane conversion (i.e., R), propylene production (i.e., P), and hydrogen production (i.e., H_2) are presented here to understand kinetics involved in the process. The reactor was set to an exit and inlet flowrate, U_o of $0.15 \text{ m}^3/\text{s}$ for the processing of 1 m^3 of propane (V_p) into propylene, while the reactor volume, V_r , was obtained as a function of $n_{feed} N k_B \frac{T_{reactor}}{P_{reactor}}$ and the amount of feed is expressed in the form $V_p \frac{P_o}{RT}$ for propane charged into the reactor.

- *Propane disappearance model.* The prediction model for the propane disappearance rate with time as the reaction progresses is expressed in Equations (8a) and (8b):

$$\frac{dP_{C_3H_8}}{dt} = (1 - \Phi) \frac{n_{feed} RT}{X_o V_r} (-R_{f1} + R_{b1}) + \frac{U_o}{V_r} (P_{C_3H_8,0} - P_{C_3H_8}) \quad (8a)$$

$$\frac{dY_{C_3H_8}}{dt} = \frac{1}{P_{t=0}} \frac{dP_{C_3H_8}}{dt} = (1 - \Phi) \frac{n_{feed} RT}{P_{t=0} X_o V_r} (-R_{f1} + R_{b1}) + \frac{U_o}{V_r P_{t=0}} (P_{C_3H_8,0} - P_{C_3H_8}) \quad (4b)$$

- *Propylene appearance model.* The propylene appearance or production rate is expressed in Equation (9):

$$\frac{dY_{C_3H_6}}{dt} = (1 - \Phi) \frac{n_{feed} RT}{P_{t=0} X_o V_r} (-R_{f5} + R_{b5}) + \frac{U_o}{V_r P_{t=0}} (P_{C_3H_6,0} - P_{C_3H_6}) \quad (9)$$

- *Hydrogen appearance model.* The hydrogen production rate is expressed in Equation (10):

$$\frac{dY_{H_2}}{dt} = (1 - \Phi) \frac{n_{feed} RT}{P_{t=0} X_o V_r} (-R_{f4} + R_{b4}) + \frac{U_o}{V_r P_{t=0}} (P_{H_2,0} - P_{H_2}) \quad (5)$$

where V_r is the reactor volume, U_o is the flow rate, $P_{X,0}$ is the inlet pressure, P_X is the exit pressure for specie X, Φ is the catalyst porosity. $P_{t=0}$ is the initial propane pressure at time $t=0$, Y_{H_2} is the normalized surface concentration expressed as a function of $\frac{P_{H_2}}{P_{t=0}}$ and $\sum R_i$ is the overall reaction rate for the concerned species.

Rate-control analysis

The thermodynamic rate control, X_{TRC} models (at a steady equilibrium constant) [46, 47] in Equations (11) and (12) were employed to analyze the reaction paths to understand the influence of the respective reaction steps and states involved in the reaction.

$$X_{TRC,TS} = \frac{d \ln(R_{C_3H_8})}{d(G_{TS,i}/RT)} \quad (6)$$

$$X_{TRC,IS} = \frac{d \ln(R_{C_3H_8})}{d(G_{IS,i}/RT)} \quad (7)$$

where $R_{C_3H_8}$ is the propylene rate of production, R is the gas constant, G_i denotes the respective energy states, while the production rate is expressed as $\frac{U_o}{V_r} \left(\frac{\Delta P_i}{P_{t=0}} \right)$ in $1/\text{s}$. The model for X_{TRC} employed in this study was adopted from the literature. This analysis would identify the transition state (TS) and intermediate state (IS) greatly influencing the reaction rate, which would have to be explored to improve the catalyst performance.

Effect of temperature, pressure, flow rate and catalyst porosity on the reaction kinetics

The impact of temperature, pressure, flow rate, and catalyst porosity on the dehydrogenation process in the presence of the catalyst was evaluated using the central composite design (CCD) technique within the response surface methodology (RSM) framework. This was done to assess both the individual and interactive effects of the aforementioned factors on the reaction kinetics. The contributions of each factor were reported in percentage terms. Temperature, pressure, flow rate, and catalyst porosity were selected as study variables within a narrow range, where higher yield and selectivity had been previously observed in process simulation studies [31, 32]. These prior simulations evaluated the influence of temperature and pressure on product distribution in the absence of catalyst

effects. The current study used the propylene yield, obtained by solving the models presented earlier in Equations (8–10) using Python, as the response variable.

Statistical evaluation of the selected parameters' effects and contributions to the kinetics of the reaction process

The effects and contributions of the selected parameters like temperature, pressure, porosity, and reactor flowrate were evaluated using the central composite design (CCD) of the response surface methodology (RSM). The investigation was carried out within the following factor levels of 581 to 650 °C for temperature, 0.2 to 1.0 atm for pressure, and 0.15 to 0.20 m^3/s for flow rate, with reference to the previous related studies [31, 32]. As for the porosity, the range of 0.50 to 0.99 was evaluated due to the fact that porosity lower than 0.5 can potentially contribute to mass transfer problem and high pressure drop, according to the literature report [45]. The results obtained from the analysis were compiled and reported.

RESULTS AND DISCUSSION

Kinetic modeling & simulation of propane dehydrogenation

The kinetics of the dehydrogenation process was modeled and simulated in a continuously stirred tank reactor (CSTR) operated for 1200 sec (i.e., 20 min) in the presence of chromium oxide catalyst. The baseline operating conditions were set at 581 °C, 1 atm pressure, with a catalyst porosity of 0.99 and a reactor inlet/outlet flow rate of 0.15 m^3/s . The effects of varying key parameters were investigated:

temperature (400–650 °C), pressure (0.2–1.0 atm), flow rate (0.15–0.20 m^3/s), and porosity (0.50–0.99). The process was modeled to simulate the conversion of 1 m^3 of propane in the reactor, with the reactor volume estimated using the ideal gas law model (nRT/P). The results obtained, including those from the rate-control analysis, are presented in the subsequent sections.

Effect of pressure on the reaction kinetics

The results collected to evaluate the effects of pressure on the reaction kinetics are presented in Figure 3, showing the results collated for pressures of 0.2 and 1.0 atm.

The results indicate that increasing the pressure from 0.2 to 1.0 atm negatively affects the reaction kinetics, as evidenced by the decrease in propane conversion and propylene yield from 71% to 43%, as shown in Figure 3 (production profile). Further analysis of the surface profiles in Figure 3 reveals that the adsorbed propane species (C_3H_8X) remained largely stable for an extended period before the transition point at which the adsorbed hydrogen species (HX) became more stable than the adsorbed propane. However, the stability of adsorbed hydrogen (HX) was observed to be more pronounced at lower pressures and significantly reduced at higher pressures.

Effect of temperature on the reaction kinetics

The results obtained for the temperature's impact on the reaction's kinetics evaluated in the presence of a chromium oxide catalyst are presented in Figure 4, where the production and surface profiles were reported for 400, 581, and 650 °C for a fixed period of reaction time.

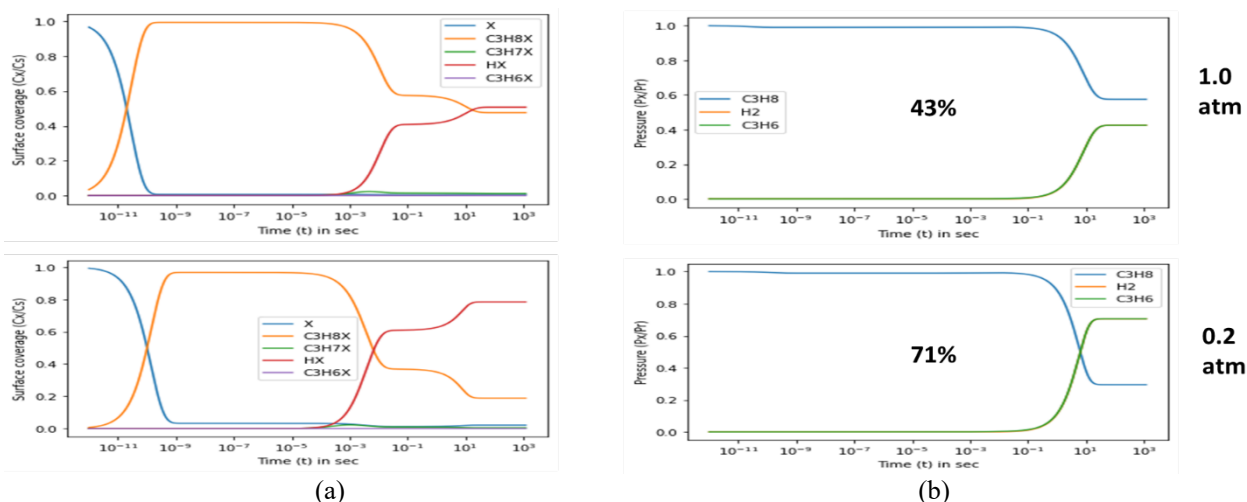


Figure 3. Impact of reaction pressure (from 0.2 to 1 atm) on the reaction kinetics: (a) surface profile for surface species, and (b) production profile for non-surface species.

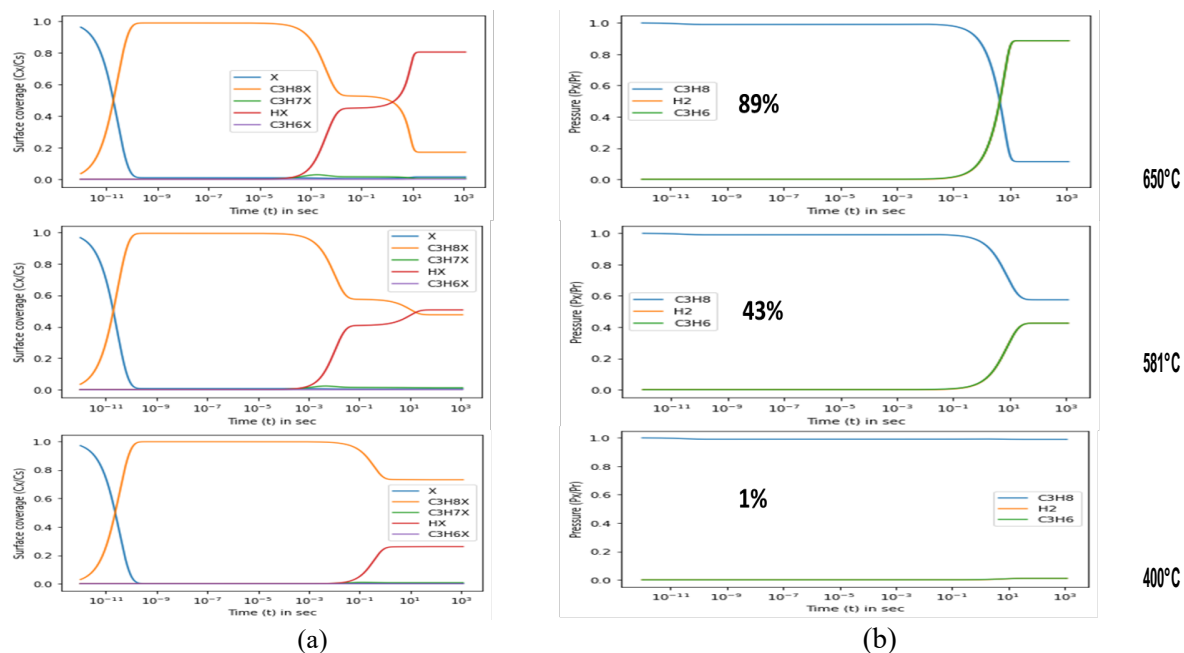


Figure 4. Impact of reaction temperature (from 400 to 650 °C) on the reaction kinetics: (a) surface profile for surface species, and (b) production profile for non-surface species.

The analysis of the results presented in Figure 4, evaluating the effect of temperature on the reaction kinetics, shows that increasing the temperature from 400 °C to 650 °C significantly enhances the propylene yield, rising from 1% to 89%. The yield observed at 400 °C was the lowest among all the temperature levels considered in this study. This suggests that low temperatures are unfavorable for promoting the dehydrogenation reaction, which agrees with values reported in the literature [7,13,48–50], confirming that 550 °C is the minimum temperature favorable for the dehydrogenation of propane to propylene.

Effect of reactor flow rate on the reaction kinetics

The results evaluating the impact of reactor flow rate on the kinetics of propane dehydrogenation to propylene are presented in Figure 5, where both the production and surface profiles were assessed at flow rates of 0.15 and 0.20 m³/s. The analysis indicates that increasing the flow rate in the CSTR from 0.15 to 0.20 m³/s leads to a decrease in propylene yield from 43% to 30%. These findings reveal that a lower flow rate extends the residence time within the reactor, resulting in a higher yield, which is consistent with trends reported in the literature [51, 52].

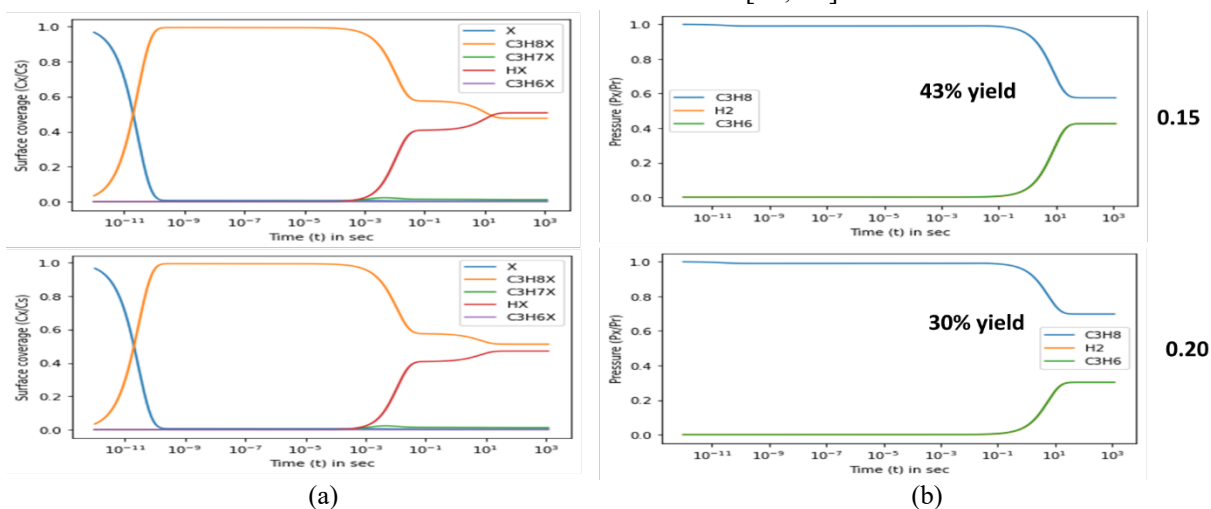


Figure 5. Impact of reactor flow rate (from 0.15 to 0.20 squared meter per second) on the reaction kinetics: (a) the surface profile for surface species, and (b) the production profile for non-surface species.

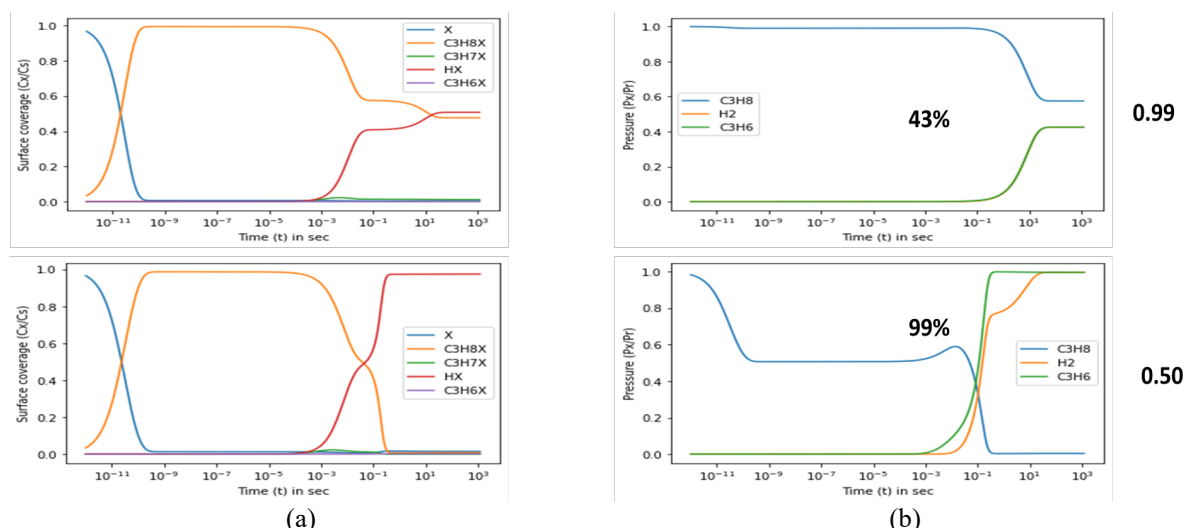


Figure 6. Impact of catalyst porosity (from 0.50 to 0.99) on the reaction kinetics: (a) the surface profile for surface species, and (b) the production profile for non-surface species.

Analysis of the surface profiles reported in Figure 5 unveils that the adsorbed propane (i.e., C_3H_8X) was largely stable. In contrast, the adsorbed hydrogen (i.e., HX) was partially stable for an extended period on the surface profiles before the transition time. Further study of the surface profile confirms that the reactor flow rates' change did not significantly affect the surface profile trend.

Effect of catalyst porosity on the reaction kinetics

The role of the catalyst porosity on the reaction kinetics was investigated. The results collected are presented in Figure 6, where its impacts on the surface reaction activities and production profiles are reported. The results presented in Figure 6 display the impact of the catalyst porosity, where it was deduced that the change in the catalyst porosity from 0.99 to 0.50 has significantly influenced the surface reaction activity and the production profiles. Moreover, it was unveiled that both the adsorbed propane (i.e., C_3H_8X) and the adsorbed hydrogen (i.e., HX) was largely stable for an extended period on the surface profiles. In addition, the production profile indicated that the propane consumption rate became more rapid for the 0.50 porosity compared to 0.99 porosity, with 0.50 porosity displaying higher propylene yield compared to 0.99 porosity which is evident in Figure 6. A better rate reported for the 0.50 porosity was found to have fallen within the acceptable validation value in the literature [53] where values less than 0.7 were said to be acceptable.

Statistical evaluation of the parameter effects on the kinetics

The results obtained for the statistical evaluation of the effect and contribution of the parameters (i.e., temperature, pressure, porosity, and flow rate) are presented in Table 2.

Table 2. Effect and contribution of selected parameters on the reaction kinetics

Parameter	Effect, unitless	Contribution, %
Temperature	0.06256	22.6269
Pressure	-0.02567	9.2835
Porosity	-0.17252	62.3959
Flowrate	-0.01574	5.6937
		100.0000

The result obtained for the contribution of the selected parameters in influencing the production rate are presented in the trend: Porosity (-62.40%) > Temperature (+22.63%) > Pressure (-9.28%) > Flowrate (-5.69%). All the selected parameters were found to have contributed negatively to the production rate except for the temperature, which positively promoted the reaction or production rate. It was also deduced that catalyst porosity and reaction temperature significantly influenced the reaction kinetics compared to other parameters like the pressure and reactor flow rate.

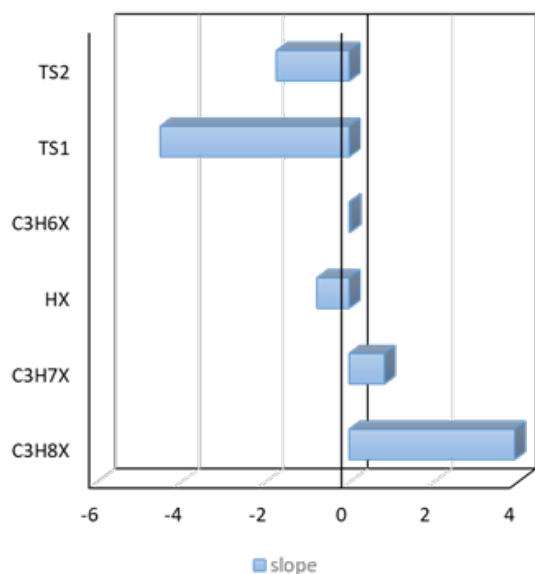


Figure 7. Rate-control analysis profile for the dehydrogenation process steps.

Rate-control analysis

The results of the reaction rate-control analysis for the propane dehydrogenation reaction network are presented in Figures 7 and 8, showing the impact of each reaction step on the overall kinetics. The findings indicate that the order of rate-control contribution follows the trend: TS1 (first hydrogen abstraction transition state) > C₃H₈X (adsorbed propane) > TS2 (second hydrogen abstraction transition state) > C₃H₇X (adsorbed propyl) > HX (adsorbed hydrogen) > C₃H₆X (adsorbed propylene). Among all the evaluated intermediates and transition states, TS1 exhibited the highest influence, confirming it as the rate-controlling transition state (RC-TS). Similarly, C₃H₈X was identified as the most influential intermediate, designating it as the rate-controlling intermediate state (RC-IS). The identification of TS1 as the RC-TS is consistent with literature reports [17, 54, 55], where the first hydrogen abstraction step was also found to be rate-limiting in studies involving platinum-based catalysts. These key rate-controlling steps—particularly TS1, which had the highest overall impact—should be the primary targets for improving the reaction rate, independent of thermodynamic considerations.

CONCLUSIONS

A micro-kinetic modeling approach was employed in modeling and simulating the kinetics involved in the dehydrogenation process, which was done with a Python-based micro-kinetic code. The

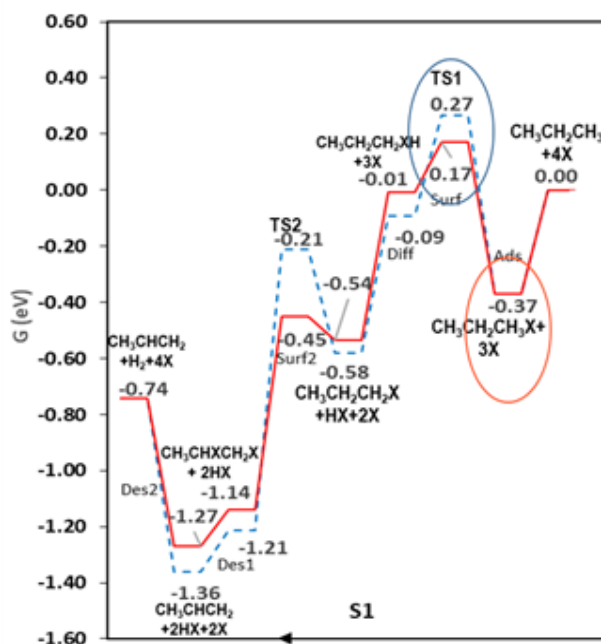


Figure 8. The key reaction state influencing the reaction rate [26].

results obtained from parametric studies unveil that an increase in reactor flow rate, pressure, and porosity reduces the reaction kinetics. Moreover, the rise in temperature increases the reaction kinetics which confirms the overall reaction to be endothermic, where the impact (i.e., the contribution) of the reactor flow rate, pressure, porosity, and temperature were found to be 5.69, 9.28, 62.40, and 22.63 %, respectively. While the rate control analysis results indicated that among all the intermediate and transition states evaluated, the TS1 (i.e., 1st hydrogen abstraction TS) was identified to have shown the TS with the highest impact, confirming it to be the rate-controlling transition state (RC-TS). At the same time, the C₃H₈X (i.e., adsorbed propane) was found to be the intermediate state with the highest impact, which confirms C₃H₈X, the adsorbed propane, to be the rate-controlling intermediate state (RC-IS). Therefore, among the identified RC-TS and RC-IS, RC-TS was found to have shown the highest impact among all reaction states evaluated, which implies that it would be the most critical reaction state that would significantly have to be used for improving the rate of the reaction outside the potential contributions obtainable from the change in the reaction thermodynamic conditions.

The study, therefore, suggests the improvement of catalyst porosity and possibly impregnation or introduction of catalyst promoters or any other metals [14, 55, 56] to the catalyst surface as a means which would potentially improve the reaction rate

and selectivity outside the potential contributions obtainable from the change in the reaction thermodynamic conditions.

REFERENCES

1. M. Martino, E. Meloni, G. Festa, V. Palma, S. Wacławek, D. Dion, D. Dionysiou, A. Kudelski, J. A. Lauterbach, *Catalysts*, **11**, 1070 (2021).
2. X. Liang, Z. Mi, Y. Wu, L. Wang, E. Xing, *Reaction Kinetics and Catalysis Letters*, **80** (2), 207 (2003).
3. B. M. Lipinski, L. S. Morris, M. N. Silberstein, G. W. Coates, *J. Am. Chem. Soc.*, **142**, 6800 (2020).
4. Z. Gholami, F. Gholami, Z. Tışler, M. Tomas, M. Vakili, *Energies*, **14**, 1089 (2021).
5. A. Farshi, F. Shaiyegh, S. H. Burogerdi, A. Dehgan, *Pet. Sci. Technol.*, **29**, 875 (2011).
6. D. Christopher, *Digital Refining Processing, Operations & Maintenance Report*, PTQ Publication, 2013.
7. J. J. Sattler, J. Ruiz-Martinez, E. Santillan-Jimenez, B. M. Weckhuysen, *Chem Rev*, **114**, 10613 (2014).
8. T. Oyegoke, F. N. Dabai, A. Uzairu, B. Y. Jibril, *Hittite Journal of Science & Engineering*, **7**, 297 (2020).
9. A. Benzaouak, H. Mahir, A. Hamidi, M. Kacimi, L. F. Liotta, *Catalysts*, **12**, 811 (2022).
10. S. K. Matam, C. Moffat, P. Hellier, M. Bowker, I. P. Silverwood, C. R. A. Catlow, J. S. David, J. Craswell, P. P. Wells, S. F. Parker, E. K. Gibson, *Catalysts*, **10**, 1370 (2020).
11. A. Zubkov, T. Bugrova, M. Salaev, G. Mamontov, *Crystals*, **11**, 1435 (2021).
12. L. Wang, G. Q. Yang, X. Ren, Z. W. Liu, *Nanomaterials*, **12**, 417 (2022).
13. W. Zhang, H. Wang, J. Jiang, Z. Sui, Y. Zhu, D. Chen, X. Zhou, *ACS Catal.*, **10**, 12932 (2020).
14. R. Zhang, Q. Y. Chang, F. Ma, M. Zeeshan, M. L. Yang, Z. J. Sui, D. Chen, X. G. Zhou, Y. A. Zhu, *Chemical Engineering Journal*, **446**, 136913 (2022).
15. T. Oyegoke, F. N. Dabai, A. Uzairu, B. Y. Jibril, *Bayero Journal of Pure and Applied Sciences*, **11**, 178 (2019).
16. C. F. Li, X. Guo, Q. H. Shang, X. Yan, C. Ren, W. Z. Lang, Y. J. Guo, *Ind. Eng. Chem. Res.*, **59**, 4377 (2020).
17. Q. Li, Z. Sui, X. Zhou, D. Chen, *Appl. Catal. A, Gen.*, **398**, 18 (2011).
18. T. K. Katranas, A. G. Vlessidis, V. A. Tsiatouras, K. S. Triantafyllidis, N. P. Evmiridis, *Microporous and Mesoporous Materials*, **61**, 189 (2003).
19. T. Saelee, S. Namuangruk, N. Kungwan, A. Junkaew, *Journal of Physical Chemistry C*, **122**, 14678 (2018).
20. D. Akporiaye, S. F. Jensen, U. Olsbye, F. Rohr, E. Rytter, M. Rønnekleiv, A. I. Spjelkavik, *Ind. Eng. Chem. Res.*, **40**, 4741 (2021).
21. J. H. Yun, R. F. Lobo, *J. Catal.*, **312**, 263 (2014).
22. J. Schäferhans, S. Gómez-Quero, D. V. Andreeva, G. Rothenberg, *Chemistry - A European Journal*, **17**, 12254 (2011).
23. M. L. Yang, Y. A. Zhu, X. G. Zhou, Z. J. Sui, D. Chen, *ACS Catal.*, **2**, 1247 (2012).
24. J. Liu, Y. Liu, Y. Ni, H. Liu, W. Zhu, Z. Liu, *Catal. Sci. Technol.*, **10**, 1739 (2020).
25. T. Oyegoke, F. N. Dabai, A. Uzairu, B. Y. Jibril, *Journal of the Serbian Chemical Society*, **86**, 44 (2021).
26. T. Oyegoke, F. N. Dabai, A. Uzairu, B. Y. Jibril, *European Journal of Chemistry*, **11**, 342 (2020).
27. E. E. Peter, T. Oyegoke, A. Y. Atta, A. Uzairu, B. O. Aderemi, B. Muktar, B. Y. Jibril, Computational Design of Metal-Exchanged ZSM-5 Catalyst For Propane Dehydrogenation, *International Conference on Theoretical Aspects of Catalysis*, June 13-17, 2022.
28. S. Chen, Z. J. Zhao, R. Mu, X. Chang, J. Luo, S. C. Purdy, A. J. Kropf, G. Sun, C. Pei, J. T. Miller, X. Zhou, E. Vovk, Y. Yang, J. Gong, *Chem.*, **7**, 387 (2021).
29. C. F. Li, X. Guo, Q. H. Shang, X. Yan, C. Ren, W. Z. Lang, Y. J. Guo, *Ind. Eng. Chem. Res.*, **59**, 4377 (2020).
30. J. Lin, M. Shen, C. Zhang, S. Bi, G. Shen, F. Gao, W. Li, *Chemical Engineering Journal*, **519**, 165243 (2025).
31. T. Oyegoke, F. N. Dabai, S. M. Waziri, A. Uzairu, B. Y. Jibril, *Physical Sciences Reviews*, **9**, 1049 (2024).
32. T. Oyegoke, F. N. Dabai, S. M. Waziri, A. Uzairu, B. Y. Jibril, *Sustainable Chemistry Research*, **1**, 1 (2023).
33. S. Rimaz, L. Chen, S. Kawi, A. Borgna, *Appl. Catal. A, Gen.*, **588**, 117266 (2019).
34. G. Yang, X. Yan, Y. Chen, X. J. Guo, W. Z. Lang, Y. J. Guo, *Appl. Catal. A, Gen.*, **643**, 118778 (2022);
35. M. L. Yang, J. Zhu, Y. A. Zhu, Z. J. Sui, Y. D. Yu, X. G. Zhou, D. Chen, *J. Mol. Catal. A, Chem.*, **395**, 329 (2014).
36. J. Zhang, T. Yu, J. He, J. Chen, G. Wang, Z. Shi, F. Yang, J. Zhao, R. Zhuo, R. Wang, *Molecular Catalysis*, **553**, 113717 (2024).
37. B. B. Li, H. Y. Ma, G. C. Wang, *Langmuir*, **40**, 19043 (2024).
38. H. Y. Ma, G. C. Wang, *Molecular Catalysis*, **563**, 114253 (2024).
39. T. H. Kim, K. H. Kang, M. Baek, J. H. Song, U. G. Hong, D. S. Park, W. C. Choi, Y. K. Park, I. K. Song, *Molecular Catalysis*, **433**, 1 (2017).
40. L. H. Sprowl, C. T. Campbell, L. Árnadóttir, *Journal of Physical Chemistry C*, **120**, 9719 (2016).
41. C. T. Campbell, L. H. Sprowl, L. Árnadóttir, *Journal of Physical Chemistry C*, **120**, 10283 (2016).
42. L. H. Sprowl, C. T. Campbell, L. A. Rnadóttirnadóttir, *Journal of Physical Chemistry C*, **121**, 9655 (2016).
43. I. A. W. Filot, Introduction to Microkinetic Modeling, Technische Universiteit Eindhoven, 2018.
44. S. Fogler, Essentials of Chemical Reaction Engineering, Prentice Hall, 2010.
45. M. E. Davis, R. J. Davis, Fundamentals of Chemical Reaction Engineering, Dover Publications, 2013.
46. C. T. Campbell, *ACS Catal*, **7**, 2770 (2017).

47. C. Stegelmann, A. Andreasen, C. T. Campbell, *J. Am. Chem. Soc.*, **131**, 13563 (2009).
48. T. Otroshchenko, G. Jiang, V. A. Kondratenko, U. Rodemerck, E. V. Kondratenko, *Chem. Soc. Rev*, **50**, 486 (2021).
49. W. Wannapakdee, T. Yutthalekha, P. Dugkhuntod, K. Rodponthukwaji, A. Thivasasith, S. Nokbin, T. Witoon, S. Pengpanich, C. Wattanakit, *Catalysts*, **9** (2), 174 (2019).
50. N. Raman, S. Maisel, M. Grabau, N. Taccardi, J. Debuschewitz, M. Wolf, H. Wittkämper, T. Bauer, M. Wu, M. Hauman, C. Papp, A. Görling, E. Spiecker, J. Libuda, H. P. Steinrück, P. Wasserscheid, *ACS Catal.*, **9**, 9499 (2019).
51. I. M. Mándity, S. B. Ötvös, F. Fülöp, *ChemistryOpen*, **4**, 212 (2015).
52. G. Laudadio, N. J. W. Straathof, M. D. Lanting, B. Knoops, V. Hessel, T. Noël, *Green Chemistry*, **19**, 4061 (2017).
53. Purdue, Gradient Check for Heterogeneous Catalysis Purdue University, 2016.
54. A. W. Hauser, P. R. Horn, M. Head-Gordon, A. T. Bell, *Physical Chemistry Chemical Physics*, **18**, 10906 (2016).
55. T. Oyegoke, F. N. Dabai, S. M. Waziri, A. Uzairu, B. Y. Jibril, *Kemija u industriji*, **71**, 583 (2022).
56. N. F. Kalantari, M. Bekheet, K. N. P. Delir, J. O. Back, A. Farzi, S. Penner, N. Delibaş, S. Schwarz, J. Bernardi, D. Salari, A. Niaei, *Journal of Industrial and Engineering Chemistry*, **111**, 168 (2022).

Modeling of blood flow in a stenotic artery using nanoparticles

Priyanshu, M. M. Mandal*

University School of Chemical Technology, Guru Gobind Singh Indraprastha University, New Delhi – 110078, India

Received: July 15, 2024; Revised: September 29, 2025

In recent years, investigations have been conducted to understand the influence of nanoparticles on blood flow *via* stenosed arteries. The purpose of the present study was to investigate the hydrodynamics and heat transfer of blood flow carrying metallic nanoparticles through a stenotic artery. A computational fluid dynamics study was conducted using COMSOL Multiphysics software to solve the governing equations with appropriate boundary conditions and thermophysical models. Different viscous models were applied and compared to model the viscosity of blood flow. The blood flow velocity, shear stress, and temperature contours of the stenotic artery were investigated for different dimensions. The magnetic field's impact on blood flowing through stenosis is reported here. The findings suggest that the effect of the viscous model for blood could be significant for arteries with smaller sizes. Applying a magnetic field to the stenosis resulted in reduced fluid velocity and higher shear stress near the wall in arteries with smaller dimensions. This model can help screen different anti-angiogenic drugs used in the treatment of stenotic arteries. The present study can further benefit the design of a technology for drug delivery in stenotic arteries using drugs with magnetic properties.

Keywords: Computational fluid dynamics, stenotic artery, nanoparticle, magnetic field, viscosity

INTRODUCTION

Arterial stenosis, also known as blood artery narrowing, is a serious medical condition that can result in cardiovascular illnesses. Arterial diseases, such as arterial stenosis, obstruct blood flow and impact blood pressure, contributing to cardiovascular complications. This progressive disease affects a significant number of individuals, particularly those aged 75 and above. In India, even those marginally older than 45 years of age have a significant prevalence of cardiovascular illnesses [1]. Arterial stenosis, characterized by narrowing of arteries, poses a serious threat and is a leading cause of mortality in both underdeveloped and developed countries. Its causes, symptoms, and complications are well-documented. Lipid accumulation in the vascular system might contribute to the progression of stenosis in blood vessels. Lesions in the arteries can result from the formation of stenosis, which narrows the blood vessels. The circulatory system relies on blood vessels to transport oxygen and nutrients, and remove waste products, making blood flow dynamics crucial in the development and progression of cardiovascular diseases. Significant changes to the flow characteristics within the arteries can be caused by stenosis and aneurysms. One of the severe consequences of arterial stenosis is increased resistance and reduced blood flow through the affected artery.

For the development of efficient therapeutic approaches, it is essential to comprehend the flow properties and heat transfer processes within stenotic arteries. Various researchers have focused on studying arterial diseases using different methods. Recent studies have explored the incorporation of nanomaterials in base fluids. Several theoretical studies have also been carried out to comprehend how the concentration of nanoparticles affects blood flow through stenosed arteries [2–6]. A particular kind of fluid called a nanofluid has nanoparticles that have been carefully engineered (size varying from 1 to 100 nm) and dispersed in a fluid medium. Nanomaterials such as carbon in different forms, metals, and nanostructures are often utilized in nanofluids. Researchers have used nanoparticles for enhancing heat transfer, studying blood flow through stenoses, and analyzing two or three-dimensional flow models [2–5]. It has been demonstrated that the use of nanofluids, which are fluids containing metallic nanoparticles, can improve heat transfer efficiency in a variety of applications. Various nanoparticles have several applications in diagnostics and treatment of cardiovascular diseases, offering improved treatment strategies and targeted delivery into arteries based on their physical properties, such as shape, surface, and size modifications. Nanoparticles like silver and gold are particularly significant in nanomedicine, serving as drug carriers, photovoltaic agents, and contrast

* To whom all correspondence should be sent:
E-mail: monishamridha1@ipu.ac.in

agents [2, 3, 7]. Their unique properties make them attractive for biomedical diagnosis and treatment. Applications for gold nanoparticles in biomedicine are numerous and include targeted drug delivery, immunological modulation, diagnostics, therapies, gene delivery, cancer treatment, and prosthetics. Silver nanoparticles are also gaining importance in the fields of visual imaging, medicinal sciences, catalysis, anti-angiogenic drugs, etc. [7]. Given their unique physicochemical characteristics, simple synthesis and characterization, variable shape and size, and biocompatibility, biologically produced silver nanoparticles are one of the most attractive choices in biomedical research.

Magnetic field has been shown to have a significant impact on the biological fluids present in all living organisms [9, 10]. Owing to haemoglobin presence, the blood is magnetically responsive. The paramagnetic properties of blood are due to the presence of Fe^{++} chains in deoxygenated haemoglobin [11]. When blood is exposed to an external magnetic field, it experiences both Lorentz and magnetization forces. Blood viscosity can be impacted by magnetic fields, particularly at higher levels [12]. Due to the increased apparent viscosity of blood caused by the magnetic field, it has been observed that the blood flow rate has decreased [13].

Studies of partially blocked arteries have shown that a magnetic field does not always decrease blood velocity; the effect varies depending on the direction of the applied magnetic field, with some orientations generating acceleration and others slowing down [14–16]. According to a study that developed a mathematical model treating blood as a Newtonian fluid, the dimensionless velocity magnitude is significantly reduced in a stenotic channel when a magnetic field is applied perpendicular to the direction of flow. Several researchers have investigated the combined effect of nanofluid flow under a magnetic field in arteries [6, 8, 9]. Elelamy *et al.* investigated the temperature distribution, slip effects, and blood flow with nanofluids in a heart valve. They observed that there can be a reduction in vascular resistance when the heart valve prosthesis induces a magnetic field. Vascular resistance values enhance the concentration of antibiotics and other compounds that can infiltrate bacteria. It has been found that as the magnetic field intensity increases, the temperature rises, and the velocity of the nanofluid decreases [17]. The strong, broad-spectrum antibacterial qualities of silver nanoparticles are enhanced by their large surface area due to particle size and capacity to release silver ions, making them useful against harmful bacteria, fungi, and viruses. They are also helpful in wound

healing, drug delivery, tissue engineering, and as parts of medical devices and diagnostic instruments, owing to their anti-inflammatory, anti-cancer, and anti-angiogenic properties [18]. Silver nanoparticles are utilized in stenosis applications, including airway stents and endodontic treatments. They prevent infections and inflammation that lead to stenosis by releasing silver ions, which harm internal biological components, including proteins and DNA, and break down bacterial cell walls. Silver nanoparticles' anti-hyperplastic qualities also lessen the development of granulation tissue, which can lead to stenosis. Further, when dispersed to create nanofluids, silver's high thermal conductivity ($429 \text{ W/m}\cdot\text{K}$ at ambient temperature) greatly improves the fluids' thermal characteristics and facilitates heat transfer, thus controlling the temperature of the blood flow. Hence, silver nanoparticles were considered for the present study. Since silver is a non-ferromagnetic substance, it lacks the inherent magnetic properties necessary to be drawn to a magnet. Silver nanoparticles in their original state do not respond to magnetic fields. However, by functionalizing with superparamagnetic elements like iron oxides, which create a transient magnetic response without permanently magnetizing the silver, these nanoparticles can be made responsive to magnetic fields [19].

The application of nanocomposites in treating vascular disorders is limited, and the use of silver nanoparticles in treating arterial diseases is still in the developmental stage. Therefore, the goal of the current investigation was to investigate the hydrodynamics of silver nanoparticles in blood flowing through a carotid stenosis artery. In this study, a mathematical model was developed to analyze the characteristics of blood flow with silver nanoparticles when artery stenosis is present. The simulation considered a 2D artery with a cosine-shaped stenosis, and the dimensions, as well as the initial conditions, were defined. The effect of different dimensions, magnetic field, and viscous models on the hydrodynamics of the nanofluid was investigated. Velocity distributions, shear stress contours, magnetic field, and temperature distributions of the nanofluid were obtained and reported here.

MATERIALS AND METHODS

The COMSOL Multiphysics software was used to numerically solve the Navier-Stokes equations to account for continuity, energy, and momentum conservation of the flow of blood with nanoparticles. Based on existing literature data, the shape of the stenotic artery was created, and the suitable

boundary conditions were applied [7]. For validation of the model with literature data, blood was assumed to flow through a stenosed artery as an incompressible Newtonian fluid. The equations for the fluid flow, heat convection, and conduction phenomena in conjunction with the suitable boundary conditions were computed. The continuity equation is:

$$\frac{1}{r} \frac{\partial}{\partial r} (ru) + \frac{\partial}{\partial z} (w) = 0 \quad (1)$$

$$\rho \nabla \cdot u = 0 \quad (2)$$

where w and u correspond to the nanofluid's velocities in the z and r directions, respectively. In the present study, the Eulerian-Eulerian multiphase modeling approach was used, which treats the phases as interpenetrating continua with a no-slip condition assumed between them. In the Mixture model for nanofluid flow, nanoparticles were assumed to have the same velocity as the base fluid.

The governing momentum equation was computed as:

$$\rho(u_t + uu_r + ww_z) = -P_r + \partial_z(w_r - u_z)\mu \quad (3)$$

$$\rho(w_t + uw_r + ww_z) = -P_r - \left(\partial_r + \frac{1}{r}\right)(w_r - u_z)\mu \quad (4)$$

The equations can be written as:

$$\rho(u \cdot \nabla u) = \nabla \cdot [-PI + K] + F \quad (5)$$

$$K = \mu(\nabla u + (\nabla u)^T) \quad (6)$$

where μ and ρ represent the nanofluid's viscosity and density, respectively, P is the pressure, and I is the identity tensor.

The equation to calculate the wall shear stress (WSS) is given as [20]:

$$WSS = \mu \times \frac{\delta u}{\delta x}$$

The governing heat transfer equation was computed as:

$$(\rho C_p) \left(\frac{\partial}{\partial t} + u \frac{\partial}{\partial r} + w \frac{\partial}{\partial z} \right) T = k \left(\frac{\partial^2}{\partial r^2} + \frac{\partial}{r \partial r} + \frac{\partial^2}{\partial z^2} \right) T \quad (7)$$

$$d_z \rho C_p \frac{\partial T}{\partial t} + d_z \rho C_p u \cdot \nabla T + \nabla \cdot q = d_z Q + q_o + d_z Q_p + d_z Q_{vd} \quad (8)$$

where $q = -d_z k \nabla T$; $q_o = \frac{q}{A_s \Delta T}$; $Q_{vd} = \tau \cdot \nabla u$; $Q_p = \alpha_p T \left(\frac{\partial P}{\partial t} + u \cdot \nabla P \right)$; $\alpha_p = -\frac{1}{\rho} \frac{\partial P}{\partial t}$; $\tau = -PI + K$; d_z is the thickness of the fluid; Q is the heat source; Q_{vd} is the viscous dissipated heat source; ∇T shows the temperature gradient; C_p is the specific heat; and k is the thermal conductivity of the nanofluid. The initial values considered are:

$$T = T_o \text{ and } P = 0 \quad (9)$$

The thermophysical properties of the nanofluids are defined as follows [21, 22]:

$$\left. \begin{aligned} \rho &= \rho_f \left[(1 - \phi) + \phi \left(\frac{\rho_s}{\rho_f} \right) \right] \\ \mu &= \frac{\mu_f}{(1 - \phi)^{2.5}} \\ (\rho C_p) &= (\rho C_p)_f \left[1 - \phi + \phi \frac{(\rho C_p)_s}{(\rho C_p)_f} \right] \\ \frac{k}{k_f} &= \frac{k_s + (s-1)k_f - (s-1)\phi(k_f - k_s)}{k_s + (s-1)k_f + \phi(k_f - k_s)} \end{aligned} \right\} \quad (10)$$

where ϕ is the volume fraction of the dispersed phase, silver nanoparticles; μ_f is the viscosity of the fluid (blood); ρ_f is the continuous phase (blood) density; ρ_s is the discrete phase (silver nanoparticles) density; k_f is the thermal conductivity of the fluid (blood); k_s is the thermal conductivity of the solid nanoparticles; $(\rho C_p)_s$ is the heat capacity of the solid nanoparticles; $(\rho C_p)_f$ is the heat capacity of the fluid.

Magnetic field

To determine the effect of the magnetic field, an AC/DC module in COMSOL Multiphysics was used. The formulae for the Ampere-Maxwell equation that were used to calculate the static magnetic field are as follows [23]:

$$\nabla \times \bar{H} = \bar{J} \quad (11)$$

The magnetic flux density using Gauss's law is:

$$\nabla \cdot B = 0 \quad (12)$$

Here, H is the strength of the magnetic field; B represents the magnetic flux density.

The relationship between B and H , provided by the following formulas, can be used to characterize the magnetic flux density for stenotic domains:

$$\bar{B} = \mu_0 (\bar{H} + \bar{M}_b(H)) \quad (13)$$

where μ_0 is the magnetic permeability of blood; the blood stream's magnetization vector (A/m) is defined as $M_b(H)$, and it depends on the magnetic field, H .

The body force acting on a fluid flow was calculated using Maxwell's electromagnetic equation. The Magnetic Fields, No Currents, Boundary Elements interface in COMSOL Multiphysics was employed to compute magnetostatic fields from permanent magnets and other current-free magnetic sources. The physics interface solves Gauss' Law for the magnetic field using the scalar magnetic potential as the dependent variable. Stress tensors under the influence of magnetic fields were computed using Maxwell's

equations of electromagnetic force [24]. Volume forces acting on a body in electromagnetic fields were included to estimate electromagnetic forces. τ_{xx} and τ_{yy} are the typical stress tensors operating in the x and y axes, respectively. The shear stress tensors in the x and y directions were taken to be $\tau_{xy} = \tau_{yx}$ for a fixed-volume system. The divergence of the stress tensors yields the volume force throughout the body. For blood flow in the arterial channel, eq. 18 calculates the magnetic forces F_x and F_y in the x and y directions, respectively. These forces show up in the Navier-Stokes equations as volume forces F and are coupled with Gauss' Law.

$$T_{xx} = \frac{1}{2\mu_0\mu_r}(B_x^2 - B_y^2) \quad (14)$$

$$T_{yy} = \frac{1}{2\mu_0\mu_r}(B_y^2 - B_x^2) \quad (15)$$

$$T_{xy} = T_{yx} = \frac{1}{\mu_0\mu_r}(B_x B_y) \quad (16)$$

The stress tensor is written as:

$$T = \begin{bmatrix} T_{xx} & T_{xy} \\ T_{yx} & T_{yy} \end{bmatrix} \quad (17)$$

The volume force was calculated using the equation:

$$F = \nabla \cdot T \quad (18)$$

Boundary conditions

The boundary conditions were set at the inlet, outlet, and wall in the laminar flow module of COMSOL Multiphysics software. The velocity and area of the inflow passage were utilized to control the blood volume. The boundary condition for the inlet was as follows [7]:

$$u(r, z, t) = -u_0 n$$

The location of the outlet was where the blood left the artery and was located across from the entrance. A solution of the governing equations was obtained at the outlet. The following was the outlet's boundary condition:

$$\tau n = -p n,$$

where $p = p_0$, the absolute pressure was $p_0 = 0$ and $\mathbf{n} = (\mathbf{n}_r, \mathbf{n}_z)$ was the normal outflow velocity.

The no-slip condition was set at the wall of the artery, which meant that the bulk blood's velocity was zero.

$$u=0, w=0$$

Thermal insulation was used by the following equation using the heat transfer module in the COMSOL software at the inlet and outlet boundaries:

$$n \cdot q = 0$$

It has been reported that treating cardiovascular disorders requires an understanding of heat transport in stenotic arteries since it aids in determining the degree of stenosis, forecasting risks such as ischemic stroke, and directing therapies like targeted drug delivery or heat-based therapies [25]. Therefore, in the present study, different temperatures were considered on the top wall and lower wall as an initial condition to understand the effect of the heat transfer mechanism on the blood flow. This helped to understand the changes in temperature around the specific location within an artery, especially around the plaque. The initial temperature of blood was considered as 293.15 K. Temperature was 297.15 K at the top boundary wall, whereas it was considered 300.15 K at the bottom boundary wall. In computational fluid dynamics (CFD), the quality of the computational mesh is essential. The mesh quality affects both the convergence rate and the precision of the solution. The physical controlled mesh function in COMSOL creates the mesh automatically. When compared to a standard-size mesh, a finer element size mesh typically yields higher performance and more precise outcomes. To find the best mesh needed for the computation, a grid independence test was carried out. The finer mesh option was used in this study and is shown in Fig. 1. The mesh is more refined in the stenosed area and near the wall.

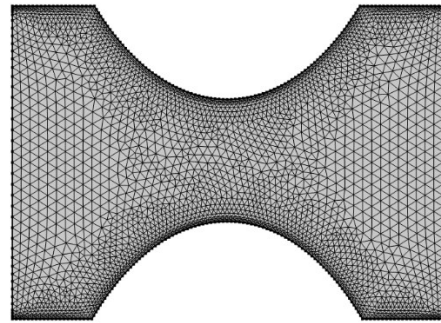


Fig. 1. Mesh of stenotic artery geometry

Consideration was given to the nanofluid's physical and chemical composition, including the characteristics of blood and silver nanoparticles. The computer model takes into account the thermophysical characteristics, including density, thermal conductivity, and specific heat capacity. The different viscous models were used in this study to explore the non-Newtonian effect of blood flow in arteries with different dimensions. The parameters used for modeling the blood dynamic viscosity μ as a function of the strain rate γ in the models employed are as follows [26, 27]:

In the Newtonian model, $\mu = 0.0035$ Pa·s was considered. In the Power law model, $\mu = \mu_0 \gamma^{n-1}$ where $\mu_0 = 0.035$ Pa·s and $n = 0.6$ was used for computation. In the Carreau model, $\mu = \mu_\infty + (\mu_0 - \mu_\infty)[1 + (\lambda\gamma)^2]^{\frac{n-2}{2}}$ where the viscosity at zero shear rate is $\mu_0 = 0.056$ Pa·s, and at high shear rate μ_∞ equals the value for the Newtonian model (i.e., 0.0035 Pa·s) [27]. Additionally, $n = 0.3568$ and $\lambda = 3.313$ s. Using the above methodology, computations were carried out. The following section presents the results obtained from the computations and their analysis.

RESULTS AND DISCUSSION

The artery was first considered with dimensions of 1.1 m long and 0.8 m wide to validate the present model with known data in the literature [7]. The process conditions and dimensions of the artery as reported by Hussain *et al.* (2022) [7] were considered in the present study. Figs. 2 and 3 show the velocity contours and pressure contours computed from the present model, as well as the results of Hussain *et al.* (2022) [7] for the same process conditions and artery dimensions. Fig. 2(a) shows the blood flow velocity from the present computation, whereas Fig. 2(b) shows the blood velocity reported in the literature. The

figure sheds light on the characteristics of blood flow behavior in the stenotic artery region. Maximum blood flow was seen at the stenotic artery, which is indicated by the color red. The blue color near the wall of the artery shows the minimum velocity because of the no-slip condition. The figure shows that the velocity computed from the current model was in good agreement with the literature. Fig. 3(a) shows the pressure variations due to the flow of blood through the stenotic artery obtained from the present computations. This was compared with the result cited in literature and shown here in Fig. 3(b). The pressure contours were found to be minimal at the center of the stenotic artery following the continuity equation. Two circular zones were found near the location of artery expansion. This was due to the reason that when the stenotic artery expands, the blood separates from the artery wall with high velocity, just as a jet. The space between the blood jet and the artery wall could be filled with blood in a vortex motion. This leads to a change in pressure after the blood passes through the contracted zone. The pressure contour from the present computation agreed well with the literature. This showed that the model worked well. Researchers have considered blood as a Newtonian fluid for computations [28].

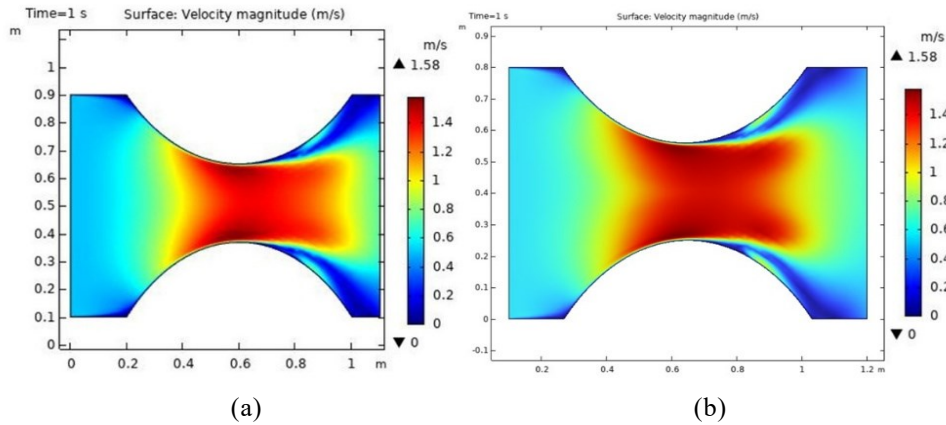


Fig. 2. Velocity in a stenotic artery from (a) present model, (b) ref. [7]

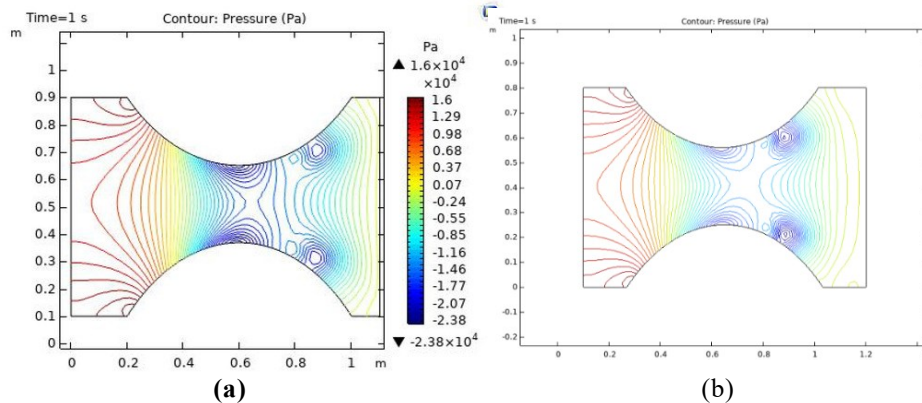


Fig. 3. Pressure contours in a stenotic artery using (a) the present model, (b) ref. [7].

However, this viscous model may not be true for cases of aneurysmal arteries and overestimates the intracranial aneurysm domes' wall shear stress, displaying local flow recirculation and low shear rates [28, 29]. Therefore, different non-Newtonian viscous models, which included the Carreau model and the Power law model, were considered to check their effect in the present study. Fig. 4 shows the

velocity of blood flow with nanoparticles using the different models for a 0.8 m wide artery at different times. The figure shows that the maximum velocity was at the stenosis region at time 0.2 min. In the Newtonian fluid, small peaks in maximum velocity in the core red region could be found after the blood flows through the stenosis region in the downstream.

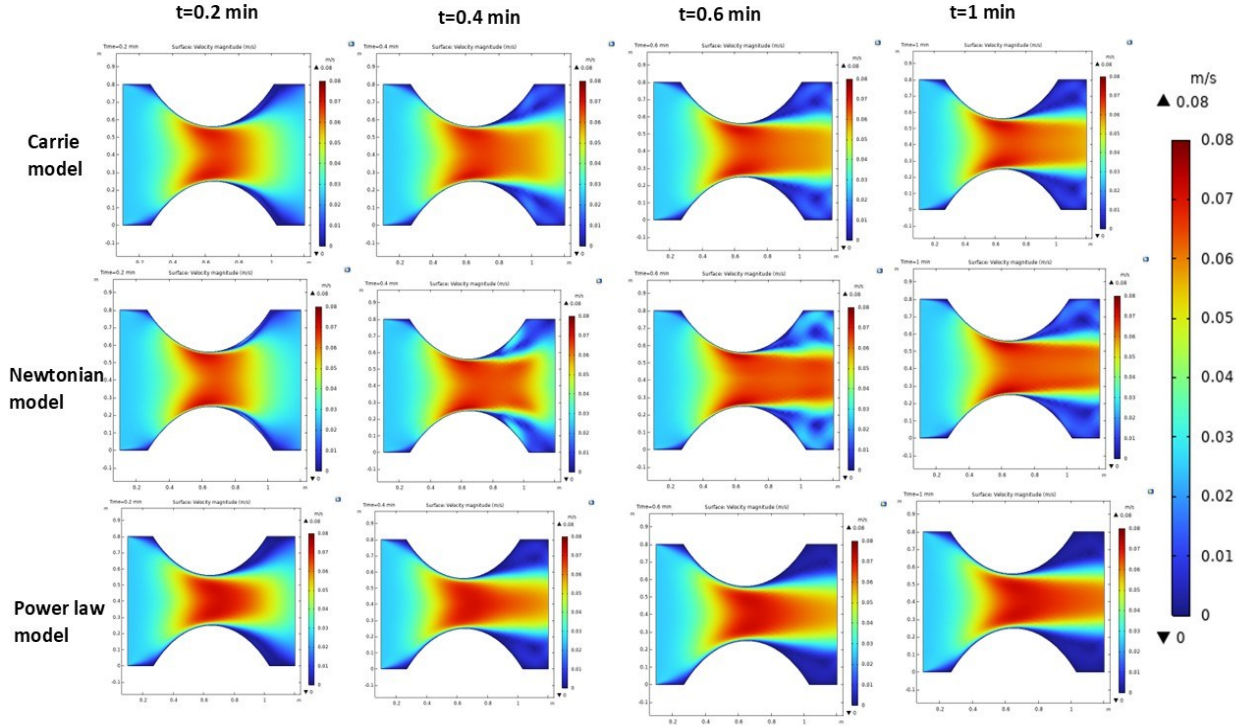


Fig. 4. Velocity in a stenotic artery using different models for $d=0.8$ m, $v=0.025$ m/s

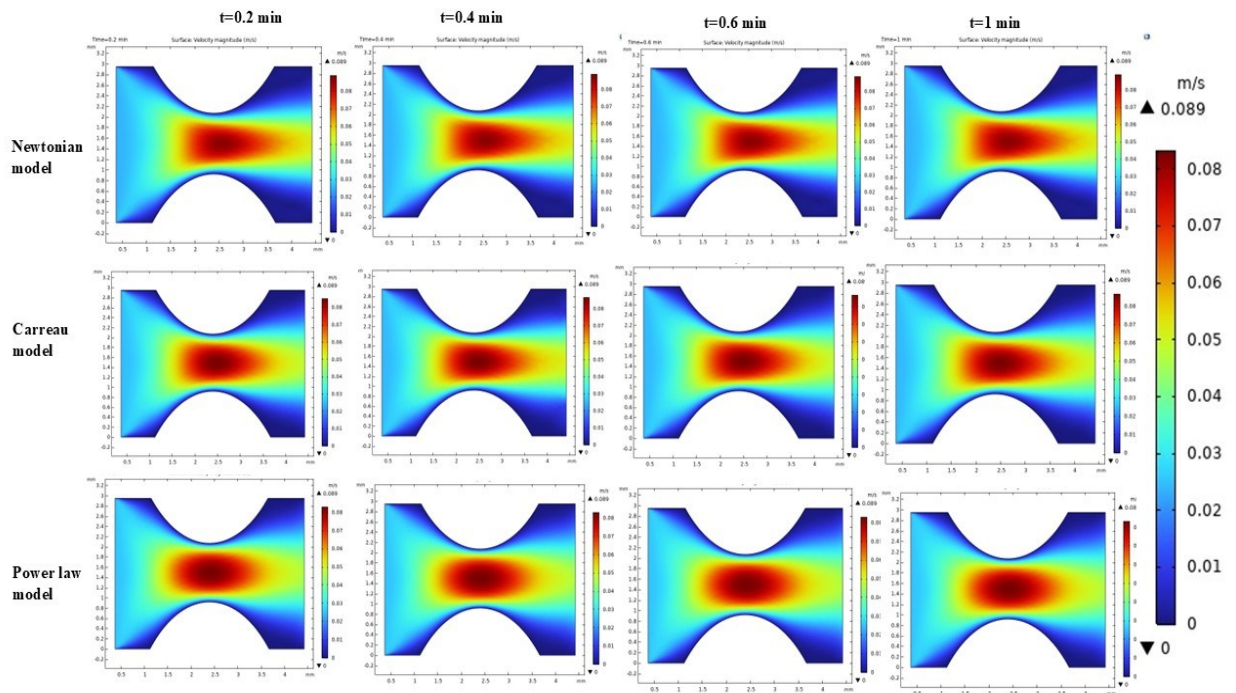


Fig. 5. Velocity in a stenotic artery for $d=0.00295$ m, $v=0.025$ m/s

In the case of the Carreau model and the Power law model, no such peaks were found. The velocity was found to be flatter and parabolic at times $t=0.2$ min and 0.4 min. The maximum velocity stretched out in the downstream of the stenosis with an increase in time. At the downstream region after the stenosis, velocity near the wall was nearly zero in the Power law model at 0.6 and 1 min. Due to the Carreau model's limitation on the viscosity's reduction with increasing strain, the change in velocity is similar to that of a Newtonian fluid. However, for the Power Law model, this is not the case. Fig. 4 clearly shows the developing velocity distribution of blood at different times till 1 min. After 1 min, there was no significant change in velocity. This showed that the blood flow was at steady state at 1 min.

Literature shows that the width of the left coronary artery could be smaller than 8 mm [30, 31]. This is due to branching patterns such as bifurcation and trifurcation of arteries. Therefore, the present model was used to study the artery with a width of 0.00295 m, as shown in Fig. 5. Research using a Newtonian model and presuming that shear rates are consistently higher than 100 s^{-1} can be considered as oversimplification of the blood flow since the instantaneous shear rate in numerous arteries fluctuates from 0 to 1000 s^{-1} over the course of one cardiac cycle [29, 32]. Therefore, different viscous models, such as the Power law model and Carreau model, were applied for blood flow with nanofluids to check the effect on blood flow velocity. It is observed from the figure that the velocity was highest at the center of the stenosis in accordance with the continuity equation and higher than the velocity (depicted in dark red color) in the artery with 0.8 m. The viscous sublayer (in blue color) near the wall was more than that in the artery with

$d=0.8$ m. The maximum velocity in the Power law model was less stretched out in the downstream of the stenotic region as compared to the Newtonian model. This could be due to the characteristic of the Power law model to shear thin because of its viscosity reducing under strain. The Carreau fluid exhibited Power law behavior at high shear rates and Newtonian behavior at low shear rates. It was further observed that there was no change in velocity distribution after 0.2 min for blood flow in an artery with a smaller dimension, $d=0.00295$ m, as shown in Fig. 5. This showed that the steady state was already achieved. It took less time to get to a steady state in an artery with smaller dimensions as compared to a larger artery with $d=0.8$ m.

Effect of the magnetic field

Using nanoparticles in combination with an applied magnetic field has generated a lot of interest as a way to minimize the effects on surrounding tissue while controlling the release and accumulation of drugs in target tissues, because biological tissues respond very little to magnetic fields. When there is a magnetic field present, the magnetophoretic force attracts the particles in the vicinity of the illness site and has sufficient strength to push them into the tissue. To comprehend the contours that resulted from the magnetic field, computations were conducted for the stenosed vessel, as well as the normal vessel having the same boundary conditions. In this study, a magnetic field of 1 T was applied to the stenotic wall. The magnetic field that was applied to the blood flow was perpendicular to the artery axis and permeated the entire artery [33]. The distribution and magnitude of magnetic field strength with and without stenosis of the artery were studied, as illustrated in Fig. 6.

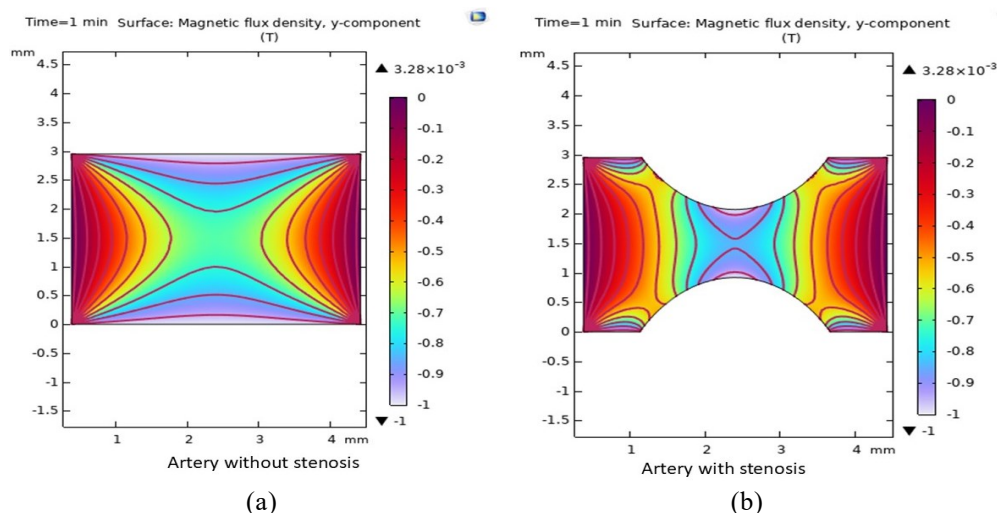


Fig. 6. Distribution of magnetic field in artery (a) without stenosis, and (b) with stenosis at 1 min

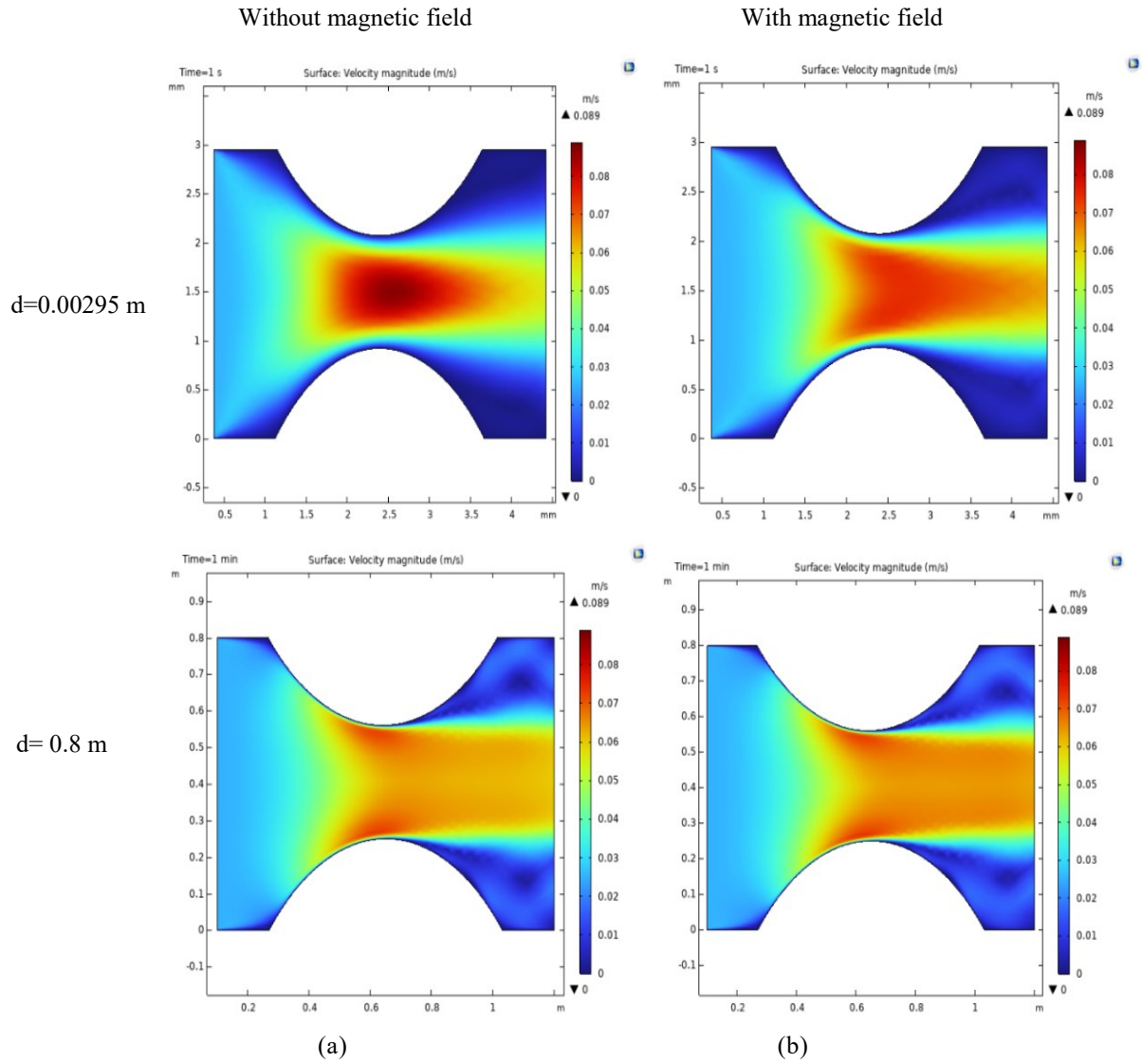


Fig. 7. Velocity of blood (a) without, and (b) with a magnetic field at 1 min.

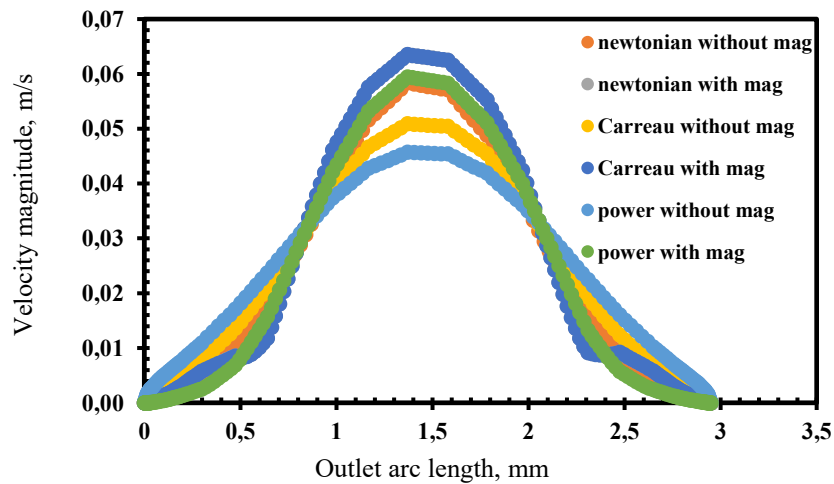


Fig. 8. Velocity profile of blood without and with a magnetic field, for different viscous models

To demonstrate the presence of stenoses and the impact of the magnetic field on the fluid domain, only the fluid domain is displayed. It has been reported that under various fluid flow conditions, the

distribution of the magnetic lines changes significantly depending on the geometry's shape and the fluid's characteristics [24]. The effect of the blockage's dimensions and form on the distribution

of magnetic field lines along the geometry was observed in the present study. It was found that the simulated geometry's decreased cross-sectional area increased the magnetic field's non-uniformity. The magnetic lines got denser in the stenosis zone and near the wall. The wall has the strongest magnetic field, which weakens with distance. As a result, the field is inherently strongest close to the source of the magnetic field, i.e., nearby artery wall. The magnetic field lines converged, close to a constriction. So, a denser magnetic field was produced by this increased concentration of field lines in a restricted area.

Fig. 7 displays the blood velocity for arteries with dimensions $d=0.00295$ m and $d=0.8$ m at 1 min with and without a magnetic field using the Newtonian model. The figure clearly shows that the effect of a magnetic field with 1 Tesla on velocity was more significant for the artery with a smaller width. The dark red color depicting the maximum blood velocity without a magnetic field at the stenotic region of the artery was absent when a magnetic field was used. This showed that the

maximum velocity was reduced when a magnetic field was applied. It has been cited that due to haemoglobin, which contains iron oxide, and the fact that blood is a suspension of red blood cells, it possesses magnetohydrodynamic flow properties and is electrically conductive [34]. In the presence of a magnetic field, a Lorentz force is produced, which opposes the blood motion and so decreases the blood velocity. Fig. 8 shows the comparison of velocity magnitudes along the stenotic width using different viscous models with and without a magnetic field. It can be observed that the velocity was flatter using the Power law model, as the maximum velocity was lower compared to the Newtonian model and Carreau model in the absence of a magnetic field. In the presence of a magnetic field, the maximum velocity decreased for all three models. The velocity magnitude computed with the Carreau model was similar to that of the Power law model in the presence of a magnetic field. However, it was found that the values of the Carreau model were comparable to those of the Newtonian model in the absence of a magnetic field.

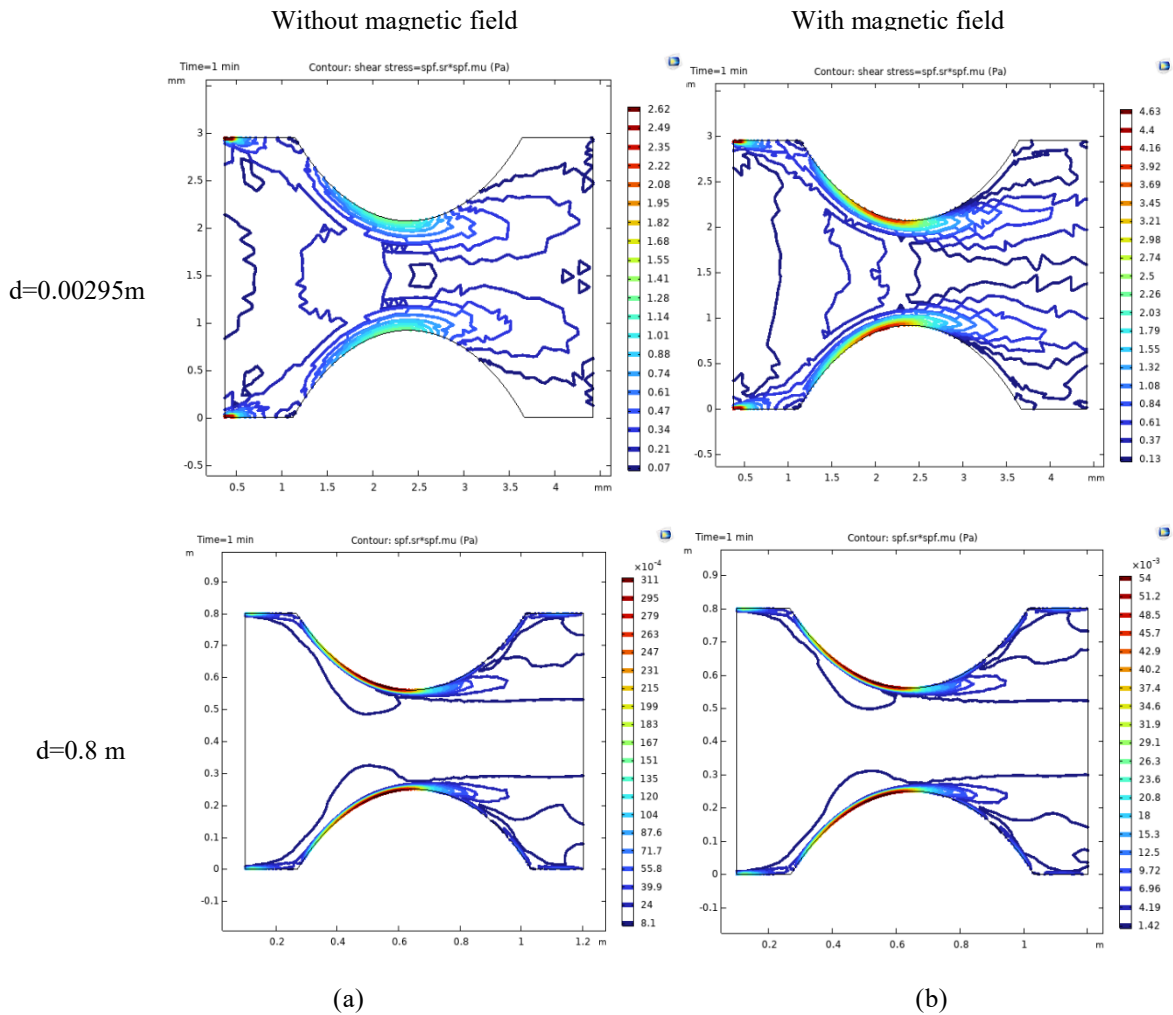


Fig 9. Shear stress of blood (a) without, and (b) with a magnetic field at 1 min

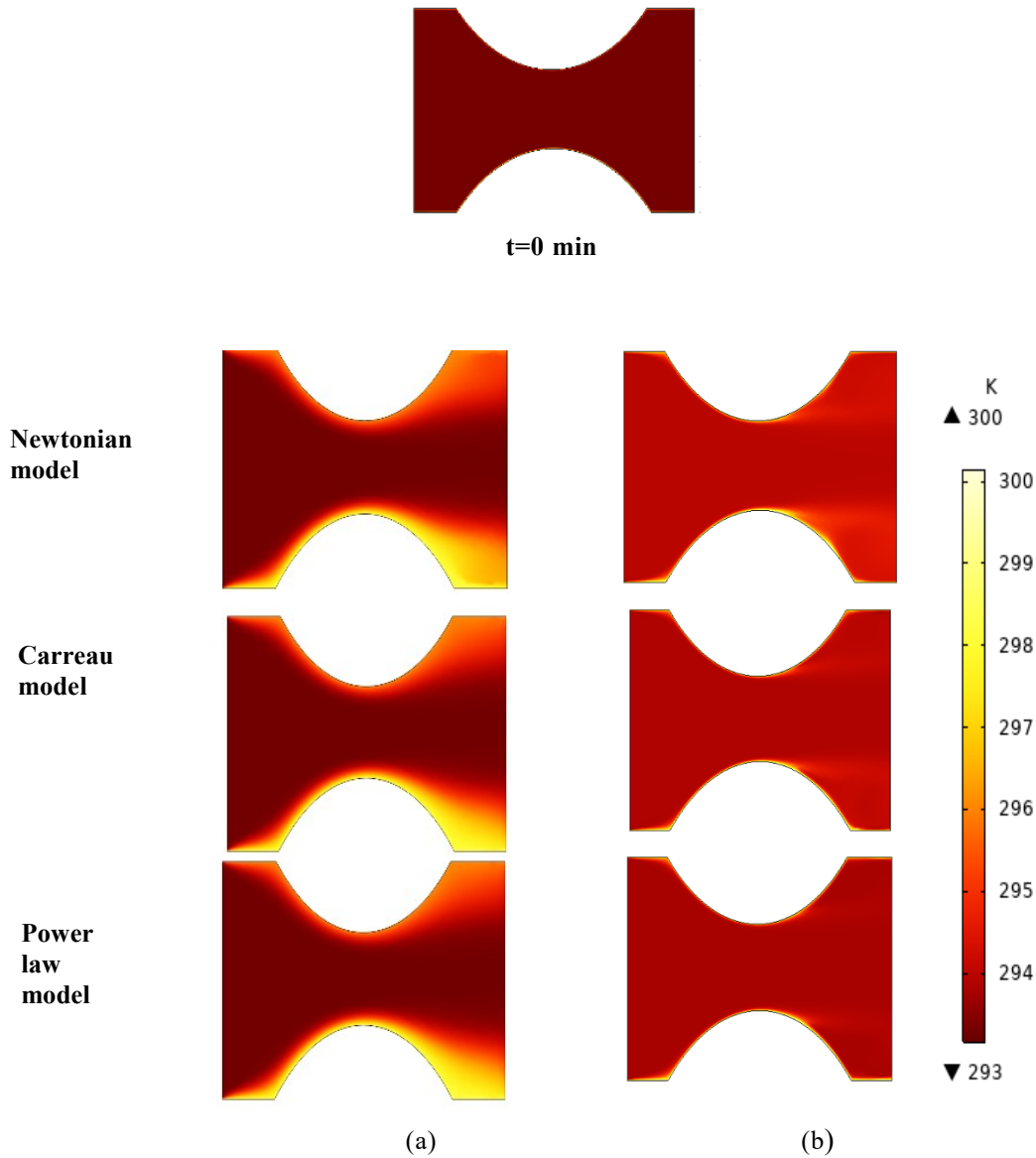


Fig. 10. Temperature in a stenotic artery in (a) $d=0.00295 \text{ m}$, (b) $d=0.8 \text{ m}$ for $v=0.025 \text{ m/s}$, $t=1 \text{ min}$

Fig. 9 shows the shear stress at different arteries with and without a magnetic field. The figure demonstrates that the shear stress near the wall increases with a decrease in dimension. This is due to an increase in the viscous sublayer region in the artery, which was also observed in the velocity distribution in Fig. 5. The highest shear stress was found in the artery with $d=0.00295 \text{ m}$ under a magnetic field in the stenotic region. It has been cited in literature that, parallel to the vorticity of the flow, a magnetic moment usually has little effect on viscosity [35]. However, if the direction of vorticity is perpendicular to the magnetic field, the fixed magnetic moment in the blood can hinder free rotation. The resultant local gradients in the magnetic fluid's velocity raise the magnetic fluid's viscosity [34].

Temperature contours

The artery's radius influences blood flow and changes the rate at which heat is transferred. The effects of surgically enlarging a blocked blood vessel pose a risk to the health of the human body due to changes in blood temperature [35]. Analyzing thermal profiles can reveal problems with blood flow and tissue damage, and changes in the artery's temperature and heat transfer properties can show the course of the disease [25]. Therefore, the temperature distribution for the blood flow with nanoparticles was studied and shown in Fig. 10 for arteries with a width of 0.8 m and 0.00295 m , respectively. At time $t=0$, blood was at 293.15 K , and the top and bottom boundary walls were at temperatures 297.15 K and 300.15 K , respectively. Fig. 10 shows that the color of the blood temperature changed from dark red to a

lighter shade, which indicates that the temperature increased from 293.15 K to a higher value at time $t=1$ min. The distribution of the blood temperature changed with time because of convective heat transfer caused by blood movement and heat conduction from the walls with higher temperatures. For the case of a 0.8 m wide artery, the temperature was found to be higher (yellow color) in the region where the velocity gradient was high at 1 min. However, in the case of an artery with a width of 0.00295 m, the blood near the region of the wall was at a higher temperature (yellow color). In this case, heat transfer was mainly due to heat conduction at the viscous sublayer, where the velocity was low compared to the central region. This shows that the fluid's convective heat transfer may not be the dominant factor for heat transfer in smaller arteries.

CONCLUSIONS

Hydrodynamics and heat transfer of blood flow with silver nanoparticles in a stenotic artery were investigated. The model's findings were in accordance with the existing literature. This study demonstrated the potential significance of the viscous model for smaller arteries. The Carreau fluid exhibited Newtonian behavior at low shear rates and Power law behavior at high shear rates. When a magnetic field was introduced, the maximum velocity decreased, and the shear stress close to the wall increased, particularly for smaller arteries. Heat conduction in the viscous sublayer, where the velocity was lower than in the core region, could be the primary cause of heat transmission in smaller arteries. This model can be used for future studies such as evaluating the long-term effects of hybrid nanofluids on blood flow and heat transfer in stenotic arteries, investigating alternate nanoparticle compositions, and optimizing nanoparticle concentrations. Further research work can be conducted, considering the functionalization of silver nanoparticles with superparamagnetic elements like iron oxides, which can be made responsive to magnetic fields. This would be particularly beneficial in applications such as drug administration, stem cell distribution, and hyperthermia, where it can deliver a therapeutic substance to a target site in the human body, thereby minimizing adverse effects and enhancing therapeutic efficacy.

Acknowledgement: With the financial support of the FRGS grant (F.35(1)(1)/2025/RDC/2975/24), the writers would like to thank Guru Gobind Singh Indraprastha University, New Delhi, for providing

the necessary administrative and financial support to complete this research project.

REFERENCES

1. N. K. Kodali, L. D. Bhat, N. E. Phillip, S. F. Koya, *Indian Heart J.*, **75**(1), 31 (2023).
2. T. Hayat, S. Nadeem, *Results Phys.*, **7**, 2317 (2017).
3. H. Waqas, U. Farooq, A. Hassan, D. Liu, S. Noreen, R. Makki, M. Imran, M.R. Ali, *Results Phys.*, **44**, 106152 (2023).
4. S. Nadeem, S. Ijaz, *AIP Adv.*, **5**, 107217 (2015).
5. S. Nadeem, S. Ijaz, M. A. Sadiq, *Curr. Nanosci.*, **10**(5), 753 (2014).
6. A.F. Elelamy, N.S. Elgazery, R. Ellahi, *Int. J. Numer. Methods Heat Fluid Flow*, **30**(11), 4883 (2020).
7. A. Hussain, L. Sarwar, A. Rehman, S. Akbar, F. Gamaoun, H.H. Coban, A.H. Almaliki, M.S. Alqurashi, *Appl. Sci.*, **12**(3), 1601 (2022).
8. R. Kotcherlakota, S. Das, C. R. Patra, in: Green Synthesis, Characterization and Applications of Nanoparticles, A. K. Shukla, S. Iravani (eds.) Elsevier, 2019.
9. Y. Haik, C. J. Chen, J. Chatterjee, *J. Vis.*, **5** (2), 187 (2002).
10. K. Teimouri, M. R. Tavakoli, A. Ghafari, K. C. Kim, *Comput. Biol. Med.*, **135**, 104600 (2021).
11. L. Pauling, C. D. Coryell, *Proc. Natl. Acad. Sci.* **22** (4), 210 (1936).
12. V. Zablotskii, T. Polyakova, A. Dejneka, *Cells*, **11** (1), 81 (2022).
13. Y. Haik, V. Pai, C.J. Chen, *J. Magn. Magn. Mater.*, **194** (1), 254 (1999).
14. Xenos, M. A., E. E. Tzirtzilakis, *Adv. Dyn. Syst. Appl.* **8**(2), 427 (2013).
15. B. Tashtoush, A. Magableh, *Heat Mass Transf.*, **44** (3), 297 (2008).
16. G. Varshney, V. Katiyar, S. Kumar, *Int. J. Eng. Sci. Technol.* **2**(2), 967 (2010).
17. M.G. Reddy, O.D. Makinde, *J. Mol. Liq.*, **223**, 1242 (2016).
18. A. Meher, A. Tandi, S. Moharana, S. Chakroborty, S. S. Mohapatra, A. Mondal, S. Dey, P. Chandra, *Hybrid Adv.*, **6**, 100184 (2024).
19. A. A. H. El-Bassuony, H. K. Abdelsalam, *Phys. Scr.*, **98** (5), 055919 (2023).
20. S. W. I. Onwuzu, A. C. Ugwu, G. C. E. Mbah, I. S. Elo, *Radiography*, **27** (2), 581 (2021).
21. S. S. Ghadikolaei, M. Yassari, H. Sadeghi, Kh. Hosseinzadeh, D. D. Ganji, *Powder Technol.*, **322**, 428 (2017).
22. S. S. Ghadikolaei, M. Gholinia, M. E. Hoseini, D. D. Ganji, *J. Taiwan Inst. Chem. Engrs.*, **97**, 12 (2019).
23. E. P. Furlani, *Permanent Magnet and Electromechanical Devices: Materials, Analysis, and Applications*, Academic Press, 2001.
24. C. S. Maurya, A. Kumar, *Comput. Biol. Med.*, **184**, 109464 (2025).
25. S. Pabi, Mohd. K. Khan, A. Raj, *Int. Commun. Heat Mass Transf.*, **159**, 108236 (2024).

26. B. M. Johnston, P. R. Johnston, S. Corney, D. Kilpatrick, *J. Biomech.*, **37** (5), 709 (2004).
27. M. Siebert, P. Fodor, *Proceedings of the COMSOL Conference, Boston*, **27** (2009).
28. S. Lynch, N. Nama, C. A. Figueroa, *Sci. Rep.*, **12** (1), 20568 (2022).
29. J. Xiang, M. Tremmel, J. Kolega, E. I. Levy, S. K. Natarajan, H. Meng, *J. Neurointerv. Surg.*, **4** (5), 351 (2012).
30. N. O. Ajayi, L. Lazarus, E. A. Vanker, K. S. Satyapal, *Int. J. Morphol.*, **31** (4), 1393 (2013).
31. J. T. Dodge, B. G. Brown, E. L. Bolson, H. T. Dodge, *Circulation*, **86** (1), 232 (1992).
32. B. M. Johnston, P. R. Johnston, S. Corney, D. Kilpatrick, *J. Biomechanics*, **39** (6), 1116 (2006).
33. M. R. Sadeghi, M. Jahangiri, M. Saghafian, *J. Braz. Soc. Mech. Sci. Eng.*, **42** (11), 570 (2020).
34. S. Sharma, U. Singh, V. K. Katiyar, *J. Magn. Magn. Mater.*, **377**, 395 (2015).
35. X. Liu, X. Chen, Y. Zhang, J. Xie, X. Jia, T. Deng, Y. Zheng, T. Davood, Z. Majid, *Alex. Eng. J.*, **61** (9), 7195 (2022).

Phytonano synthesis of MgO nanoparticles using aqueous leaf extract of *Hibiscus rosa sinensis*: comprehensive characterization and assessment of their antibacterial and anti-oncogenic activities

G.K. Prashanth^{1,2*}, H.S. Lalithamba³, S. Rao⁴, N.P. Bhagya⁵, K.V. Rashmi⁶, H. N. Akolkar⁷

¹Research and Development Center, Department of Chemistry, Sir M. Visvesvaraya Institute of Technology, Bengaluru-562 157, India

²Visvesvaraya Technological University, Belagavi-590 018, India

³Department of Chemistry, Siddaganga Institute of Technology, Tumkur-572 103, India

⁴Department of Chemistry, Nitte Meenakshi Institute of Technology, Nitte (Deemed to be University), Bengaluru-560 064, India

⁵Department of Chemistry, Sai Vidya Institute of Technology, Bengaluru-560 064, India

⁶Department of Bio-Technology, Sir M. Visvesvaraya Institute of Technology, Bengaluru-562 157, India

⁷Department of Chemistry, Abasaheb Marathe Arts, and New Commerce, Science College, Ratnagiri-415 612, India

Received: November 03, 2024; Revised: October 06, 2025

In the realm of nanostructured materials and nanotechnology, MgO nanoparticles (MgO-NPs) have garnered significant attention due to their unique properties and myriad applications. This work explores the synthesis of MgO-NPs via green chemistry principles, utilizing a sustainable approach with *Hibiscus rosa sinensis* leaf extract through the solution combustion synthesis technique. Characterization using PXRD confirmed a cubic crystal structure with an average crystallite size of ~25 nm, while SEM revealed porous morphology and BET analysis showed a surface area of 32.76 m²/g. The antibacterial activity demonstrated strong inhibition against *E. coli* and *S. aureus*, with minimum inhibitory concentration (MIC) values of 15.62 µg/mL and 31.25 µg/mL, respectively, and maximum zones of inhibition of 14.5 mm and 19.5 mm. Anti-oncogenic evaluation against MDA-MB-231 and HeLa cell lines revealed dose-dependent cytotoxicity with an IC₅₀ value of 378.7 µg/mL. Blood hemolysis testing confirmed <5% hemolysis up to 10 mg/mL, affirming the biocompatibility of the synthesized MgO-NPs. These results underscore the potential of MgO-NPs as eco-friendly antibacterial and anticancer agents.

Keywords: MgO-NPs; Solution combustion; Green fuel; Antibacterial; MTT assay; Blood hemolysis

INTRODUCTION

In recent decades, there has been significant interest in nanostructured materials and nanotechnology as they intersect within the techno-economic sphere [1]. This heightened attention arises primarily from the potential of reducing materials to the nanoscale, which can result in distinctive properties not achievable in bulk materials at larger scales [2]. MgO-NPs stand out among essential metal oxide nanoparticles due to their biocompatibility, exceptional stability, cost-effectiveness, high ionic properties, crystal structure, and effectiveness as safe and efficient contaminant adsorbents [3, 4]. Over the past two decades, the myriad applications and distinctive characteristics of MgO-NPs have garnered significant attention from researchers worldwide, surpassing interest in other metal oxide nanoparticles [5-8]. They are economically viable, highly biocompatible, and stable under extreme conditions [9].

MgO-NPs possess a unique set of properties that make them highly effective across diverse applications. They are cost-effective, biocompatible, and remain stable even under extreme conditions [10-12]. Owing to their strong adsorption capability, MgO-NPs serve as efficient and safe adsorbents for a range of contaminants [13,14]. Their wide band gap, exceptional thermodynamic stability, low dielectric constant, and low refractive index further support their use in catalysis, ceramics, toxic-waste remediation, and as functional additives in diesel engines, paints, and superconducting materials [15-20]. Beyond these industrial roles, MgO-NPs also show notable biomedical potential as antibacterial [21] and anti-oncogenic agents [22]. Their antibacterial action is attributed to multiple mechanisms, including protein denaturation, DNA damage, disruption of cell membranes and enzymes, interference with transmembrane electron transport, and damage to cellular storage granules [23, 24].

* To whom all correspondence should be sent:
E-mail: prashanth_chem@sirmvit.edu

The green synthesis method for NPs aligns with the twelve principles of green chemistry. This involves designing and creating nanoparticles using non-toxic chemicals, renewable materials, environmentally friendly solvents, and generating degradable waste products [25]. From a green chemistry perspective, three critical stages in NPs preparation include utilizing benign solvent media, non-toxic reducing agents, and environmentally safe stabilization agents [26]. Additionally, selecting an appropriate capping agent to passivate the NPs surface is another crucial factor [27]. Currently, the production of nanoscale metals predominantly relies on chemical processes, leading to unintended consequences such as environmental contamination, high energy usage, and potential health risks. To address these issues, a sustainable approach known as green synthesis has emerged, utilizing plant extracts in lieu of conventional industrial chemicals to reduce metal ions. Green synthesis offers advantages over traditional methods, including lower costs, reduced pollution, and enhanced safety for both the environment and human health.

The solution combustion synthesis technique stands out as a versatile approach for producing NPs applicable across various fields. Its adaptability is evident in its ability to generate numerous compounds, particularly oxides, making it a cornerstone technique in materials science. Its effectiveness lies in its straightforward implementation, high throughput, diverse chemical capabilities, and ability to create powders with high surface areas.

Based on the provided background, we propose a straightforward method for producing a versatile oxide material, MgO nanoparticles (NPs), possessing various desirable properties such as a wide band gap, exceptional thermodynamic stability, low dielectric constant, and a low refractive index. These properties render them suitable for a wide range of applications including catalysis, ceramics, toxic waste remediation, antibacterial agents, and as additives in refractory, paint, and superconductor products. We utilized a green synthesis approach employing aqueous leaf extract of hibiscus through the SCS method. The resulting nanoparticles underwent characterization through techniques such as PXRD, SEM, and BET surface area analysis. Furthermore, we evaluated the antibacterial activity of the nanoparticles against *S. aureus* and *E. coli*, determining their MIC values. Additionally, we assessed their anti-oncogenic activity using the MTT assay against MDA-MB-231

and HeLa cell lines, while their biocompatibility was evaluated through blood hemolysis testing.

MATERIALS AND METHODS

Chemicals and reagents

Magnesium nitrate hexahydrate [$\text{Mg}(\text{NO}_3)_2 \cdot 6\text{H}_2\text{O}$, AR 99% Himedia], citric acid [$\text{C}_6\text{H}_8\text{O}_7$, AR, 99 %, SD Fine], nutrient agar [Himedia], potato dextrose agar [Himedia], Dulbecco's modified eagle's medium [DMEM, Gibco], dimethyl sulfoxide [$\text{C}_2\text{H}_6\text{SO}$, AR 99% Merck], MTT [$\text{C}_{18}\text{H}_{16}\text{BrN}_5\text{S}$, 97.5%, Sigma-Aldrich] were procured commercially and hibiscus leaves were plucked from Sir MVIT campus, Bengaluru. The cell lines used for cytotoxicity testing were procured from the ATCC.

Aqueous leaf extract and its phytochemical screening

The process began with cleansing of the leaves using water, followed by a 15-day period of air drying. Subsequently, a solution of hibiscus leaf extract was prepared through Soxhlet extraction over 72 h, utilizing 10 g of leaves in 150 mL of double distilled water.

Combustion synthesis of MgO-NPs

To synthesize MgO-NPs, the appropriate quantity of $\text{Mg}(\text{NO}_3)_2 \cdot 6\text{H}_2\text{O}$, was dissolved in 5 mL of plant extract, followed by the addition of 10 mL of distilled water. The resulting mixture was transferred to a crystallizing dish and placed into a preheated muffle furnace set at $500 \pm 10^\circ\text{C}$. Within 5 min, a visible flame emerged, indicating the initiation of an exothermic reaction between the phytochemicals present in the plant extract and the magnesium ions, leading to the formation of MgO-NPs.

Characterization

Various techniques were employed to characterize the synthesized MgO-NPs. PXRD analysis was conducted using a PANalytical X'pert diffractometer with Cu K α radiation ($\lambda = 1.541 \text{ \AA}$) operating at 50 kV voltage and 30 mA current, covering a 2θ range from 20° to 80° to investigate phase purity and crystalline structure. Surface morphology and composition were examined using JEOL Model JSM - 6390LV with an EDS system (OXFORD XMX N). Surface area measurements using the BET method were conducted utilizing Quantachrome ASiQwin.

Evaluating the biological potential of green-synthesized MgO-NPs

- **Antibacterial activity.** The antibacterial activity of MgO NPs was carried out by the well diffusion method in MH agar media as followed in our previous work [28]. The bacteria (*E. coli*, and *S. aureus*) were cultured overnight at 37 °C in MH and adjusted to a final density of 107 CFU/mL by 0.5 McFarland standards. About 25 mL of molten MH agar was poured into sterile petri plates. The plates were allowed to solidify, after which 100 µL of the pathogenic bacteria cultures were transferred onto plate and made culture lawn by using sterile L-rod spreader. Homogeneous dispersions of MgO-NPs with different concentrations ranging from 1000-250 µg/mL (with two-fold dilution) were prepared by ultrasonication. Wells were cut and dispersions of MgO NPs (of different concentrations) were loaded. The plates were incubated at 37 °C for 24 h. The antibacterial activity was determined by measuring the diameter of the ZOI formed around the wells. Bacterial cultures grown in tryptic soy broth (adjusted to $1-2 \times 10^5$ cells/mL) were utilized for inoculation. Aqueous dispersions of MgO-NPs ranging from 1000 to 1.953 µg/mL (two-fold dilutions) in MH broth were tested against these cultures. RPMI media (MH broth) with and without MgO NPs served as controls. In 96-well plates, 90 µL of test sample dispersions at different concentrations were mixed with 10 µL of inoculum in triplicate. Control wells contained 90 µL of RPMI media (MH agar) without the drug mixed with 10 µL of inoculum. Treated bacterial cultures were incubated at 35°C. After 24-48 h, the plates were observed, and optical density was measured at 600 nm using a Tecan plate reader.

Percent inhibition was calculated using the formula: [absorbance control (untreated) - absorbance (treated)] / absorbance control. The MIC was determined as the lowest concentration of MgO-NPs that resulted in at least 50% inhibition of OD compared to the control.

- **Anti-oncogenic activity.** The anti-oncogenic potential of MgO-NPs was evaluated using the MTT assay, as described in our previous research with slight modifications [28-33]. MDA-MB-231 and HeLa cell lines were trypsinized when they reached 80% confluency. A total of 15,000 viable cells/well were seeded in a 96-well plate and incubated for 24 h at 37°C in a 5% CO₂ incubator. MgO-NPs ranging from 0 to 320 µg/mL in DMEM without 10% fetal bovine serum were added and incubated for 24 h. Following NPs treatment, the media were removed, and 200 µL/well of a 10% MTT working solution was added and incubated for another 24 h.

Afterward, the media were aspirated, and 200 µL of a medium containing 10% MTT reagent was added to each well, resulting in a final concentration of 0.5 mg/mL. The plate was then incubated at 37°C in a 5% CO₂ atmosphere for 3 h. After incubation, the culture medium was removed without disturbing the formed crystals, and 100 µL of solubilization solution (DMSO) was added to each well. The plate was gently shaken on a gyratory shaker to dissolve the formazan crystals, and the absorbance was measured at 630 nm using a microplate reader. The percentage of growth inhibition was calculated after subtracting the background and blank values, and the concentration of the test drug required to inhibit cell growth by 50% (IC₅₀) was determined from the dose-response curve for each cell line. Camptothecin was used as the standard drug, with IC₅₀ values of 75 µM and 50 µM for MDA-MB-231 and HeLa cell lines, respectively.

- **Evaluation of cytotoxicity through blood hemolysis.** The hemolysis activity test for MgO NPs followed the protocol outlined by Das *et al.* (2013) [34]. Briefly, 9 mL of sheep blood was mixed with 1 mL of 3.8% sodium citrate to prevent blood coagulation. The mixture was centrifuged at 3000 rpm for 5 min to remove platelet-rich plasma. The remaining RBC pellet was suspended in 10 mL of PBS at pH 7.4 to create a uniform cell suspension. MgO-NPs at concentrations ranging from 0.25 to 10.0 mg/mL were prepared in separate test tubes. To each test tube, 2 mL of erythrocyte suspension was added, and the tubes were inverted and gently shaken to ensure contact between the blood and MgO NPs. The tubes were then incubated at 37°C for 90 min. After incubation, the samples were centrifuged at 3000 rpm for 5 min to pellet the RBCs. The supernatant was collected, and its absorbance was measured at 540 nm using a UV-visible spectrophotometer against a blank PBS solution.

RESULTS AND DISCUSSION

Crystal structure, surface morphology and BET surface area

PXRD pattern of MgO-NPs is presented in Fig. 1. The diffraction peaks observed at 2θ angles of 37.76°, 43.12°, 64.97°, 74.45°, and 78.12° were found to correspond to the crystallographic planes (111), (200), (220), (311), and (222), respectively, within the face-centered cubic (FCC) lattice of magnesium. These findings strongly supported the crystalline nature of MgO-NPs. The obtained diffraction pattern aligned closely with the established diffraction data for MgO-NPs (JCPDS file No. 89-4248). By applying the Scherrer equation

to the diffraction peaks, the average crystallite size was determined to be ≈ 25 nm.

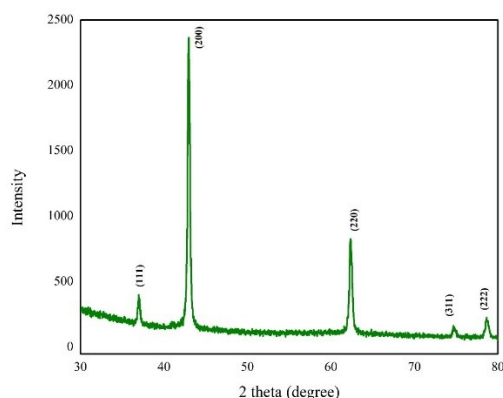


Figure 1. PXRD pattern of MgO NPs

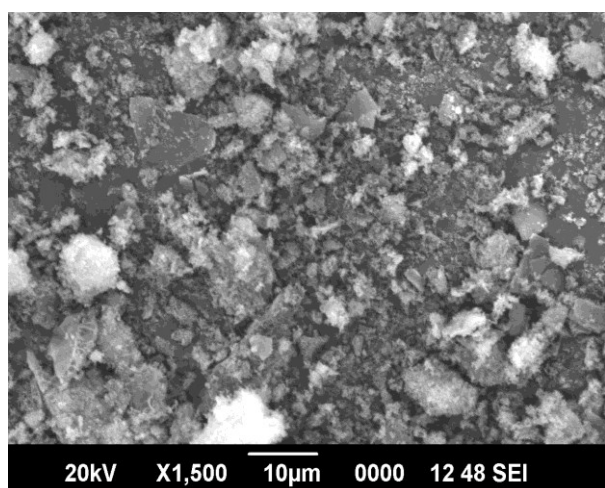


Figure 2. SEM image of MgO NPs

The SEM findings (Fig. 2) indicate that the MgO-NPs appear to exhibit porosity and significant agglomeration with nanoentities. Consequently, the accurate determination of MgO particle size from the current SEM results is challenging.

Results of surface area measurements indicated a BET surface area of $32.762 \text{ m}^2/\text{g}$.

Biological potential of MgO-NPs

- **Antibacterial activity.** The observed ZOI of MgO-NPs against *E. coli* and *S. aureus*, along with the MIC values, are summarized in Table 1 and depicted in Figure 3. The results clearly demonstrate that MgO-NPs possess significant antibacterial activity against both Gram-negative and Gram-positive strains, with inhibition zones increasing in a concentration-dependent manner. For *E. coli*, the maximum ZOI reached 14.5 mm at $1000 \text{ } \mu\text{g/mL}$ with an MIC of $15.62 \text{ } \mu\text{g/mL}$, while for *S. aureus*, a maximum ZOI of 19.5 mm was observed at the same concentration, with an MIC of $31.25 \text{ } \mu\text{g/mL}$. These

results highlight the broad-spectrum antibacterial efficacy of MgO-NPs.

The difference in sensitivity between the two bacterial strains can be correlated to their structural features. Gram-negative *E. coli*, with its thinner peptidoglycan layer and outer lipid membrane, exhibited greater susceptibility at lower concentrations, whereas Gram-positive *S. aureus*, despite its thicker cell wall, showed strong inhibition at higher concentrations. The antibacterial effect of MgO-NPs may be attributed to multiple mechanisms acting simultaneously. One possible mechanism is the generation of reactive oxygen species (ROS) on the surface of MgO-NPs, which induces oxidative stress in bacterial cells. In addition, Mg^{2+} ions released from the nanoparticles can penetrate bacterial cells, disrupting enzymatic activities and impairing metabolic processes. The direct interaction of MgO-NPs with the bacterial cell membrane may also lead to increased permeability, leakage of intracellular components, and eventual cell lysis.

Table 1. Results of antibacterial activity of MgO NPs and standard antibiotic (ZOI in mm)

Pathogen	Conc. ($\mu\text{g/mL}$)	ZOI Mean \pm SD (mm)		MIC ($\mu\text{g/mL}$)
		MgO-NPs	Positive control (Ofloxacin $100 \text{ } \mu\text{g/mL}$)	
<i>E. coli</i>	125	0.00 ± 0.00	40.77 ± 1.05	15.62
	250	7.00 ± 0.00		
	500	8.50 ± 0.00		
	1000	14.50 ± 0.816		
<i>S. aureus</i>	125	0.00 ± 0.00	38.0 ± 1.06	31.25
	250	0.00 ± 0.00		
	500	0.00 ± 0.00		
	1000	19.50 ± 0.577		

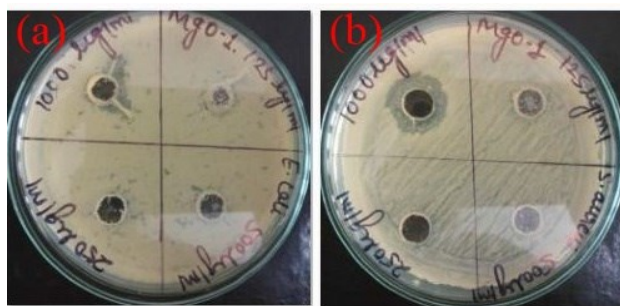


Figure 3. ZOI against (a) *E. coli*, and (b) *S. aureus*

Taken together, these findings confirm that the biosynthesized MgO-NPs are highly effective antibacterial agents, acting through a combination of ROS generation, ion release, and membrane disruption mechanisms, as illustrated in Figure 4 [35].

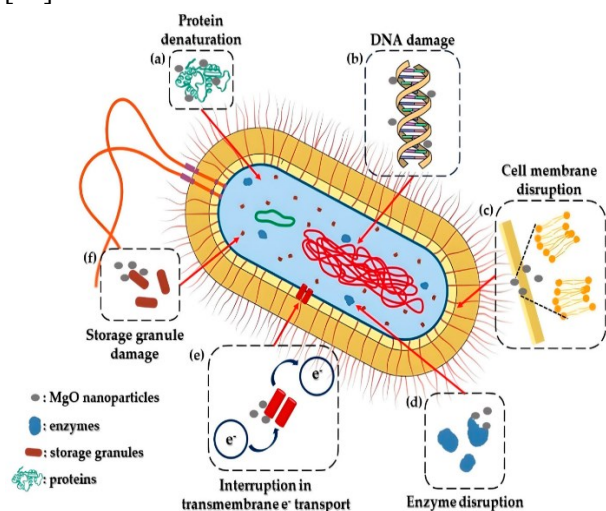


Figure 4. Probable mechanism of antibacterial activity of MgO-NPs [20]

- **Anti-oncogenic activity.** The effect of MgO-NPs on the viability of MDA-MB-231 and HeLa cells was investigated using the MTT assay, and the results are presented in Figure 5. A concentration-dependent reduction in cell viability was observed, with higher nanoparticle concentrations leading to greater cytotoxic effects. The IC₅₀ value for MgO-NPs was determined to be 378.7 $\mu\text{g/mL}$ (Figure 6), confirming moderate anticancer potential. Optical microscopy images (Figure 8) further illustrate the progressive morphological changes in cancer cells, including shrinkage, membrane blebbing, and loss of adherence with increasing nanoparticle concentration, in comparison to untreated controls. The anticancer activity of MgO-NPs can be attributed to multiple factors. The generation of

reactive oxygen species (ROS) within the cellular environment may induce oxidative stress, leading to DNA damage, mitochondrial dysfunction, and apoptosis. Additionally, the release of Mg^{2+} ions could interfere with intracellular signaling pathways, contributing to reduced proliferation. The direct interaction of MgO-NPs with the cancer cell membrane may further destabilize its integrity, triggering cell death. The plausible mechanism of action is schematically illustrated in Figure 7. Collectively, these findings suggest that MgO-NPs exhibit promising anticancer properties, mediated through ROS generation, ion release, and induction of apoptosis in cancer cells.

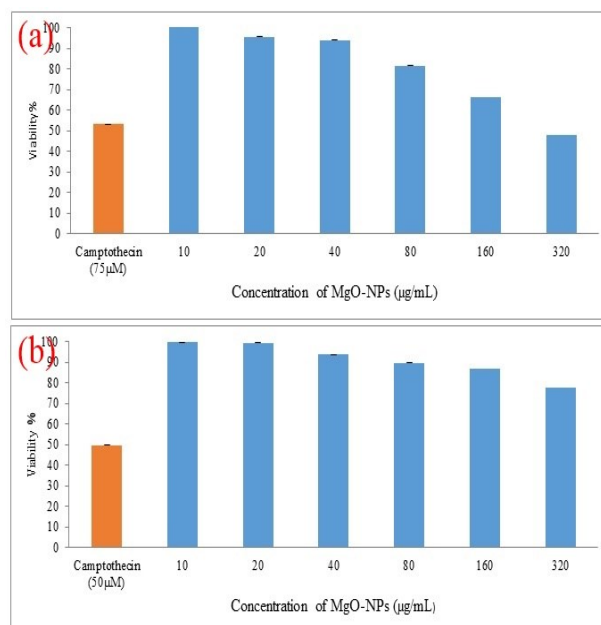


Figure 5. Cell viability of (a) MDA-MB-231, and (b) HeLa by the action of MgO-NPs

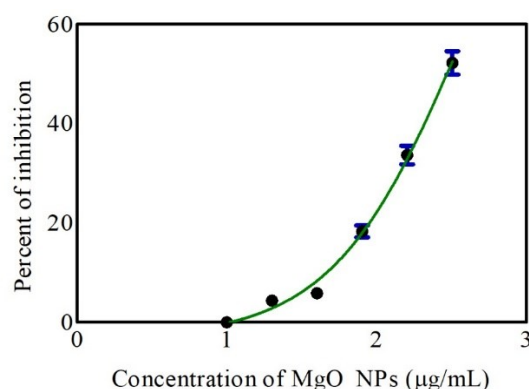


Figure 6. IC₅₀ determination of MgO-NPs in MDA-MB-231 cell line

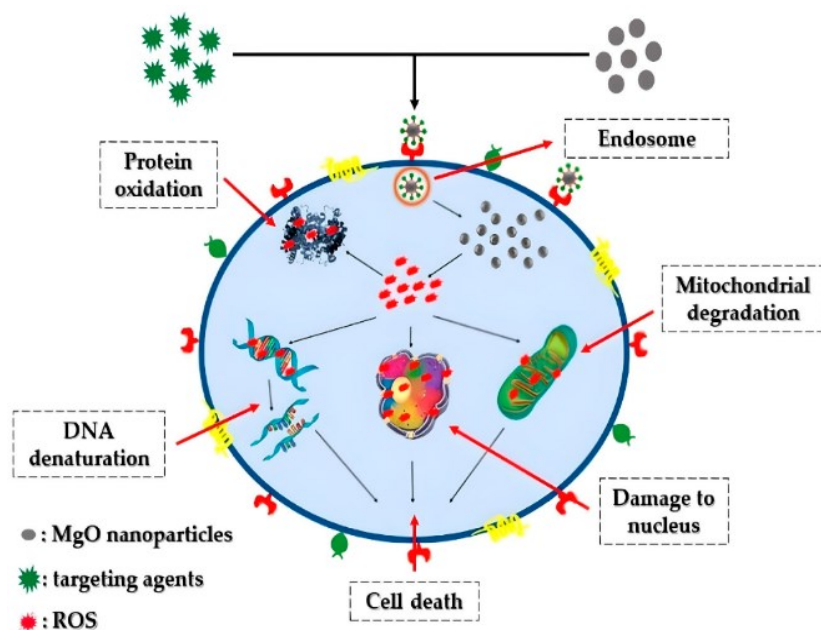


Figure 7. Probable anti-oncogenic mechanism of MgO-NPs [35]

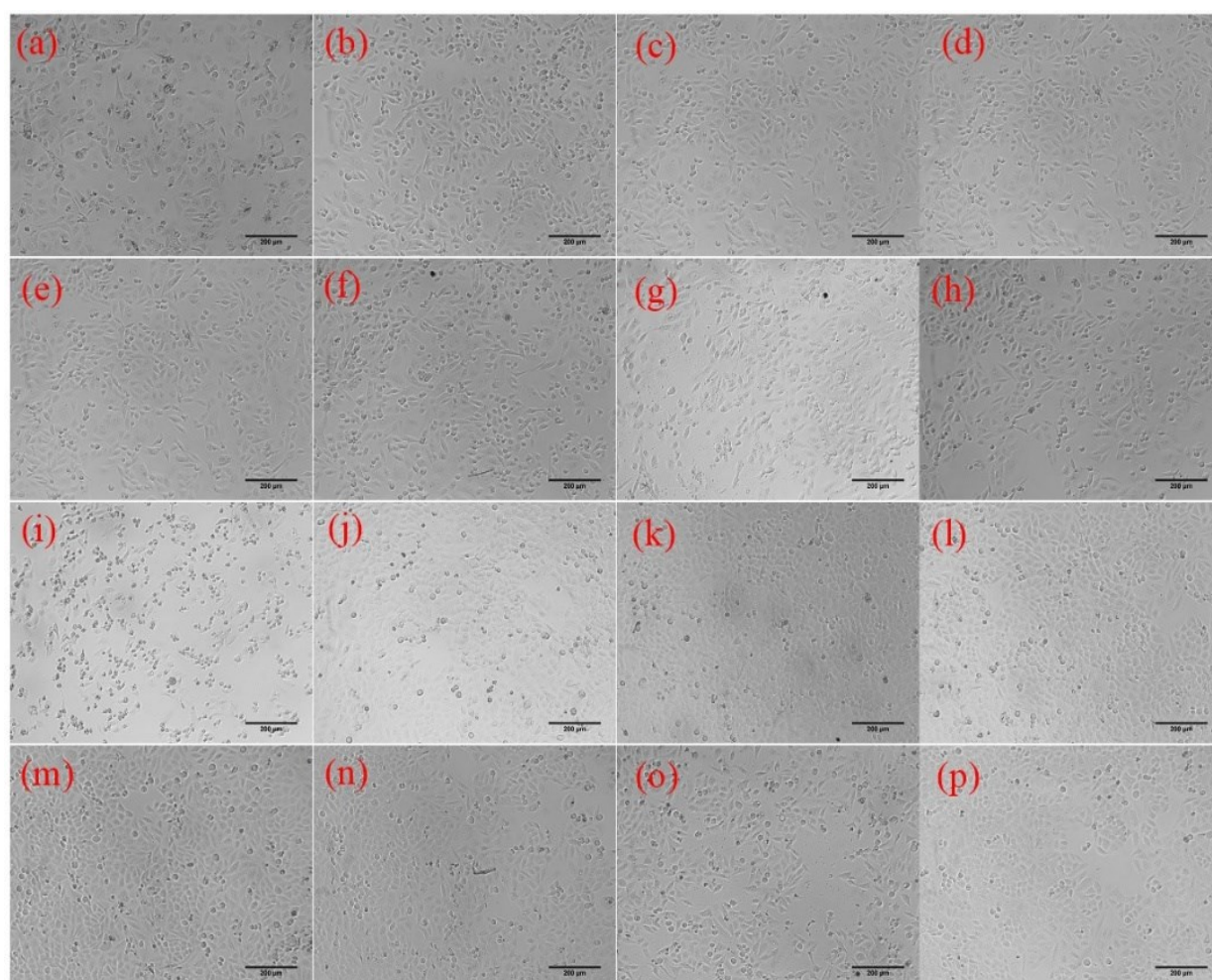


Figure 8. MDA-MB-231 treated with (a) Camptothecin 50 μ M, (b) 10 μ g/mL, (c) 20 μ g/mL, (d) 40 μ g/mL, (e) 80 μ g/mL, (f) 160 μ g/mL, (g) 320 μ g/mL of MgO-NPs, (h) Untreated; HeLa treated with (i) Camptothecin 50 μ M, (j) 10 μ g/mL, (k) 20 μ g/mL, (l) 40 μ g/mL, (m) 80 μ g/mL, (n) 160 μ g/mL, (o) 320 μ g/mL of MgO-NPs, and (p) Untreated

• **Blood hemolysis.** The cytocompatibility of MgO-NPs was further assessed by hemolysis assays using sheep erythrocytes. The results, presented in Table 2, demonstrate that hemolysis percentages remained below 5% even at the highest tested concentration of 10 mg/mL. This indicates that the synthesized MgO-NPs exhibit good hemocompatibility and are unlikely to cause significant damage to red blood cells.

The low hemolytic activity suggests that the surface characteristics of the MgO-NPs, including their phytochemical capping from *Hibiscus rosa sinensis* extract, may help minimize adverse interactions with erythrocyte membranes. A hemolysis percentage below 5% is widely considered as the threshold for blood compatibility, implying that the concentrations used in antibacterial and anticancer studies fall well within the biocompatible range. The minimal disruption of erythrocyte membranes observed in this study supports the safe application of MgO-NPs in biomedical contexts, particularly in antibacterial and anticancer therapies where systemic exposure is a consideration.

Table 2. Blood hemolysis by MgO-NPs

S. No.	Concentration of MgO-NPs (mg/mL)	Hemolytic activity (%)
1	0.25 mg	0.57
2	0.5 mg	1.06
3	1 mg	1.30
4	2.5 mg	2.19
5	5 mg	3.08
6	10 mg	4.63

CONCLUSION

This study successfully illustrates the synthesis of MgO-NPs via SCS, utilizing hibiscus leaf extract as a bio-fuel. Analysis through PXRD revealed the cubic crystal structure of MgO, with an average crystallite size of 25 nm. SEM image displayed the spherical morphology of the particles, albeit with uneven sizes, while BET results indicated a surface area of 32.762 m²/g. Antibacterial assessments demonstrated the efficacy of MgO against both Gram-negative *E. coli* and Gram-positive *S. aureus*, with MIC values of 15.62 µg/mL and 31.25 µg/mL, respectively. Further, MTT assay results unveiled moderate anti-oncogenic activity of MgO-NPs, with an IC₅₀ value of 378.7 µg/mL. Furthermore, blood hemolysis testing affirmed the biocompatibility of MgO-NPs up to a concentration of 10 mg/mL.

Abbreviations

MgO: Magnesium oxide
 NPs: Nanoparticles
 SCS: Solution combustion synthesis
 PXRD: Powder-X-ray diffraction
 SEM: Scanning electron microscopy
 BET: Brunauer–Emmett–Teller
 MH: Mueller–Hinton
 RPMI: Roswell Park Memorial Institute
 MTT: (3-[4,5-dimethylthiazol-2-yl]-2,5-diphenyl tetrazolium bromide)
 ATCC: American Type Culture Collection
 ZOI: zone of inhibition
 RBC: Red blood cells
 PBS: Phosphate-buffered saline
E. coli: *Escherichia coli*
S. aureus: *Staphylococcus aureus*

Declarations

Funding: The authors declare that no specific grant was received from funding agencies in the public, commercial, or not-for-profit sectors for this work.

Conflict of interest: The authors declare no conflict of interest.

Ethical approval: Not required.

Consent to participate: Not applicable.

Consent for publication: All authors have read and approved the final manuscript and consent to its publication.

Availability of Data and Materials: All data generated or analyzed during this study are included in this article.

Authors' contributions: **G.K. Prashanth:** Conceptualization, methodology, supervision, writing—review & editing; **Srilatha Rao:** Data curation, formal analysis, writing—original draft;

- **H.S. Lalithamba:** Characterization studies, validation; **K.V. Rashmi:** Cytotoxicity and hemolysis assays, Biological assays, data interpretation; **N.P. Bhagya** and **H. K. N. Akolkar:** Literature review, writing—review & editing.

REFERENCES

1. F. Trotta, A. Mele, Nanosponges, John Wiley & Sons, Ltd., Hoboken, NJ, USA, 2019, p. 142.
2. S.B. Mitra, Chapter 2-Nanoparticles for dental materials: Synthesis, analysis, and applications, in: K. Subramani, W. Ahmed (eds.), Emerging Nanotechnologies in Dentistry, 2nd edn., William Andrew Publishing, Norwich, NY, USA, 2018, p. 17.
3. F. Mahmoudi, F. Mahmoudi, K.H. Gollo, M.M. Amini, *Biol. Trace Elem. Res.*, **199**, 1967 (2021).
4. A.A.A.A. Alrashed, O.A. Akbari, A. Heydari, D. Toghrarie, M. Zarringhalam, G.A.S. Shabani, A.R. Seifi, M. Goodarzi, *Phys. B Condens. Matter*, **537**, 176 (2018).

5. M.A. Amin, A.M. Abu-Elsaoud, A.I. Nowwar, A.T. Abdelwahab, M.A. Awad, S.E.D. Hassan, F. Boufahja, A. Fouda, A. Elkelish, *Green Process. Synth.*, **13** (1), 20230215 (2024).
6. S. Abinaya, H.P. Kavitha, *ACS Omega*, **8** (6) 5225 (2023).
7. Z. Abbas, M.A. Hassan, W. Huang, H. Yu, M. Xu, X. Chang, X. Fang, L. Liu, *Agronomy*, **14** (3), 617 (2024).
8. S.M. Shaikh, P.V. Desai, *Indian J. Exp. Biol.*, **62** (4), 229 (2024).
9. S. Faisal, J. Abdullah, S.A. Shah, S. Shah, M. Rizwan, N. Zaman, Z. Hussain, M.N. Uddin, N. Bibi, A. Khattak, *Catalysts*, **11** (7), 780 (2021).
10. N., Thakur, J., Ghosh, S.K., Pandey, A. Pabbathi, J., Das, *Inorganic Chemistry Communications*, **146**, 110156 (2022).
11. A. Muhaymin, H.E.A. Mohamed, K. Hkiri, A. Safdar, S. Azizi, M. Maaza, *Scientific Reports*, **14**(1), 20135 (2024).
12. I. Humaira Ahmad, H.A. Shakir, M. Khan, S. Ali, M. Alshahrani, M. Franco, M. Irfan, *ChemBioEng Reviews*, **11**(3), 447 (2024).
13. H.C.S. Perera, V. Gurunathanan, A. Singh, M.M.M.G.P.G. Mantilaka, G. Das, S. Arya, *Journal of Magnesium and Alloys*, **12**(5), 1709 (2024).
14. Kuruthukulangara, Nethra, I. V. Asharani, *Journal of Cluster Science*, **35** (8), 2681 (2024).
15. K. Tharani, A.J. Christy, S. Sagadevan, L.C. Nehru, *Chemical Physics Letters*, **763**, 138216 (2021).
16. B. Debnath, S. Das, S. Debnath, M. Debbarma, S. Chattopadhyaya, *Computational Condensed Matter*, **41**, e00959 (2024).
17. S. Rani, P. Kumar, N. Kataria, *Journal of the Taiwan Institute of Chemical Engineers*, **166**, 105566. 2025.
18. S.B. Arun, K.V. Yatish, G. Tigari, G.K. Prashanth, H.S. Lalithamba, K. Pramoda, *Renewable Energy*, 124218 (2025).
19. H. Tang, S. Li, Y. Zhang, Y. Na, C. Sun, D. Zhao, J. Liu, Z. Zhou, *Journal of Cleaner Production*, **380**, 135035 (2022).
20. F. Yu, Y. Xue, C. Zhong, J. Song, Q. Nie, X. Hou, B. Wang, *Micromachines*, **14**(10), 1914 (2023).
21. X. Li, H. Liu, Y. He, Z. Li, F. Y. Zhan, Li, J. Zhao, *Ceramics International*, **50**(21), 42877 (2024).
22. P. Arthi, K. Hema, S.V.G. Rani, R. Sugarthi, A. Sivapunniyam, T. Perumal, P.K. Seetharaman, K.R. Ramalingam, C. Jayashree, *Journal of Inorganic and Organometallic Polymers and Materials*, 1 (2025).
23. M. Ramezani Farani, M. Farsadrooh, I. Zare, A. Gholami, O. Akhavan, *Catalysts*, **13**(4), 642 (2023).
24. M.A. Gatou, E. Skylla, P. Dourou, N. Pippa, M. Gazouli, N. Lagopati, E.A. Pavlatou, *Crystals*, **14**(3), 215 (2024).
25. J. Virkutyte, R.S. Varma, *Chem. Sci.*, **2** 837 (2011).
26. P. Raveendran, J. Fu, S.L. Wallen, *J. Am. Chem. Soc.*, **125**, 13940 (2003).
27. A. Annu, A. Ali, S. Ahmed, *Nanomedicine*, 1 (2018).
28. K.R. Mohana, P.A. Prashanth, B.M. Nagabhushana, G.M. Krishnaiah, H.G. Nagendra, M.S. Dileep, G.K. Prashanth, *Int. J. Adv. Sci. Technol.*, **29** (8s), 3668 (2020).
29. G.K. Prashanth, H.M. Sathyananda, P.A. Prashanth, M. Gadewar, M. Mutthuraju, S.B. Prabhu, B.M. Nagabhushana, C. Shivakumara, S. Rao, D. Mohanty, *Appl. Phys. A*, **128** (7) 614 (2022).
30. S. Nagarajaiah, A. Shivanna Giresha, P. Gopala Krishna, M. Manikrao Gadewar, M. Praveen, N. Nanda, D. Urs, K. Krishnappa Dharmappa, B. Mutta Nagabhushana, S. Rao, M. Mahadeva Swamy, *Chem. Biodivers.*, e202301533 (2024).
31. S. Nagarajaiah, N. Nanda, P. Manjappa, B.M. Nagabhushana, M. Gadewar, S. Rao, P.G. Krishna, *Appl. Phys. A*, **129** (6), 461 (2023).
32. P.G. Krishna, P.P. Ananthaswamy, T. Yadavalli, N.B. Mutta, A. Sannaiah, Y. Shivanna, *Mater. Sci. Eng. C*, **62**, 919 (2016).
33. P.G. Krishna, P. Ananthaswamy, P. Trivedi, V. Chaturvedi, N.B. Mutta, A. Sannaiah, A. Erra, T. Yadavalli, *Mater. Sci. Eng. C*, **75**, 1026 (2017).
34. D. Das, B.C. Nath, P. Phukon, A. Kalita, S.K. Dolui, *Colloids Surf. B: Biointerfaces*, **111**, 556 (2013).
35. M.A. Gatou, E. Skylla, P. Dourou, N. Pippa, M. Gazouli, N. Lagopati, E.A. Pavlatou, *Crystals*, **14** (3), 215 (2024).

Fractionation of potentially toxic and essential elements in sewage sludge from wastewater treatment plants

V. V. Lyubomirova*, I. N. Belovezhdova

Faculty of Chemistry and Pharmacy, Sofia University "St. Kliment Ohridski", 1 James Bourchier Blvd., 1164 Sofia, Bulgaria

Center of Competence "Clean technologies for sustainable environment – waters, wastes, energy for circular economy", 1000 Sofia, Bulgaria

Received: September 11, 2025; Revised: October 13, 2025

The application of sewage sludge in agriculture is controlled regarding the total concentrations of the potentially toxic elements (PTEs) Cd, Cu, Ni, Pb, Zn, Hg, Cr and As. Additionally, the essential elements K, Ca, Mg and P are included without concentration thresholds. Their bioavailability, however, depends on their speciation. In the present work, single extraction with deionized water and BCR sequential extraction were applied for two types of sewage sludge and two certified reference materials CRM 029 and ERM-CC144. The concentrations of the controlled elements and of Na, Mn, Fe, B, and Mo in the obtained fractions were determined by ICP-MS. The results showed water solubility between 0.04% and 11.5% for the PTEs and varying degrees between 0.03% to 60% for the essential elements. The BCR fractionation indicated a high degree of bioavailability for the essential elements being concentrated in the exchangeable or oxide fractions. A high tendency to form organic complexes was found for P and Mo, which indicated their low bioavailability for plants. The fractionation of PTEs showed low sum extraction for Pb and Hg and immobilization in organic complexes of Cu and Cr. A risk of soil and plant pollution exists for Zn, As, Cd and Ni. Zn and As dominated in the exchangeable and oxide fractions, Cd - in the oxide fraction, while for Ni the dominant fraction varied between the samples.

INTRODUCTION

The current approaches to management of sewage sludge include recycling into construction materials [1], landfilling, incineration, composting, reclamation of unused land, and the highest share in the European Union (EU), including Bulgaria, is their use as fertilizer in agriculture [2-4]. According to Bulgarian [5] and European [6] legislations, strict limit values for a number of toxic pollutants, including the potentially toxic elements (PTEs) Cd, Cu, Ni, Pb, Zn, Hg, Cr and As, both in sludges and soils have been set.

The determination of the total concentrations of chemical elements provides general information about the content of potentially toxic and essential elements and, accordingly, on the level of contamination or the positive effects when used in agriculture [7-10]. An opportunity to provide an assessment of the mobility of the elements in the sewage sludge, the degree of their release into the soil solution and their bioavailability to plants is given by the fractionation of the sewage sludge [11-13]. In recent years, fractionation studies have been of great interest and a lot of literature data have been published, mainly for PTEs, e.g. [12-16]. The extraction procedures vary in the different studies in terms of the procedure used, or the use of

the same extractant for a particular phase but under different experimental conditions [11]. For example, the determination of the exchangeable fraction is usually done using 0.11M CH₃COOH for 16 h at room temperature [15-19] according to the BCR procedure, as well as at extraction times of 4 h [20] and 7 min [13]; using 0.5M KNO₃ for 16 h [21] and 17 h [22]; using 0.5M MgCl₂ at pH 7.0 for 1 h [23] or 1M MgCl₂ at pH 7.0 for 1 h [24, 25]. Furthermore, the distribution of the metal ions in the different chemical fractions depends on the solid matrix composition, its physico-chemical properties, the stabilization process of the sewage sludge [13, 17, 22] and on the nature of the metal itself [21]. All this makes it difficult to compare the data obtained in different studies, as well as to predict the element distribution and mobility according to their total concentrations. However, according to published data, several trends in the distribution of elements emerge. In general, an appreciable part of Cu in sewage sludge is mainly associated with organic matter [13, 17, 21-23], carbonate [17, 22] and silicate phases [17, 22, 26]; Ni is bound to the residual [13, 17, 26], exchangeable [17, 27] and carbonate phases [17, 21, 22]; Cd is bound to the exchangeable phases [27], residual matrix [13, 28], carbonate [21, 22] and organic phase [17]; Pb is

* To whom all correspondence should be sent:
E-mail: vlah@chem.uni-sofia.bg

bound to the residual matrix [13, 17, 26], organic matter [17, 23] and carbonates [21, 22]; Zn is bound to carbonate [21, 22], exchangeable [27], and reducible phases [17, 23, 26], organic and residual fractions [23]; Cr is bound to organic [17, 23] and residual fractions [17, 21, 26, 28]; Fe is bound to the residual fraction [17, 26], or distributed among oxide, organic and residual fractions [23]. The data on the impact of sludge stabilization on the metal distribution are also not unambiguous. It was found that the stabilization treatment undergone by the sludges strongly influenced the heavy metal distribution and the phases to which they were associated [17, 26]. Other studies have found that the sewage sludge processing has no significant effect on the prevailing metal fraction [21, 22]. Despite the variations depending on the sample and element, the literature data indicate that PTEs non-specifically adsorbed in the most mobile and bioavailable exchangeable fraction, represent a small portion of the total amount of metals found in the sewage sludge. Most of them are associated with silicates, as well as sulfides and organic matter, which are practically inaccessible to plants under natural conditions [12, 13].

The objective of the present study was to assess the water solubility and the fractionation of the regulated PTEs (Cd, Cu, Ni, Pb, Zn, Hg, Cr and As) and the essential elements Na, K, Ca, Mg, P, Mn, Fe, B, and Mo, according to the BCR extraction procedure in two types of sewage sludge – municipal and industrial and two sewage sludge certified reference materials (CRMs) CRM 029 and ERM-CC144. The obtained data revealed the fractionation, mobility and bioavailability of both potentially toxic and essential elements in sewage sludge samples.

EXPERIMENTAL

Sewage sludge samples and certified reference materials

A sewage sludge sample from an urban wastewater treatment plant (Sewage sludge 1, SS1) and another from a mixed flow of domestic, fecal and industrial water treatment (Sewage sludge 2, SS2) were analyzed. Both samples were taken from sludge drying fields after biological treatment. The extraction procedures were also applied to CRM 029 (Trace Metals—Sewage Sludge 2—Sigma-Aldrich, Laramie, WY 82070, USA) and ERM-CC144 (Sewage Sludge—elements, European Commission—Joint Research Centre Directorate F—Health, Consumers and Reference Materials, Geel, Belgium).

The CRM BCR-701 (lake sediment, trace

elements, European Commission – Joint Research Centre Directorate F – Health, Consumers and Reference Materials, Retieseweg 111, B - 2440 Geel, Belgium) with certified values for Cd, Cr, Cu, Ni, Pa and Zn in Fractions 1, 2 and 3 of the BCR extraction scheme was analyzed to assess the accuracy of the results.

Sample preparation

Extraction of 1 g of sewage sludge sample or CRMs with 20 mL of deionized water was performed by shaking for 16 h on a rotator, followed by centrifugation at 3600 rpm for 15 min and decantation.

The BCR sequential extraction procedure [29] defines the metal content as exchangeable (Fraction 1), Fe/Mn-oxides (reducible, Fraction 2) and organic and sulfide (oxidizable, Fraction 3) fractions.

The determination of the total concentrations of the investigated elements was carried out after acid digestion of the sewage sludge samples and CRMs. The detailed procedure of the microwave digestion is presented in [30]. The sludge pH was measured on sludge extract at a sludge/deionized water ratio of 1:10 (w/v). The total organic carbon (TOC) content was determined by the loss on ignition at 200°C (total inorganic carbon) and 900°C (total carbon).

Instrumentation

Metal determination in the extracts and digests was carried out using inductively coupled plasma mass spectrometry (ICP-MS, Perkin-Elmer SCIEX Elan DRC-e) with a cross-flow nebulizer. The calibration standards, experimental conditions and the determined isotopes are described in [10]. A mechanical rotator (MX-RL-E), a centrifuge (Rotofix 32 A Hettich, Germany), and a pH meter (Sartorius PT-15) were used throughout the extraction experiments. For microwave digestion of the samples, the Microwave Reaction System (Anton Paar, Multiwave 3000) was used.

RESULTS AND DISCUSSION

Total concentrations of the elements

The concentrations measured in each fraction, the sum concentration in the three BCR fractions (Fr.1+Fr.2+Fr.3), and the total concentrations are presented in Table 1 for the essential elements and in Table 2 for the PTEs. The results are an average of three replicates, characterized by the respective standard deviations. For the CRMs ERM-CC144 and CRM 029 the experimental results for the total concentrations, as well as the certified/indicative values (in brackets) are presented.

Table 1. Concentrations (mg/kg) of the essential elements in the studied fractions. Reported values are means \pm standard deviation.

	Distilled water extract	Fraction 1	Fraction 2	Fraction 3	Sum BCR	Total concentration: Experimental value (Certified value)
Sewage sludge 1 (pH 4.83, TOC 44.0%)						
Na	427 \pm 21	688 \pm 32	69 \pm 3	55 \pm 3	812	5124 \pm 105
K	621 \pm 30	1365 \pm 61	578 \pm 26	189 \pm 9	2132	10251 \pm 230
Ca	3873 \pm 190	9140 \pm 450	6195 \pm 305	564 \pm 26	15899	16029 \pm 610
Mg	1098 \pm 55	2211 \pm 108	646 \pm 31	429 \pm 21	3286	4845 \pm 208
Mn	17.6 \pm 0.7	111 \pm 4	71 \pm 3	11.0 \pm 0.5	193	194 \pm 6
P	1273 \pm 61	3583 \pm 176	4775 \pm 236	3085 \pm 150	11443	21564 \pm 650
Fe	63 \pm 3	135 \pm 6	5869 \pm 290	1047 \pm 51	7051	26804 \pm 1210
B	0.089 \pm 0.005	0.19 \pm 0.01	0.22 \pm 0.01	0.29 \pm 0.02	0.70	0.82 \pm 0.03
Mo	0.082 \pm 0.004	0.030 \pm 0.002	0.10 \pm 0.01	3.35 \pm 0.07	3.48	3.5 \pm 0.2
ERM-CC144 (pH 6.40, TOC 33.1%)						
Na	361 \pm 17	627 \pm 31	160 \pm 7	63 \pm 3	850	1780 \pm 73 (1800)
K	533 \pm 23	920 \pm 46	457 \pm 23	112 \pm 5	1489	2920 \pm 140 (2900)
Ca	2953 \pm 144	19777 \pm 980	9192 \pm 440	1566 \pm 72	30535	30885 \pm 896 (31000)
Mg	335 \pm 15	1110 \pm 54	863 \pm 43	290 \pm 15	2263	3780 \pm 163 (3800)
Mn	5.61 \pm 0.21	159 \pm 7	166 \pm 8	22 \pm 1	346.9	348 \pm 16 (352 \pm 14)
P	258 \pm 12	372 \pm 16	1168 \pm 56	3363 \pm 168	4903	16680 \pm 584 (16600)
Fe	100 \pm 5	841 \pm 41	8795 \pm 410	2710 \pm 132	12346	32875 \pm 887 (32900 \pm 1600)
B	17.7 \pm 0.7	20.5 \pm 0.9	10.1 \pm 0.5	3.51 \pm 0.17	34.04	54.1 \pm 0.9
Mo	1.62 \pm 0.08	0.72 \pm 0.04	0.15 \pm 0.01	4.04 \pm 0.08	4.91	12.7 \pm 0.6
CRM 029 (pH 6.60, TOC 28.2%)						
Na	2248 \pm 110	3318 \pm 161	225 \pm 11	33 \pm 2	3576	3860 \pm 158 (3773 \pm 275)
K	1438 \pm 70	2218 \pm 110	577 \pm 26	56 \pm 3	2851	5110 \pm 245 (4918 \pm 975)
Ca	2506 \pm 123	22638 \pm 1129	13313 \pm 661	1083 \pm 52	37034	37986 \pm 1140 (38016 \pm 2800)
Mg	1430 \pm 70	7209 \pm 350	2438 \pm 120	886 \pm 44	10533	12073 \pm 520 (11858 \pm 266)
Mn	3.53 \pm 0.09	81 \pm 4	167 \pm 8	13.6 \pm 0.6	262	259 \pm 13 (264 \pm 10)
P	475 \pm 21	2688 \pm 131	3395 \pm 163	3804 \pm 190	9887	20987 \pm 734 (21100 \pm 2600)
Fe	52 \pm 3	185 \pm 9	3435 \pm 170	1046 \pm 52	4666	20126 \pm 543 (20199 \pm 1343)
B	116 \pm 5	152 \pm 4	27.0 \pm 0.8	8.1 \pm 0.3	187	601 \pm 27 (606 \pm 49)
Mo	72 \pm 3	5.0 \pm 0.2	1.57 \pm 0.08	142 \pm 6	149	152 \pm 7 (155 \pm 4)
Sewage sludge 2 (pH 7.58, TOC 52.3%)						
Na	2067 \pm 103	2475 \pm 121	157 \pm 7	43 \pm 2	2675	4068 \pm 102
K	1199 \pm 57	1722 \pm 84	444 \pm 22	78 \pm 4	2244	3418 \pm 165
Ca	792 \pm 40	29635 \pm 1480	10542 \pm 525	1137 \pm 56	41314	41649 \pm 1180
Mg	223 \pm 10	1923 \pm 98	539 \pm 26	164 \pm 8	2626	3587 \pm 108
Mn	2.90 \pm 0.06	814 \pm 23	2255 \pm 112	186 \pm 9	3255	3316 \pm 329
P	51 \pm 2	74 \pm 3	61 \pm 3	317 \pm 14	452	32806 \pm 1300
Fe	74 \pm 3	128 \pm 6	44355 \pm 2200	11245 \pm 560	55728	238603 \pm 10900
B	<0.002	<0.002	<0.002	<0.002	<0.002	<0.002
Mo	2.35 \pm 0.07	0.010 \pm 0.001	0.056 \pm 0.003	1.67 \pm 0.07	1.74	13.2 \pm 0.2

^a result obtained in [30]

Table 2. Concentrations [mg/kg] of PTEs in the studied fractions. Reported values are means \pm standard deviation.

	Distilled water extract	Fraction 1	Fraction 2	Fraction 3	Sum BCR	Total concentration: Experimental value (Certified value)
Sewage sludge 1						
Ni	1.23 \pm 0.05	5.02 \pm 0.20	10.7 \pm 0.4	9.56 \pm 0.4	25.3	29 \pm 1
Zn	46.9 \pm 0.8	543 \pm 10	488 \pm 9	32.4 \pm 0.6	1063	1108 \pm 60
Cd	0.069 \pm 0.004	0.52 \pm 0.02	1.32 \pm 0.03	0.15 \pm 0.01	1.99	2.0 \pm 0.1
Cu	1.34 \pm 0.05	4.05 \pm 0.12	16.8 \pm 0.16	204 \pm 8	225	229 \pm 7
Pb	0.040 \pm 0.002	0.15 \pm 0.01	5.30 \pm 0.01	0.86 \pm 0.04	6.31	32 \pm 1
Cr	0.12 \pm 0.01	1.00 \pm 0.05	3.36 \pm 0.05	61 \pm 3	65.0	88 \pm 4
As	0.35 \pm 0.02	0.83 \pm 0.05	3.58 \pm 0.04	2.51 \pm 0.12	6.92	15 \pm 1
Hg	<0.002	<0.002	<0.002	<0.002	<0.002	<0.002
ERM-CC144						
Ni	4.75 \pm 0.15	8.10 \pm 0.08	9.90 \pm 0.09	16.6 \pm 0.2	34.6	92 \pm 6 (91 \pm 7)
Zn	14.9 \pm 0.3	405 \pm 8	354 \pm 7	215 \pm 4	974	985 \pm 33 (980 \pm 40)
Cd	0.14 \pm 0.07	2.45 \pm 0.09	9.07 \pm 0.5	0.87 \pm 0.04	12.4	14.7 \pm 0.9 (14.5 \pm 1.4)
Cu	29.1 \pm 0.9	25.2 \pm 0.7	11.0 \pm 0.4	316 \pm 11	352	351 \pm 12 (348 \pm 18)
Pb	0.074 \pm 0.004	0.40 \pm 0.02	1.99 \pm 0.08	2.03 \pm 0.08	4.42	159 \pm 6 (157 \pm 9)
Cr	0.84 \pm 0.03	1.74 \pm 0.09	1.34 \pm 0.07	42 \pm 2	45.1	167 \pm 8 (168 \pm 14)
As	0.90 \pm 0.05	1.71 \pm 0.08	3.40 \pm 0.20	2.56 \pm 0.09	7.67	7.8 \pm 0.4 (7.7 \pm 0.7)
Hg	0.024 \pm 0.002	0.030 \pm 0.002	0.010 \pm 0.001	0.009 \pm 0.001	0.05	6.1 \pm 0.3 (5.9 \pm 0.6)
CRM 029						
Ni	7.97 \pm 0.11	30.4 \pm 0.7	36 \pm 1	10.8 \pm 0.4	77.4	127 \pm 4
Zn	8.83 \pm 0.12	5.90 \pm 0.08	1015 \pm 20	44.4 \pm 0.8	1065	1080 \pm 20
Cd	0.73 \pm 0.04	21.8 \pm 0.6	73 \pm 3	2.93 \pm 0.07	98.0	122 \pm 7
Cu	15.5 \pm 0.3	24.3 \pm 0.7	17.6 \pm 0.7	689 \pm 23	731	736 \pm 33
Pb	0.22 \pm 0.01	0.33 \pm 0.02	2.15 \pm 0.08	2.06 \pm 0.05	4.54	119 \pm 5
Cr	1.54 \pm 0.07	8.31 \pm 0.4	23.5 \pm 0.9	308 \pm 14	340	353 \pm 12
As	10.6 \pm 0.6	77 \pm 3	48 \pm 2	72 \pm 4	197	256 \pm 9
Hg	0.29 \pm 0.02	0.17 \pm 0.01	0.060 \pm 0.004	0.93 \pm 0.06	1.16	18.7 \pm 0.8
Sewage sludge 2						
Ni	8.61 \pm 0.13	26.5 \pm 0.8	63 \pm 2	18.7 \pm 0.7	108	108 \pm 3
Zn	1.82 \pm 0.04	31.3 \pm 0.6	578 \pm 12	27.0 \pm 0.5	634	670 \pm 30
Cd	0.010 \pm 0.001	0.045 \pm 0.002	0.38 \pm 0.02	0.036 \pm 0.002	0.42	0.57 \pm 0.02
Cu	36.4 \pm 0.8	8.68 \pm 0.3	77 \pm 3	415 \pm 16	500	504 \pm 12
Pb	0.0038 \pm 0.0002	0.015 \pm 0.002	0.063 \pm 0.003	0.19 \pm 0.01	0.27	9.6 \pm 0.4
Cr	0.12 \pm 0.01	0.91 \pm 0.05	5.08 \pm 0.15	170 \pm 8	176	185 \pm 11
As	0.79 \pm 0.05	0.40 \pm 0.02	4.05 \pm 0.12	0.17 \pm 0.01	4.62	12 \pm 1
Hg	<0.002	<0.002	<0.002	<0.002	<0.002	<0.002

The data for the total concentrations show that Fe, P, Ca, K, Na, Mg and Mn are the macroelements in all the samples. The order of decreasing concentrations is: Sewage sludge 1: Fe>P>Ca>K>Na>Mg>Mn; ERM-CC144: Fe>Ca>P>Mg>K>Na>Mn; CRM 029: Ca>P>Fe>Mg>K>Na>Mn; Sewage sludge 2: Fe>Ca>P>Na>Mg>K>Mn.

The analyzed samples and CRMs are of different types – domestic (SS1, CC144 and CRM 029) and industrial (SS2) sewage sludge. The data in Table 1 show that the total concentrations range from 1800 to 5124 mg/kg for Na, 2900-10251 mg/kg for K, 16029-41649 mg/kg for Ca, 3587-11858 for Mg, and 16600-32806 mg/kg for P. Wider concentration

ranges were established for Fe (20199-238603 mg/kg), and Mn (194-3316 mg/kg), being in one order higher concentrations in Sewage sludge 2. With regard to the PTEs, wide concentration ranges were found for Mo (3.5-155 mg/kg), B (<0.002-606 mg/kg), Cd (0.57-122 mg/kg), Pb (9.6-157 mg/kg), As (7.7-256 mg/kg), and Hg (<0.002 to 18.7 mg/kg), the maximum concentrations were determined in the domestic sludge CRM 029. The rest of the microelements show narrower concentration ranges, e.g., 670-1108 mg/kg for Zn, 229-736 mg/kg for Cu, 88-353 mg/kg for Cr, and 29-127 mg/kg for Ni. The concentrations of B, Cd, Pb are much lower in the examined Bulgarian samples than in the analyzed CRM; Hg is below the LOD. Although the

concentration intervals varied to a different extent for the individual elements, the application of ANOVA showed statistically significant differences between the samples for all elements.

Water solubility

The water-soluble fractions of the studied elements, expressed as a percentage of the total concentrations, are presented in Fig. 1.

The results show a linear relationship between the increase in sample pH and the water solubility of K and an inverse relationship for Ca and Mg. The solubility of Na also increased from sample pH 4.83 (SS1) to sample pH 6.60 (CRM 029) and decreased slightly at sample pH 7.58 (SS2). An increase in the solubility of K in the direction from very acidic to alkaline sample pH was also found in [31] for soil samples. Despite the low percentages, a tendency for decrease of water solubility with sample pH increase was found for Mn, and P. Low solubility with maximum of 0.3% in ERM-CC144 was found for Fe. The solubility of Mo and B varies widely and is between 2.3% and 47% for Mo and in the range from 11% to 33% for B. A low degree of water solubility, was found for the PTEs. The data show no dependence of their solubility on the acidity of the samples, with the exception of a slight increase for Ni, resp. decrease for Zn on increasing sample pH. The presented results indicate low mobility in water for the PTEs, irrespective of their total concentrations. The lowest solubility was

established for Pb (0.04%) and Cr (0.06%) and the highest for As (11.5%). These data indicate that there is no potential ecological threat when the sewage sludge samples are leached with water under natural conditions. With the decrease in the pH of the water, however, for example in the case of acid rain, an increase in the extraction efficiency is expected. The effect of pH on the heavy metal extraction with nitric and hydrochloric acid on the degree of extraction of Ni, Cu, Zn, Cr, and Pb in the pH range from 1 to 4 was studied in [32]. Although there was a wide variation of the extraction efficiency for the metals within the studied pH interval, for all elements an increase in the degree of extraction with decreasing pH was found.

BCR extraction scheme

The accuracy of the obtained results was assessed by analysis of the CRM BCR-701, for which certified values for the concentrations of Cd, Cr, Cu, Ni, Pb and Zn in Fraction 1, Fraction 2 and Fraction 3 of the BCR sequential extraction procedure are available. A comparison of the experimental and certified values is presented in Table 3. The experimental and the certified values agree well within uncertainty limits.

The results of the BCR extraction scheme of the sewage sludge samples and CRMs, expressed as a percentage of the total concentrations, are presented in Fig. 2.

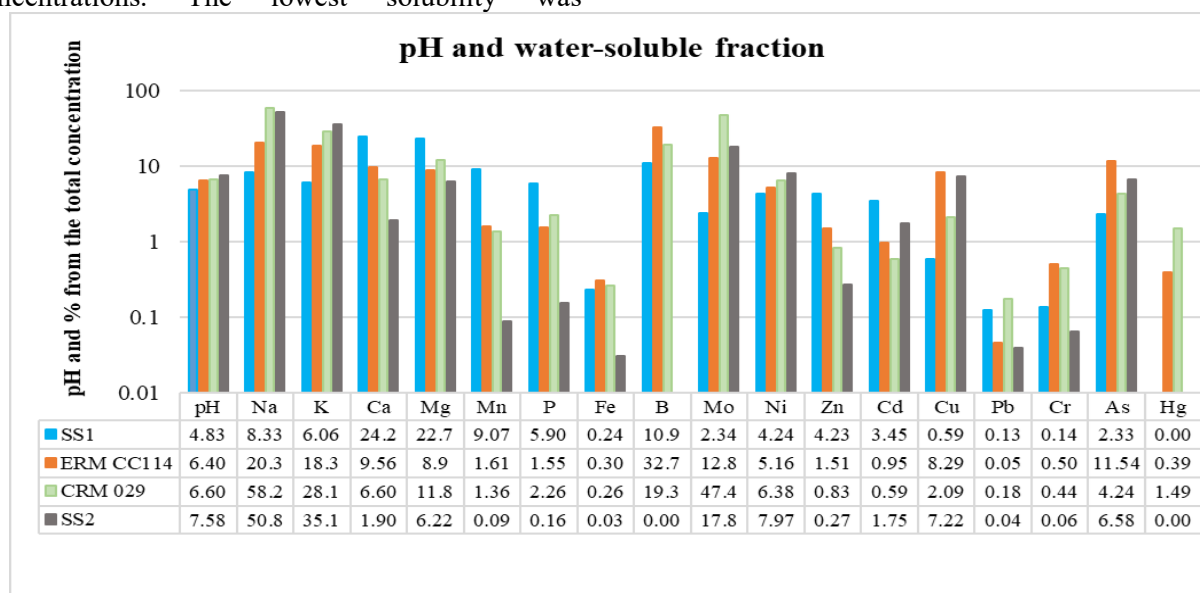
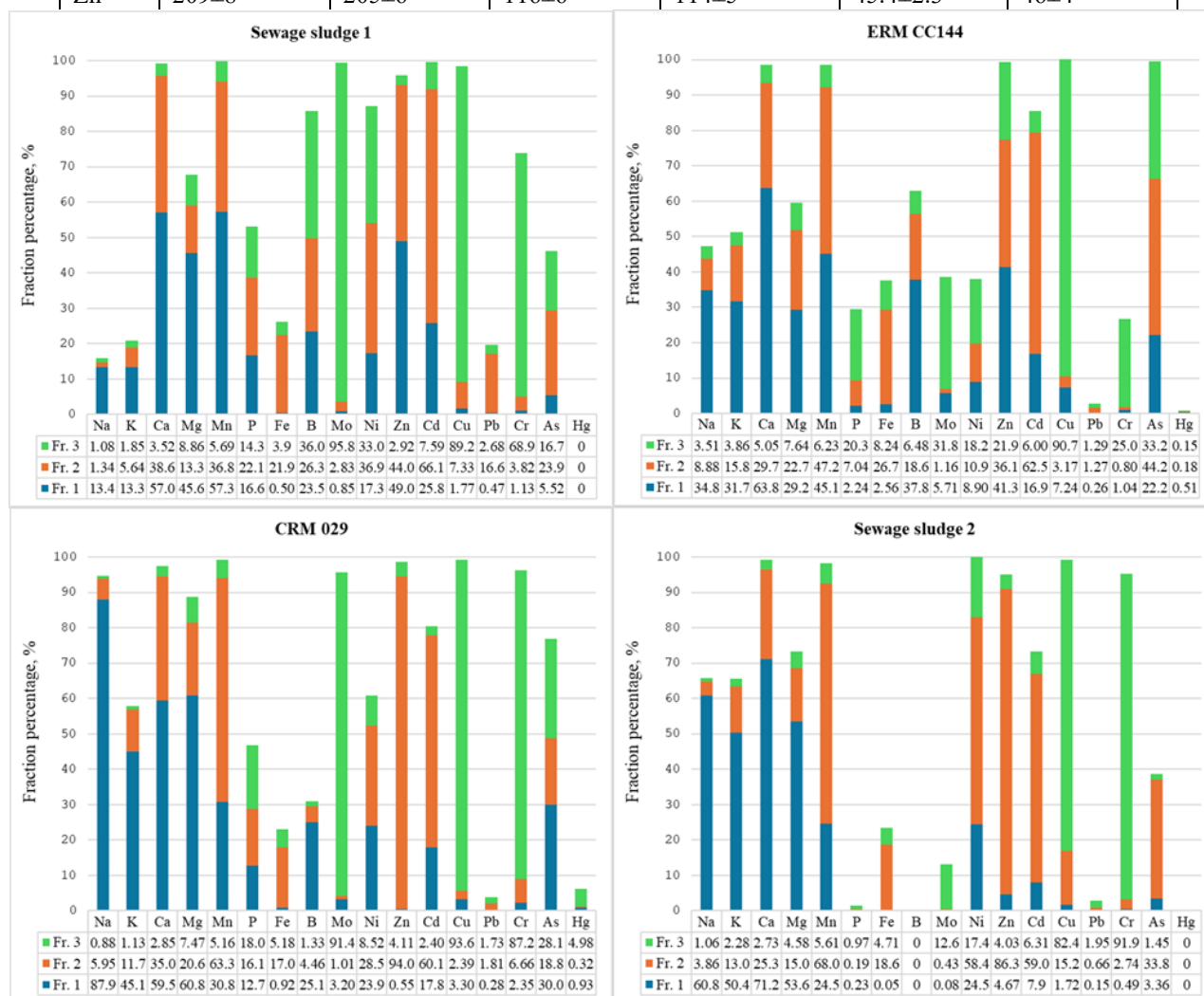


Figure 1. Water-soluble fractions of essential and PTEs. BCR extraction scheme

Table 3. Experimental and certified concentrations of Cd, Cr, Cu, Ni, Pb and Zn in CRM BCR – 701, obtained by the BCR extraction procedure.

	Fraction 1		Fraction 2		Fraction 3	
	Determined	Certified	Determined	Certified	Determined	Certified
Cd	7.70±0.50	7.3±0.4	3.81±0.34	3.77±0.28	0.30±0.07	0.27±0.06
Cr	2.41±0.15	2.26±0.16	47.0±3.0	45.7±2.0	146±6	143±7
Cu	50.4±2.5	49.3±1.7	128±5	124±3	54±5	55±4
Ni	16.4±0.9	15.4±0.9	29.0±2.0	26.6±1.3	14.8±0.9	15.3±0.9
Pb	3.29±0.35	3.18±0.21	123±5	126±3	10.5±1.4	9.3±2.0
Zn	209±8	205±6	116±6	114±5	45.4±2.3	46±4

**Figure 2.** Percentage of essential and PTEs in the sludge samples.

The results show an increase of the sum BCR extraction percentage (Fr.1+Fr.2+Fr.3) for Na with increasing pH of the samples from 4.83 (SS1) to 6.60 (ERM-CC144) and a decrease at 7.58 (SS2), which is fully consistent with the data of the water extraction. High mobility and linear increase of the sum extraction with increasing sample pH was also found for K. A trend of increasing the available fraction of K with increasing pH was established for soil samples [31]. The decrease in the concentration of mobile K forms at low pH could be explained by competition with high concentrations of H^+ and

other soluble ions (Al, Ca). Increasing the pH leads to the formation of insoluble calcium phosphate species and aluminum hydroxide precipitates and an increase of the mobile species of K. Despite the varying percentage of sum extractions in the analyzed samples, the highest percentage of Na and K was extracted in the exchangeable fraction, which was between 1.2 and 2.2 times higher than that in the water-soluble fraction.

High sum BCR extraction close to 100% was obtained for Ca. Its distribution shows mainly the presence of easily mobile species in the

exchangeable fraction, which represent more than 50% of the total extracted Ca independent of the sample pH. The total extracted percentage of Mg is lower and ranges from 60% to 89%. In all the samples, Mg is also predominantly associated with the exchangeable phase. Main binding in the exchangeable fraction of Na, K, Ca and Mg was also found in [23]. High mobility and sum extraction close to 100% were observed for Mn. In the acidic Sewage sludge 1 it is predominately associated with the exchangeable fraction (57%), in ERM-CC144 it is evenly distributed in the exchangeable and oxide fractions (45%, resp. 47%), in CRM 029 the percentage of Mn in the oxide fraction dominates over the exchangeable (31% vs. 63%), which is even more pronounced in Sewage sludge 2 (25%-68%). The fractionation of P also shows a strong dependence on sample pH and the differences in sum extraction are consistent with the water solubility data. The highest degree of sum extraction (average 50%) was observed in the acidic Sewage sludge 1 and CRM 029. In both samples, P was relatively evenly distributed in the three fractions. In ERM-CC144, the sum extraction was below 30%, predominantly in the form of organic complexes. A very low degree of mobility (total 1.4%) was found in the alkaline Sewage sludge 2, due to the formation of insoluble compounds which reduce its availability. The sum extraction of Fe was in the range from 23% to 38%, the main part of it being in the oxide fraction, which also corresponds to the low water solubility. The total extracted fraction of B varied between 31% and 86%, and decreased with increasing the sample pH from 4.86 to 6.6. The fractionation also depends on the sample matrix. In the acidic Sewage sludge 1, it is fairly even distributed in the three fractions, while in ERM-CC144 and CRM 029 binding to the exchangeable fraction predominates. The data in Fig. 2 show that the total solubility of Zn amounts to 100% in all the samples. It is mainly bound in exchangeable and oxide fractions in Sewage sludge 1 and ERM-CC144 and in the oxide fraction in CRM 029 and Sewage sludge 2. The data show that main binding to the organic fraction in all the samples was found only for Mo, Cu and Cr. The total extracted percentages varied from 13% to 99% for Mo, from 27% to 96% for Cr, and above 98% for Cu. The percentage of the elements in the organic fraction does not depend on the organic carbon concentration in the sewage samples. The fractionation of Cu and Cr confirmed literature data on the high tendency of these elements to form organic complexes [14, 22], which suggests their low mobility and bioavailability.

High degree of sum extraction from 73% to 100% was also obtained for Cd with more than 60% of it was bound in the oxide fraction in all samples. For the remaining PTEs, the sum extraction and the fractionation depended on both the sample matrix and the element itself. The sum BCR extraction of Ni in the acidic sludge SS1 was 87%, evenly distributed in the oxide and organic fractions, and least in the exchangeable fraction. The sum extraction tended to 100% in the alkaline SS2, but it was mostly bound in the oxide fraction and had a lower and approximately equal tendency to bind to the other two fractions.

In ERM-CC144 the sum extraction was 38%, half of which in the organic fraction, followed by oxide and exchangeable fractions, while in CRM 029 the sum extraction of 61% was mainly due to the formation of oxide and exchangeable species. Very low sum extraction, below 4%, was found for Pb, except for the acidic Sewage sludge 1, in which the total extracted percentage was 19.7%. The extracted part of Pb was mainly bound in the form of oxides and organic complexes, similar to the data obtained in [14, 28, 33, 34]. The present results indicate low mobility of Pb in sewage sludge due to its binding in immobilized forms in sewage sludge samples. Hg was below the limit of detection in SS1 and SS2. In ERM-CC144 and CRM 029 the total extraction was below 1%, and 6.2%, resp., mainly in the form of organic complexes. Due to the low total extraction percentages, and the predominant binding of Pb and Hg in the oxide and organic fractions, they also do not pose an environmental pollution risk. The data for As show sum extraction below 50% in the acidic SS1 and alkaline SS 2, and an increase to 100% in ERM-CC144. Regardless of the varying sum extraction, a major binding in the oxide fraction was established for these samples. Different fractionation was observed in CRM 029. The total mobility reached 77%, 30% of which were in the exchangeable, 28% in the organic and 19% in the oxide fraction. A fractionation study for Cd, Cr, Cu, Ni, Pb, Zn and Hg in ERM-CC144 was conducted in [15] as well. The obtained concentrations in the individual fractions differ from the present data for some elements, the most significant differences being for Cd in Fraction 1, Ni in Fraction 2 and Fraction 3, Pb in Fraction 2 and Fraction 3 and Hg in Fraction 1. However, in both studies an identical distribution of the elements in the studied fractions is obtained.

CONCLUSIONS

The main aim of this study was to conduct a fractionation study of essential and potentially toxic

elements in domestic (SS1, ERM CC-144 and CRM 029) and industrial (SS2) sewage sludge. The total concentrations of the studied elements showed statistically significant differences between the samples. The results from the sequential extraction showed that the most mobile metals are Na, K, Ca and Mg, being concentrated in the exchangeable fraction. Mn, Fe and B are mainly accumulated in the easily assimilable fractions (exchangeable and reducible) which indicates their high bioavailability. Low mobility is expected for Mo with dominant binding to the organic phase and for P, concentrated in the organic phase or distributed among the three phases. Metals contained in the sludge can be rereleased, when added to soil, depending on the soil pH, soluble metals, acid rain, dissolved oxygen content, decomposition of organic substances with the participation of microorganisms, redox potential, etc. [34]. The storage of sludge under different atmospheric conditions, may cause release of metals from the sludge.

The concentrations of the PTEs in Bulgarian sewage sludge samples are far below the permitted levels. The data show water leachability below 12%. The BCR fractionation indicates low tendency to form exchangeable species for Cu, Pb, Cr and Hg. Although Ni, Zn, Cd and As show high affinity to the oxide fraction, significant percentages are extracted as exchangeable species. Because the exchangeable, followed by the reducible fraction are highly mobile, the data indicate a potential risk of soil and plant pollution with Ni, Zn, Cd and As.

Acknowledgement: This research was financially supported by the Project Grant № BG16rfpr002-1.014-0015: "Clean technologies for sustainable environment – water, waste, energy for circular economy", financed by the European Regional Development Fund through the Bulgarian programme "Research, innovation and digitalization for smart transformation". The financial support by INFRAMAT (modern research infrastructure in support of science, culture and technological development) is gratefully acknowledged. The authors are grateful to Prof. Stefan Tsakovski for the help in the statistical processing of the results.

REFERENCES

1. Z. Chang, G. Long, J. L. Zhou, C. Ma, *Resour. Conserv. Recycl.*, **154**, 104606 (2020).
2. N. Anderson, R. Snaith, G. Madzharova, J. Bonfait, L. Doyle, A. Godley, M. Lam, G. Day. Sewage sludge and the circular economy. European Environmental Agency, 2021.
3. Y. El Hammoudani, F. Dimane, H. El Ouarghi, H., *Env. Wat. Sci. pub. H. Ter. Int. J.*, **3(1)**, 47 (2019).
4. R. Pöykiö, G. Watkins, O. Dahl, *Ecol. Chem. Eng. S*, **26(3)**, 547 (2019).
5. Regulation on procedure and manner for use of sludge from the treatment of waste waters through their application in agriculture. Adopted by CMD No 339 of 14.12.2004.
6. Council Directive 86/278/EEC of 12 June 1986 on the protection of the environment, and in particular of the soil, when sewage sludge is used in agriculture.
7. J. Feng, I. T., Burke, X. Chen, D. I. Stewart, *Rev. Environ. Sci. Biotechnol.*, **22(4)**, 1037 (2023).
8. D. Olejnik, *Sustainability*, **16(12)**, 5198 (2024).
9. M. Urbaniak, A. Baran, J. Giebułtowiec, A. Bednarek, L. Serwecińska, *Sci. Total Environ.*, **912**, 168856 (2024).
10. D. Valchev, I. Ribarova, B. Borisov, V. Radovanov, V. Lyubomirova, I. Kostova, G. Dimova, O. Karpuzova, S. Lazarova, *Environ. Sci. Eur.*, **36**, 11 (2024).
11. L. Dabrowska, *Ecol. Chem. Eng. A*, **23(1)**, 63 (2016).
12. M. Tytła, K. Widziewicz-Rzońca, J. Kernert, Z. Bernaś, K. Słaby, *Water*, **15(4)**, 666 (2023).
13. A. Wojciula, D. Boruszko, G. Pajewska, *J. Ecol. Eng.*, **22(4)**, 98 (2021).
14. M. Jakubus, M., *Environ. Pollut. Bioavailab.*, **32(1)**, 87 (2020).
15. M. Tytła, K. Widziewicz-Rzońca, Z. Bernaś, Z., *Molecules*, **27(15)**, 4947 (2022).
16. C. P. Diao, C. H. Wei, *Environ. Prot. Eng.*, **43(4)**, 191 (2017).
17. A. Fuentes, *J. Hazard. Mater.*, **108(3)**, 161 (2004).
18. R. Hedia, R., *Egypt. J. Soil Sci.*, **54(3)**, 195 (2014).
19. G. Rauret, J.-F. López-Sánchez, A. Sahuquillo, E. Barahona, M. Lachica, M., A. M. Ure, C. M. Davidson, A., Gomez, D. Lück, J. Bacon, M. Yli-Halla, H. Muntau, Ph. Quevauviller, *J. Environ. Monit.*, **2(3)**, 228 (2000).
20. E. Bezak-Mazur, A. Mazur, R. Stoińska, *Environ. Prot. Eng.*, **40(3)**, 61 (2014).
21. V. Paulauskas, E. Zaleckas, N. Sabienė, *Proc. 15th Int. Sci. Conf., Akademija, Aleksandras Stulginskis University*, **5(1)**, 422 (2011).
22. E. Zaleckas, V. Paulauskas, E. Sendžikienė, *J. Environ. Eng. Landsc. Manag.*, **21(3)**, 189 (2012).
23. R. Zufiaurre, A. Olivar, P. Chamorro, C. Nerin, A. Callizo, *The Analyst*, **123(2)**, 255 (1998).
24. H. A. Elliott, B. A., Dempsey, P. J. Maille, *J. Environ. Qual.*, **19(2)**, 330 (1990).
25. M. N. Rashed, M. E. Soltan, E. M. Fawzey, M. A. El-Taher, M. A. *Int. J. Environ. Prot.*, **1(4)**, 37 (2011).
26. C. Wang, C., X.-C. Li, H.-T. Ma, J. Qian, J. -B. Zhai, *J. Hazard. Mater.*, **137(3)**, 1277 (2006).
27. M. K. Jamali, T. G. Kazi, M. B., Arain, H. I. Afridi, N. Jalbani, G. A. Kandhro, A. Q. Shah, J. A. Baig, J. A., *J. Hazard. Mater.*, **163(2-3)**, 1157 (2009).
28. A. Łukowski, *J. Ecol. Eng.*, **18(1)**, 132 (2017).

29. A. M. Ure, Ph. Quevauviller, H. Muntau, B. Griepink, *Int. J. Environ. Anal. Chem.*, **51**(1–4), 135 (1993).
30. V. Lyubomirova, I. Belovezhdova, R. Djingova, P. Petrov, E. Todorova, *Processes*, **11**(12), 3379 (2023).
31. M. Fotyma, P. Ochal, J. Łabętowicz, in: *Soil Processes and Current Trends in Quality Assessment*, M. C. Hernandez Soriano (ed.), IntechOpen, 2013.
32. S. Gaber, M. Rizk, M. Yehia, *Biokemistry*, **23**(1), 41 (2011).
33. J. Liu, S. Sun, *Trans. Nonferrous Met. Soc. China*, **23**(8), 2397 (2013).
34. M. Janas, A. Zawadzka, R. Cichowicz, *Environ. Sci. Pollut. Res.*, **25**(33), 33240 (2018).

Efficient synthesis of 5-oxo-5,6,7,8-tetrahydro-4*H*-chromenes using zinc ferrite nanoparticles as a catalyst

A. K. Mhaske¹, V. V. Vikhe¹, A. G. Gadhave¹, Y. R. Baste², B. K. Uphade^{1*}

¹Research Center, Department of Chemistry, Padmashri Vikhe Patil College of Arts, Science and Commerce (Affiliated to S.P.P.U., Pune) Pravaranagar, 413713, India

²Department of Chemistry, KSKW Arts, Science and Commerce College, Uttamnagar, Nashik 422008, India

Received: July 16, 2025; Revised: September 04, 2025

In this work we report an environmentally green and efficient zinc ferrite-nanocatalyzed protocol for the synthesis of 5-oxo-5,6,7,8-tetrahydro-4*H*-chromenes by one-pot three-component condensation of aromatic aldehydes, malononitrile, and dimedone under reflux. The best yield was obtained by appropriate one-pot condensation reactions using different aromatic aldehydes with electron-donating or electron-withdrawing groups. Additionally, this catalyst is easily removed and can be recycled six times without considerable decrease in its activity. The advantages of this work include nanocatalyst reusability, short reaction time, non-toxic reaction, high purity, and excellent yield.



Keywords: Zinc ferrite nanoparticles, aromatic aldehyde, dimedone, malononitrile, 4*H*-chromenes, Knoevenagel condensation.

INTRODUCTION

Multicomponent reactions (MCRs) have an interesting function in organic and medicinal synthesis [1] consisting in combining three or more starting compounds to produce a final product. Almost all atoms in the starting compounds participate in the new final product [2-5]. In the last few years, MCRs have been powerful and effective bond forming mechanisms in organic and medicinal chemistry [6]. Typically, the MCRs technique gives an extensive amount of atom economy, convenience of a one-pot process, potential structural modifications, and a synthesis that takes less time and yields the target product [7]. The MCRs can save solvents and reagents, be used to synthesize complex compounds in a single conventional step and reduce complex purification processes due to the final product's inclusion of all starting materials [6, 7].

The synthesis of 5-oxo-5,6,7,8-tetrahydro-4*H*-chromene and its derivatives has recently generated a lot of interest due to their biological and pharmacological activities [8]. The 4*H*-chromene has many pharmacological properties, such as anticancer [9], diuretic [10], spasmolytic [11], anticoagulant [12], anti-anaphylactic [13], antitumor [14], cytotoxic [6],

hypotensive [15], antibacterial [16], antiviral [17], antimalarial [18] and anti-anxiety [19]. 4*H*-chromenes are the fundamental structural component of a number of natural compounds. Furthermore, nitrile-functionalized 4*H*-chromene derivatives are helpful intermediates for the synthesis of a variety of chemicals, including lactones, pyridines, 1, 4-dihydropyridines, methyl acetoacetate, malonylurea, imido-esters, 1,3-cyclohexanedione, and aminopyrimidines [20-22]. In addition, other applications can be mentioned, such as lasers, dyes, pigments, cosmetics, optical brighteners, and biodegradable agrochemical products [20, 21].

In this work, the synthesis of 4*H*-chromene derivatives was performed using zinc ferrite nanoparticles. The mixture of aldehyde, malononitrile, and dimedone was used in the presence of various catalytic systems such as poly(4-vinylpyridine) [1], WETSA [11], Zn(L-proline)₂ [7], HDMBAB [12], Yb(PFO)₃ [8], β-CD-glycerin [16], SBSSA [6], MCM-41@Schiff base-Co(OAc)₂ [23], Fe₃O₄@SiO₂@propyl-ANDSA [17], β-CD [13], Fe₃O₄@GO-N-(pyridin-4-amine) [15], RGO-Pr-SH@AuNPs [24], BaFe₁₂O₁₉@IM [21], HMS/Pr-Rh-Zr [25], Bis-Su [26], aspartic acid [27], CuO nanoparticles [28], Fe₃O₄@UiO@DAS [29], and CaO@SiO₂-SO₃H [30].

* To whom all correspondence should be sent:
E-mail: bhagwatuphade@gmail.com

However, most of these reactions suffer from several drawbacks like expensive catalyst, toxic metal, drastic reaction conditions, long reaction time and low yields. Hence, there is still a demand for ecofriendly, efficient, feasible, and cost-effective synthetic protocols for the synthesis of 4H-chromenes. In this respect, significant efforts are being made to give out the hazardous catalysts for cheap, safe, and environmentally friendly biodegradable alternatives [20]. As we continue our long-term research focused on creating more advanced synthetic methodologies, herein we would like to share a simple green method for the efficient synthesis of 5-oxo-5,6,7,8-tetrahydro-4H-chromene derivatives.

EXPERIMENTAL

Material

The 4H-chromene products were identified by comparing their spectral, analytical, and physical properties to those published in the literature. The physical constants were determined in an open capillary. The progress of the reaction was monitored by thin-layer chromatography on silica gel-coated ALUGRAM SIL G UV254 plates. ^1H NMR and ^{13}C NMR spectra were recorded on a Bruker Avance NEO 500 MHz spectrometer using $\text{DMSO}-d_6$ as a solvent. A mass spectrum was recorded on a SYNAPT DB A064 spectrometer.

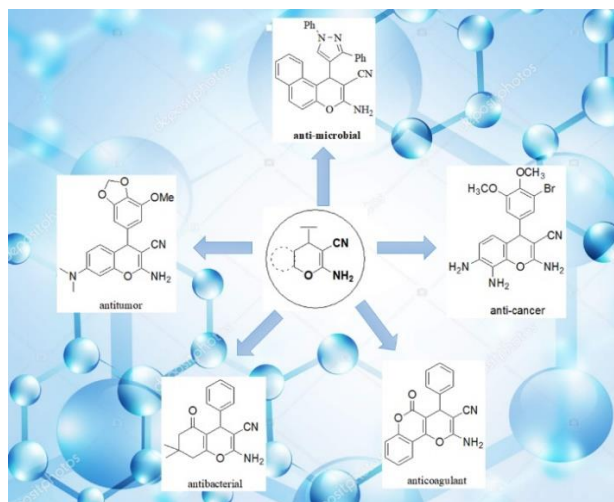


Figure 1. Some bioactive molecules containing chromene derivatives

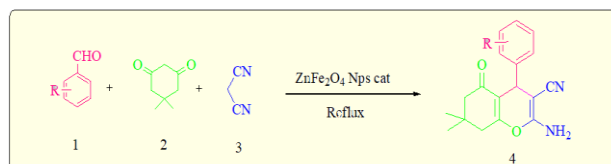
Synthesis of zinc ferrite nanocatalyst

The zinc ferrite nanoparticles were synthesized by the reported method [31]. The zinc ferrite nanoparticles were characterized by FT-IR, XRD, SEM, TEM, EDAX, TG-DTA, and BET techniques [31].

General procedure for synthesis of 5-oxo-5,6,7,8-tetrahydro-4H-chromene derivatives

A mixture of aromatic aldehyde (1 mmol), malononitrile (1 mmol), dimedone (1 mmol) and zinc ferrite nanoparticles (0.04 g) as a catalyst was

used. Then ethanol (10 ml) was added to the above reaction mixture, and the mixture was refluxed. The progress of the reaction was followed by thin-layer chromatography using n-hexane:ethyl acetate (4:1) as an eluent. After completion of the reaction, the crude product was filtered and dried, then recrystallized from ethanol to afford a pure product. The excellent purity of the product was confirmed by comparing physical and spectroscopic data (^1H NMR, ^{13}C NMR, and MS) to actual samples reported in the literature.



Scheme 1. Synthesis of 5-oxo-5,6,7,8-tetrahydro-4H-chromene derivatives

Spectral data of some 4H-chromene derivatives

- 2-amino-7, 7-dimethyl-5-oxo-4-phenyl-5, 6, 7, 8-tetrahydro-4H-chromene-3-carbonitrile (4a): Colorless crystal; m.p. 230-232°C; ^1H NMR (500 MHz, $\text{DMSO}-d_6$) δ (ppm): 0.95-0.99 (s, 3H, CH_3), 1.03-1.07 (s, 3H, CH_3), 2.08-2.26 (d, 1H, CH, $J = 16.3$ Hz), 2.23-2.26 (d, 1H, CH, $J = 16.3$ Hz), 2.49-2.51 (s, 2H, CH_2), 4.17 (s, 1H, CH), 6.98-7.16 (s, 2H, NH_2), 7.17-7.19 (m, 3H, ArH, $J = 5.7$ Hz), 7.26-7.29 (d, 2H, ArH, $J = 5.4$ Hz); ^{13}C NMR (125 MHz, $\text{DMSO}-d_6$) δ (ppm): 26.70, 28.29, 31.69, 35.48, 49.88, 58.24, 112.65, 119.60, 126.46, 127.04, 128.22, 144.63, 158.40, 162.38, 195.53; MF = $\text{C}_{18}\text{H}_{18}\text{N}_2\text{O}_2$, MS; Calc. [M] $m/z = 294.35$; Obs. $m/z = 295.16$ ($\text{M}+\text{H}$) $^+$.

- 2-amino-4-(4-methoxyphenyl)-7, 7-dimethyl-5-oxo-5,6,7,8-tetrahydro-4H-chromene-3-carbonitrile (4b): White crystal; m.p. 194-196°C; ^1H NMR (500 MHz, $\text{DMSO}-d_6$) δ (ppm): 0.94 (s, 3H, CH_3), 1.03 (s, 3H, CH_3), 2.07-2.10 (d, 1H, CH, $J = 16.08$ Hz), 2.22-2.25 (d, 1H, CH, $J = 16.08$ Hz), 2.48-2.50 (m, 2H, CH_2), 3.71 (s, 3H, OCH_3), 4.11 (s, 1H, CH), 6.82-6.84 (d, 2H, ArH, $J = 8.64$ Hz), 6.93 (s, 2H, NH_2), 7.03 (d, 2H, ArH, $J = 8.60$ Hz); ^{13}C NMR (125 MHz, $\text{DMSO}-d_6$) δ (ppm): 27.69, 28.88, 32.20, 34.76, 40.69, 50.70, 55.22, 63.82, 113.99, 114.25, 118.74, 128.63, 135.47, 157.38, 158.62, 161.26, 195.99; MF = $\text{C}_{19}\text{H}_{20}\text{N}_2\text{O}_3$, MS; Calc. [M] $m/z = 347$; Obs. $m/z = 347$ ($\text{M}+\text{H}$) $^+$.

- 2-amino-4-(4-bromophenyl)-7, 7-dimethyl-5-oxo-5,6,7,8-tetrahydro-4H-chromene-3-carbonitrile (4c): White crystal; m.p. 212-214°C; ^1H NMR (500 MHz, $\text{DMSO}-d_6$) δ (ppm): 0.94 (s, 3H, CH_3), 1.03 (s, 3H, CH_3), 2.08-2.12 (d, 1H, CH, $J = 16.08$ Hz), 2.23-2.26 (d, 1H, CH, $J = 16.04$ Hz), 2.50-

2.51 (m, 2H, CH₂), 4.18 (s, 1H, CH), 7.04 (s, 2H, NH₂), 7.10-7.12 (d, 2H, ArH, $J = 8.36$ Hz), 7.47-7.48 (d, 2H, ArH, $J = 8.24$ Hz); ¹³C NMR (125 MHz, DMSO-*d*₆) δ (ppm); 26.93, 28.37, 31.88, 35.27, 50.02, 57.86, 112.31, 119.66, 119.72, 129.59, 131.31, 144.22, 158.58, 162.86, 196; MF = C₁₈H₁₇N₂O₂Br, MS; Calc. [M] $m/z = 373.24$; Obs. $m/z = 373$ (M+H)⁺.

Application of ZnFe₂O₄ nanocatalyst for synthesis of 5-oxo-5,6,7,8-tetrahydro-4H-chromene derivatives

In the present work, the ZnFe₂O₄ nanocatalyst [28] was successfully utilized for the one-pot synthesis of 5-oxo-5,6,7,8-tetrahydro-4H-chromene derivatives using substituted aromatic aldehydes, malononitrile, and dimedone under reflux conditions (Scheme 1). A model reaction of aromatic aldehydes (1 mmol), malononitrile (1 mmol) and dimedone (1 mmol) was used for the synthesis of 5-oxo-5,6,7,8-tetrahydro-4H-chromene derivatives (4a). Initially, the reaction conditions were optimized, including solvent, temperature, and time, as shown in Table 1. To identify the most effective solvent for this transformation, the model reaction was performed using different solvents like H₂O, EtOH and EtOH:H₂O (1:1) under different conditions. The reaction performed as indicated above with ethanol under reflux conditions was considered most suitable for the successful synthesis of 5-oxo-5,6,7,8-tetrahydro-4H-chromenes.

Table 1. Optimization of reaction conditions for the synthesis of 5-oxo-5,6,7,8-tetrahydro-4H-chromenes

Entry	Condition	Temp. (°C)	Time (min)	Yield (%)
1	H ₂ O	r.t	180	No reaction
2	H ₂ O	60-80	120	No reaction
3	H ₂ O	reflux	75	24
4	EtOH:H ₂ O	60-70	90	28
5	EtOH:H ₂ O	reflux	75	49
6	EtOH	r.t	60	34
7	EtOH	60-80	60	47
8	EtOH	reflux	10	74
9	EtOH	reflux	15	88
10	EtOH	reflux	20	92
11	EtOH	reflux	30	95
12	EtOH	reflux	40	95

Reaction conditions: aromatic aldehyde (1 mmol), dimedone (1 mmol) and malononitrile (1 mmol) in presence of ZnFe₂O₄ nanoparticles.

The amount of catalyst has played an important role in the reaction. In the absence of a catalyst, the reaction did not proceed. The results showed that as

the amount of catalyst increases, the amount of product also increases up to 0.04 g of ZnFe₂O₄ nanoparticles (Table 2). All of these reactions were completed in a reaction time of around 30-60 min with good yields of product 4(a-n). In a similar way, the most suitable condition for the synthesis of 5-oxo-5,6,7,8-tetrahydro-4H-chromene derivatives, was found to be using 0.04 g of catalyst under reflux conditions.

Table 2. Optimization of catalyst in the synthesis of 5-oxo-5,6,7,8-tetrahydro-4H-chromenes

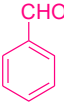
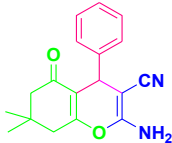

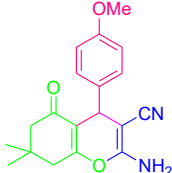
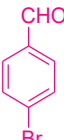
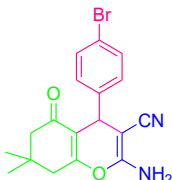
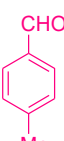
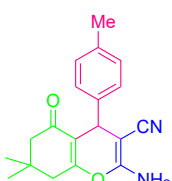
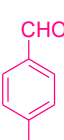
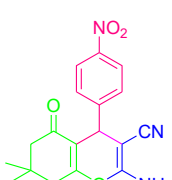
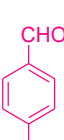
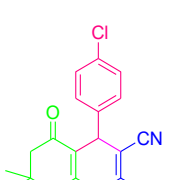
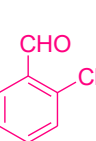
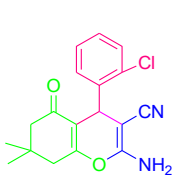
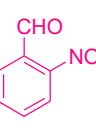
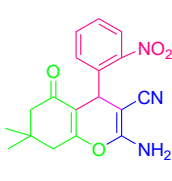
Entry	Amount of catalyst (g)	Reaction time (min)	Yield (%)
1	0	40	0
2	0.010	20	56
3	0.020	20	68
4	0.030	20	79
5	0.040	20	92
6	0.040	30	95
7	0.050	40	94

Reaction conditions: aromatic aldehyde (1 mmol), dimedone (2 mmol) and malononitrile (1 mmol) in presence of ZnFe₂O₄ nanoparticles in ethanol reflux.

We analysed the broadness, efficiency, variety, and scope of the reactions between aromatic aldehydes, malononitrile, and dimedone with zinc ferrite nanoparticles as a catalyst under reflux conditions in the presence of ethanol. The catalytic function of zinc ferrite nanoparticles was investigated using multiple aromatic aldehydes having -Me, -OMe, -NO₂, -Cl, -OH, -Br, -F groups (see Table 3). The present results were expanded to include several aromatic aldehydes with substituents donating and withdrawing electrons, including methyl, nitro, hydroxyl, methoxy, halogens and so on (Table 3). All reactions were performed to obtain the corresponding 5-oxo-5,6,7,8-tetrahydro-4H-chromenes with good product yield (86-96 %). The findings in Table 3 show that the yields of the products were not affected by the electronic effect of the various substituents on the aromatic aldehydes. With both (electron-donating/withdrawing) substituents, all of the reactions were similarly active at the positions of ortho, meta, and para on the aromatic aldehyde (Table 3).

As a way to show its suitability, the selected procedure was compared with the methods reported in Table 4. The safe and cost-effective zinc ferrite nanoparticles have high catalytic activity, excellent result in terms of reaction conditions, short reaction time, and good yield, suitable for a wide range of aldehydes.

Table 3. Synthesis of 5-oxo-5,6,7,8-tetrahydro-4H-chromenes using ZnFe₂O₄ nanoparticles

Entry	Substrate	Product	Time (min)	Yield (%)	M.P. (°C)		Ref.	TON	TOF
					Obs.	Rep.			
4a			30	95	230-232	229-231	[32]	5.7	11.4
4b			30	96	194-196	193-195	[9]	5.8	11.6
4c			55	92	212-214	210	[16]	5.5	6.04
4d			35	94	210-212	210	[33]	5.6	9.6
4e			35	86	172-174	174-176	[34]	5.2	8.9
4f			30	93	210-212	208-210	[35]	5.6	11.2
4g			40	92	202-204	201-203	[36]	5.5	8.3
4h			45	93	230-232	228-230	[10]	5.6	7.4

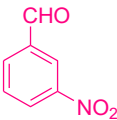
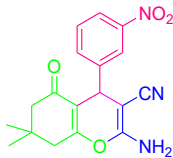

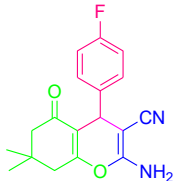
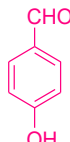
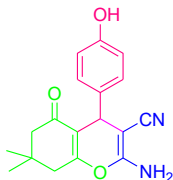
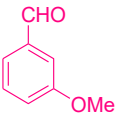
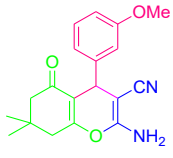
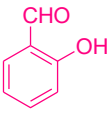
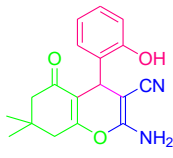

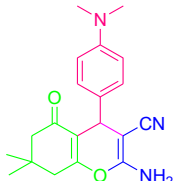
4i			35	89	208-210	210-211	[37]	5.3	9.1
4j			35	88	188-190	186-189	[1]	5.3	9.1
4k			40	90	216-218	215-220	[16]	5.4	8.1
4l			35	94	188-190	187-189	[9]	5.6	9.6
4m			40	90	184-186	185-186	[36]	5.4	8.1
4n			60	92	200-202	202-204	[8]	5.5	5.5

Table 4. Comparison of catalytic efficiencies for synthesis of 5-oxo-5,6,7,8-tetrahydro-4*H*-chromenes

Entry	Catalyst	Solvent	Temp. (°C)	Time (min)	Yield (%)	Reference
1	Zn(L-proline) ₂	EtOH:H ₂ O (2:3)	reflux	3h	85	[7]
2	HDMBAB	H ₂ O	80-90	5h	92	[12]
3	Yb(PFO) ₃	EtOH	60	5h	90	[8]
4	β-CD (aq. glycerine)	H ₂ O	35-40	2h	90	[16]
5	SBSSA	EtOH:H ₂ O (1:1)	reflux	75	94	[6]
6	L ₄ /Co(OAc) ₂	H ₂ O	50	3h	94	[23]
7	B-CD	H ₂ O	r.t	5h	92	[13]
8	Aspartic acid	EtOH:H ₂ O (1:1)	r.t	1h	93	[27]
9	ZnFe ₂ O ₄ nanoparticles	EtOH	reflux	30	95	Present work

Proposed mechanism

A plausible mechanism for the synthesis of 5-oxo-5,6,7,8-tetrahydro-4H-chromenes using zinc ferrite nanoparticles is shown in Figure 2. In the first step is the Knoevenagel condensation by the reaction of aromatic aldehyde with malononitrile. Also, we believe that the cyanide group of intermediates is activated by the zinc ferrite nanocatalyst for the nucleophilic attack of dimedone to form a Michael adduct. The intermediate undergoes ring closure and tautomerization yielding the desired products.

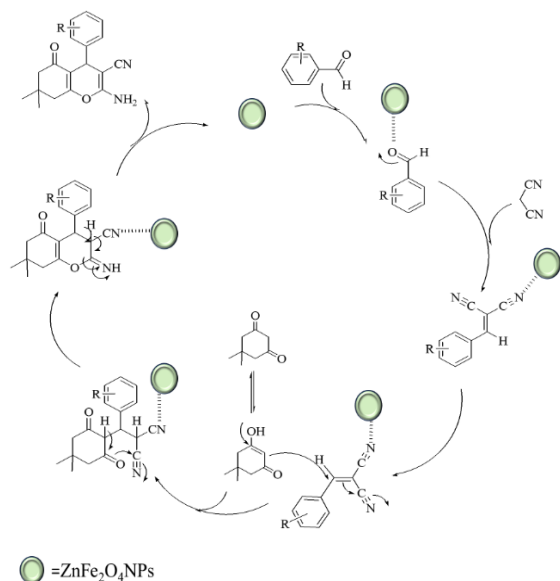


Figure 2. Plausible reaction mechanism for synthesis of 5-oxo-5,6,7,8-tetrahydro-4H-chromenes

CONCLUSION

In conclusion, in this study we have developed a very simple, efficient and green methodology for the synthesis of 5-oxo-5,6,7,8-tetrahydro-4H-chromene derivatives in the presence of ZnFe_2O_4 nanoparticles. The availability of the catalyst, easy reaction, simple setup, short reaction time, and excellent product yields are the most important features of this study.

The FT-IR, XRD, SEM, TEM, EDAX, TG-DTA, BET, NMR and MS data are in the Supplementary file.

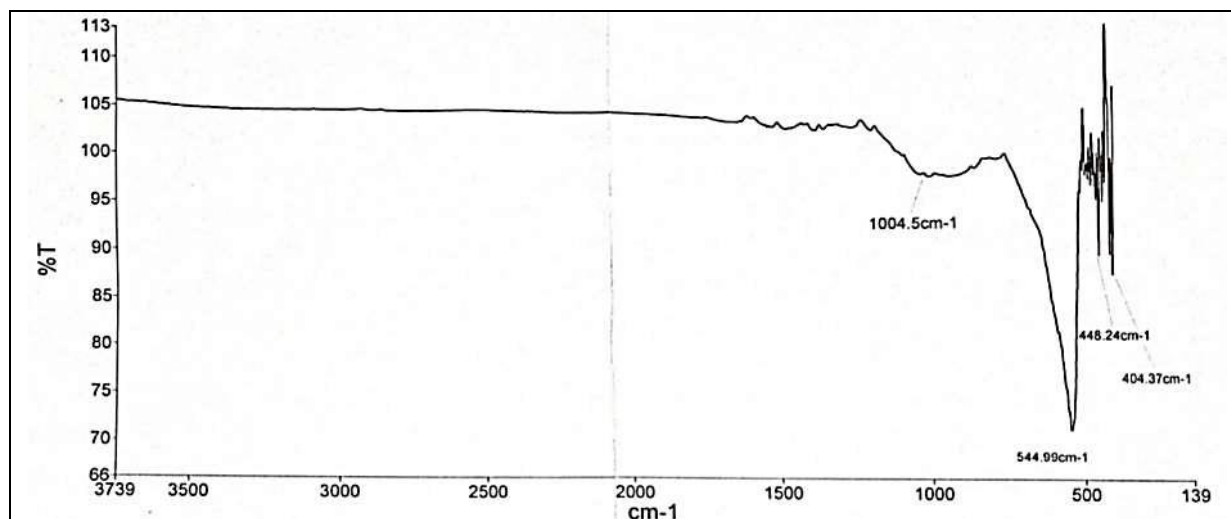
Acknowledgement: The authors are thankful to the Management and Principal (P.V.P. College, Pravaranagar) for providing the necessary facilities. We are also thankful to SAIF, Panjab University (Chandigarh), for providing all necessary spectral analysis facilities.

REFERENCES

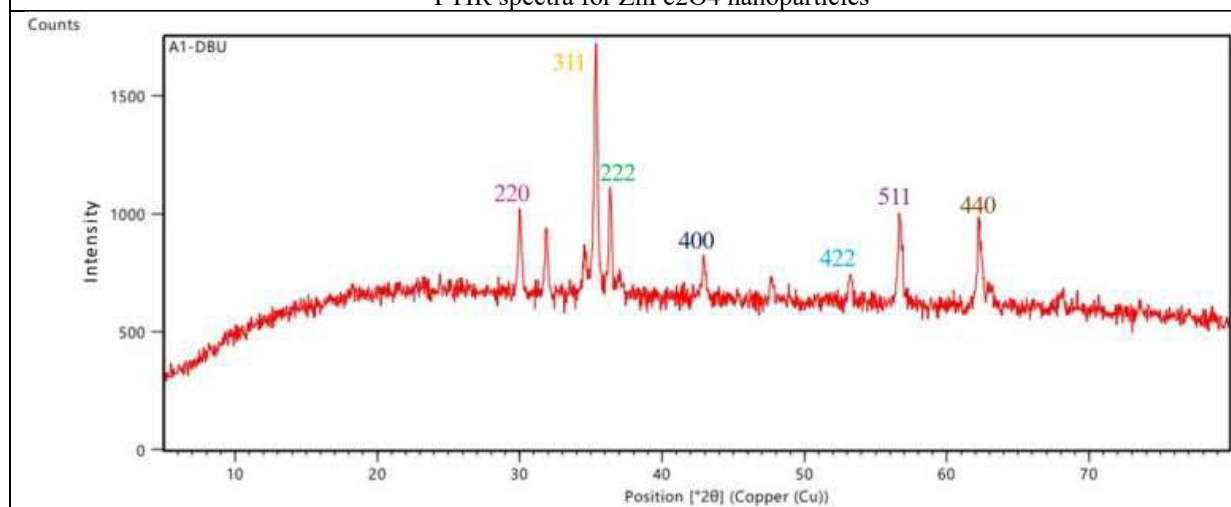
1. L. N. Nasirmahale, F. Shirini, H. Tajik, O. G. Jolodar, *Polycycl. Aromat. Compd.*, **40**, 475 (2020).

2. A. Khazaei, H. A. A. Nik, A. R. Moosavi-Zare, H. Afshar-Hezarkhani, *Z. Naturforsch. B*, **73**, 707 (2018).
3. V. Vikhe, A. Kshirsagar, B. Uphade, A. Gadhave, *Res. Chem. Intermed.*, **50**, 4199 (2024).
4. A. K. Mhaske, D. V. Vikhe, A. G. Gadhave, B. K. Uphade, *Polycycl. Aromat. Compd.*, **1** (2024).
5. V. Vikhe, D. Aute, V. Kadnor, G. Shirole, B. Uphade, A. Gadhave, *Polycycl. Aromat. Compd.*, **1** (2024).
6. K. Aswin, S. Sheik Mansoor, K. Logaiya, S. P. N. Sudhan, V. Saleem Malik, H. Ramadoss, *Res. Chem. Intermed.*, **40**, 2583 (2014).
7. D. Tahmassebi, J. E. Blevins, S. S. Gerardot, *Appl. Organomet. Chem.*, **33**, e4807 (2019).
8. L. M. Wang, J. H. Shao, H. Tian, Y. H. Wang, B. Liu, *J. Fluor. Chem.*, **127**, 97 (2006).
9. F. Kamali, F. Shirini, *Polycycl. Aromat. Compd.*, **41**, 73 (2021).
10. R. Ramesh, S. Maheswari, J. G. Malecki, A. Lalitha, *Polycycl. Aromat. Compd.*, **40**, 1581 (2020).
11. B. Halder, H. S. Maity, F. Banerjee, A. B. Kachave, A. Nag, *Polycycl. Aromat. Compd.*, **42**, 3302 (2022).
12. T. S. Jin, A. Q. Wang, F. Shi, L. B. Han, T. S. Li, *Arkivoc.*, **14**, 78 (2006).
13. J. Lu, X. W. Fu, G. Zhang, C. Wang, *Res. Chem. Intermed.*, **42**, 417 (2016).
14. A. Ramazani, H. Ahankar, K. Slepokura, T. Lis, P. A. Asiabi, M. Sheikhi, H. Yahyaei, *J. Chem. Crystallogr.*, **50**, 99 (2020).
15. D. Azarifar, M. Khaleghi-Abbasabadi, *Res. Chem. Intermed.*, **45**, 199 (2019).
16. S. R. Kamat, A. H. Mane, S. M. Arde, R. S. Salunkhe, *Int. J. Pharm.*, **4**, 1012 (2014).
17. H. Sanati, Z. Karamshahi, R. Ghorbani-Vaghei, *Res. Chem. Intermed.*, **45**, 709 (2019).
18. B. Amirheidari, M. Seifi, M. Abaszadeh, *Res. Chem. Intermed.*, **42**, 3413 (2016).
19. N. G. Shabalala, N. P. Hadebe, N. Kerru, S. Maddila, W. E. Van Zyl, S. B. Jonnalagadda, *Polycycl. Aromat. Compd.*, **42**, 505 (2022).
20. R. Ramesh, P. Vadivel, S. Maheswari, A. Lalitha, *Res. Chem. Intermed.*, **42**, 7625 (2016).
21. S. Amirnejat, A. Nosrati, R. Peymanfar, S. Javanshir, *Res. Chem. Intermed.*, **46**, 3683 (2020).
22. L. Chen, S. Bao, L. Yang, X. Zhang, B. Li, and Y. Li, *Res. Chem. Intermed.*, **43**, 3883 (2017).
23. S. Pan, P. Li, G. Xu, J. Guo, L. Ke, C. Xie, Y. Hui, *Res. Chem. Intermed.*, **46**, 1353 (2020).
24. H. Naeimi, M. F. Zarabi, *Res. Chem. Intermed.*, **44**, 3227 (2018).
25. S. Abdolahi, M. Haijani, F. Gholamian, *Res. Chem. Intermed.*, **47**, 1883 (2021).
26. F. Hassanzadeh, N. Daneshvar, F. Shirini, M. Mamaghani, *Res. Chem. Intermed.*, **46**, 4971 (2020).
27. A. Ahad, M. Farooqui, *Res. Chem. Intermed.*, **43**, 2445 (2017).
28. A. Mulik, P. Hegade, S. Mulik, M. Deshmukh, *Res. Chem. Intermed.*, **45**, 5641 (2019).
29. M. R. Khodabakhshi, M. H. Baghersad, *Sci. Rep.*, **12**, 5531 (2022).

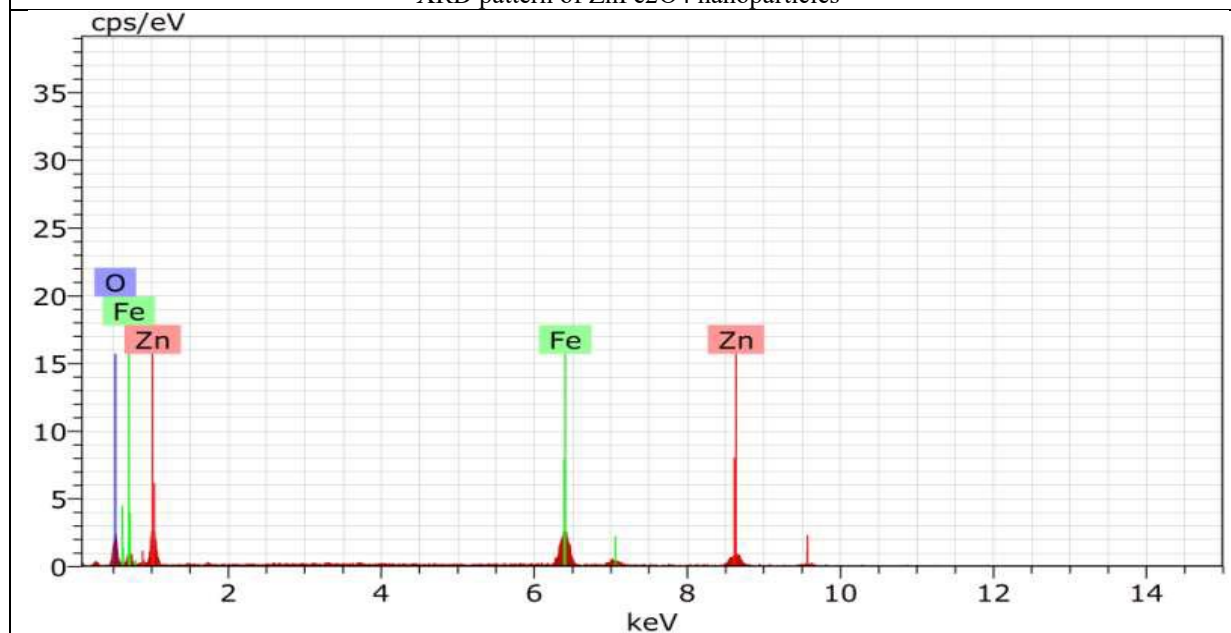
30. F. Sameri, A. Mobinikhaledi, M. A. Bodaghifard, *Silicon*, **14**, 1395 (2022).
31. A. K. Mhaske, A. G. Gadhave, A. G. Dholi, B.K. Uphade, *J. Inorg. Organomet. Polym. Mater.*, **34**, 999 (2024).
32. B. Eshtehardian, M. Rouhani, Z. Miriafary, *J. Iran. Chem. Soc.*, **17**, 469 (2020).
33. A. G. Mulik, D. R. Chandam, D. R. Patil, P. P. Patil, G. N. Mulik, S. T. Salunkhe, M. B. Deshmukh, *Res. Chem. Intermed.*, **41**, 10085 (2015).
34. A. Amoozadeh, S. F. Hosseininya, S. Rahmani, *Res. Chem. Intermed.*, **44**, 991 (2018).
35. J. Zhao-Qin, L. Shun-Jun, Y. Jin-Ming, *Chin. J. Chem.*, **23**, 1085 (2005).
36. A. Maharramov, R. Kaya, P. Taslimi, M. Kurbanova, A. Sadigova, V. Farzaliyev, I. Gulcin, *Arch. Pharm.*, **352**, 1800317 (2019).
37. F. Matloubi Moghaddam, M. Eslami, G. Hoda, *Sci. Rep.*, **10**, 20968 (2020).



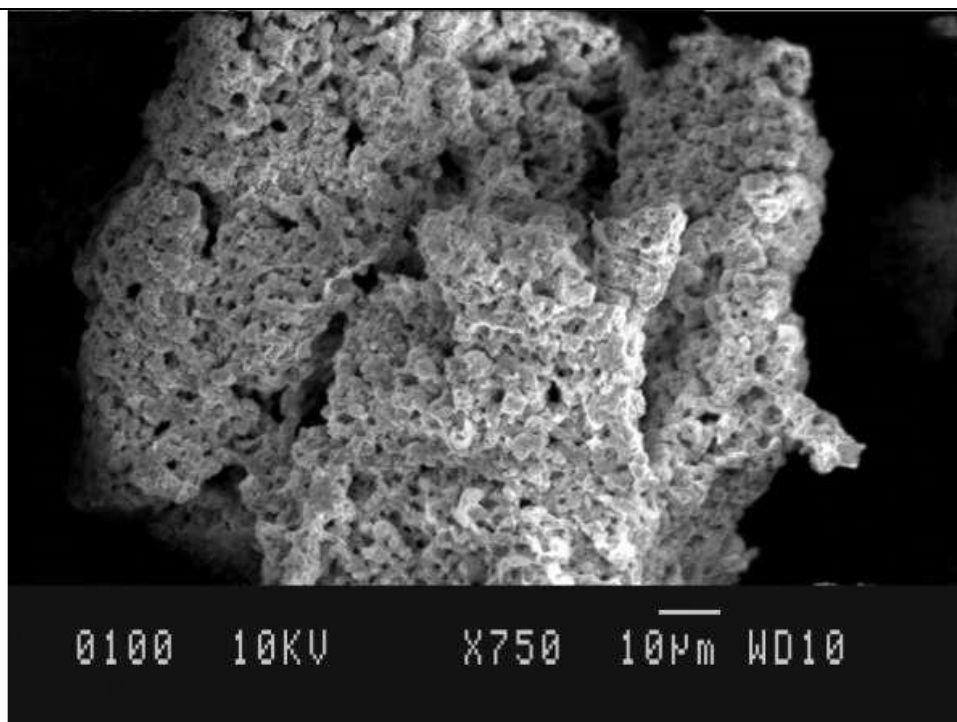
FTIR spectra for ZnFe_2O_4 nanoparticles



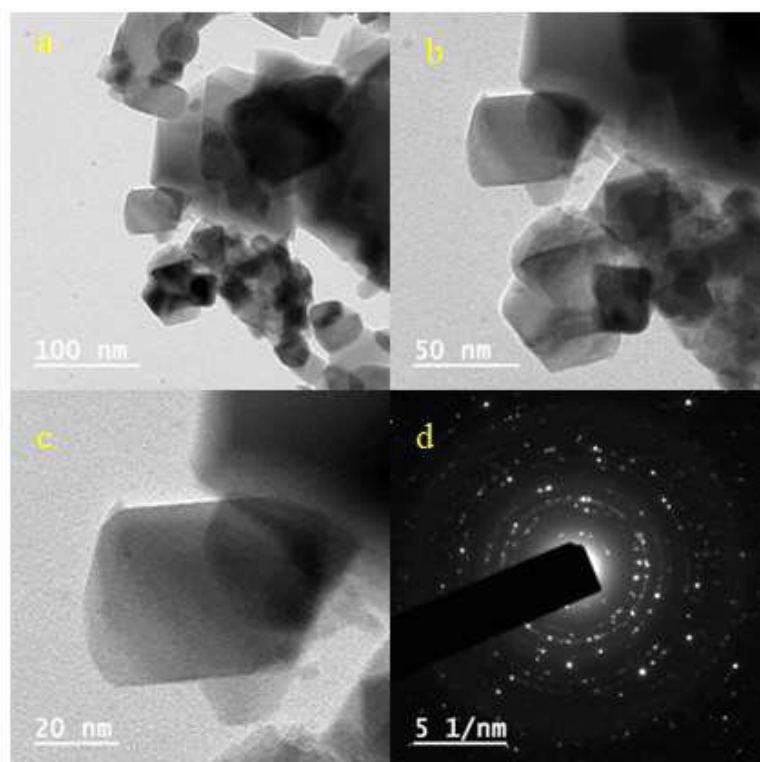
XRD pattern of ZnFe_2O_4 nanoparticles



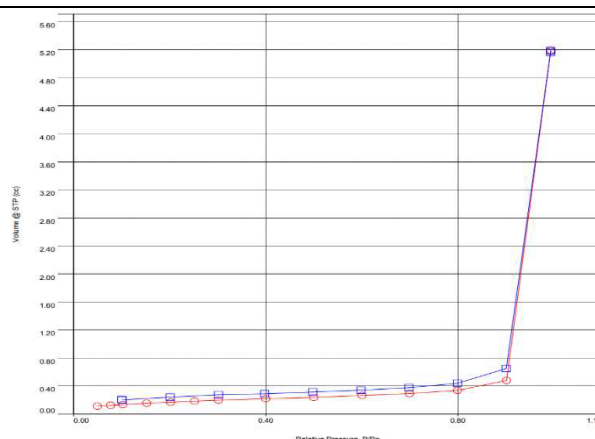
EDAX spectrum of ZnFe_2O_4 nanoparticles



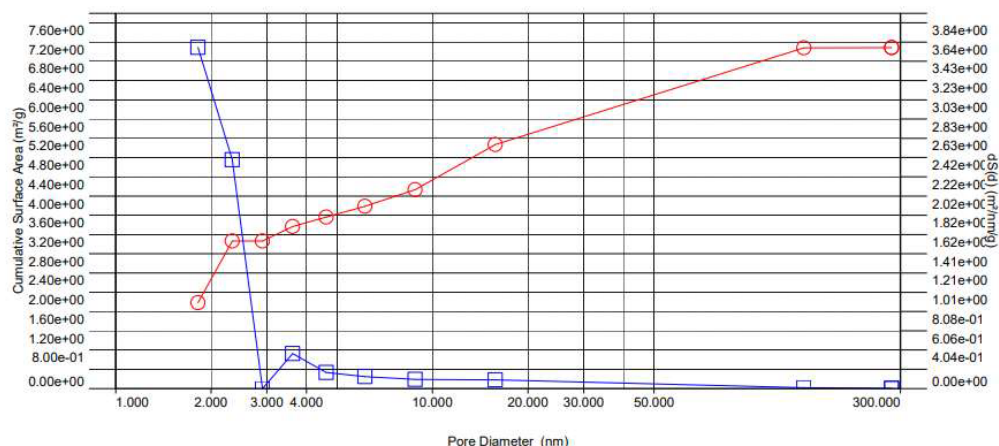
SEM image of ZnFe₂O₄ nanoparticles



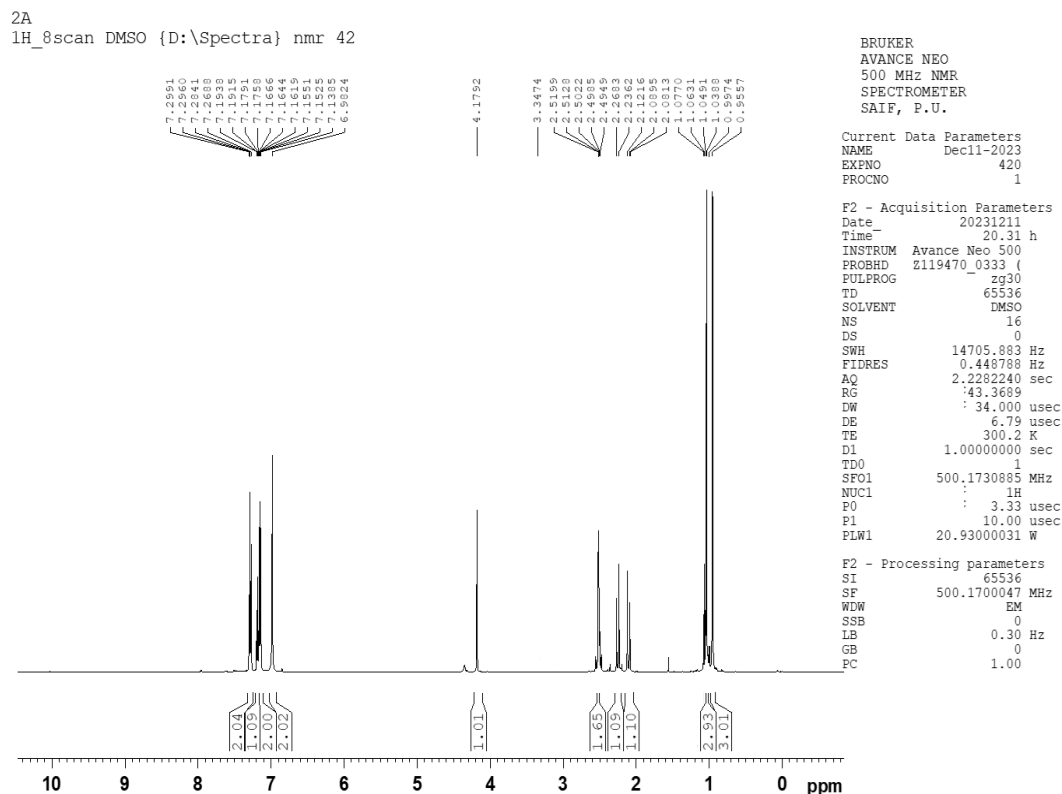
FETEM of ZnFe₂O₄ nanoparticles



BET spectrum of ZnFe₂O₄ nanoparticles: BET N₂adsorption-desorption curves



BET spectrum of ZnFe₂O₄ nanoparticles: Average pore radius for ZnFe₂O₄nanoparticles



2-amino-7,7-dimethyl-5-oxo-4-phenyl-5,6,7,8-tetrahydro-4H-chromene-3-carbonitrile (4a)

AUTHOR INDEX

- Abd Alhassan Mahmood, H., See Lateef et al. 277
- Abdulsahib, Yu. S., See Lateef et al. 277
- Acknowledgement to reviewers for vol. 56 (2024) 47
- Akolkar, H. N., See Prashanth et al. 331
- Akyol, E., See Simsek et al. 202
- Ali Köse, D., See Serdaroglu et al. 170
- Aliyev, A. Sh., See Majidzade et al. 102
- Al-Mahmoud, S. M., One-step chemical modification of pine cones for the removal of methyl orange from aqueous media 302
- Angelov, A. T., Bratkova, S. G., Nikolova, K. T., Plochev, S. K., Genova, P. G., Ivanov, R. V., Velichkova, P. G., Efficiency of algae-assisted photo-bioelectrochemical system in anaerobic wastewater treatment 295
- Appaz, A. N., See Appazov et al. 14
- Appazov, N. O., Espanova, I. D., Niyazova, D. Zh., Moldanazar, A. A., Zhapparbergenov, R. U., Turmanov, R. A., Toibazarova, A. B., Appaz, A. N., Syzdykbayev, M. I., Extraction of cellulose from rice straw by microwave irradiation 14
- Authors Index 358
- Aydın, A., See Özbakış et al. 160
- Azizova, A. N., See Majidzade et al. 102
- Balarew, Chr., The theory for the disperse structure of real crystals by Dimiter Balarew, as a predecessor of the nonclassical crystallization of mesocrystals 37
- Baloat, L., See Meena et al. 259
- Baste, Y. R., See Mhaske et al. 348
- Belovezhdova, I. N., See Lyubomirova et al. 339
- Beschkov, V., See Ganey et al. 114, 123
- Bhagya, N. P., See Prashanth et al. 331
- Biltekin, M. E., Gurkan, B., Yalcin Gurkan, Y., DFT-based theoretical investigation of hydroxyl radical-induced degradation mechanisms of antineoplastic drugs in aqueous media 185
- Blazheva, D., See Delinska et al. 108
- Bolat, M., See Serdaroglu et al. 170
- Bratkova, S. G., See Angelov et al. 295
- Burdin, B., See Ganey et al. 114
- Bussan, D., See Douvris et al. 32
- Byzova, Y., Dyuryagina, A., Ostrovnoy, K., Shirina, T., The effect of modifiers on the microstructure of road bitumen and strength of asphalt concrete: a mini-review 249
- Christov, C., Tsenov, T., Ivanova, N., Donchev, S., Solid-liquid phase equilibrium in the LiBr-CaBr₂-H₂O system at 35°C and 50°C 26
- Çifçi, G., See Uygünöz et al. 148
- Dadashova, S. D., See Majidzade et al. 102
- Delinska, N., Perifanova-Nemska, M., Blazheva, D., Slavchev, A., Research on the potential of postbiotics in soaps for improving their quality and functionality 108
- Didem Çorbacioğlu, B., Küçük, İ., Effect of heavy metals in metal plating plant waste sludge on tea plant primary development 144
- Dimova-Gabrovska, M., See Ganey et al. 123
- Dinović, N., Pevicharova, G., Slavova, V., Textural properties of sweet pepper depending on genotype and method of cultivation 20
- Disha, See Meena et al. 259
- Dobrev, G. T., See Zhekova et al. 7
- Dobрева, V. T., See Zhekova et al. 7
- Donchev, S., See Christov et al. 26
- Douvris, Ch., Bussan, D., An efficient and economical approach to hydrogen peroxide detection and neutralization utilizing molybdenum sensors 32
- Doymaz, I., See Kurt et al. 154
- Dyuryagina, A., See Byzova et al. 249
- El Hajjaji, S., See Samghouli et al. 85
- El Hajji, A., See Samghouli et al. 85
- Erkoyuncu, D., See Özdemir et al. 245
- Espanova, I. D., See Appazov et al. 14
- Evcimen, M. D., Yaşa Şahin, Ö., Farma-Bant: obtaining a wound covering membrane from *Calendula Officinalis*, *Centella Asiatica* and *Carthamus Tinctorius* plant extract mixtures 198
- Gadhve, A. G., See Mhaske et al. 348
- Ganay, E., Beschkov, V., Kirilova, E., Nikolova, D., Vladova, R., Dimova-Gabrovska, M., Optimization approach for the design of a sustainable hydrogen supply chain through steam methane reforming 123
- Ganay, E., Nikolova, D., Kirilova, E., Vladova, R., Beschkov, V., Valkanova, T., Burdin, B., Slavcheva, E., Iliev, J., Sustainable design approach of a hydrogen production supply chain through water electrolysis 114
- Geniş, G., İsmail, O., Drying of sour cherry with microwave and infrared drying methods; investigation of drying kinetics and parameters 59
- Genova, P. G., See Angelov et al. 295
- Gradinarska-Ivanova, D. N., See Momchilova et al. 94
- Guenoun, L., See Samghouli et al. 85
- Gupta, B., Nikita, Rolaniya, A., Yadav, A., Jain, P., Sailani, R., Unraveling the mechanism of ruthenium (III)-catalyzed aspirin oxidation by hexacyanoferrate(III): kinetic and spectrophotometric approach 206
- Gürakin, H. K., See Karagöz et al. 189
- Gürakin, H. K., See Topaç et al. 193
- Gurkan, B., See Biltekin et al. 185
- Iliev, J., See Ganey et al. 114
- Instructions to authors 48, 131, 258, 363
- Ipsalalı, Ö., Uğur Nigiz, F., Evaluation of smart packaging functions of black carrot extract with polysaccharide-based films 218
- Ipsalalı, Ö., Uğur Nigiz, F., Green tea-boron nitride incorporated pumpkin pectin-alginate food packaging film preparation and characterization 224
- İsmail, O., See Geniş et al. 59
- Ivanov, R. V., See Angelov et al. 295
- Ivanova, N., See Christov et al. 26
- Jafarova, S. F., See Majidzade et al. 102

Jain, P., See Gupta et al.	206	Momchilova, M. M., Gradinarska-Ivanova, D. N., Valkova-Yorgova, K. I., Yordanov, D. G., Comparative analysis of the effect of cricket powder and spirulina in model meat systems as substitutes for soy in raw pork products	94
Jariwala, H. M., Rotliwala, Y. C., Energy-efficient enrichment of bioslurry and methanecontent of biogas from wheat flour in a bio-electrochemical anaerobic digester	40	Möröyodor Derun, E., See Uygunöz et al.	148
Javadova, S. P., See Majidzade et al.	102	Nikita, See Gupta et al.	206
Kahraman, S., Katirci, A., Uğur Nigiz, F., Fabrication and filtration of gum arabic doped electrospun PLA membrane for rejection of gray water pollutants .	229	Nikolova, D., See Ganev et al.	114, 123
Kantürk Figen, A., See Özdemir et al.	245	Nikolova, K. T., See Angelov et al.	295
Karagöz, S., Gürakin, H. K., Şakar, D., Treatment of lab-scale factory wastewater including disperse orange 30 dye with low cost H ₂ SO ₄ -activated rubber particle adsorbent obtained from waste tyre.....	189	Niyazova, D. Zh., See Appazov et al.	14
Karakuş, N., See Serdaroğlu et al.	170	Ostrovnoy, K., See Byzova et al.	249
Katirci, A., See Kahraman et al.	229	Oyegoke, T., Computational study of propane dehydrogenation into propylene over chromium oxide <i>via</i> a combined use of central composite design & microkinetic simulation.....	309
Khaoulaf, R., See Samghouli et al.	85	Oyegoke, T., Unlocking the potential of computational fluid dynamics in Nigerian polymer research: current trends and future directions	267
Kıpcak, A. S., See Ozyalcin et al.	213, 252	Ozan Demirci, Ö., See Uygunöz et al.	148
Kıpçak, E., See Salık et al.	235	Özbakiş, S., Aydın, A., Terzioğlu, P., Investigating the properties of recycled and virgin poly (ethylene terephthalate) textured yarns: Effect of different blending ratios.....	160
Kirilova, E., See Ganev et al.	114, 123	Ozcan, E., See Sabudak et al.	166
Küçük, İ., See Didem Çorbacıoğlu et al.	144	Özdemir, G., Erkoyuncu, D., Kantürk Figen, A., Application of gas foaming technique for improving porous properties of chitosan-polyvinyl alcohol (CS/PVA) nanofiber-based biodegradable scaffolds.....	245
Küçük, I., See Kurt et al.	154	Ozdemir, R., Unlu, D., Improved biobutanol recovery through mixed-matrix PVDF membrane with hydrophobic MAF-6 as filler	181
Kucuk, I., See Simsek et al.	202	Öztemür, Z., See Serdaroğlu et al.	170
Kurt, C., Küçük, I., Doymaz, I., Effect of different drying techniques on the drying characteristics of celery.....	154	Ozyalcin, Z. O., Kipcak, A. S., Blanching and osmotic dehydration effects on lyophilized shrimp.....	252
Lalithamba, H. S., See Prashanth et al.	331	Ozyalcin, Z. O., Kipcak, A. S., Freeze-drying of squid: a study to investigate the effect of different pre-treatments	213
Lalithamba, H. S., See Sai Varun et al.	282	Panajotova, H. N., See Zhekova et al.	7
Lateef, M. T., Abd Alhassan Mahmood, H., Abdulsahib, Yu. S., Purification and characterization of lipoxxygenase enzyme from Iraqi patients with type 2 diabetes mellitus	277	Perifanova-Nemska, M., See Delinska et al.	108
Lyubomirova, V. V., Belovezhdova, I. N., Fractionation of potentially toxic and essential elements in sewage sludge from wastewater treatment plants	339	Petkova, M., See Marcheva et al.	68
Majidzade, V. A., Jafarova, S. F., Javadova, S. P., Azizova, A. N., Dadashova, S. D., Aliyev, A. Sh., Tagiyev, D. B., Electrodeposition of Mo-Se thin films and influence of the main factors on their composition.....	102	Pevicharova, G., See Đinović et al.	20
Mandal, M. M., See Priyanshu et al.	319	Plochev, S. K., See Angelov et al.	295
Marcheva, M., Petkova, M., Slavova, V., Popov, V., Biochemical, transcriptional and fluorescence spectroscopy analysis of fatty acids in seeds of camelina varieties in the organic intercropping system	68	Popov, V., See Marcheva et al.	68
Meena, A. S., See Meena et al.	259	Pradeepa, S., See Sai Varun et al.	282
Meena, D., Susawat, A., Meena, G., Meena, R. K., Baloat, L., Disha, Meena, A. S., Role of chemicals in dye-sensitized solar cells based on liquid-phase electrolyte for generation of electrical energy	259	Prashanth, G. K., Lalithamba, H. S., Rao, S., Bhagya, N. P., Rashmi, K. V., Akolkar, H. N., Phytonano synthesis of MgO nanoparticles using aqueous leaf extract of <i>Hibiscus rosa sinensis</i> : comprehensive characterization and assessment of their antibacterial and anti-oncogenic activities	331
Meena, G., See Meena et al.	259	Prashanth, G. K., See Sai Varun et al.	282
Meena, R. K., See Meena et al.	259	Priyanshu, Mandal, M. M., Modeling of blood flow in a stenotic artery using nanoparticles.....	319
Mhaske, A. K., Vikhe, V. V., Gadhave, A. G., Baste, Y. R., Uphade, B. K., Efficient synthesis of 5-oxo-5,6,7,8-tetrahydro-4 <i>H</i> -chromenes using zinc ferrite nanoparticles as a catalyst	348	Professor Christo Balarew's 90 th anniversary	5
Moldanazar, A. A., See Appazov et al.	14	Rao, S., See Prashanth et al.	331
		Rao, S., See Sai Varun et al.	282
		Rashmi, K. V., See Prashanth et al.	331
		Rghioui, L., See Samghouli et al.	85
		Rolaniya, A., See Gupta et al.	206

Rotliwala, Y. C., See Jariwala, et al.....	40	Stefanova, K. V., Determination of boundary conditions from experimental data for computational fluid dynamics simulations for phases change material solutions in the ground mass with emphasis on ground heat exchangers	78
Sabudak, T., Ozcan, E., Determination of fatty acids in plant oils by gas chromatography, production and analysis of solid soap from these oils.....	166	Subject Index.....	361
Sai Aishwarya Reddy, N., See Sai Varun et al.	282	Susawat, A., See Meena et al.	259
Sai Varun, N. J., Sai Aishwarya Reddy, N., Pradeepa, S., Lalithamba, H. S., Rao, S., Prashanth, G. K., Eco-engineered ZnO nanoparticles via <i>Convolvulus prostratus</i> with Al- and Zr-doping: structural, mechanical, and antifungal enhancement for sustainable construction applications	282	Syzdykbayev, M. I., See Appazov et al.....	14
Sailani, R., See Gupta et al.	206	Tagiyev, D. B., See Majidzade et al.....	102
Şakar, D., See Karagöz et al.	189	Tan, A., See Salık et al.	235
Şakar, D., See Topaç et al.	193	Terzioğlu, P., See Özbakış et al.....	160
Salık, B., Tan, A., Kıpçak, E., Infrared drying of aronia berries: the effect of sustainable pretreatments on drying behavior	235	Toibazarova, A. B., See Appazov et al.....	14
Samghouli, N., Rghioui, L., Sebbahi, S., El Hajji, A., Guennoun, L., Khaoulaf, R., Serghini Idrissi, M., El Hajjaji, S., Removal of methylene blue from aqueous solution by loquats nuclei.....	85	Topaç, K., Gürakin, H. K., Şakar, D., Disperse orange 30 dye removal with H ₂ SO ₄ -functionalized activated carbon: adsorption isotherms and kinetics	193
Sebbahi, S., See Samghouli et al.	85	Tsenov, T., See Christov et al.	26
Serdaroğlu, G., Bolat, M., Ali Köse, D., Öztömür, Z., Karakuş, N., <i>In silico</i> insight on hyaluronic acid and boron hyaluronate.....	170	Turmanov, R. A., See Appazov et al.....	14
Serdaroğlu, G., Computational evaluation of cymenes: substituent group effect, pharmacokinetics, and drug-likeness	175	Uğur Nigiz, F., See Ipsalalı et al.	218, 224
Serghini Idrissi, M., See Samghouli et al.....	85	Uğur Nigiz, F., See Kahraman et al.	229
Shirina, T., See Byzova et al.....	249	Unlu, D., See Ozdemir et al.	181
Simsek, S., Akyol, E., Kucuk, I., Development of a high-performance liquid chromatography (HPLC) method for coumarin quantification in medicinal plants extracted <i>via</i> Soxhlet.....	202	Uphade, B. K., See Mhaske et al.....	348
Slavchev, A., See Delinska et al.	108	Uygunöz, D., Çifçi, G., Ozan Demirci, Ö., Möröydor Derun, E., Obtaining valuable components from various citrus product wastes by different extraction methods	148
Slavcheva, E., See Ganey et al.....	114	Valkanova, T., See Ganey et al.	114
Slavova, V., See Đinović et al.	20	Valkova-Yorgova, K. I., See Momchilova et al.	94
Slavova, V., See Marcheva et al.	68	Velichkova, P. G., See Angelov et al.	295
Stanchev, V. S., See Zhekova et al.	7	Vikhe, V. V., See Mhaske et al.	348
		Vladova, R., See Ganey et al.....	114, 123
		Yadav, A., See Gupta et al.	206
		Yalcin Gurkan, Y., See Biltekin et al.	185
		Yaşa Şahin, Ö., See Evcimen et al.	198
		Yordanov, D. G., See Momchilova et al.	94
		Zhapparbergenov, R. U., See Appazov et al.	14
		Zhekova, B. Y., Dobrev, G. T., Panajotova, H. N., Dobрева, V. T., Stanchev, V. S., Kinetics of β -cyclodextrin production by cyclodextrin glucanotransferase from <i>Bacillus megaterium</i>	7

SUBJECT INDEX

4 <i>H</i> -chromenes.....	348	DFT.....	139, 170, 175, 185
acid-activated carbon.....	193	diabetes mellitus.....	277
adsorption.....	85	digestate (bioslurry).....	40
adsorption isotherms.....	189, 193	dimedone.....	348
adsorption kinetics.....	189	disperse orange 30 dye.....	189, 193
Aleppo pine cones.....	302	doping.....	282
aluminum.....	282	drug.....	139
anaerobic digester.....	40	drug likeness.....	175
antibacterial.....	331	drying kinetics.....	154, 235
antidepressant.....	139	drying techniques.....	154
antimicrobial.....	198	dye removal.....	189, 193
antimicrobial activity.....	282	eco-friendly nanomaterials.....	282
antineoplastic drugs.....	185	economic.....	123
aromatic aldehyde.....	348	elasticity.....	20
Aronia berry.....	235	electrodeposition.....	102
aspirin.....	206	electrolysis.....	114
<i>Bacillus megaterium</i>	7	electrospinning.....	229, 245
bee-like structures.....	249	emulsion stability.....	94
BES (bio-electrochemical system).....	40	enrichment.....	40
bioactive component.....	148	environmental criteria.....	123
biobutanol.....	181	enzyme kinetics.....	7
biochemical analysis.....	68	epirubicin.....	185
bioelectrochemical systems.....	295	extraction.....	148
bio-fertilizer.....	40	fatty acid.....	166
biotechnology.....	245	field.....	20
bitumen microstructure.....	249	filtration.....	229
bitumen modification.....	249	fluorescence spectroscopy analysis.....	68
blanching.....	213, 252	food package.....	224
blending ratio.....	160	freeze-drying.....	213, 252
blood hemolysis.....	331	Freundlich.....	85
boron fertilizer.....	144	FTIR.....	282
boron hyaluronate.....	170	gas chromatography.....	166
boron nitride.....	224	gas foaming.....	245
bromide minerals solubility.....	26	GHG.....	114
<i>Camelina sativa L.</i>	68	gray water.....	229
<i>Capsicum annuum L.</i>	20	green fuel.....	331
carrot pectin.....	218	green synthesis.....	282
Celeriac.....	154	green tea extract.....	224
cellulose.....	14	greenhouse.....	20
CFD.....	267	ground heat-exchanger (GHE).....	78
chemical treatment.....	302	ground source heat pump (GSHP).....	78
citrus waste.....	148	H ₂ SO ₄ -activated rubber particles obtained from scrap waste tyre.....	189
color.....	94	heavy metal.....	144
compound fertilizer.....	144	hexacyanoferrate (III).....	206
computational approach.....	267	high-performance liquid chromatography (HPLC).....	202
computational fluid dynamics (CFD).....	319	hyaluronic acid.....	170
conversion efficiency.....	259	hydrogen.....	114
<i>Convolvulus prostratus</i>	282	hydrogen fuel cell vehicle.....	114
Coulombic efficiency.....	295	hydrogen peroxide.....	32
coumarin extraction.....	202	hydrogen production.....	123
crystal growth.....	37	hydroxyl radicals.....	185
current.....	259	Indian Pennywort.....	198
cyclodextrin glucanotransferase.....	7	infrared drying.....	59, 235
cyclodextrins.....	7	intercropping.....	68
cymene.....	175	kinetic parameters.....	193
deformation work.....	20	Knoevenagel condensation.....	348
dehydrogenation.....	309	lipoxygenase (LOX).....	277
Density Functional Theory (DFT).....	309		

loquats nuclei.....	85	pumpkin pectin films.....	224
MAF-6.....	181	purification of enzyme.....	277
magnetic field.....	319	PVDF.....	181
malononitrile.....	348	PXRD.....	282
Marigold.....	198	quality.....	59
material design.....	267	quantitative analysis.....	148
material science.....	245	reaction mechanism.....	206
mathematical modeling.....	154, 213	recycled polyester.....	160
meat products.....	94	recycling.....	160
membrane.....	181	renewable energy sources (RES).....	78
mesocrystals.....	37	rice straw.....	14
methotrexate.....	185	rupture force.....	20
methyl orange.....	302	ruthenium (III).....	206
methylene blue.....	85	Safflower.....	198
MgO-NPs.....	331	saltwater.....	252
microalgae.....	295	SEM.....	282
microbial fuel cells.....	295	semiconductors.....	102
microbial sulfate reduction.....	295	sensing devices.....	32
microkinetics.....	309	shrimp.....	252
microwave drying.....	59	skin benefits.....	108
microwave irradiation.....	14	smart packaging.....	218
mixed system LiBr-CaBr ₂ -H ₂ O.....	26	soap analysis.....	166
modeling.....	267, 309	soaps.....	108
molybdenum.....	32	social criteria.....	123
MoSe ₂ thin films.....	102	solar cells.....	102
MTT assay.....	331	solubility.....	170
multi-objective optimization.....	123	solution combustion.....	331
multiple impurities.....	229	solvent selection.....	202
nanofiber.....	245	sour cherry.....	59
nanoparticles.....	37, 319	Soxhlet extraction.....	202
natural solid soap.....	166	squid.....	213
Nigeria.....	267	steam methane reforming.....	123
nonclassical crystallization.....	37	stenotic artery.....	319
OH radical.....	139	storage capacity.....	259
olefins.....	309	strength of asphalt concrete.....	249
osmotic dehydration.....	213, 252	substituent effect.....	175
oxidation kinetics.....	206	supply chain.....	114
oxidative stress.....	277	supply chain design.....	123
oxygen generation.....	295	sustainable concrete.....	282
paper products.....	14	sustainable textiles.....	160
paraffin wax.....	78	tartaric acid.....	102
paraffins.....	309	tea plant.....	144
Paroxetine HCl.....	139	textile waste.....	160
Paxil.....	139	textural traits.....	94
pervaporation.....	181	thermal energy storage (TES).....	78
pharmacokinetics.....	175	thermal properties.....	160
phase equilibrium.....	26	thermodynamic parameters.....	193
phases change material (PCM).....	78	thermodynamic study.....	85
photogalvanic effect.....	259	toxic effect.....	144
plant oil.....	166	transcriptional analysis.....	68
polylactic acid.....	229	ultrasonic pretreatment.....	235
polymer.....	267	viscosity.....	319
polymer chemistry.....	245	wastewater treatment.....	185
polysaccharide-based.....	218	water pollution.....	302
postbiotics.....	108	wound dressing.....	198
potential.....	259	yield force.....	20
product inhibition.....	7	zinc ferrite nanoparticles.....	348
protein.....	94	zinc oxide NPs.....	282
pseudo-second-order.....	85	zirconium.....	282

Instructions about Preparation of Manuscripts

General remarks: Manuscripts are submitted in English by e-mail. The text must be prepared in A4 format sheets using Times New Roman font size 11, normal character spacing. The manuscript should not exceed 15 pages (about 3500 words), including photographs, tables, drawings, formulae, etc. Authors are requested to use margins of 2 cm on all sides.

Manuscripts should be subdivided into labelled sections, e.g. INTRODUCTION, EXPERIMENTAL, RESULTS AND DISCUSSION, etc. **The title page** comprises headline, author(s)' names and affiliations, abstract and key words. Attention is drawn to the following:

a) **The title** of the manuscript should reflect concisely the purpose and findings of the work. Abbreviations, symbols, chemical formulae, references and footnotes should be avoided. If indispensable, abbreviations and formulae should be given in parentheses immediately after the respective full form.

b) **The author(s)**' first and middle name initials and family name in full should be given, followed by the address (or addresses) of the contributing laboratory (laboratories). **The affiliation** of the author(s) should be listed in detail (no abbreviations!). The author to whom correspondence and/or inquiries should be sent should be indicated by an asterisk (*) with e-mail address.

The abstract should be self-explanatory and intelligible without any references to the text and containing up to 250 words. It should be followed by keywords (up to six).

References should be numbered sequentially in the order, in which they are cited in the text. The numbers in the text should be enclosed in brackets [2], [5, 6], [9–12], etc., set on the text line. References are to be listed in numerical order on a separate sheet. All references are to be given in Latin letters. The names of the authors are given without inversion. Titles of journals must be abbreviated according to Chemical Abstracts and given in italics, the volume is typed in bold, the initial page is given and the year in parentheses. Attention is drawn to the following conventions: a) The names of all authors of a certain publications should be given. The use of "et al." in the list of references is not acceptable; b) Only the initials of the first and middle names should be given. In the manuscripts, the reference to author(s) of cited works should be made without giving initials, e.g. "Bush and Smith [7] pioneered...". If the reference carries the names of three or more authors it should be quoted as "Bush et al. [7]", if Bush is the first author, or as "Bush and co-workers [7]", if Bush is the senior author.

Footnotes should be reduced to a minimum. Each footnote should be typed double-spaced at the bottom of the page, on which its subject is first mentioned. **Tables** are numbered with Arabic numerals on the left-hand top. Each table should be referred to in the text. Column headings should be as short as possible but they must define units unambiguously. The units are to be separated from the preceding symbols by a comma or brackets. Note: The following format should be used when figures, equations, etc. are referred to the text (followed by the respective numbers): Fig., Eqns., Table, Scheme.

Schemes and figures. Each manuscript should contain or be accompanied by the respective illustrative material, as well as by the respective figure captions in a separate file. As far as presentation of units is concerned, SI units are to be used. However, some non-SI units are also acceptable, such as °C, ml, l, etc. Avoid using more than 6 (12 for review articles) figures in the manuscript. Since most of the illustrative materials are to be presented as 8-cm wide pictures, attention should be paid that all axis titles, numerals, legend(s) and texts are legible.

The authors are required to submit the text with a list of three individuals and their e-mail addresses that can be considered by the Editors as potential reviewers. Please note that the reviewers should be outside the authors' own institution or organization. The Editorial Board of the journal is not obliged to accept these proposals.

The authors are asked to submit **the** final text (after the manuscript has been accepted for publication) in electronic form by e-mail. The main text, list of references, tables and figure captions should be saved in separate files (as *.rtf or *.doc) with clearly identifiable file names. It is essential that the name and version of the word-processing program and the format of the text files is clearly indicated. It is recommended that the pictures are presented in *.tif, *.jpg, *.cdr or *.bmp format. The equations are written using "Equation Editor" and chemical reaction schemes are written using ISIS Draw or ChemDraw programme.

EXAMPLES FOR PRESENTATION OF REFERENCES

REFERENCES

1. D. S. Newsome, Catal. Rev.–Sci. Eng., 21, 275 (1980).
2. C.-H. Lin, C.-Y. Hsu, J. Chem. Soc. Chem. Commun., 1479 (1992).
3. R. G. Parr, W. Yang, Density Functional Theory of Atoms and Molecules, Oxford Univ. Press, New York, 1989.
4. V. Ponec, G. C. Bond, Catalysis by Metals and Alloys (Stud. Surf. Sci. Catal., vol. 95), Elsevier, Amsterdam, 1995.
5. G. Kadinov, S. Todorova, A. Palazov, in: New Frontiers in Catalysis (Proc. 10th Int. Congr. Catal., Budapest (1992), L. Guzzi, F. Solymosi, P. Tetenyi (eds.), Akademiai Kiado, Budapest, 1993, Part C, p. 2817.
6. G. L. C. Maire, F. Garin, in: Catalysis. Science and Technology, J. R. Anderson, M. Boudart (eds.), vol. 6, Springer Verlag, Berlin, 1984, p. 161.
7. D. Pocknell, GB Patent 2 207 355 (1949).
8. G. Angelov, PhD Thesis, UCTM, Sofia, 2001, pp. 121-126.
9. JCPDS International Center for Diffraction Data, Power Diffraction File, Swarthmore, PA, 1991.
10. CA 127, 184 762q (1998).
11. P. Hou, H. Wise, J. Catal., in press.
12. M. Sinev, private communication.
13. <http://www.chemweb.com/alchem/articles/1051611477211.html>.

Texts with references which do not match these requirements will not be considered for publication!!!

CONTENTS

<i>D. Meena, A. Susawat, G. Meena, R.K. Meena, L. Baloat, Disha, A.S. Meena</i> , Role of chemicals in dye-sensitized solar cells based on liquid-phase electrolyte for generation of electrical energy.....	259
<i>T. Oyegoke</i> , Unlocking the potential of computational fluid dynamics in Nigerian polymer research: current trends and future directions.....	267
<i>M. T. Lateef, H. Abd Alhassan Mahmood, Yu. S. Abdulsahib</i> , Purification and characterization of lipoxygenase enzyme from Iraqi patients with type 2 diabetes mellitus.....	277
<i>N. J. Sai Varun, N. Sai Aishwarya Reddy, S. Pradeepa, H. S. Lalithamba. Srilatha Rao, G. K. Prashanth</i> , Eco-engineered ZnO nanoparticles via <i>Convolvulus prostratus</i> with Al- and Zr-doping: structural, mechanical, and antibacterial enhancement for sustainable construction applications.....	282
<i>A. T. Angelov, S. G. Bratkova, K. T. Nikolova, S. K. Plochev, P. G. Genova, R. V. Ivanov, P. G. Velichkova</i> , Efficiency of algae-assisted photo-bioelectrochemical system in anaerobic wastewater treatment.....	295
<i>S. M. Al-Mahmoud</i> , One-step chemical modification of pine cones for the removal of methyl orange from aqueous media.....	302
<i>T. Oyegoke</i> , Computational study of propane dehydrogenation into propylene over chromium oxide via a combined use of central composite design & microkinetic simulation.....	309
<i>Priyanshu, M. M. Mandal</i> , Modeling of blood flow in a stenotic artery using nanoparticles... <i>G.K. Prashanth, H.S. Lalithamba, S. Rao, N.P. Bhagya, K.V. Rashmi, H. K. N. Akolkar</i> , Phytonano synthesis of MgO nanoparticles using aqueous leaf extract of <i>Hibiscus rosa sinensis</i> : comprehensive characterization and assessment of their antibacterial and anti-oncogenic activities.....	319
<i>V. V. Lyubomirova, I. N. Belovezhdova</i> , Fractionation of potentially toxic and essential elements in sewage sludge from wastewater treatment plants.....	331
<i>A. K. Mhaske, V. V. Vikhe, A. G. Gadhave, Y. R. Baste, B. K. Uphade</i> , Efficient synthesis of 5-oxo-5,6,7,8-tetrahydro-4 <i>H</i> -chromenes using zinc ferrite nanoparticles as a catalyst.....	339
<i>AUTHORS INDEX</i>	348
<i>SUBJECT INDEX</i>	358
<i>INSTRUCTIONS TO AUTHORS</i>	361
	363